REPUBLIQUE ALGERIENNE DEMOCRATIQUE ET POPULAIRE
MINISTERE DE L'ENSEIGNEMENT SUPERIEUR ET DE LA RECHERCHE SCIENTIFIQUE

UNIVERSITE ABOU-BEKR BELKAID - TLEMCEN

THÈSE

Présentée à :

FACULTE DES SCIENCES – DEPARTEMENT DE CHIMIE

Pour l'obtention du diplôme de :

DOCTORAT EN SCIENCES

Spécialité : Chimie de L'environnement

Par :

M^lle BOUDGHENE STAMBOULI Ghizlene

Sur le thème

Adsorbants fonctionnels : Application au traitement d'effluents aqueux

---

Soutenue publiquement le /10/2025 à Tlemcen devant le jury composé de :

M^me BEDRANE Sumeya	Professeur	Université de Tlemcen	Présidente
M^r BENGUELLA Belkacem	Professeur	Université de Tlemcen	Directeur de thèse
M^r MAKHOUKHI Benamar	Professeur	Université de Tlemcen	Co-Directeur de thèse
M^me BOUHADJERA Keltoum	Professeur	Université de Sidi bel Abbés	Examinatrice
M^me HAMZA REGUIG Sanaa	Professeur	Université de Tlemcen	Examinatrice
M^r AIT AMER Ahcene	MCA	Université de Sidi bel Abbés	Examinateur
M^r AYMANE HELMY Kamel	Professeur	Université de Bahrain	Invité

Laboratoire Chimie Inorganique et Environnement (L.C.I.E)
BP 119, 13000 Tlemcen - Algérie

REMERCIEMENTS

« La science est une œuvre collective, et nul ne peut prétendre accomplir seul un tel voyage. »

En premier lieu, je rends grâce à Dieu Tout-Puissant, source de toute force et de toute sagesse, pour m'avoir accordé la santé, la persévérance et la détermination nécessaires pour mener à bien ce travail de recherche. Sans Son soutien, ce long chemin n'aurait pu être parcouru.

Je tiens à exprimer ma profonde gratitude à mon directeur de thèse, Monsieur Benguella Belkacem, Professeur à l'université de Tlemcen, pour son expertise, sa rigueur scientifique et son encadrement exceptionnel. Ses conseils éclairés, sa disponibilité et son soutien indéfectible ont été des piliers essentiels dans l'accomplissement de ce travail. Qu'il trouve ici l'expression de ma plus haute considération pour la confiance qu'il m'a accordée et pour l'honneur de diriger mes recherches.

Je tiens à remercier chaleureusement mon co-directeur de thèse, Monsieur le Professeur Makhoukhi Benamar, professeur à l'Université de Tlemcen, pour ses orientations précieuses, son engagement constant et ses remarques constructives qui ont grandement contribué à l'enrichissement de ce travail. Son accompagnement bienveillant et son soutien inestimable ont été d'une aide précieuse tout au long de ce parcours.

Je tiens à adresser mes remerciements les plus sincères à Monsieur le Professeur Ayman Helmy Kamel, professeur de chimie analytique à l'Université de Bahreïn, pour son accompagnement précieux et son soutien constant tout au long de mon stage d'étude. J'ai énormément appris à ses côtés, tant sur le plan scientifique que méthodologique. Son expertise, sa disponibilité et sa bienveillance ont été d'une grande richesse pour mon parcours. Son encadrement a représenté un véritable repère, et je lui suis profondément reconnaissante pour tout ce qu'il m'a apporté.

Ma reconnaissance va également aux membres du jury, éminents professeurs et chercheurs, qui ont accepté de consacrer leur temps à l'évaluation de ce travail. Leurs critiques et suggestions seront autant de pistes pour poursuivre et approfondir cette recherche.

Je n'oublie pas mes frères et sœurs, ma famille et mes amis (e), qui ont été une source de réconfort et de motivation tout au long de ce parcours exigeant. Leurs mots d'encouragement et leur présence ont illuminé les moments de doute.

Je souhaite également exprimer ma gratitude à l'ensemble de mes collègues aux laboratoire de **Chimie Inorganique et Environnement** (LCIE) ainsi que laboratoire **d'Application des Electrolytes et des Polyélectrolytes Organiques** (LAEPO) et **laboratoire de Catalyse et Synthèse en Chimie Organique** (LCSCO) de l'Université Aboubekr Belkaid de Tlemcen, pour leur aide précieuse lors des analyses des matériaux, la mise à disposition des produits chimiques, ainsi que pour les échanges scientifiques enrichissants. L'ambiance de travail stimulante et l'esprit de camaraderie qui ont régné tout au long de cette expérience ont largement contribué à la richesse de cette aventure scientifique. À tous ceux qui, de près ou de loin, ont contribué à la réalisation de ce projet, qu'ils trouvent ici l'expression de ma sincère reconnaissance.

« Le savoir est une lumière qui se partage sans jamais s'éteindre. »

DEDICACE

Je dédie ce travail

A mes chers parents

Toutes les lettres ne sauraient trouver les mots qu'il faut... Tous les mots ne sauraient

Exprimer la gratitude, l'amour, le respect, la reconnaissance... Aussi, c'est tout simplement

Que je souhaite que Dieu vous préserve une longue vie.

A ma chère sœur et mes chers frères.

A tous les membres de ma famille, mes enseignants, mes collègues, a tous ceux qui me sont chers.

Table des Matières

Liste des Figures

Liste des Tableaux

Liste des Abréviations

LM : Lemna minor

ALM-P : Lemna minor activée avec l'acide phosphorique

ALM-C : Lemna minor activée avec l'acide citrique

PAOT: Poly [aniline + o-toluidine]

4-NP : 4-Nitrophénol

4-AP : 4-Aminophénol

DRX : Diffraction des rayons X

IRTF : Infrarouge à transformée de Fourier

BET : Brunauer, Emett et Teller

Sp : Surface spécifique

dhkl : Distance interfeuillet (Å)

q_e : Quantité d'adsorbât par gramme d'adsorbant à l'équilibre (mg/g)

q_t : Quantité d'adsorbât par gramme d'adsorbant à un temps t (mg/g)

K_f : Constante de vitesse d'adsorption pour le premier ordre (min-1)

Ks : Constante de vitesse d'adsorption pour le pseudo deuxième ordre ($g.min^{-1}.mg^{-1}$)

F : Nombre unidimensionnel

K_d : Coefficient de distribution de métal

ΔH : Variation de l'Enthalpie (cal/mole)

ΔS : Variation de l'Entropie (cal/mole K)

C_0 : Concentration initiale de l'adsorbât

C_e : Concentration à l'équilibre de l'adsorbât

R : Coefficient de corrélation

nm : Nanomètre

ppm : Parties par million

λ : Longueur d'onde (nm)

T : Température

pH : Potentiel d'Hydrogène

BRSM : Rouge-Bezaktiv

Introduction Générale

L'évolution technologique et industrielle a provoqué une augmentation importante de la pollution environnementale, nuisant gravement à la faune, à la flore et surtout aux ressources en eau. L'une des formes de pollution les plus préoccupantes est la pollution de l'eau, principalement due aux déversements industriels massifs provenant de secteurs tels que le textile, l'agrochimie, la pharmacie et la pétrochimie. L'industrie du textile rejette chaque année d'importantes quantités d'eaux usées fortement chargées en colorants organiques, dont une part importante est directement déversée dans l'environnement aquatique sans traitement adéquat. Ces colorants sont toxiques et cancérigènes, leurs décompositions est difficile à cause de la complexité de leurs structures moléculaires. Les composés organiques aromatiques tels que le 4-nitrophénol (4-NP), fréquemment employés dans la fabrication de pesticides, de plastifiants, de teintures et de médicaments, constituent également un facteur significatif de la pollution aquatique.

Le 4-NP est une substance très toxique en raison de ses impacts sur la santé humaine. La difficulté d'élimination de ce produit chimique, due à sa forte solubilité et stabilité dans l'eau, met en évidence la nécessité à développer des techniques de dépollution durables et respectueuses de l'environnement.

Cette étude se porte sur l'évaluation de deux techniques de dépollution des rejets contaminés, l'adsorption et la réduction catalytique. La première approche est basée sur l'adsorption, une technique physico-chimique économique et simple à mettre en œuvre, fréquemment choisie pour sa capacité à retenir les polluants et la possibilité de régénérer le matériau adsorbant. Parmi les adsorbants on peut citer, les débris végétaux riches en lignine et cellulose, sont couramment employés comme matières premières pour la fabrication de charbons actifs, grâce à leur abondance et leur faible impact environnemental.

La lentille d'eau (Lemna minor), une plante aquatique à croissance rapide, constitue une ressource prometteuse dans ce secteur. Ses caractéristiques physico-chimiques et son aptitude à absorber les métaux lourds font d'elle un matériau parfait pour la production de charbons actifs. L'activation par l'acide phosphorique et citrique conduit à la production d'un matériau fortement mésoporeux, possédant une large surface spécifique, ce qui améliore l'élimination de teintures complexes telles que le Rouge-BEZAKTIV (BRSM).

Ainsi, cette thèse doctorale suggère une étude comparative entre deux approches de dépollution qui s'inscrivent dans une démarche durable :

- L'élimination d'un colorant textile par adsorption sur des charbons actifs issus de Lemna minor chimiquement modifiée.
- La transformation catalytique du 4-nitrophénol en 4-aminophénol s'effectue à l'aide d'un composite composé de ferrite de nickel recouvert de poly (aniline-co-o-toluidine.

Ces deux approches complémentaires ont pour objectif de concevoir des solutions efficientes, accessibles et durables pour le traitement des eaux industrielles polluées, ce qui contribue à la préservation de l'environnement et à l'optimisation de ressources renouvelables.

Ce travail s'inscrit dans le cadre de la préparation et de l'application de nouveaux matériaux adsorbants et catalytiques destinés à la dépollution des eaux contaminées. L'idée de départ est d'exploiter, d'une part, un adsorbant naturel (Lemna minor) transformée en charbon actif par activation acide, et d'autre part, un catalyseur nanocomposite magnétique à base de $NiFe_2O_4$ recouvert de poly(aniline-co-o-toluidine). Cette double approche vise à valoriser des ressources renouvelables et à développer des matériaux efficaces et économiques pour l'élimination de polluants organiques.

Notre travail est structuré autour de deux grandes parties :

- **La première partie** concerne la préparation et la caractérisation de **Lemna minor** activée par acide phosphorique et acide citrique, et son application dans l'adsorption d'un colorant anionique (Rouge-Bezaktiv).
- **La deuxième partie consacrée** à la synthèse et à l'application d'un nanocomposite **$NiFe_2O_4$/ poly(aniline-co-o-toluidine)**, utilisé comme catalyseur pour la réduction du 4-nitrophénol, un polluant organique toxique et persistant.

Chapitre I :

Étude Bibliographique

Partie I : les matériaux

Les Plantes

1. Introduction sur les plantes

Les plantes aquatiques jouent un rôle très essentiel dans la dépollution des eaux usées [1], grâce à leur capacité naturelle à adsorber, accumuler, absorber et dégrader différents polluants présents dans l'eau [2]. Ces plantes, comme les jacinthes d'eau [3], les lentilles d'eau [4], Lotus [5], Azolla [6], Spiruline [7], Chlorelle vulgaris [8] et les roseaux [9], Ont la capacité d'éliminer des substances toxiques telles que les métaux lourds, les pesticides, les colorants. Ces plantes agissent comme des bio-filtreurs naturels ce qui permet d'améliorer la qualité de l'eau [10]. En outre, les plantes aquatiques contribuent à l'oxygénation et à l'équilibre des écosystèmes aquatiques, ce qui favorise la biodiversité et l'équilibre des écosystèmes aquatiques. Leur intégration dans les systèmes de traitement des eaux usées représente une approche durable et écologique [11], offrant une alternative aux méthodes de dépollution classiques et contribuant à la préservation des ressources en eau. Ces dernies poussent rapidement et produisent une énorme quantité de biomasse, qui peut être utilisée dans diverses domaines.

2. Divers types de plantes

Plusieurs plantes aquatiques sont d'un grand intérêt dans plusieurs secteurs, y compris la médecine, les études scientifiques et le traitement des eaux résiduaires. On compte parmi elles la Spiruline, l'Azolla et Lemna minor, qui disposent de caractéristiques distinctes appropriées à diverses applications.

2.1. Spiruline

Algue microscopique de couleur bleue verte en forme spirale [12], qui pousse spontanément sur les eaux riches en azote et en sels minéraux des régions semi-arides, notamment en Afrique. Apparue sur Terre il y a environ 3,5 milliards d'années, est une espèce de cyanobactéries, très reconnus dans le domaine médical. La spiruline contient autant de protéines qu'un œuf.

Figure I. 1. Microalgue Spiruline

➢ **Domaine d'applications**

- **Médecine et santé** : La spiruline a des effets bénéfiques pour la santé tels que les maladies cardiaques (accidents vasculaires, l'athérosclérose) **[13]**, diminution des inflammations renforcement du système immunitaire, régulation de glycémie **[14]**.
- **Traitement des eaux usée :** Traiter les effluents organiques et inorganique par adsorption **[15, 16].**
- **Recherche scientifique** : Les études biologiques Cellulaires **[17]**, recherche sur les effets des nutriments et des compléments alimentaires **[18]**.

2.2. Azolla

L'Azolla est une petite fougère aquatique. Grâce à une bactérie appelée « algue bleu-vert » qui se développe sur ses feuilles, elle se nourrit principalement de l'azote de l'air **[19].** Elle fertilise les rizières inondées. La culture du riz en présence d'Azolla permet d'éviter les pertes d'eau par évaporation, supprime le désherbage et apporte une augmentation des bénéfices d'environ 50 % sur deux cycles culturaux par rapport aux cultures traditionnelles **[20]**.

Figure I. 2. Plante aquatique Azolla

➢ **Domaine d'applications**

- **Médecine et santé :** Contient 20% de protéine, des substances bioactifs jouent un rôle thérapeutique, et aussi des antioxydants qui pourraient réduire le stress oxydatif **[21].**
- **Traitement des eaux usées** : Traiter les eaux polluantes par les pesticides, les colorants, les métaux lourds **[22]**.
- **Recherche scientifique :** Augmentation du rendement de l'agriculture sachant qu'elle est utilisée dans la culture du riz **[23-25],** enrichissement le sol en azote, réduction des gaz à effet de serre, production du biogaz. De plus, elle est un nutriment animal et humain.

2.3. Lemna minor

La lentille d'eau est une plante aquatique de petite taille, flottant librement à la surface des milieux d'eau douce. Appartenant à la famille des Lemnaceae, elle se caractérise par des frondes de forme ovale ou circulaire, dont la superficie ne dépasse généralement que quelques millimètres carrés. Cette espèce présente une croissance particulièrement rapide, ce qui la rend propice à des applications environnementales telles que le traitement des eaux usées. Facile à cultiver et à maintenir, elle montre une grande capacité d'adaptation à divers environnements aquatiques.

Par ailleurs, la biomasse végétale issue de ces systèmes de traitement peut être valorisée de manière durable, notamment comme aliment pour les poissons et le bétail, ou encore utilisée comme fertilisant naturel en agriculture **[26].**

Figure I. 3. Plante aquatique Lemna minor

- **Domaine d'applications**
  - **Médecine et santé :** Propriétés antioxydantes et anti-inflammatoires, traiter les affections cutanées, les maladies respiratoires, les rhumatismes, sources de vitamines et minéraux, (B12, K, Fe, Mg) et aussi de protéine végétale **[27].**
  - **Traitement des eaux usées :** Améliorer la qualité des eaux par adsorption des métaux lourds (Cd, Zn, Cu, Ni, Pb), les colorants (Bezaktive, bleue de méthylène, black five…) adsorber les phosphates et azotes, prolifération d'algues nocives, et améliore les conditions de l'écosystème aquatique **[28].**
  - **Recherche scientifique :** Production de bioplastique et biocarburant, bétail pour les poissons, les vaches, et les moutons production de protéine végétales, applications médicales, agriculture, épuration d'eau **[29].**
- **Intérêts d'utilisation** : Lemna minor présente des atouts principaux dans le traitement des eaux contaminées grâce à : sa facilité de culture, croissance rapide et adaptée aux milieux environnementaux aquatiques variés, sa capacité à adsorber les polluants de différents

natures. C'est une biomasse végétale non toxique et s'intègre parfaitement aux installations industrielles de traitement des effluents, elle peut être recycler sous forme d'engrais organique contribuant à diminuer l'usage d'engrais chimiques onéreux et potentiellement nocifs pour l'environnement **[30]**. Elle représente une voie prometteuse vers le développement de carburants renouvelables et moins polluants, car elle peut être transformer en biogaz ou en bioéthanol **[31]**. De plus, l'économie de Lemna minor fait partie d'un modèle en plein essor, en particulier, en raison de son faible cout qui rend le procédé de traitement plus rentable **[32].** Suite à ces avantages, cette plante a été choisi comme un biomatériau de traitements des effluents dans cette étude.

3. Description de Lemna minor

Lemna minor est une plante flottante qui possède de petites feuilles ovales de 2 à 3 mm de diamètre et de 2 à 5 mm de longueur. Ces feuilles sont remplies d'air, ce qui permet à la plante de flotter, sa face aérienne est vert clair et en-dessous vert foncé avec des racines plongeantes blanche elle sert à stabiliser la plante et récupérer les nutriments dans l'eau sa croissance est très rapide, si les conditions lui convient-elle deviens rapidement envahissante, préfère les plans d'eau plutôt stagnante ou très peu de courant **[33].**

Les noms communs : Arabe : عدس الماء; Français : Lemna minor ; Anglais : Duckweed.

➢ **Répartition**

La plante aquatique Lemna minor est répandue dans différents écosystèmes à l'échelle mondiale **[33] :**

- **Afrique** : (Algérie, Égypte, Libye, Maroc, Tunisie, Éthiopie, Soudan, Kenya, Ouganda, Rwanda, Zaïre, Mozambique et Afrique du Sud, Soudan, Kenya, Ouganda, Rwanda, Zaïre Mozambique et Afrique du Sud),
- **Asie** : (Yémen, Afghanistan, Iran, Irak, Palestine, Jordanie, Liban, Syrie, Turquie, Azerbaïdjan, Géorgie, Kazakhstan, Kirghizstan, Tadjikistan, Ouzbékistan, Fédération de Russie, Chine, Inde, Népal et Pakistan),
- **Europe** : (Danemark, Finlande, Irlande, Norvège, Suède, Royaume-Uni, Autriche, Belgique, République tchèque, Allemagne, Hongrie, Liechtenstein, Luxembourg, Pologne, Slovaquie, Suisse, Belarus, Estonie, Lettonie, Lituanie, Moldavie, Fédération de Russie, Fédération de Russie-Partie européenne, Ukraine, Albanie, Bosnie, et Herzégovine, Bulgarie, Croatie, Grèce, Italie, Monténégro, Roumanie, Serbie, Slovénie, France, Portugal et Espagne),

- **Amérique du Nord** : États-Unis et Canada.

➢ **Habitat et physiologie de croissance**

Lemna minor peut vivre dans des eaux très variées avec un intervalle de pH 6 à 8 et une dureté jusqu'à 15°TH, et la température idéale pour sa croissance est situé entre (18-26) °, elle supporte aussi bien les températures très élevées en été que les températures très basses en hiver. De plus, elle a besoin de lumière et ne nécessite pas d'apport en CO_2, qu'elle capte directement dans l'air grâce à ses feuilles aériennes **[34-35].**

➢ **Composition chimique**

Lemna minor reconnue par sa richesse en protéines végétales, ce qui en fait un excellent complément nutritionnel. Elle est aussi intégrée dans l'alimentation animale (volaille, poissons, bétail) et envisagée comme une source de protéines pour l'alimentation humaine**.** Les tableaux suivants montrent analyse chimique et éléments nutritifs de Lemna minor **[33].**

Tableau I. 1: La Composition nutritionnelle de Lemna minor

Constituant	**Teneur**
Protéines brutes	16–45 %
Matières grasses	4.0–4.4 %
Acide p-coumarique	0.015 %
Fibres	8–10 %
Cendres	4–5 %
Caroténoïdes	Présents
Iode (ions iodure)	0.0294 ± 0.001 %
Flavonoïdes (lutéoline-7-glucoside)	0.38 ± 0.01 %

Tableau I. 2: Teneur en éléments minéraux de Lemna minor (mg/100 g)

Élément	**Teneur (mg/100 g)**
Calcium	4990
Potassium	—
Silicium	2495
Sodium	1870

Magnésium	155
Fer	934
Phosphore	515
Aluminium	0.93
Manganèse	935
Nickel	0.93
Cuivre	0.78
Plomb	0.03
Molybdène	0.02
Zinc	0.01

Tableau I. 3: Composition en acides aminés de Lemna minor

Type d'acides aminés	**Proportion (%)**
Essentiels	39.20
Non essentiels	53.64
Non protéinogènes	7.13
Leucine, isoleucine, valine	48.67
Acide glutamique	25.87
Autres (citrulline, hydroxyproline, taurine, histidine, lysine, méthionine, phénylalanine, thréonine, tryptophane)	Présents

Les polymères

1. Introduction sur les polymères

Les polymères sont des macromolécules qui se constituent par la succession de monomères, unis par des liaisons covalentes. Ils ont une importance cruciale dans différents domaines industriels et technologiques grâce à leurs caractéristiques distinctives et leur large variété de structures. On les observe sous des formes naturelles (comme les protéines, cellulose et la chitine) ou synthétiques (telles que le polyéthylène, nylon, et l'aniline) **[36].**

2. Classification des polymères selon leur origine

On peut diviser les polymères en trois grandes catégories selon leur origine **[37-38].**

- Polymères naturels : présents dans la nature, souvent produits par des organismes vivants, comme amidon, cellulose, protéines, ADN, et caoutchouc naturel.

- Polymères synthétiques : fabriqués par des procédés chimiques, Comme polyéthylène (PE), polystyrène (PS), nylon, et poly aniline (PANI).

- Polymères semi-synthétiques : dérivés de polymères naturels modifiés chimiquement, comme acétate de cellulose, chitosane, chitine, et nitrocellulose.

Parmi les polymères synthétiques, la polyaniline (PANI) s'est progressivement imposée comme un matériau de choix, en raison de ses performances physico-chimiques. Les polymères conducteurs sont devenus des sujets de recherche majeurs en raison de leurs multiples domaines d'application potentiels.

3. Polyaniline

La polyaniline (PANI) est un polymère conducteur appartenant à la catégorie des matériaux conjugués, et se distingue par sa propriété d'adopter divers états d'oxydation. Cette caractéristique lui permet d'avoir une conductivité modifiable en fonction de son état de dopage et de son contexte électrochimique. Malgré son potentiel technologique actuel, sa découverte date du XIXe siècle, période à laquelle Runge a effectué la première synthèse en 1834 **[39]**. La préparation peut être réalisée par des moyens chimiques ou électrochimiques, chaque technique ayant un impact sur la morphologie, la structure et les caractéristiques finales du matériau.

Depuis les années 1980, la PANI est régulièrement étudiée grâce à ses résultats prometteurs dans divers domaines tels que les capteurs, le stockage d'énergie, les dispositifs électroniques et la catalyse. Sa stabilité chimique et son coût en font un matériau très prisé en recherche appliquée **[39].**

- **Domaine d'application**

La polyaniline (PANI) est reconnue pour son efficacité dans le domaine du traitement des eaux usées, en raison de la présence des groupes fonctionnels tels que les amines et les imines, lui permettent d'interagir efficacement avec une large gamme de polluants, organiques ou inorganiques. Elle peut être exploitée telle quelle ou incorporée dans des matériaux composites, notamment en association avec des oxydes métalliques **[40],** du graphène ou encore des polymères d'origine naturelle. Ces combinaisons favorisent une adsorption sélective et efficace **[41].**

Pour améliorer ses performances, en particulier dans les procédés catalytiques, la PANI peut être modifiée par copolymérisation avec des monomères aromatiques substitués comme l'o-toluidine. Ce composé organique, issu de l'aniline et caractérisé par un groupement méthyle en position ortho du noyau benzénique **[42]**, influence la configuration électronique du polymère. La copolymérisation de l'aniline avec l'o-toluidine permet ainsi d'obtenir le poly(aniline-co-o-toluidine) (POAT) **[43]**, un matériau hybride aux propriétés électroniques et structurales améliorées, ouvrant la voie à des applications avancées en catalyse environnementale.

4. Le Poly (aniline-co-o-toluidine)

Le poly(aniline-co-o-toluidine) est un copolymère conducteur obtenu par la réaction de copolymérisation de la poly aniline (PANI) et de l'o-toluidine. Ce matériau fusionne les caractéristiques des deux monomères, créant un polymère possédant de meilleures performances électriques.

- **Meilleure solubilité et stabilité** comparativement à la poly aniline pure, améliorant ainsi ses performances dans divers environnements **[44].**
- **Capacité de dopage élevée**, permettant d'ajuster ses propriétés électriques en fonction des besoins spécifiques **[45].**
- **Excellente compatibilité avec les oxydes métalliques**, facilitant ainsi la création de composites aux fonctionnalités avancées **[46].**

Les Spinelles

1. Introduction sur les spinelles

Les composés appartenant à la famille des spinelles représentent une classe importante d'oxydes métalliques cristallisant selon une structure cubique bien définie, de formule générale AB_2X_4 (A et B sont des cations et X un anion : O, S, Se, Te). Cette architecture cristalline particulière résulte de la répartition ordonnée de cations divalents et trivalents au sein des sites tétraédriques et octaédriques d'un réseau d'oxygène. Ce type de structure, modulable par substitution ionique, confère à ces matériaux une grande diversité de comportements physico-chimiques **[47]**.

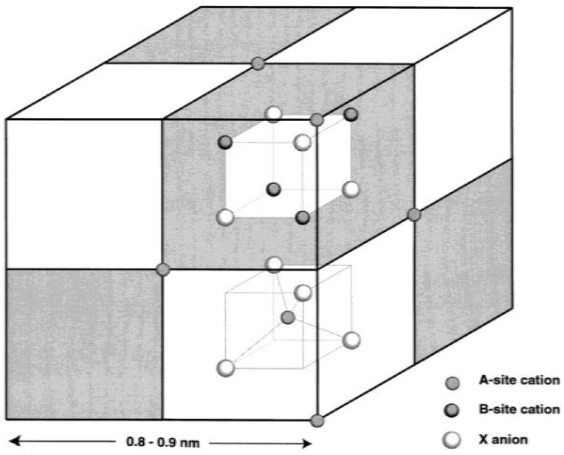

Figure I. 4. Structure générale des spinelles

2. Propriétés fonctionnelles et applications des spinelles ferrites

Les spinelles présentent une excellente stabilité thermique, une bonne résistance chimique, ainsi que des propriétés magnétiques et électroniques ajustables, ce qui les rend particulièrement adaptés à des domaines d'application variés. Parmi ceux-ci, on retrouve la catalyse hétérogène, la purification de l'eau, la détection magnétique, ou encore les dispositifs de stockage d'énergie. Des exemples notables incluent les ferrites tels que $NiFe_2O_4$ **[48]**, qui

font l'objet de nombreuses études pour leur comportement multifonctionnel et leur compatibilité avec des supports polymériques des systèmes hybrides.

2.1. Le Nickel Ferrite ($NiFe_2O_4$)

Le Nickel Ferrite est classé parmi les ferrites de type spinelle, sa structure cristalline bien organisée et ses remarquables propriétés magnétiques. Grâce à sa stabilité chimique, sa résistance aux milieux agressifs et ses capacités magnétiques, ce matériau trouve de nombreuses applications, notamment dans :

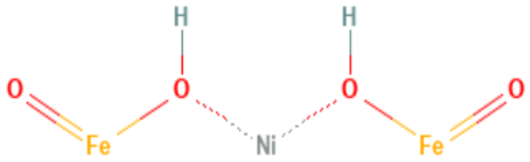

Figure I. 5. Nickel Ferrite ($NiFe_2O_4$)

- **Catalyse hétérogène**, où il joue un rôle clé dans la dégradation des composés organiques polluants **[49].**
- **Capteurs électrochimiques**, bénéficiant de sa conductivité modérée et de sa réponse magnétique ajustable **[50].**
- **Technologies environnementales**, notamment pour l'adsorption et l'élimination des contaminants présents dans les milieux aqueux **[48].**

3. Matériaux Hybrides à Base de Nickel Ferrite et Copolymère Conducteur

Les matériaux composites combinant des oxydes métalliques et des polymères conducteurs suscitent un intérêt important en raison de leurs caractéristiques physico-chimiques uniques. Parmi ces matériaux hybrides, le nickel ferrite ($NiFe_2O_4$), un oxyde mixte de fer et de nickel reconnu pour ses propriétés magnétiques **[51],** et catalytiques, se distingue par sa stabilité et sa polyvalence. Lorsqu'il est couplé au poly(aniline-co-o-toluidine), un copolymère dérivé de la polyaniline (PANI) connu pour sa conductivité et sa facilité de dopage, il en résulte un matériau fonctionnalisé aux propriétés améliorées. Cette synergie confère au composite des avantages notables en matière de performances électrochimiques, de capacité d'adsorption et d'activité catalytique, le rendant particulièrement adapté aux domaines du stockage d'énergie, du traitement des polluants et des capteurs avancés **[51]**.

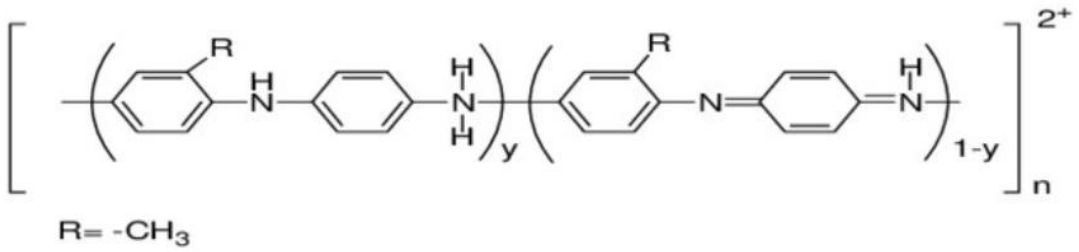

Figure I. 6. Poly(aniline-co-o-toluidine)

3.1. Propriétés synergiques d'un composite à base de nickel ferrite et de poly(aniline-co-o-toluidine)

L'association du nickel ferrite et du poly(aniline-co-o-toluidine) repose principalement sur des techniques telles que la polymérisation in situ ou le revêtement des nanoparticules d'oxyde par le polymère. Ce composite présente plusieurs avantages synergiques, notamment

- **Activité catalytique renforcée**, due aux interactions entre la structure du polymère et la surface active de la ferrite **[52].**
- **Applicabilité dans le domaine des supercondensateurs**, où la combinaison des propriétés conductrices du polymère et de la réponse magnétique de la ferrite offre des performances optimales **[53].**
- **Potentiel en adsorption et en remédiation environnementale**, grâce à la complémentarité des interactions chimiques entre le polymère et les sites actifs de la ferrite **[54].**

Partie II : Les Polluants

Les colorants

1. Introduction sur les colorants

William Henry Perkin a découvert la Mauveine en 1856, un dérivé de l'aniline qui est un colorant basique, c'était le tout premier colorant synthétique de l'histoire, alors qu'il cherchait à synthétiser la Quinine, un médicament utilisé pour soigner la Malaria, un fléau qui affecte de nombreux pays tropicaux.

Au 21e siècle, la prédiction des couleurs a connu une croissance grâce à la présence de nombreux fabricants de pigments et de colorants **[55]**.

2. Définition :

Nous vivons dans un monde où tout est coloré nos aliments, vêtements, produits cosmétiques, et pharmaceutiques etc. un colorant est une substance organique naturel ou synthétique capable de colorer un matériau de maniéré persistante ou permanente **[56]**, généralement sous forme de poudre, liquide ou pate. Ce dernier agit en absorbant certaines longueurs d'onde de la lumière et en réfléchissant d'autres, il permet à l'œil humain de percevoir une couleur particulière. Leurs propriétés sont liées à la composition chimique du colorant et plus précisément aux groupements chromophores et auxochromes qu'ils contiennent. Les groupes chromophores présentent dans un colorant sont responsable de l'absorption de la lumière visible, ce qui conduit à l'apparition d'une couleur, les auxochromes sont des groupes fonctionnels attachés à la structure du chromophore qui modifie la capacité de ce dernier à absorber la lumière, ils peuvent aussi intensifier la couleur ou en changer la teinte **[57]**.

3. Classification des colorants

- **Selon la structure chimique**

Le classement chimique des colorants repose sur la nature du groupe chromophore qu'ils contiennent **[57]**. Le chromophore est constitué de groupes d'atomes dont les plus courants sont les groupes nitro (─NO_2), azo (─N═N─), nitroso (─N═O), thiocarbonyle (─C═S), carbonyle (─C═O), ainsi que les alcènes (─C═C─). L'absorption des ondes électromagnétiques par le chromophore est due à l'excitation des électrons d'une molécule **[58]**.

Tableau I. 4: les principaux groupes chromophores et auxochromes des colorants organiques classés par intensité croissante [57].

Groupements Chromophore	Groupements Auxochrome
Azo –N=N–	Amine tertiaire – N– R_2
Azométhine –CH= N–	Amine secondaire – NHR
Azoxy –N=N=O	Amine primaire – NH_2
Nitor – NO_2	Hydroxyle – OH
Nitroso – N= O	Metoxy – OCH_3
Carbonyl CO	Iode – I
Thio CS	Brome – Br
Ethényl C=C	Chlore – Cl

Divers colorants

- **Les colorants azoïques** : Caractérisés par la présence de la molécule d'un groupement azoïque (-N=N-) reliant deux noyaux benzéniques, représentent plus de 25 % de la production mondiale de matières colorantes **[59]**.

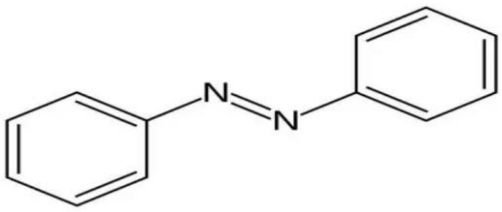

Figure I. 7. Structure du l'azobenzène.

- **Les colorants anthraquinone** : sont importants après les colorants azoïques. Leur formule générale dérivée de l'anthracène.

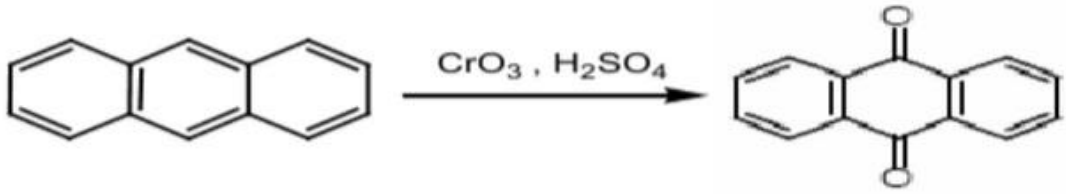

Anthracéne Anthraquinone

- **Les colorants indigoïdes** : Colorant organique appartenant à la famille des colorants vat (ou colorants de cuve).

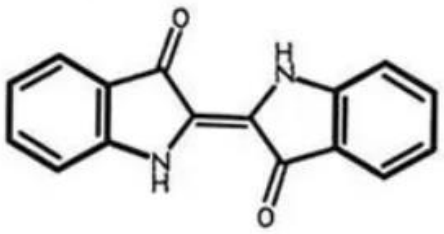

Figure I. 8. Structure de l'indigo.

- **Colorants xanthène** : Les xanthènes présentent des propriétés intéressantes en raison de leur structure moléculaire, ce sont des composés organiques tricycliques, leur noyau xanthène est composé de deux cycle benzénique fusionnés. Ils présentent des propriétés fluorescentes, pouvant émettre de la lumière une fois exposés à certaine longueur d'onde **[60]**.

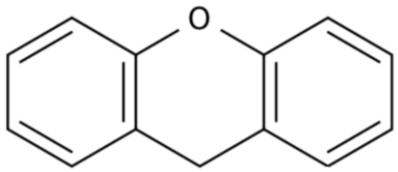

Figure I. 9. Structure du xanthène.

- **Colorants phtalocyanines (métallifères)** : Les colorants phtalocyanines sont utilisés comme colorants en alimentaire, cosmétique, textile et impression. Ils possèdent une structure complexe avec un atome métallique central et sont synthétisés par la réaction du dicyanobenzène en présence d'un halogénure métallique (Cu,Ni, Co, Pt, etc.) **[61].**

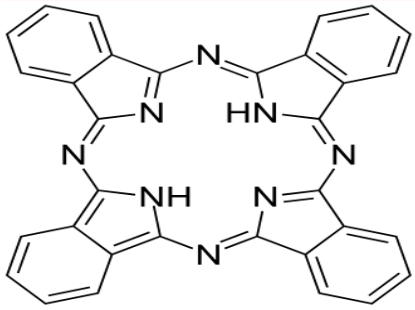

Figure I. 10. Structure du phtalocyanine.

- **Colorants nitrés et nitrosés** : Les colorants nitrés et nitrosés sont une classe très limitée de colorants et plutôt vielle, ils sont encore utilisés actuellement vu leurs prix abordables. Leur structure moléculaire est simple est caractérisée par la présence d'un groupe nitro (NO_2) en position ortho par rapport à un groupement électro donneur (hydroxyle ou aminés) **[62]**.

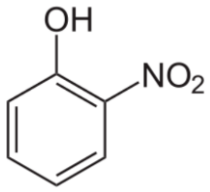

Figure I. 11. Structure de l'ortho nitrophénol.

- **Selon la solubilité**
  - **Colorants acides ou anionique** : Solubles dans l'eau, ils sont souvent utilisés pour colorer les fibres animales comme la soie la laine, cachemire, ainsi que pour colorer produits cosmétiques, et les produits aliments **[63].**

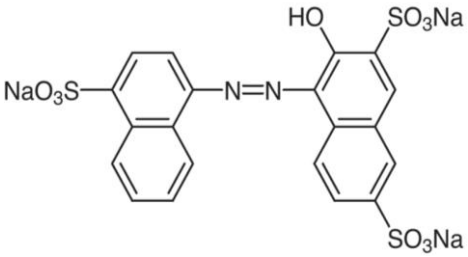

Figure I. 12. Structure du rouge acide 27.

  - **Colorants basiques ou cationique :** Solubles dans les milieux basiques (alcalins), ils sont utilisés pour colore le cuir, les papiers, les vitres **[64].**

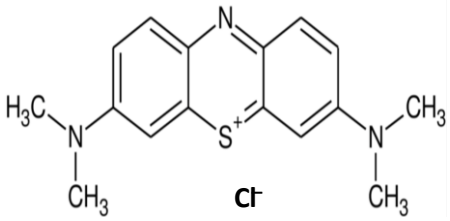

Figure I. 13. Structure du bleu de méthylène.

  - **Colorants directs :** Appliqués directement sur les textiles sans nécessiter de mordant (substance fixante), et généralement utilisé pour teindre les tissus en coton **[65].**

- **Selon la nature**
  - **Colorants naturels : Animaux** (Cochenille (rouge), cerf (noir de cerf), calcination d'os animaux (noir d'ivoire)). **Végétales (**les feuilles (verts), curcuma (jaune), indigotier (bleu)) **[66].**
  - **Colorants synthétiques :** Colorants xanthène, Colorants nitrés et nitrosés, Colorants Bezaktiv-He **[67].**

4. Toxicité des colorants sur l'environnement et la santé humaine

Au cours des dernières décennies, la quantité des colorants synthétiques produite à l'échelle mondiale atteint 800 000 tonnes par an **[68-69]**. L'industrie textile est l'une des sources les plus polluantes avec des rejets qui dépassent un million de mètre cubes par an **[70]**, en effet, la teinture textile utilise d'importants volumes d'eau et génère des rejets significatifs de colorants dans les milieux aquatiques. **[69]**. Ces derniers présentent un danger extrême vis-à-vis la faune, la flore, et par conséquence l'homme à travers la chaine alimentaire, de plus de leur toxicité, sont aussi cancérigènes en raison de leurs structures complexes les rendent faiblement biodégradables et à la teneur en groupements aromatiques, cyanurés, et de plomb.

- Dangers à court terme
  - La turbidité et l'odeur dues à l'accumulation des matières colorantes dans l'eau **[70]**.
  - Irritations cutanées, intoxications et réactions allergiques **[71]**.
  - L'eutrophisation ainsi que la sous oxygénation **[72]**.
  - Inhibition de la photosynthèse et perturbation des mécanismes naturels **[73]**.
- Dangers à long terme
  - La persistance ainsi que la bioaccumulation dues à leurs poids moléculaires élevés ainsi qu'à leurs structures complexes **[74]**.
  - La formation de sous-produits de chloration causant le cancer des poumons, du foie, de la peau et les reins **[75]**.
  - Perturbation endocrinienne **[75]**.
  - Maladies chroniques **[75]**.

5. Méthodes de traitement des eaux colorées

Le contrôle de la pollution des eaux est devenu très important ces dernières années, de nombreux travaux ont eu pour but de réduire ou éliminer la propagation de ces colorants par divers méthodes et techniques **[76]** :

- Les procédés physiques, comportant des méthodes de précipitation (coagulation, floculation, sédimentation), l'osmose inverse-filtration, l'adsorption (plante aquatique, charbon actif, argile), et l'incinération…
- Les procédés chimiques, en utilisant un traitement d'oxydation (ozone, oxygène), échange d'ions, complexation…

- Les procédés biologiques, en utilisant un traitement aérobie (présence d'oxygène) ou anaérobie (absence d'oxygène) …

Les nitrophénols

1. Introduction sur les nitrophénols

Les nitrophénols sont les matières premières les plus utilisées dans les industries chimiques, pharmaceutiques et pesticides. En raison d'une mauvaise gestion des déchets et d'une utilisation excessive, le nitrophénol est classé comme polluant important et a suscité l'intérêt de la recherche scientifique.

2. Définition

Le nitrophénol est composé d'un cycle benzénique, de groupes nitro (NO_2) et de groupes hydroxyles (-OH), et trouve de nombreuses applications dans la préparation de pesticides, peintures, produits pharmaceutiques, et colorants. Les composés nitrophénolés sont moins solubles dans l'eau et sont très toxiques et constituent une menace pour les humains et les organismes aquatiques en raison de leur nature inhibitrice et bio-réactive **[77].**

Example le 4-Nitrophenol est un sous-produit industriel, notamment issu de la dégradation des insecticides organophosphorés comme le parathion et le méthyl-parathion. Il est également rejeté lors de certaines réactions de combustion et dans les effluents industriels. Sa présence dans les milieux aquatiques et les sols peut engendrer des perturbations écologiques, affectant les écosystèmes et la biodiversité. Chez l'homme, une exposition prolongée peut induire des troubles hépatiques, neurologiques et respiratoires **[78].**

Figure I. 14. Structure du 4-Nitrophenol

3. Classification de nitrophénols

Les nitrophénols peuvent être classés selon le nombre de groupes nitro présents sur leur structure aromatique, donnant lieu à trois catégories : mono-nitrophénols, di-nitrophénols et tri-nitrophénols **[73-79].**

- **Mono-nitrophénols**

Ces composés sont des isomères structuraux contenant un seul groupe nitro positionné en ortho, méta ou para sur le cycle benzénique. Les principaux représentants sont le 2-nitrophénol (ortho), le 3-nitrophénol (méta), et le 4-nitrophénol (para), parmi ceux-ci, le 2-nitrophénol et le 4-nitrophénol sont connus pour leur toxicité élevée.

- **Di-nitrophénols**

Ils se caractérisent par la présence de deux groupes nitro fixés à différentes positions sur le noyau aromatique. On en compte six isomères : le 2,3-, 2,4-, 2,5-, 2,6-, 3,4-, et 3,5-dinitrophénol, parmi eux, le 2,4-dinitrophénol est particulièrement utilisé dans les procédés industriels pour la fabrication de colorants soufrés, des pesticides et des médicaments**.**

- **Tri-nitrophénols**

Leur structure dépend des emplacements des trois groupes nitro sur l'anneau benzénique. L'isomère 2,4,6-trinitrophénol, légèrement soluble dans l'eau, est largement employé dans la production de colorants acides, de produits phytosanitaires, d'astringents, d'explosifs et comme carburant pour fusées.

Ces composés sont des polluants environnementaux persistants, retrouvés à la fois dans le sol et dans l'eau. En raison de leur faible biodégradabilité.

4. Toxicité des produits nitrés sur l'environnement et la santé humaine

Le nitrophénol est un composé chimique nocif souvent rejeté dans l'environnement à cause d'une mauvaise gestion des déchets industriels. Il peut contaminer l'air, l'eau potable ou encore entrer en contact avec la peau, constituant ainsi plusieurs voies d'exposition pour l'homme. Une fois absorbé par inhalation, ingestion ou contact cutané, il pénètre dans la circulation sanguine et peut atteindre divers organes vitaux tels que le foie, les reins, le cerveau et les yeux **[79]**.

En termes d'environnement, le nitrophénol pose un problème majeur du fait de sa faible solubilité et de sa persistance dans les écosystèmes aquatiques. Il se dépose facilement au fond des cours d'eau, où il conserve sa toxicité même après dilution. Les sources de pollution incluent les émissions directes, le ruissellement agricole et les précipitations contaminées dans l'atmosphère **[79]**.

5. Méthodes de traitement des eaux contaminées par les nitrophénols

La présence excessive de nitrophénols dans les ressources en eau représente un enjeu environnemental et sanitaire majeur. Pour réduire leur concentration et préserver la qualité de l'eau potable, plusieurs techniques de traitement ont été développées :

- **Procédés physico-chimiques :** représentent des méthodes performantes pour réduire la concentration des nitrophénols dans l'eau. Parmi les procédés les plus utilisés, l'adsorption, l'oxydation et la réduction.
  - **Adsorption** : Utilisation de matériaux adsorbants comme les charbons activés, les composites magnétiques et les nanomatériaux pour capturer et immobiliser la molécule **[80].**
  - **Réduction catalytique hétérogène** : Transformation du 4-NP en 4-aminophénol (4-AP) via des nano-catalyseurs à base de métaux nobles ou d'oxydes métalliques talque les **spinelles [81].**
  - **Oxydation avancée** : Techniques basées sur la photocatalyse, le procédé Fenton et l'ozonation, permettant une dégradation efficace en produits non toxiques **[80].**
- **Traitements biologiques :** les traitements biologiques permettent d'éliminer naturellement les nitrophénols de l'eau. La dénitrification biologique utilise des micro-organismes anaérobies, les bio-filtres.
  - **Bioremédiation** : Utilisation de micro-organismes capables de métaboliser le 4-NP, bien que cette approche soit plus lente que les procédés chimiques **[80].**

Partie *III* : Méthodes de Traitements

Adsorption

1. Introduction sur l'adsorption

La méthode la plus simple et la plus économique pour fixer les colorants, les pesticides, et les produits pharmaceutiques dans des milieux aqueux est l'adsorption qui constitue un processus fondamental d'élimination de particules en solution**.**

Le nombre annuel de publications en rapport avec l'adsorption ne cesse d'augmenter face aux effets néfastes vis-à-vis de l'environnement et la santé, ce qui génère des risques importants à de faibles concentrations envers l'environnement (persistance en raison de sa stabilité chimique, bioaccumulation dans les organismes aquatiques, affectation de la biodiversité microbienne, etc.), ainsi que pour la santé humaine (réactions allergiques, effets neuropsychiatriques…).

Parmi les matériaux les plus souvent utilisées dans la dépollution est l'adsorption par les matériaux : biosorbants, spinelle, argiles, charbon actif, zéolithes, oxydes métalliques, matériaux hybrides MOFs, à cause de leur simple utilisation et leur performance **[82-83]**.
L'adsorption est un phénomène de surface entre l'adsorbat (solide, liquide, gaz) et l'adsorbant (solide) qui se relie entre eux par des liaisons faibles de type Van Der Waals, L'adsorption se caractérise par l'accumulation de molécules à la surface de l'adsorbant, décrite par la concentration de surface, qui constitue une grandeur essentielle dans l'étude de ce phénomène. **[84].**

2. Types d'adsorption

On distingue deux types d'adsorption physique et chimique, présentés dans le **tableau I. 5.[85]** :

- La physisorption : est une adsorption de type physique, où la fixation des molécules d'adsorbat sur la surface d'adsorbant se fait essentiellement par les forces de Van der Waals et les forces dues aux interactions électrostatiques. L'adsorption physique se produit sans modification de la structure moléculaire et elle est parfaitement réversible.
- La chimisorption : est une adsorption de type chimique, qui résulte des forces de liaison de nature chimique, nettement supérieures aux forces de Van der Waals avec mise en commun ou transfert d'électrons ; Il y a donc des ruptures et des créations de liaisons chimiques en surface entre le réactif et les sites actifs de l'adsorbant. Le processus est beaucoup moins réversible et même parfois irréversible.

Tableau I. 6: Critères de distinction entre l'adsorption physique et chimique **[85].**

Propriétés	Adsorption physique	Adsorption chimique
Température du processus	Relativement basse	Plus élevé
Chaleur d'adsorption	5Kcal /mol environ	10Kcal/mol environ
Liaison	Physique Van der Waals	Chimique
Cinétique	Rapide, réversible	Lente, irréversible
Spécificité	Processus non spécifique	Processus très spécifique
Désorption	Facile	Difficile
Couches formées	Mono ou multicouches	Uniquement monocouche

3. Mécanisme d'adsorption

Le mécanisme d'adsorption se déroule en trois étapes, illustrées par la **figure I. 15**

- Diffusion externe (1) : elle correspond au transfert de l'adsorbat (molécule de la phase liquide) du sein de la solution à la surface externe des particules. Le transfert de la matière externe dépend des conditions hydrodynamiques de l'écoulement d'un fluide dans un lit d'adsorbant. Etape très rapide
- Diffusion interne (2) : les particules de fluide entre profondément dans les pores. Elle dépend du gradient de concentration de l'adsorbat. Etape lente

L'expression cinétique de diffusion intra particulaire est souvent présentée simplement par l'équation : $q_t = k_{id}\, t_{1/2} + C$

Avec :

t : Temps (min) ;

C : Constante ;

k_{id} : Constante de vitesse de diffusion intra-articulaire.

- Diffusion de surface (3) : elle correspond à la fixation des molécules à la surface des pores. Etape très rapide.

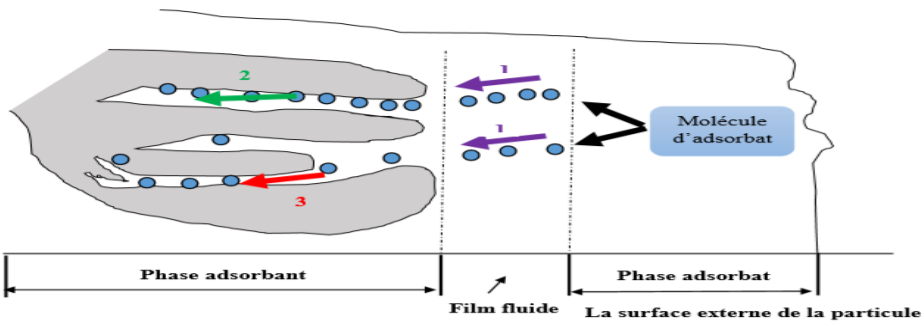

Figure I. 16. Mécanisme du transport d'un adsorbat au sein d'un grain solide **[86].**

4. Paramètres affectant l'adsorption :

Les différents facteurs physiques, chimiques et opérationnels ont une influence sur le phénomène d'adsorption. Il est important d'avoir un contrôle de ces facteurs afin d'améliorer les processus d'adsorption dans différentes applications, comme la purification de l'eau, le traitement des gaz et la récupération de métaux. L'équilibre d'adsorption dépend de nombreux facteurs dont les principaux sont décrits ci-dessous **[87]** :

4.1. Nature de l'adsorbant

- **Surface spécifique** : Plus la surface spécifique de l'adsorbant est grande, plus il y a de sites disponibles pour l'adsorption. Les matériaux poreux comme le charbon actif ont une surface spécifique élevée.
- **Structure poreuse** : La taille, la forme et la distribution des pores influencent l'accès des molécules adsorbées aux sites d'adsorption.
- **Nature chimique de la surface** : La présence de groupes fonctionnels sur la surface de l'adsorbant peut créer des sites actifs spécifiques pour l'adsorption.

4.2. Nature de l'adsorbat

- **Taille et forme des molécules** : Les molécules plus petites et de forme appropriée peuvent accéder plus facilement aux pores de l'adsorbant.
- **Polarité** : Les molécules polaires interagissent plus fortement avec des surfaces polaires ou chargées.
- **Solubilité** : En général, les molécules moins solubles dans le solvant sont mieux adsorbées.

4.3.Température

- **Effet sur l'adsorption physique** : Pour l'adsorption physique (physisorption), l'adsorption diminue généralement avec l'augmentation de la température en raison de la nature exothermique du processus.
- **Effet sur l'adsorption chimique** : Pour l'adsorption chimique (chimisorption), l'effet de la température peut être plus complexe et dépend du mécanisme de la réaction chimique impliquée.

4.4.pH de la solution

- **Ionisation des molécules** : Le pH peut affecter l'ionisation des molécules d'adsorbat et de la surface de l'adsorbant, influençant ainsi les interactions électrostatiques.
- **Solubilité et spéciation** : Le pH peut également affecter la solubilité et la spéciation des molécules d'adsorbat, modifiant leur affinité pour l'adsorbant.

4.5.Vitesse d'agitation

- **Vitesse d'agitation** : Une agitation adéquate peut améliorer le transport des molécules d'adsorbat vers la surface de l'adsorbant, réduisant ainsi la résistance à la diffusion externe.

5. Isothermes d'adsorption

L'isotherme d'adsorption **[87],** est une représentation graphique de la quantité adsorbée par unité de masse ou unité de surface en fonction de la concentration du soluté à l'équilibre. Cette représentation permet de caractériser les interactions adsorbant/adsorbat en étudiant l'effet de la concentration initiale du soluté sur la capacité d'adsorption des adsorbants.

La quantité adsorbée par unité de masse peut être calculée selon l'équation suivante :

$$q_t=(C_i-C_e)\,.V/m$$

Avec :

q_t : Quantité adsorbée exprimée en mg de soluté par gramme d'adsorbant (mg/g) ;

C_i : Concentration initiale de soluté en (mg/L) ;

C_e : Concentration du soluté à l'équilibre en (mg/L) ;

V : Volume du soluté en litre (L) ;

m : masse d'adsorbant en gramme (g).

6. Classification des isothermes d'adsorption

Les isothermes d'adsorption expliquent comment la quantité d'adsorbant adsorbée sur une surface est liée à la concentration ou à la pression de l'adsorbat à une température fixe. La classification des isothermes d'adsorption revêt une importance afin de modéliser les processus d'adsorption dans différents contextes. La classification la plus répandue est celle de Brunauer, Deming, Deming et Teller (BDDT), qui distingue cinq types principaux d'isothermes, présentés dans le **tableau I. 7 [85].**

Tableau I. 8: Classification des isothermes selon Brunauer, Deming, Deming et Teller.

Type d'isotherme	Forme	Caractéristique
Type I	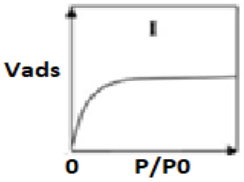	-Saturation rapide des pores. -Adsorption monomoléculaire. -Formation de plateau. -Matériaux microporeux.
Type II	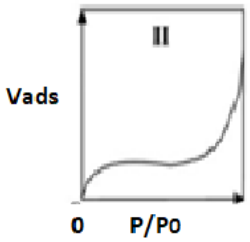	-Adsorption multimoléculaire. - Formation de plusieurs couches d'adsorption. - Adsorption sur une surface non microporeuse. - Matériaux non macroporeux ou poreux.
Type III	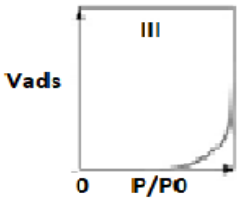	Adsorption faible. - Pas de plateau, courbe concave vers le haut. - Interaction adsorbat-adsorbant plus faible que les interactions adsorbat-adsorbat. - matériaux non poreux.
Type IV	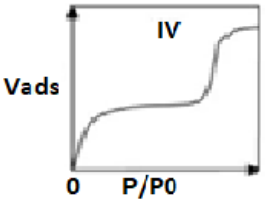	Adsorption multimoléculaire suivie d'une condensation capillaire. - Plateau à haute pression. - Hystérésis possible (Type IVa et IVb). - Matériaux mésoporeux.
Type V	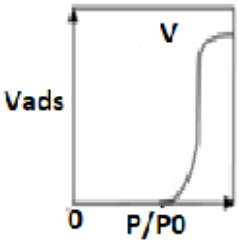	-Similaire au Type III avec une adsorption plus forte à haute pression. -Condensation capillaire dans les mésopores. - Interaction adsorbat-adsorbant plus faible au départ. -Matériaux mésoporeux.

7. Modèles d'adsorption

L'un des objectifs poursuivis par la recherche dans le domaine de l'adsorption est d'établir des équations permettant de rendre compte de la forme des isothermes. Pour cela, différents modèles ont été proposés dans la littérature, les plus utilisés sont :

7.1. Modélisation Cinétiques d'adsorption

L'évolution de la quantité d'adsorbat fixée sur le solide en fonction du temps décrit la cinétique du processus. C'est un outil très important au même titre que les isothermes d'adsorption qui permet de comprendre le ou les mécanismes du processus d'adsorption et aussi évaluer et interpréter les paramètres d'adsorption ; ce modèle est basé sur les réactions suivantes :

- **Cinétique du premier ordre**

L'analyse la plus simple de la cinétique d'adsorption est donnée par le modèle de pseudo-premier ordre. L'équation différentielle s'exprime comme suit **[85]** :

$$\frac{dq_t}{dt} = k_1(q_e - q_t)$$

Avec :

q_e;q_t sont respectivement les quantités de soluté adsorbé en (mg. g^{-1}) à l'équilibre et à un instant **t** et k_1 est la constante de vitesse de premier ordre (min^{-1}).

La valeur de q_t en mg/g à l'instant t est obtenue par la relation suivante :

$$q_t = (C_i - C_e).\frac{V}{m}$$

Avec :

V: Volume de la solution (L) ;

m : masse de l'adsorbant (g) ;

C_i : Concentration initiale de la solution (mg. L^{-1}) ;

C_t : Concentration du soluté à l'équilibre (mg. L^{-1}).

- **Cinétique du second ordre**

La cinétique d'adsorption peut également dans certains cas suivre un modèle de pseudo-second ordre et son équation différentielle s'écrit **[85]** :

$$\frac{dq_t}{dt} = k_2 (q_e - q_t)^2$$

Avec :

K_2 : constante de vitesse de second ordre (g.mg^{-1}.min^{-1}).

L'intégration de cette équation entre 0 et q_t pour le temps de contact adsorbat- adsorbant et la quantité adsorbée respectivement conduit à : $\frac{1}{q_t} = \frac{1}{k_2\ q_e^2} + \frac{1}{q_e}.t$

La droite obtenue en portant $\frac{1}{q_e}$ en fonction de **t** permet de déterminer **qe** et k_2

7.2. Modélisation des isothermes d'adsorption

- **Modèle de Langmuir**

La première théorie fondamentale de l'adsorption des gaz sur des solides fut proposée par Langmuir en 1918 est basé sur les hypothèses suivants **[84] :**

- L'adsorption se produit en une seule couche complétement saturée ;
- Une seule molécule peut s'adsorber par site ;
- Les interactions entre les molécules adsorbées et leurs voisines sont négligées ;
- La surface de l'adsorbant est idéalement uniforme, c'est à dire que tous les sites d'adsorption ont les mêmes propriétés d'adsorption.

L'équation de l'isotherme de Langmuir est donnée par :

$$q_e = \frac{q_m\ k_L\ C_e}{1\ + k_l\ + C_e}$$

Avec :

q_e **:** la quantité de substance adsorbée (mg. g^{-1}) ;

q_m:la capacité maximale d'adsorption (mg. g^{-1}) ;

C_e : concentration de la substance en solution à l'équilibre (mg. L^{-1}) ;

K_L : constante de Langmuir ($L.mg^{-1}$).

- **Modèle de Freundlich**

Le modèle de Freundlich présenté en 1926 **[84],** repose sur les hypothèses ci-dessous :

- L'adsorption se fait en multicouches.
- Plusieurs molécules peuvent s'adsorber par site.
- Les niveaux d'énergie différèrent sur les site actives.

L'équation de l'isotherme de Freundlich est donnée par :

$$q_e = K_f\ .C_e^{\frac{1}{n}}.$$

Avec :

q_e : Quantité de substance adsorbée (mg. g^{-1}) ;

C_e : Concentration de la substance en solution à l'équilibre (mg. L^{-1}) ;

K_f ; 1/n : Constantes de Freundlich reliées à la capacité d'adsorption et l'intensité d'adsorption respectivement.

7.3. Thermodynamique d'adsorption

L'étude thermodynamique reflète la faisabilité et la nature spontanée du processus d'adsorption. Les paramètres tels que l'énergie libre (ΔG°), la variation d'enthalpie (ΔH°) et la variation d'entropie (ΔS°) peuvent être estimées à partir des constantes d'équilibres à différentes températures.

- **L'énergie Libre de Gibbs (ΔG°)**

L'énergie libre de Gibbs est largement utilisée en chimie pour déterminer les conditions de spontanéité des réactions chimiques, la variation d'énergie libre de la réaction d'adsorption est donnée par **[87]** :

$$\Delta G°=-RT.\ln k_C$$

Avec :

ΔG : Variation d'énergie libre ($kJ.mol^{-1}$) ;

R : Constante universelle des gaz (8,314 $J.\ mol^{-1}.\ K^{-1}$) ;

T : Température absolue (K) ;

K_c : Constante d'équilibre.

La variation de l'énergie libre de Gibbs (ΔG°) indique si une réaction chimique est spontanée ou non, si :

- **ΔG=0** : le système est à l'équilibre ;
- **ΔG<0** : la réaction est spontanée ;
- **ΔG>0** : la réaction n'est pas spontanée.

- **Variation d'enthalpie (ΔH)**

La variation d'enthalpie (ΔH) est une mesure de la quantité de la chaleur totale adsorbée dans une réaction chimique, à pression constante, est donnée par **[87-88]** :

$$\Delta H=\Delta U+P\Delta V$$

Avec :

ΔU : Variation de l'énergie interne du système ;

P : Pression constante ;

ΔH : Variation de volume du système.

Si :

- **Réactions exothermiques** : ΔH<0, la réaction libère de la chaleur (réaction exothermique).
- **Réactions endothermiques** : ΔH>0, la réaction absorbe de la chaleur (réaction endothermique).

➢ **Variation d'entropie (ΔS)**

L'entropie (S) est une mesure du désordre de l'énergie dans une réaction chimique ou un système, est donnée par, la variation d'entropie est liée à l'enthalpie de changement de phase (ΔH) **[88]** :

$$\mathbf{\Delta S = \frac{\Delta H}{T}}$$

Où :

ΔH : L'enthalpie de changement de phase ;

T : Température de changement de phase (en Kelvin).

Si :

- **ΔS>0** : L'entropie de la réaction augmente, ce qui signifie que le désordre de l'énergie a augmentée. Ceci est typique pour des processus spontanés.
- **ΔS<0** : L'entropie de la réaction diminue, indiquant une réduction du désordre.

Réduction catalytique

1. Introduction sur la réduction catalytique

La réduction catalytique est une approche chimique couramment employée pour l'élimination des contaminants organiques dans divers domaines industriels et environnementaux **[89]**. Ce procédé repose sur l'action d'un catalyseur qui accélère la transformation des substances toxiques en composés moins dangereux, voire inoffensifs. Il se révèle particulièrement efficace pour dégrader des polluants, tels que les métaux lourds, les colorants, ainsi que les nitrates et nitrites, contribuant ainsi à l'assainissement de l'eau, de l'air et des sols **[90].**

En fonction du type de polluant et du catalyseur utilisé, la réduction catalytique peut s'effectuer selon différents mécanismes, impliquant souvent des agents réducteurs comme l'acide formique, éthylène glycol ou le borohydrure de sodium **[91].**

Les catalyseurs, généralement à base de métaux de transition tels que le nickel, le fer, le palladium ou le platine, jouent un rôle clé en abaissant l'énergie d'activation de la réaction et en améliorant son efficacité **[92].**

Dans le domaine du traitement des eaux, cette technique permet par exemple la réduction des nitrites et nitrates en azote gazeux, minimisant ainsi la pollution de l'eau potable. Dans le secteur industriel, elle est employée pour la dépollution des effluents liquides contenant des colorants, des pesticides ou des produits pharmaceutiques. De plus, dans la lutte contre la pollution atmosphérique, la réduction catalytique est exploitée dans les pots d'échappement des véhicules et les systèmes de traitement des gaz industriels pour éliminer les oxydes d'azote (NOx), responsables des pluies acides et de l'effet de serre **[93]**.

2. Types de reduction catalytique

On peut classifier la réduction catalytique en différentes catégories selon le mécanisme engagé, l'environnement réactionnel et le genre de catalyseur employé. Voici les types principaux :

➢ Réduction catalytique hétérogène

Dans ce genre de réduction **[94],** le catalyseur est en phase solide et la réaction a lieu à l'interface entre le catalyseur et les réactifs dans un état liquide ou gazeux. Cette méthode est fréquemment employée pour le traitement et la transformation des contaminants en substances moins nocives.

Exemples d'utilisations :

- Utilisation de catalyseurs à base de métaux (Pt, Pd, Rh, Cu, V_2O_5) pour la réduction catalytique des oxydes d'azote (NOx) dans les pots d'échappement et les gaz industriels.
- La réduction sélective des composés organiques, comme la transformation du 4-nitrophénol en 4-aminophénol à l'aide de nanoparticules de métaux précieux ou d'oxydes métalliques.
- L'utilisation de catalyseurs solides ($NiFe_2O_4$, Pd/C, CuO) dans le traitement des eaux usées industrielles permet de réduire les polluants organiques nocifs.

➢ Réduction catalytique homogène

Dans ce cas de reduction **[95],** le catalyseur et les réactifs se trouvent dans la même phase, généralement en solution. Ce type de catalyse permet souvent un meilleur contrôle des conditions réactionnelles et une sélectivité accrue.

Exemples d'utilisations :

- Conversion des nitrates et nitrites en azote moléculaire à l'aide de complexes métalliques solubles à base de rhodium, ruthénium ou fer.
- Transformation des aldéhydes et cétones en alcools sous l'action de catalyseurs homogènes, notamment des complexes de ruthénium.
- Procédé d'hydrogénation homogène utilisé en industrie pharmaceutique pour élaborer des composés organiques sophistiqués.

➢ **Réduction catalytique assistée par des réducteurs chimiques**

Ce procédé utilise un agent réducteur en combinaison avec un catalyseur pour accélérer et facilite la transformation de composés ciblés en produits moins réactifs ou moins toxiques **[91]**.

Exemples d'utilisations :

- Le borohydrure de sodium ($NaBH_4$) est fréquemment utilisé pour convertir les nitrophénols en aminophénols.
- Le formiate de sodium sert à transformer le dioxyde de carbone (CO_2) en méthanol en présence d'un catalyseur métallique.
- L'éthylène glycol intervient dans la réduction de divers oxydes métalliques pour obtenir des métaux à l'état pur.

➢ **Réduction photo-catalytique**

Ce procédé repose sur l'utilisation d'un catalyseur sensible à la lumière, généralement un semi-conducteur, qui initie la réaction lorsqu'il est exposé à un rayonnement lumineux, qu'il soit ultraviolet ou visible **[96].**

Exemples d'utilisations :

- Conversion du dioxyde de carbone (CO_2) en composés énergétiques tels que le méthane ou le méthanol grâce à des photocatalyseurs comme le dioxyde de titane modifié ou certains oxydes métalliques.
- Élimination des colorants organiques présents dans les eaux polluées sous l'effet d'une irradiation UV-visible, en utilisant des matériaux photocatalytiques comme ZnO, $NiFe_2O_4$ ou WO_3.
- Transformation des ions métalliques toxiques, notamment la réduction du chrome hexavalent (Cr^{6+}) en une forme moins dangereuse, le chrome trivalent (Cr^{3+}).

➢ **Réduction enzymatique catalysée**

Ce processus repose sur l'utilisation d'enzymes naturelles ou modifiées jouant le rôle de catalyseurs pour faciliter des réactions de réduction ciblées, généralement dans des conditions respectueuses de l'environnement et à faible impact énergétique **[97].**

Exemples d'applications :

- Conversion des nitrates en azote gazeux grâce à l'action des nitrates réducteurs, une technique employée dans le traitement des eaux contaminées.
- Élimination des polluants organiques par l'intermédiaire d'enzymes oxydoréductases présentes dans certains microorganismes**.**
- Synthèse de biocarburants via la transformation enzymatique des sucres en alcools.

3. Mécanisme de la réduction catalytique

Le processus de la réduction catalytique s'appuie sur l'action d'un catalyseur, qui diminue l'énergie nécessaire pour initier la réaction, favorisant ainsi la conversion des espèces chimiques visées en produits réduits. Cette procédure peut différer selon le type de catalyse (hétérogène, homogène, photo-catalytique, enzymatique, électrochimique), mais respecte généralement les phases essentielles suivantes **[98-99]** :

➢ **Adsorption des réactifs sur le catalyseur :**

- Dans la catalyse **hétérogène**, les espèces chimiques impliquées dans la réaction (telles que les polluants organiques, les oxydes métalliques ou les gaz nocifs) s'adsorbent sur la surface du catalyseur, qui est généralement constitué de métaux comme le palladium (Pd), le platine (Pt), le nickel (Ni) ou le fer (Fe), ainsi que d'oxydes métalliques tels que $NiFe_2O_4$ ou TiO_2.
- Dans la catalyse **homogène**, les réactifs et le catalyseur sont présents dans la même phase, ce qui favorise une interaction directe au sein du milieu réactionnel.
- Dans le cas de la **réduction enzymatique**, le substrat s'attache spécifiquement au site actif de l'enzyme, permettant ainsi l'initiation de la réaction.

➢ **Activation des molécules et transfert d'électrons**

- Le catalyseur joue un rôle clé en facilitant la dissociation des liaisons chimiques des réactifs et en accélérant le transfert des électrons indispensables au processus de réduction.

- Par exemple, dans la conversion du 4-nitrophénol, le catalyseur permet le passage des électrons depuis un agent réducteur tel que le borohydrure de sodium ($NaBH_4$) vers la molécule cible, transformant ainsi le groupe nitro ($-NO_2$) en amine ($-NH_2$).
- Dans les systèmes **électrochimiques**, ce transfert d'électrons est contrôlé par l'application d'un potentiel électrique.
- En **photocatalyse**, l'absorption de lumière par un semi-conducteur excite ses électrons, générant des paires électron-trou capables d'initier la réaction de réduction.

➢ **Formation des produits réduits et désorption**

- Une fois la réaction terminée, les composés réduits (comme le 4-aminophénol, le méthanol issu de la conversion du CO_2 ou le Cr^{3+} obtenu à partir du Cr^{6+}) sont relâchés par le catalyseur.
- Dans le cas de la **catalyse hétérogène**, cette étape de désorption libère la surface active du catalyseur, lui permettant de participer à de nouvelles réactions.
- En **catalyse enzymatique**, l'enzyme retrouve sa structure initiale après la libération du produit, lui permettant de catalyser d'autres transformations.

➢ **Régénération du catalyseur**

- Dans des conditions optimales, le catalyseur conserve son intégrité et peut être employé sur plusieurs cycles de réaction sans altération majeure.
- Cependant, certains facteurs tels que l'empoisonnement du catalyseur, l'accumulation de dépôts ou son oxydation progressive peuvent réduire son efficacité au fil du temps, limitant ainsi ses performances.

4. Facteurs influençant la réduction catalytique

Plusieurs facteurs influencent la performance et l'efficacité d'un processus de réduction catalytique, agissant à la fois sur la vitesse de réaction et la stabilité du catalyseur **[100].**

4.1.Nature du catalyseur :

- **Composition du catalyseur** : peut être composé de métaux précieux comme le palladium (Pd), le platine (Pt) ou l'or (Au), en plus des oxydes métalliques tels que la ferrite de nickel ($NiFe_2O_4$), le dioxyde de titane (TiO_2) ou l'oxyde de zinc (ZnO).
- **Porosité et la surface spécifique** : plus la porosité et la surface spécifique du catalyseur est importante, plus la réaction est favorable.

- **Dispersion du catalyseur** : dispersion des particules catalytiques favorise une activité croissante.

4.2.Résistance thermique et chimique :

- **Température élevée** : peut augmentant l'énergie des réactifs et la fréquence des collisions et facilité le transfert d'électrons entre le matériau et le polluant. Bie qu'une température excessive peut endommager le catalyseur.
- **Pression** : Une pression excessive peut conduire à une occupation complète des sites catalytiques disponibles, limitant ainsi la libération des produits formés. Ce phénomène entrave le renouvellement des sites actifs et compromet l'efficacité globale du processus catalytique.

4.3.Nature du réducteur :

- L'efficacité est associée à la capacité réductrice et à l'affinité avec le catalyseur.

4.4.Environnement réactionnel

- **pH :** des variations de pH modifier la réactivité des espèces impliquées.
- **L'existence d'oxygène** : peut altérer les mécanismes réactionnels et impacter le rendement global du processus.

5. Cinétique des processus de réduction catalytique

L'évaluation de la vitesse des réactions de réduction catalytique joue un rôle clé dans la compréhension des mécanismes impliqués et l'amélioration des performances des catalyseurs. L'analyse cinétique permet de quantifier l'évolution temporelle des transformations chimiques et d'identifier les paramètres influençant leur efficacité.

5.1. Modélisation des vitesses de réaction en réduction catalytique

- **Cinétique d'ordre 1**

Les réactions de réduction suivent fréquemment une cinétique de pseudo-premier ordre. Ce comportement peut être exprimé par l'équation suivante **[101] :**

où :

$$-\mathrm{Ln}\left(\frac{C_t}{C_0}\right) = -\ln\left(\frac{A_t}{A_0}\right) = K_{app}\, t$$

C_t et C_0 désignent respectivement la concentration du composé réactif à un instant et au départ de la réaction ;

A_0 et A_t correspondent aux valeurs d'absorbance à une longueur d'onde spécifique ;

K_{app} représente la constante de vitesse apparente (min^{-1}).

Cette corrélation permet d'extraire **K_{app}** en effectuant un tracé de **$-\ln(\frac{A_t}{A_0})$** en fonction du (**t**) temps. Une tendance linéaire indique que la réaction suit bien une cinétique de pseudo-premier ordre.

- **Cinétique d'ordre 2**

Dans le cas d'une cinétique de second ordre, l'équation différentielle s'écrit **[102] :**

$$\frac{dc}{dt} = -KC^2$$

En intégrant cette équation, on obtient la relation suivante :

$$\frac{1}{C_t} - \frac{1}{C_0} = Kt$$

Pour vérifier si une réaction suit une cinétique de second ordre, on trace $\frac{1}{C_t}$ en fonction du temps (**t**). Si la courbe obtenue est une droite, alors la réaction suit bien un modèle cinétique d'ordre 2, et la pente de cette droite correspond à la constante de vitesse **k**.

Lorsqu'on suit la réaction par spectroscopie d'absorbance, on peut exprimer cette relation en fonction des valeurs d'absorbance :

$$\frac{1}{A_t} - \frac{1}{A_0} = kt$$

Ainsi, on peut tracer $\frac{1}{A_t}$ en fonction du temps (**t**)pour déterminer K à partir de la pente de la droite obtenue.

Références

1. S. Sayanthan, H. A. Hasan and S. R. S. Abdullah, *Water*, 2024, **16**, 870.

2. B. Dhir, P. Sharmila and P. P. Saradhi, *Crit. Rev. Enviro. Sci. Technol.*, 2009, **39**, 754–781.

3. R. D. Sooknah and A. C. Wilkie, *Ecol. Eng.*, 2004, **22**, 27–42.

4. X. Wang, X. Li, J. Su, S. Liu, X. Li, Q. Zhang and T. Huang, *Enviro. Res.*, 2025, **264**, 120288.

5. H. Liu, P. Dai, J. Zhang, C. Zhang, N. Bao, C. Cheng and L. Ren, *Chem. Eng. J.*, 2013, **228**, 425–434.

6. S. Ghosh, A. Benettayeb, M. Meskini, B. Lal, Z. T. Al-Sharify, O. J. Ajala, C. Osagie, A. Malloum, S. Z. Al-Najjar, H. Onyeaka, C. Bornman, S. Ahmadi, C. A. Igwegbe and A. Hosseini-Bandegharaei, *Environ. Technol. Rev.*, 2024, **13**, 359–378.

7. D. Selvaraj and M. Arivazhagan, *Environ. Pollut.*, 2024, **357**, 124435.

8. E. Sočo, D. Papciak, A. Domoń and D. Pająk, *Water*, 2024, **16**, 2388.

9. M. Abdu, S. Babaee, A. Worku, T. A. M. Msagati and J. F. Nure, *Sci. Rep.*, 2024, **14**, 18320.

10. P. Papadia, F. Barozzi, D. Migoni, M. Rojas, F. P. Fanizzi and G.-P. Di Sansebastiano, *Int. J. Mol. Sci.*, 2020, **21**, 4769.

11.R. O. Carey and K. W. Migliaccio, *Environ. Manage.*, 2009, **44**, 205–217.

12. P. Premalatha, K. Saravanan and P. Karuppannan, *J. Water Chem. Technol.*, 2024, **46**, 309-317.

13. V. Prete, A. C. Abate, P. Di Pietro, M. De Lucia, C. Vecchione and A. Carrizzo, *Nutrients*, 2024,**16**,642.

14. X. He, C. Wang, Y. Zhu, X. Jiang, Y. Qiu, F. Yin, W. Xiong, B. Liu and Y. Huang, *Algal Res.*, 2022, **66**,102791.

15. M. A. Zulfikar, H. Setiyanto, Rusnadi and L. Solakhudin, *Desalin. Water Treat.*, 2015, **56**, 2976–2987.

16. H. K. Okoro, S. Pandey, C. O. Ogunkunle, C. J. Ngila, C. Zvinowanda, I. Jimoh, I. A. Lawal, M. M. Orosun and A. G. Adeniyi, *Emerg. Contam.*, 2022, **8**, 46–58.

17. Y. Li, *J. Immunol. Res.*, 2022, **2022**, 1–8.

18. A. Paraskevopoulou, T. Kaloudis, A. Hiskia, M. Steinhaus, D. Dimotikali and T. M. Triantis, *Foods*, 2024, **13**, 1257.

19. S. Rashad, *Egypt. J. Aquat. Biol. Fish.*, 2021, **25**, 775–982.

20. S. M. Kimani, N. Sekishita, Y. Hosogoe, V. Kaustar, K. Tawaraya, T. Tokida and W. Cheng, *Soil Sci. Plant Nutr.*, 2025, 1–8.

21. K. bibi, S. S. Krishnappa, C. K. Kachintaya, S. Kalikeri and L. H. Gurusiddappa, *Int. J. Heal. Allied Sci.*, 2024, **13**, 9-17.

22. S. Ghosh, A. Benettayeb, M. Meskini, B. Lal, Z. T. Al-Sharify, O. J. Ajala, C. Osagie, A. Malloum, S. Z. Al-Najjar, H. Onyeaka, C. Bornman, S. Ahmadi, C. A. Igwegbe and A. Hosseini-Bandegharaei, *Environ. Technol. Rev.*, 2024, **13**, 359–378.

23. B. Kollah, A. K.Patra and S. R. Mohanty, *Environ. Sci. Pollut. Res.*, 2016, **23**, 4358–4369.

24. S. Sayanthan, H. A. Hasan and S. R. S. Abdullah, *Water*, 2024, **16**, 870.

25. J. S. Singh, A. Kumar, A. N. Rai and D. P. Singh, *Front. Microbiol.*,2016, **19**, 1-14.

26. A. W. Ahmadi and S. Dursun, *Cent. Asian J. Water Res.*, 2024, 115–125.

27. M. Seferli, C. Kotanidou, M. Lefkaki, T. Adamantidi, E. Panoutsopoulou, M. A. Finos, G. Krey, N. Kamidis, N. Stamatis, C. Anastasiadou and A. Tsoupras, *Appl. Sci.*, 2024, **14**, 6634.

28. Y. Zhou, A. Stepanenko, O. Kishchenko, J. Xu and N. Borisjuk, *Plants*, 2023, **12**, 589.

29. P. Fourounjian, T. Fakhoorian and X. H. Cao, 2020, pp. 1–17.

30. A. Baldi, L. Verdi, L. Piacenti and A. Lenzi, Horticulturae, 2024, **11**, 20.

31. E. R. D. Schutz, D. S. Broch Mignoni, W. Michelon and E. de Oliveira Nunes, *Biofuels*, 2025, 1–9.

32. H. Tekoğul, *J. Coast. Res.*, 2023, **39**, 296–302.

33. Ali Esmail Al-Snafi, *IOSR J. Pharm*, 2020, **10**, 1-41.

34. E. Landolt, *Aquat. Bot.*, 1975, **1**, 345–363.

35. R. Chakrabarti, W. D. Clark, J. G. Sharma, R. K. Goswami, A. K. Shrivastav and D. R. Tocher, *Front. Chem.*, 2018, **6**

36. S. K. Parida, A. Satpathy, A. Dalai and S. Mishra, 2024, pp. 1–37.

37. B. De, M. Bera, D. Bhattacharjee, B. C. Ray and S. Mukherjee, *Prog. Mater. Sci.*, 2024, **146**, 101326.

38. M. G. Tadesse, A. S. Ahmmed and J. F. Lübben, *J. Compos. Sci.*, 2024, **8**, 1-53.

39. E. M. Geniès, A. Boyle, M. Lapkowski and C. Tsintavis, *Synth. Met.*, 1990, **36**, 139–182.

40. P. Zarrintaj, R. Khalili, H. Vahabi, M. R. Saeb, M. R. Ganjali and M. Mozafari, *Fundam Emerg Appl Polyaniline, Elsevier*, 2019, **9**, 131–141.

41. C. Wang, F. Wang, H. Zhang, Y. Zhang, C. Zhang, W. Zang, M. Peng, Y. Yang, S. Wang, C. Xu, A. Wu and Y. Zhang, *Sci. Total Environ.*, 2024, **927**, 172058.

42. *Proc. R. Soc. London*, 1873, **21**, 54–56.

43. P. Raotole and S. R. Patil, *B P International*, 2024,**4**. 32–40.

44. A. H. Majeed, L. A. Mohammed, O. G. Hammoodi, S. Sehgal, M. A. Alheety, K. K. Saxena, S. A. Dadoosh, I. K. Mohammed, M. M. Jasim and N. U. Salmaan, Int. J. Polym. Sci., 2022, 2022, 1–19.

45. A. Güngör, F. Bakan-Misirlioglu, R. Genç Alturk and E. Erdem, *J. Energy Storage*, 2024, **76**, 110143.

46. S. Abirami1, E. Kumar., *J Mater Sci*, 2024,**59**, 14141–14171.

47. K. E. Sickafus, J. M. Wills and N. W. Grimes, *J. Am. Ceram. Soc.*, 1999, **82**, 3279–3292.

48. M. E. Sánchez Vergara, M. J. Agraz Rentería, A. R. Vázquez-Olmos, K. L. Rincón-Granados, J. R. Álvarez Bada and R. Y. Sato-Berrú, *Nanomaterials*, 2023, **13**, 1525.

49. Y. Cheng, Z. Zhang, Y. Hong, X. Li, H. Song and Y. Zhang, *New J. Chem*., 2025, **49**, 1062–1071.

50. Y. Wang, Z. Nie, X. Li, R. Wang, Y. Zhao and H. Wang, ACS Sustain. *Chem. Eng*., 2022, **10**, 6082–6093.

51. Z. Li, M. Ye, A. Han and H. Du, J. Mater. Sci. Mater. Electron., 2016, **27**, 1031–1043.

52. Q. MO, S. ZENG, J. YANG, C. WU and Y. ZHANG, *J. Ceram. Soc. Japan*, 2020, **128**, 135–141.

53. S. S. Scindia, R. B. Kamble and J. A. Kher, *AIP Adv*., 2019, **9**, 1-8.

54. H. A. El-saied and E. A.-T. Motawea, J. Polym. *Environ*., 2020, 28, 2335–2351.

55. W. Johnston, Biotech. *Histochem.*, 2008, **83**, 83–87.

56. M. A. M. Salleh, D. K. Mahmoud, W. A. W. A. Karim and A. Idris, *Desalination*, 2011, **280**, 1–13.

57. A. Kumar, U. Dixit, K. Singh, S. Prakash Gupta and M. S. Jamal Beg, *IntechOpen*, 2021,1-19

58. S. C. J. Meskers, *ChemPhysChem*, 2023, **24**, e202300666 .

59. B. Kamenická, *J. Water Process Eng.*, 2024, **61**, 105350.

60. O. Karaman, G. A. Alkan, C. Kizilenis, C. C. Akgul and G. Gunbas, *Coord. Chem. Rev.*, 2023, **475**, 214841.

61. X. Song, R. Xu, Q. Yao, L. Tian, J. Li, B. Yang, P. Chen, J. Zhang, H. Xin and X. Peng, *Dye. Pigment.*, 2024, **228**, 112244.

62. P. Bhatia and M. Nath, *Chemosphere*, 2022, **290**, 133188.

63. J. E. de Santana, F. G. S. de Andrade, A. F. Ferreira, M. G. Ghislandi and M. A. da Motta Sobrinho, *Environ. Sci. Pollut. Res.*, 2024, **31**, 53691–53705.

64. A. K. Tolkou, E. K. Tsoutsa, G. Z. Kyzas and I. A. Katsoyiannis, *Environ. Sci. Pollut. Res.*, 2024, **31**, 14662–14689.

65. S. Noreen, M. Tahira, M. Ghamkhar, I. Hafiz, H. N. Bhatti, R. Nadeem, M. A. Murtaza, M. Yaseen, A. A. Sheikh, Z. Naseem and F. Younas, *J. Mater. Res. Techno.*, 2021, **14**, 25–35.

66. S. Ihaddaden, D. Aberkane, A. Boukerroui and D. Robert, *J. Water Process Eng.*, 2022, **49**, 102952.

67. A. Akhtar, M. Hanif, U. Rashid, I. Bhatti, F. Alharthi and E. Kazerooni, *Separations*, 2022, **9**, 425.

68. S. Yadav, K. S. Tiwari, C. Gupta, M. K. Tiwari, A. Khan and S. P. Sonkar, *Results Chem.*, 2023, **5**,100733.

69. H. Ben Slama, A. Chenari Bouket, Z. Pourhassan, F. N. Alenezi, A. Silini, H. Cherif-Silini, T. Oszako, L. Luptakova, P. Golińska and L. Belbahri, *Appl. Sci.*, 2021, **11**, 6255.

70. T. A. Khattab, M. S. Abdelrahman and M. Rehan, *Environ. Sci. Pollut. Res.*, 2020, **27**, 3803–3818.**71**. F. Uddin, *Cellulose*, 2021, **28**, 10715–10739

72. 1 A. K. Tolkou, E. K. Tsoutsa, G. Z. Kyzas and I. A. Katsoyiannis, *Environ. Sci. Pollut. Res.*, 2024, **31**, 14662–14689.

73. C. Schönmann and K. Brockow, *Ann. Allergy, Asthma Immunol.*, 2020, **124**, 156–164.

74. M. Berradi, R. Hsissou, M. Khudhair, M. Assouag, O. Cherkaoui, A. El Bachiri and A. El Harfi, *Heliyon*, 2019, **5**, e02711.

75. N. Li, Q. Wang, J. Zhou, S. Li, J. Liu and H. Chen, *Molecules*, 2022, **27**, 3291.

76. C. Filote, M. Roșca, R. Hlihor, P. Cozma, I. Simion, M. Apostol and M. Gavrilescu, *Processes*, 2021, **9**, 1696

77. A. K. Patra and S. R. K. Pariti, *Text. Prog.*, 2022, **54**, 1–101.

78. K. Piaskowski, R. Świderska-Dąbrowska and P. K. Zarzycki, *J. AOAC Int.*, 2018, **101**, 1371–1384.

79. A. Balakrishnan, G. J. Gaware and M. Chinthala, *Chemosphere*, 2023, **310**, 136853.

80. N. El Messaoudi, Y. Miyah, M. Benjelloun, J. Georgin, D. S. P. Franco, Z. M. Şenol, Z. Ciğeroğlu, M. El Hajam, S. Knani and P. Nguyen-Tri, Nano-Structures & Nano-Objects, 2024, **40**, 101326.

81. L. Sabaghzadeh, A. Tadjarodi, N. Steinfeldt and J.Strunk, *Iran. J. Sci.*, 2024, **48**, 357–372.

82. L. Lu and C. Na, *Philos. Mag. Lett.*, 2022, **102**, 239–253.

83. A. H. Kamel, H. S. M. Abd-Rabboh, A. Abd El-Fattah, G. Boudghene Stambouli and L. Adeida, *RSC Adv.*, 2025, **15**, 6875–6901.

84. A. Boutaric, *J. Phys. le Radium*, 1940, **1**, 99–102.

85.M. Aljamali, R. A. B. Aldujaili, I. O. Alfatlawi, *Int. j. thermodyn. chem. kinet*, 2021, **7**,1-8.

86.S. Mohamed Nasser, M. Abbas and M. Trari, *Prog. React. Kinet. Mech.*, 2024, 49.

87. E. Rápó and S. Tonk, *Molecules*, 2021, **26**, 5419.

88. G. B. Stambouli, B. Benguella, B. Makhoukhi, M. S. El-ouchdi and A. H. Kamel, *Anal. Methods*, 2025, **17**, 2134–2143.

89. M. Naz, A. Rafiq, M. Ikram, A. Haider, S. O. A. Ahmad, J. Haider and S. Naz, *J. Mater. Sci.*, 2021, **56**, 15572–15608.

90. P. Zhang, Y. Lai, X. Dai, Y. Xu, X. Wu, B. Yang, D.-H. Kuo, D. Lu, Q. Wu, M. T. Mosisa, J. Lin and X. Chen, *J. Environ. Chem. Eng.*, 2024, **12**, 111831.

91. X. Yang, R. Song, F. Tian, C. Ding, H. Du, Q. Liu and R. Zhang, *Int. J. Hydrogen Energy*, 2024, **82**, 225–232.

92. A. I. Osman, A. Ayati, P. Krivoshapkin, B. Tanhaei, M. Farghali, P. Yap and A. Abdelhaleem, *Coord. Chem. Rev.*, 2024, **514**, 215900.

93. Y. Zhang, J. Du, Y. Shan, F. Wang, J. Liu, M. Wang, Z. Liu, Y. Yan, G. Xu, G. He, X. Shi, Z. Lian, Y. Yu, W. Shan and H. He, *Chem. Soc. Rev.*, 2025, **54**, 1151–1215.

94. B. Maleki, H. Esmaeili, Y. K. Venkatesh and M. Yusuf, *Process Saf. Environ. Prot.*, 2024, **187**, 903–925.

95. M. Carvalho, *Combustion Technology for a Clean Environment*, CRC Press, Boca Raton, 2024, **108**, 4-6.

96. J. Yang, Z. Chen, L. Zhang and Q. Zhang, *ACS Nano*, 2024, **18**, 21804–21835.

97. J. Yuan, X. Zeng, P. Zhang, L. Leng, Q. Du and D. Pan, *Food Biosci.*, 2024, **59**, 103833.

98. Z. Zhuang, B. Guan, J. Chen, C. Zheng, J. Zhou, T. Su, Y. Chen, C. Zhu, X. Hu, S. Zhao, J. Guo, H. Dang, Y. Zhang, Y. Yuan, C. Yi, C. Xu, B. Xu, W. Zeng, Y. Li, K. Shi, Y. He, Z. Wei and Z. Huang, Chem. Eng. J., 2024, 486, 150374.

99. S. Muhammad Farhan, W. Pan, C. Zhijian and Y. JianJun, *Fuel*, 2024, **355**, 129364.

100. G. A. Somorjai and J. Y. Park, *Angew. Chemie Int. Ed.*, 2008, **47**, 9212–9228.

101. Z. G. Asmare, B. A. Aragaw and M. Atlabachew, *ACS Omega*, 2024, **9**, 48014–48031.

102. M. Ranjbar, M. Vashishtha, S. Gadipelli, K. Ramisetty, G. Walker, D. J. L. Brett and K. V. Kumar, *CrystEngComm*, 2024, **26**, 1077–1089.

Chapitre II :

Matériels et Méthodes

Ce chapitre présente l'ensemble des outils expérimentaux et techniques mis en œuvre au cours de ce travail. Il détaille les réactifs chimiques utilisés, les procédures expérimentales adoptées, ainsi que les méthodes de caractérisation et d'analyse appliquées tout au long de l'étude. Les adsorbants sont :

- La Lemna minor utilisée dans ce travail a été collectée en Égypte puis cultivée dans des bassins aquatiques au niveau de laboratoire, sous des conditions adéquates.
- Ferrite de nickel recouverte de poly (aniline-Co-o, Toluidine).

1. Adsorbants utilisés

- **Rouge-Bezaktiv**

Les colorants synthétiques se déclinent en plusieurs catégories, définies selon leur structure et leur composition chimique. Dans cette étude, nous avons examiné l'adsorption d'un colorant textile de teinte rouge, appartenant à la famille des Bezaktiv-HE. Ce colorant réactif fait partie des colorants monocloro-thiazoiques**,** également classés parmi les colorants azoïques. Sa coloration rouge résulte de la présence de cycles aromatiques combinés à des liaisons N=N conjuguées (**Figure II.1.**). La dilution du Rouge-Bezaktiv est réalisée dans de l'eau, ce type de colorant est principalement utilisé pour la teinture par épuisement. Son principal avantage réside dans son adaptabilité aux procédés de teinture à haute température, ainsi qu'à diverses applications textiles, permettant ainsi d'optimiser la méthode de teinture en fonction du matériau et de l'équipement disponible **[1]**.

Le colorant employé dans cette recherche provient de l'Entreprise Nationale des Industries Textiles Soieries (SOITEX) située à Tlemcen.

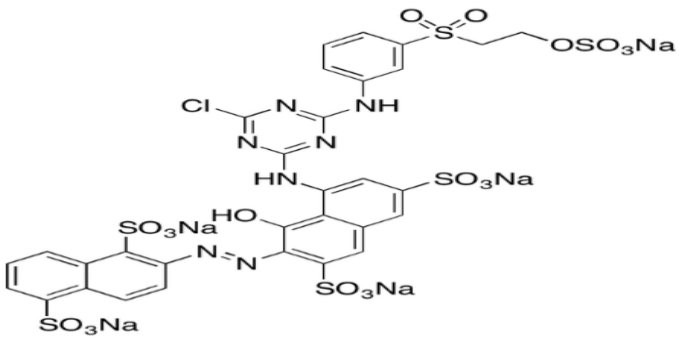

Figure II. 1. Structure de colorant Rouge-Bezaktiv

- **4-nitrophénol**

4-nitrophénol (4-NP) est un composé organique aromatique dérivé du phénol, possédant un groupe nitro (-NO_2) en position para (**Figure II. 2**). Il est couramment utilisé dans la synthèse de pesticides, de colorants, de médicaments et d'antioxydants. Cependant, sa toxicité et sa stabilité chimique en font un contaminant préoccupant, nécessitant des solutions adaptées pour limiter son impact environnemental **[2].** Ce composé se présente sous forme d'un solide cristallin jaune pâle avec une solubilité modérée dans l'eau et une meilleure affinité pour les solvants organiques. Il possède un point de fusion entre 113 et 115 °C et un point d'ébullition avoisinant 279 °C. Son acidité (pKa ≈ 7,15) lui permet de se dissocier partiellement en solution aqueuse, notamment en milieu alcalin **[3].**

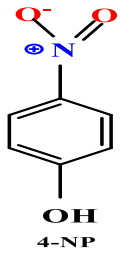

Figure II. 2. Structure de 4-nitrophénol (4-NP)

2. Produits chimiques utilisés

Tableau II. 1: Les produits chimiques servi dans cette recherche.

Produit	Provenance	Pureté (%)	Densité
HCl	SIGMA ALDRICH	39,5-38	1,19
NaOH	SIGMA ALDRICH	≥98	2,13
H_2SO_4	SIGMA ALDRICH	95-97	1,84
$C_6H_8O_7$	SIGMA ALDRICH	99,5	1,67
Aniline	SIGMA ALDRICH	≥99,5	1,02
O, Toluidine	SIGMA ALDRICH	98	1,0
$NiCl_2$	SIGMA ALDRICH	>99	3,55
$FeCl_3$	SIGMA ALDRICH	97	2,9
PEG	SIGMA ALDRICH	100	1,13
$CHCl_3$	SIGMA ALDRICH	≥99,8	1.5
$(NH_4)_2S_2O_8$	SIGMA ALDRICH	98	1.98
Rouge-Bezaktiv	SOITEX	—	—

3. Préparation des matériaux

➢ **Lemna minor**

- **Lemna minor brute**

Lemna minor a été prélevée dans un lac naturel dans la ville d'El-Fayoum, en Égypte. Elle a été transportée en Algérie dans une glacière et stockée dans un réfrigérateur à 4 °C. vingt grammes (20 g) de l'échantillon de Lemna minor ont été séchés à l'air libre après avoir été lavés trois fois avec de l'eau distillée. La plante, a été tamisés jusqu'à ce qu'elles atteignent la taille d'un tamis de 2,0 mm. Enfin, Lemna minor est stockée dans des boîtes de pétri et placé au four à 50 °C.

Figure II. 3. Lemna minor brute

- **Lemna minor Activée**

Le processus d'activation se déroule en utilisant deux acides différents : l'acide phosphorique et l'acide citrique. Une quantité de 20 g de Lemna minor a été traitée avec 1000 ml d'acide phosphorique ou d'acide citrique d'une concentration de 0,1 M pendant 3 heures sous agitation à 300 rpm pour obtenir Lemna minor activée avec l'acide phosphorique et l'acide citrique, respectivement. Lemna minor est ensuite lavé et séché dans un four à 50° pendant 24 heures, broyé et tamisé pour être utilisés dans les expériences d'adsorption [4].

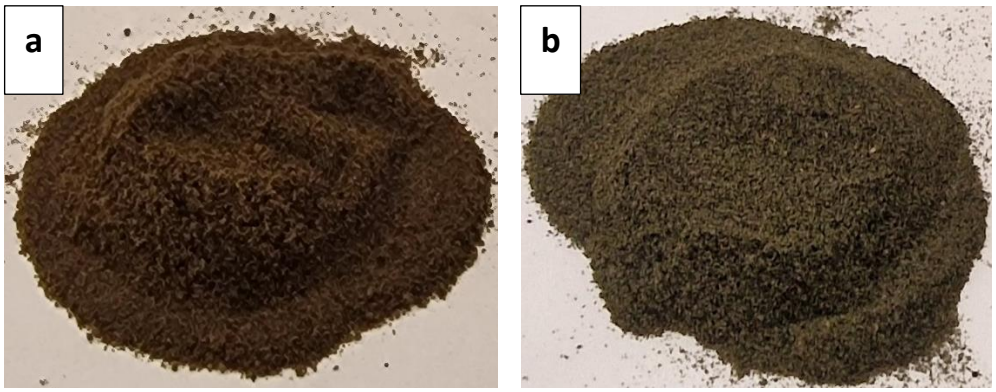

Figure II. 4. Lemna minor activée avec l'acide : (**a** (phosphorique), **b** (citrique))

➢ **Ferrite de nickel ($NiFe_2O_4$) recouvert de poly(aniline-co-o-toluidine) (POAT)**

- **Ferrite de nickel ($NiFe_2O_4$)**

La solution a été préparée à partir du chlorure ferrique (III) et chlorure de nickel (II) à une température ambiante dans un rapport molaire de 2 :1, puis agitée en continu pendant 30 minutes. Une solution de soude (NaOH) à 2,0 M a ensuite été ajoutée progressivement à un débit contrôlé de 1,0 mL/min, jusqu'à ce que le pH du mélange atteigne la valeur souhaitée (pH=11), qui a ensuite été chauffé à 100 °C sous agitation pendant une heure. Le mélange a été laissé à maturation toute la nuit. Le précipité obtenu a été soigneusement lavé à l'eau distillée jusqu'à ce que le filtrat atteigne un pH neutre.

Le résidu a ensuite été séché à 110 °C pendant six heures, ce qui a permis d'obtenir une poudre noire intense, laquelle a ensuite été calcinée à 600 °C pendant 5 heures. Le produit final a été broyé puis conservé dans un dessiccateur **[5]**.

Figure II. 5. Ferrite de Nikel

- **Synthèse du nanocomposite $NiFe_2O_4$ recouvert de poly(aniline-co-o-toluidine)**

Nanocomposite à base de ferrite de nickel recouvert de polymère ont été synthétisés par un procédé de polymérisation chimique. Dans un premier temps, 4,5 g de nanoparticules de $NiFe_2O_4$ ont été dispersées dans un mélange de solvants contenant 20 mL de chloroforme et 30 mL d'eau bidistillée. Cette dispersion a été soumise à un traitement par ultrasons pendant 1 heure à température ambiante.

Parallèlement, 0,05 mole d'aniline et 0,05 mole d'o-toluidine ont été dissoutes dans 200 mL d'acide chlorhydrique à 1,0 M, puis le mélange a été agité continuellement pendant 30 minutes. La dispersion de nanoparticules a ensuite été ajoutée à la solution de monomères, et le tout a été de nouveau sous sonification pendant 30 minutes.

La polymérisation a été amorcée par l'ajout goutte à goutte de 20 mL d'une solution aqueuse de persulfate d'ammonium (APS) à 0,1 M, à un débit contrôlé de 0,5 mL/min à l'aide d'une micropipette, tout en maintenant la sonication pendant une heure supplémentaire. Un

changement progressif de la couleur vers le noir a été observé au cours du processus. Le mélange réactionnel a ensuite été laissé au repos toute la nuit. Le composite ferrite de nickel–recouvert de poly(aniline-co-o-toluidine) formé a été récupéré par filtration sous vide, soigneusement lavé à l'eau bidistillée et au méthanol, puis séché à 60 °C. Le produit sec obtenu a été finement broyé en poudre **[5].**

Figure II. 6. Ferrite de nickel recouvert de poly(aniline-co-o-toluidine)

4. Préparation des solutions

- **Solution de rouge-Bezaktiv**

La solution mère de colorant rouge-Bezaktiv de concentration 1000 ppm a été préparée, puis diluée pour obtenir des solutions comprises entre [2-50] ppm. Chaque solution a été mise en contact avec 30 mg de (Lemna minor brute et Lemna minor activée), dans un agitateur thermostatique à bain-marie, et de pH variant de [2-12], la valeur du pH a été contrôlée à l'aide d'un pH-mètre (ST7300, JENWAY). Après les temps de contact allant de 5 à 150 minutes, les solutions ont été centrifugées, et la concentration résiduelle du colorant par spectrophotométrie UV/Vis à une longueur d'onde de 524 nm de marque (ST7300, PerkinElmer).

- **Solution de 4-Nitrophenol**

L'efficacité de réduction du nanocomposite à base de $NiFe_2O_4$/PAOT a été étudiée à l'aide de la méthode d'équilibre en mode discontinu. Des solutions aqueuses de 4-nitrophénol (4-NP) ont été préparées à différentes concentrations (2, 10 et 15 ppm). Des quantités variables de catalyseur (5, 10 et 20 mg) ont été introduites dans 10mL de chaque solution, tout en maintenant un pH stable à 7,43. Le mélange réactionnel a été maintenu à 25 °C, avec des temps de contact allant de 2 à 60 minutes, afin de permettre l'interaction entre le catalyseur et le polluant. Ensuite, le catalyseur a été séparé de la solution par centrifugation, puis récupéré à

l'aide d'un aimant pour optimiser la collecte. La transformation du 4-NP en 4-AP a été suivie et quantifiée par spectrophotométrie UV-Visible (GENESYS 10S).

5. Techniques d'analyse

Différentes méthodes d'analyse ont été mises en œuvre pour caractériser les matériaux modifiés modifiées, notamment la spectroscopie infrarouge à transformée de Fourier (FTIR), la diffraction des rayons X (XRD), La microscopie électronique à balayage (MEB), scanning électron microscope (SEM), La spectroscopie X à dispersion d'énergie (EDX), l'analyse élémentaire ainsi que la spectrophotométrie (UV-VIS-NIR).

- **Diffraction des rayons X (XRD)**

La composition minéralogique et chimique a été déterminée par des analyses effectuées via la fluorescence des rayons X, en utilisant un équipement de diffraction adapté à ce genre de caractérisation de marque (ULTIMA IV, Rigaku). Cette analyse a été réalisée au sein de l'University de Bahrain.

- **Spectroscopie Infrarouge à Transformée de Fourrier (ITFR)**

Les analyses en spectroscopie infrarouge ont été réalisées à l'aide d'un spectrophotomètre, de marque (Sp-3-300, Pye-Unicam). Les pics d'absorption sont exprimés en nombre d'onde (cm^{-1}). Les analyses de Lemna minor ont été réalisées à l'Université de Tlemcen, celles du $NiFe_2O_4$/PAOT à l'Université de Bahreïn.

- **Méthode d'analyse BET**

Les analyses mésoporeuses des matériaux ont été effectuées grâce à un appareil de marque (V350, Alliance) est une technique d'analyse physique utilisée pour déterminer le diamètre, et le volume des pores et la surface spécifique du matériau solide (m^2/g). Cette analyse a été réalisée au sein de l'University de Bahrain.

- **Microscopie électronique à balayage (MEB)**

Une méthode d'imagerie de haute résolution de marque (JSM-IT800, JEOL Ltd) employée pour analyser la morphologie de surface et la microstructure des substances solides. Les analyses de la plante Lemna minor ont été effectuées au sein de l'Université de Tlemcen (Algérie), tandis que celles du composite $NiFe_2O_4$/PAOT ont été réalisées au sein de l'University de Bahrain.

- **Spectroscopie de rayons X à dispersion d'énergie (EDX)**

L'analyse de la composition élémentaire a été réalisée grâce à la spectroscopie de dispersion d'énergie des rayons X (EDX), Le couplage de la MEB à un détecteur EDX réalise des analyses semi-quantitatives en recevant les photons émis par un échantillon après excitation électronique et en les triant selon leur énergie. La marque d'appareil (JSM-IT800, JEOL Ltd), en utilisant un microscope électronique. Cette analyse a été réalisée au sein de l'University de Bahrain.

- **Analyse élémentaire**

Les analyses élémentaires de la plante Lemna minor ont été effectuées au sein de l'University de Bahrain à l'aide d'un analyseur élémentaire CHNS/O de marque PerkinElmer (2400 Series II). Cette technique a permis de déterminer la composition élémentaire de l'échantillon en carbone, hydrogène, azote et soufre.

- **UV-VIS-NIR**

Un spectrophotomètre UV-VIS-NIR (comme modèle UV-3600 de SHIMADZU) est un appareil qui permet de mesurer comment une substance absorbe la lumière dans les domaines ultraviolet (UV), visible (VIS) et proche infrarouge (NIR). Cette analyse a été réalisée au sein de l'University de Bahrain.

- **pH point zéro charge (pH $_{PZC}$)**

Le pH PZC (point de charge nulle) est le pH auquel la charge nette de la surface d'un solide est égale à zéro. Cette valeur est obtenue en utilisant la méthode de la dérivée du pH **[6].** Une série d'opération est réalisée dans lesquelles 0,2 g d'adsorbant sont ajoutés à 40 ml d'une solution de NaCl 0.01 M à pH initial ajusté à 2, 4, 6, 8, et 11, en utilisant 0,1 M de NaOH ou 0,1 M solution de HCI. Les mélanges sont laissés sous agitation continue pendant 24h afin que l'équilibre thermodynamique soit établi, puis le pH final de chaque solution est mesuré. On trace par la suite la courbe $\Delta pH = f(pH)$ afin de déterminer la valeur du pH PZC correspondante.
Cette technique a été réaliser au sein de l'Université de Tlemcen (Algerie)

Chapitre III :

Résultats et Discussions

Partie *I* : Caractérisation des matériaux

1. Lemna minor activée

➢ **Mode opératoire**

- Vingt grammes (20 g) de Lemna minor, ont été traités avec 1000 mL d'une solution à 0,1 M d'acide phosphorique ou d'acide citrique.
- Le traitement a été effectué sous agitation à 300 rpm pendant 3 heures.
- Les échantillons obtenus ont été désignés respectivement Lemna minor activée avec l'acide (phosphorique et citrique).
- Les solides ont ensuite été séchés au four à 50 °C pendant 24 heures. Une fois secs, les matériaux ont été broyés, tamisés, puis utilisés dans les expériences d'adsorption.

➢ **Caractérisation de la plante Lemna minor**

- **Analyse élémentaire pour Lemna minor brute**

L'analyse élémentaire de la plante a été réalisée à l'Université de Bahreïn. Les résultats donnés dans le **tableau III. 1** révélé des teneurs élevées en carbone (C) et en oxygène (O), ce qui confirme le fort potentiel de cette biomasse comme précurseur pour la préparation de matériaux activés. En effet, la richesse en carbone constitue une base favorable à la formation de structures carbonées stables après activation, tandis que la présence d'oxygène, sous forme de groupements fonctionnels, améliore les propriétés de surface et favorise les interactions avec le polluant (**BRSM**).

Tableau III. 2: Composition élémentaire de la plante de Lemna minor avant activation

Elément	Teneur (%)
Carbon (C)	45
Oxygène (O)	40
Hydrogène (H)	5
Azote (N)	1

- Spectroscopie infrarouge à transformée de Fourier (**FTIR)**

Afin d'identifier les groupes fonctionnels impliqués dans le processus de bioaccumulation du colorant rouge-Bezaktiv, une analyse par spectroscopie infrarouge à transformée de Fourier (FTIR) a été réalisée sur des échantillons de Lemna minor. (**Figure III. 1.**)

Cette technique a permis de révéler la nature des groupements chimiques présents à la surface de la plante ainsi que le type d'interactions établies entre l'adsorbant et le colorant.

Une bande importante observée à 3419,7 cm^{-1} correspond à la vibration d'élongation des groupes hydroxyles (O–H) associés aux fonctions carboxyliques présentes dans Lemna minor (LM). Le spectre présente également un pic caractéristique à 1651,5 cm^{-1} indiquant la présence de groupes carboxyles. D'autres bandes situées à 1444,4 cm^{-1} et dans l'intervalle 1632,3–598,1 cm^{-1} sont attribuées respectivement à l'élongation C–O et à la déformation angulaire des liaisons O–H **[4]**.

Concernant les échantillons ALM-P (la plante traitée à l'acide phosphorique), des bandes situées à 1086,5 cm^{-1} et 1409,6 cm^{-1} sont respectivement associées aux vibrations d'élongation des liaisons P–OH et P=O, caractéristiques de la présence de groupes phosphonates **[7]**. Pour les échantillons ALM-C (la plante traitée à l'acide citrique), une modification du pic de vibration C=O, qui passe de 1651,5 à 1735 cm^{-1}, confirme l'esterification des groupes carboxyles de la surface de Lemna minor.

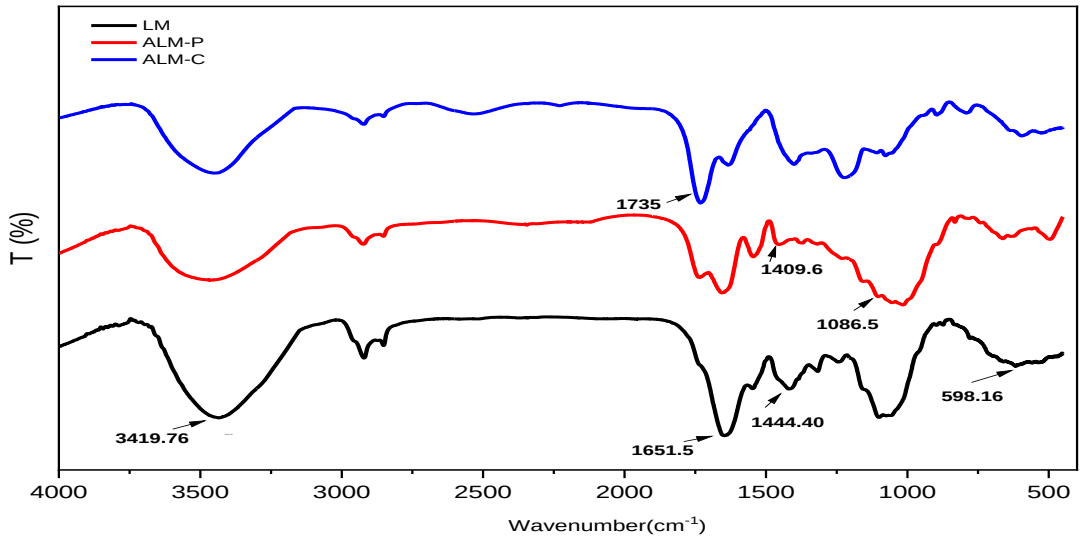

Figure III. 2. Spectres FTIR de LM et ALM

- **Microscopie électronique à balayage MEB**

Les micrographies MEB illustrent la morphologie de surface de Lemna minor avant et après activation chimique à l'acide phosphorique et citrique. L'image de la plante brute **(Figure III. 2)** révèle une surface relativement compacte, dense et faiblement poreuse, caractérisée par des structures fibreuses désordonnées et un enchevêtrement irrégulier. Cette morphologie a une accessibilité limitée des sites actifs pour l'adsorption **[8]**.

Après activation à l'acide phosphorique et citrique (**Figure III. 2**), la surface de la plante apparaît nettement modifiée, présentant une texture plus rugueuse et une porosité importante. L'action de l'acide a favorisé la décomposition partielle de la matrice organique, la création de cavités ainsi que l'ouverture des pores par le développement d'une microporosité, ce qui a considérablement augmenté la surface spécifique. Cette évolution morphologique confirme l'efficacité de l'activation chimique par l'acide (phosphorique et citrique) pour transformer la plante en un matériau adsorbant plus performant, adapté à la rétention de colorants **[9]**.

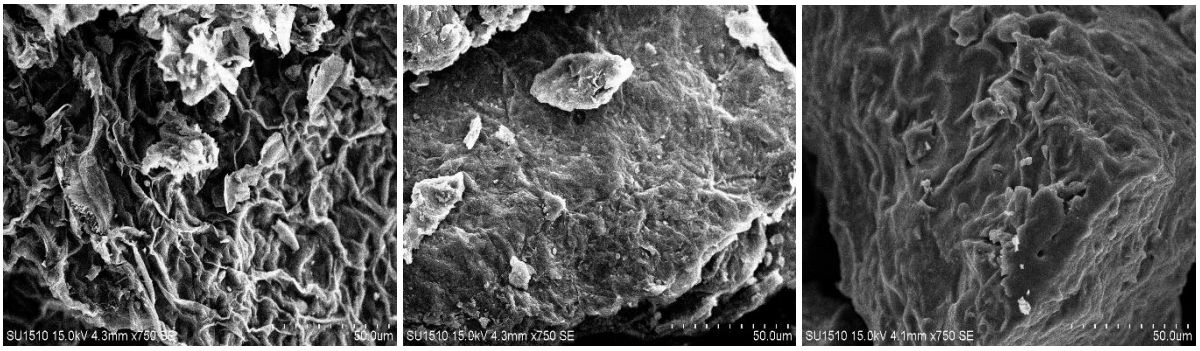

Figure III. 3. Images MEB de LM (a), ALM-P (b), ALM-C (c).

- **Analyse adsorption/désorption d'azote**

L'analyse BET a permis d'évaluer l'impact de l'activation acide sur la structure poreuse du carbone issu de Lemna minor (ALM). L'activation à l'acide citrique (ALM-C) a permis d'augmenter la surface spécifique de 73 à 209 m²/g, tandis que l'activation à l'acide phosphorique (ALM-P) a permis d'atteindre une surface encore plus élevée de 216 m²/g. Cette amélioration suggère que les traitements acides favorisent la formation de nouveaux sites actifs via l'ouverture des pores et l'élimination des impuretés. (**Tableau III. 3**)

Des résultats similaires ont été observés avec des charbons activés issus de divers adsorbants : tige de lotus (74,4 %) **[10]**, résidus de plantes (82,3 %) **[11]**, loosestrife (83,3 %) **[12]**, lignine (76,0 %) **[13]**, fibres de quenouille (78,1 %) **[14],** et polygonum orientale *linn.* (82,5 %) **[15].**

Tableau III. 4: Analyse adsorption/désorption d'azote de L. minor traitée et non traitée

Type d'adsorbant	Volume des pores (cm^3 g-1)	Diamètre des pores (nm)	Surface spécifique (m^2 g-1)
ALM	**0.02**	**35**	**73**
ALM-C	**0.15**	**4**	**209**
ALM-P	**0.2**	**2**	**216**

2. Nanocomposite $NiFe_2O_4$/PAOT

➢ Mode opératoire

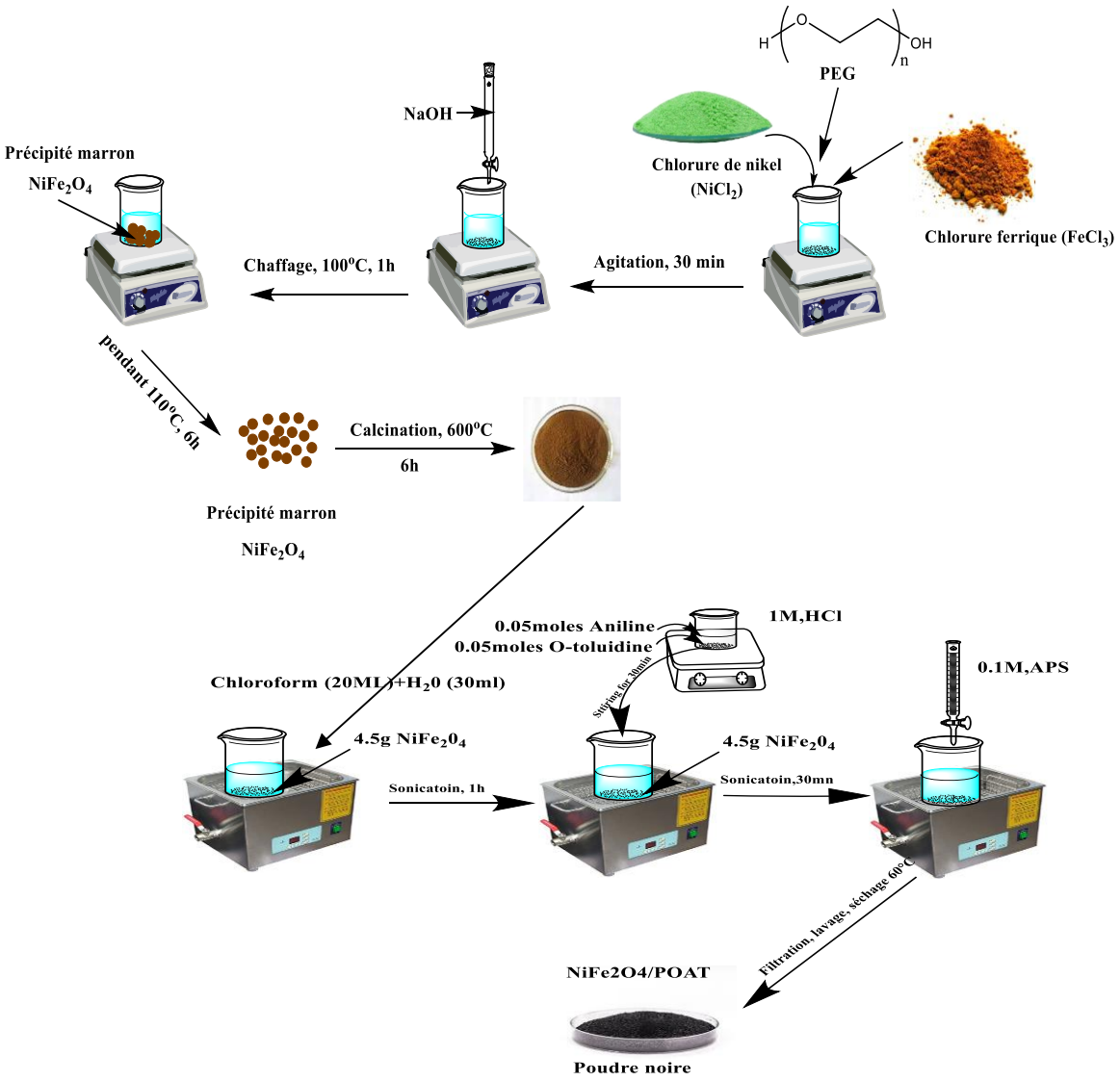

Schéma.1. Étapes de synthèse du nanocomposite $NiFe_2O_4$/PAOT.

➢ Caractérisation du Nanocomposite $NiFe_2O_4$/PAOT

- Spectroscopie infrarouge à transformée de Fourier (**FTIR)**

Les spectres FTIR des nanoparticules de $NiFe_2O_4$ après calcination ainsi que du nanocomposite $NiFe_2O_4$/PAOT après copolymérisation. Dans le spectre infrarouge des nanoparticules de $NiFe_2O_4$ calcinées, une bande large et peu intense autour de 3440 cm^{-1} est attribuée aux vibrations d'élongation O–H, liées à l'eau adsorbée lors de la préparation de la pastille de KBr. Deux autres bandes situées entre 1632 et 1382 cm^{-1} sont dues aux vibrations d'élongation asymétriques des groupes carbonates adsorbés.

Les bandes caractéristiques observées dans la région 585–453 cm^{-1} correspondent aux vibrations intrinsèques des liaisons Fe–O et Ni–O dans la structure spinelle **[16]**. Aucun autre pic n'est observé dans le spectre des nanoparticules calcinées de $NiFe_2O_4$.

Le spectre infrarouge du composite $NiFe_2O_4$/poly(aniline-co-o-toluidine) présente une large bande dans la région 3384–3230 cm^{-1}, attribuée à l'élongation N–H élargie par la formation de liaisons hydrogène. Les vibrations d'élongation du groupe $–CH_3$ de la fraction toluidine apparaissent entre 2920 et 2852 cm^{-1}. Les bandes situées entre 1587 et 1485 cm^{-1} sont associées aux vibrations d'élongation N–H et C=N. D'autres bandes dans la région 1149–1006 cm^{-1} correspondent aux déformations dans le plan des liaisons C–H. Enfin, deux bandes observées entre 572 et 415 cm^{-1} sont attribuées aux vibrations métal–oxygène à l'intérieur du réseau cristallin spinelle.

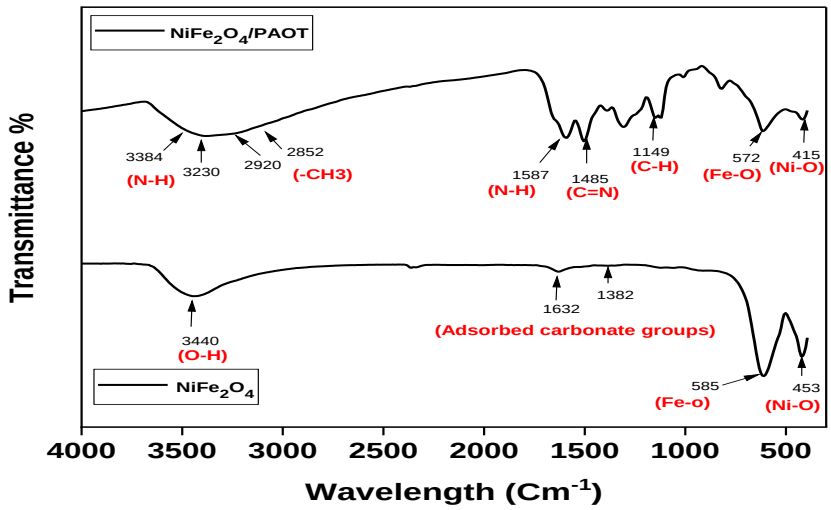

Figure III. 4. Spectres FTIR des nanoparticules de $NiFe_2O_4$ et du nanocomposite $NiFe_2O_4$/PAOT.

- **Diffraction des rayons X (DRX)**

Les matériaux synthétisés ont été soumis à une analyse de leurs propriétés structurales par diffraction des rayons X (DRX). Les diffractogrammes des nanoparticules de $NiFe_2O_4$ **[5]** et des nanocomposites $NiFe_2O_4$/PAOT ont été obtenus à l'aide d'un diffractomètre à poudre, utilisant un rayonnement CuKα (λ = 0,154 nm) dans un intervalle angulaire de balayage compris entre 10° et 70°. Les profils de diffraction, conformes à la fiche standard JCPDS (n° 10-0325), ont confirmé la formation d'une structure cristalline spinelle cubique, comme il est illustré dans la **figure III.4 [17].** Aucun pic supplémentaire n'a été observé, ce qui exclut la présence d'impuretés telles que NiO ou Fe_2O_3.

Sept pics de diffraction caractéristiques ont été identifiés aux positions 2θ suivantes : 30,24°, 35,48°, 36,94°, 43,06°, 53,80°, 57,20° et 62,88°, correspondant respectivement aux plans cristallins (220), (311), (222), (400), (422), (511) et (440). Le motif de diffraction des nanocomposites $NiFe_2O_4$/PAOT est globalement similaire à celui des nanoparticules pures de $NiFe_2O_4$, à l'exception d'une large bande observée entre 2θ=15° et 25° **[5],** attribuée au caractère amorphe de la matrice copolymère PAOT.

La diminution observée de l'intensité des pics dans les nanocomposites, comparativement aux $NiFe_2O_4$ purs, suggère une intégration efficace du PAOT à la surface des particules tout en conservant leur structure cristalline.

La taille moyenne des cristallites a été estimée à l'aide de l'équation de Scherrer :

- $\mathbf{D = (K\lambda) / (\beta \cos \theta)}$ (1)

où **D** est la taille des cristallites, **λ** la longueur d'onde du rayonnement X (CuKα, soit 0,154 nm), **θ** l'angle de diffraction de Bragg (en radians), **β** la largeur à mi-hauteur (FWHM) du pic de diffraction le plus intense correspondant au plan (311), et **K** la constante de Scherrer (K = 0,9). En appliquant cette méthode, les tailles moyennes des cristallites ont été estimées à **12,3 nm** pour les nanoparticules de $NiFe_2O_4$ et à **16,7 nm** pour les nanocomposites $NiFe_2O_4$/PAOT **[5]**.

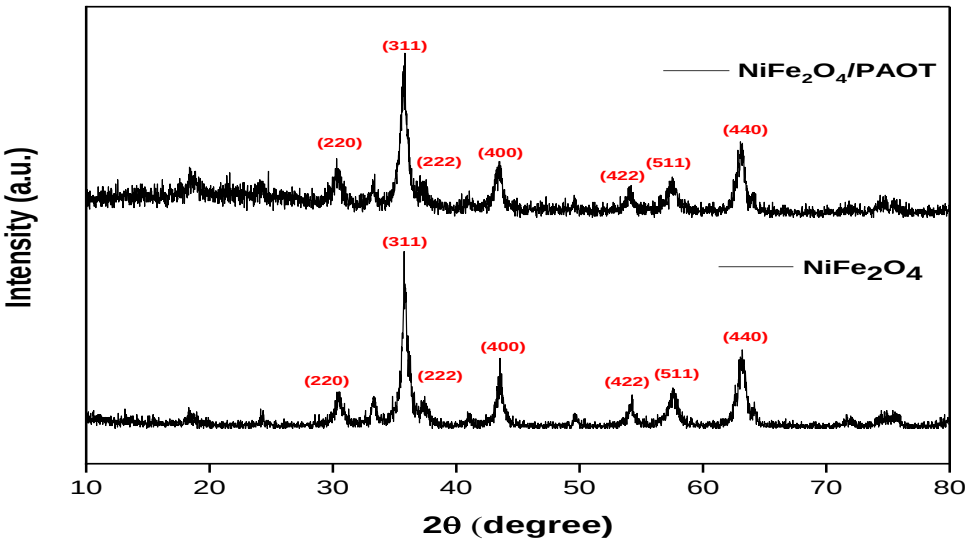

Figure III. 5. Spectres de diffraction des rayons X (XRD) des nanoparticules de $NiFe_2O_4$ et du nanocomposite $NiFe_2O_4$/PAOT.

- **Spectroscopie de rayon X à dispersion d'énergie EDX**

L'analyse EDX présentée dans la **figure III.5,** a confirmé le bon déroulement de la synthèse ainsi que de la modification de surface, en validant la composition élémentaire du $NiFe_2O_4$ et de sa forme recouverte par le polymère. Conformément à la structure spinelle attendue, les résultats ont révélé que le $NiFe_2O_4$ est principalement constitué d'oxygène, de fer et de nickel. Le fer présentait le pourcentage massique le plus élevé (**62,71 %**), ce qui souligne sa prédominance dans la structure cristalline.

La quantité plus faible de nickel (**11,13 %** en masse) correspondait au rapport stœchiométrique attendu. Les marges d'erreur associées au fer et à l'oxygène étaient faibles, indiquant une bonne précision des mesures. Dans l'échantillon de $NiFe_2O_4$ recouvert de polymère, les pourcentages massiques des éléments métalliques ont diminué, ce qui s'explique par l'introduction d'éléments plus légers tels que le carbone et l'azote issus de la couche polymère. De plus, la détection de faibles traces de chlore suggère la présence résiduelle de certains contaminants issus des réactifs.

Ces résultats montrent que le revêtement polymère a modifié la surface du matériau par l'introduction d'éléments plus légers, tout en conservant la structure spinelle du $NiFe_2O_4$. Par ailleurs, le rapport molaire **nFe/nNi** obtenu (**5,9 ≈ 6**) suggère une ségrégation du fer à la surface du matériau.

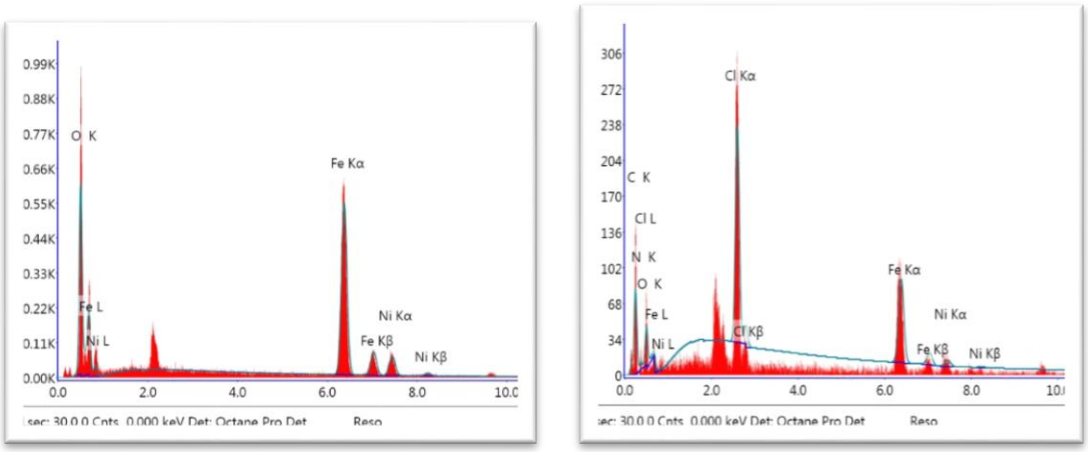

Figure III. 6. EDX du $NiFe_2O_4$ (a), Spectre EDX du $NiFe_2O_4$ recouvert de poly(aniline-co-o-toluidine) (b).

- **Microscopie électronique à balayage MEB**

Les caractéristiques morphologiques spécifiques du $NiFe_2O_4$ sont mises en évidence par l'image MEB données dans la **figure III.6**, révélant une distribution homogène des particules et une structure à l'échelle nanométrique. La taille des particules est relativement uniforme,

variant entre 45 nm et 56 nm. Cette dimension nanométrique contribue à l'augmentation de la surface spécifique du matériau, un paramètre essentiel pour ses propriétés catalytiques et magnétiques. L'arrangement dense des particules avec un faible degré d'agglomération témoigne d'une synthèse de haute qualité du $NiFe_2O_4$. Une telle morphologie est particulièrement favorable pour des applications telles que l'adsorption, la réduction catalytique, et d'autres procédés de dépollution environnementale **[18]**.

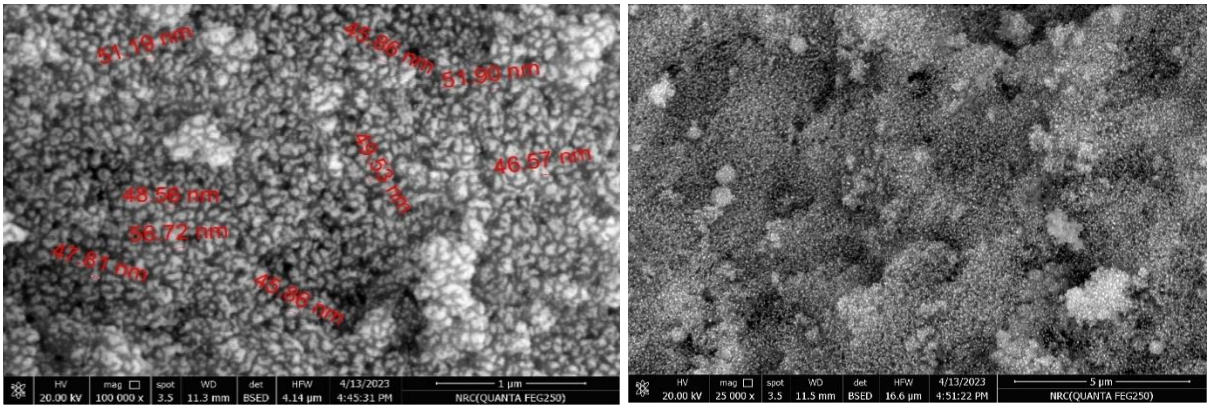

Figure III. 7. Images MEB du $NiFe_2O_4$ (a)

L'analyse de l'image MEB de la **figure III.7**, correspondant au $NiFe_2O_4$ recouvert de poly(aniline-co-o-toluidine), met en évidence les modifications morphologiques induites par la couche polymérique **[19]**. Les tailles de particules observées varient entre 32 nm et 68 nm, suggérant que le revêtement polymère influence la distribution granulométrique. Ce dernier confère au matériau une surface plus lisse et plus cohésive, tout en assurant une dispersion relativement homogène des particules. La présence du polymère semble renforcer la stabilité du matériau et limiter l'agglomération des particules. Ce revêtement préserve les caractéristiques fondamentales à l'échelle nanométrique du $NiFe_2O_4$ tout en apportant de nouvelles propriétés de surface, bénéfiques pour les applications catalytiques et environnementales.

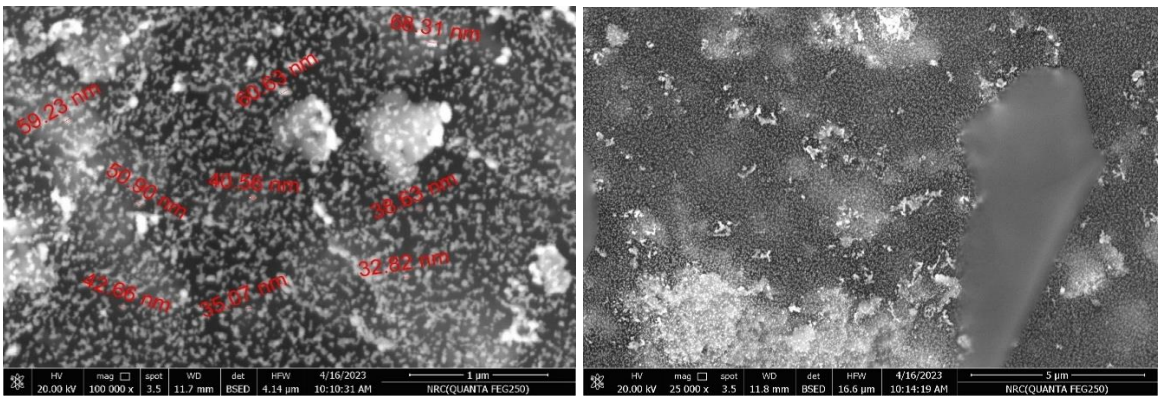

Figure III. 8. Images MEB de $NiFe_2O_4$ recouvert de Poly [Co-o-toluidine + Aniline]

Partie *II* : Méthode Expérimentale

Dans cette partie, le protocole expérimental a intégré l'étude de l'adsorption du colorant Rouge Bezaktiv sur Lemna minor brute et activée avec les acides phosphorique et citrique, utilisés comme adsorbants naturels. Les résultats expérimentaux obtenus sont discutés. De plus, les paramètres physico-chimiques influençant la capacité d'adsorption des matériaux ont été évalués. Ces paramètres sont :

- Cinétique d'adsorption (0–150 min), afin d'identifier la cinétique d'adsorption et le temps nécessaire à l'atteinte de l'équilibre.
- L'effet de la concentration initiale du colorant (2–50 ppm), afin d'établir sa corrélation avec la capacité d'adsorption à l'équilibre.
- L'effet de pH (2,4,6,8,10, et 12), pour déterminer son impact sur l'efficacité d'élimination du polluant.
- L'effet de la température, afin d'étudier l'évolution des mécanismes d'adsorption en fonction des conditions thermiques.

Par ailleurs, la nature de l'isotherme d'adsorption a été déterminée à l'aide de modèles classiques (Langmuir, Freundlich), tandis que la cinétique réactionnelle a été caractérisée en évaluant l'ordre de la réaction (premier, et second ordre). Ces approches ont permis de clarifier les mécanismes dominants (physiques ou chimiques) et d'optimiser les conditions opératoires pour une élimination maximale du colorant.

Adsorption du colorant Rouge-Bezaktiv

1- Détermination des paramètres spectroscopiques du colorant

- **Détermination de la courbe d'étalonnage du rouge-Bezaktiv**

La préparation des solutions étalons du colorant rouge Bezaktiv a été réalisée à partir d'une solution mère de concentration connue 1000 ppm. Ces solutions étalons, diluées à différentes concentrations (2–50 ppm), ont permis d'établir une courbe d'étalonnage reliant l'absorbance mesurée à la concentration du colorant. Les lectures d'absorbance ont été effectuées à l'aide d'un spectrophotomètre UV/VIS réglé sur une longueur d'onde optimale de **524 nm**, spécifique au maximum d'absorption du Bezaktiv.

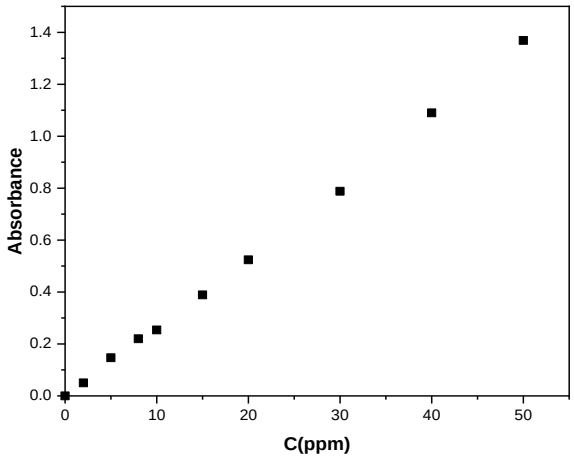

Figure III. 9. Courbe d'étalonnage de colorant (rouge Bezaktiv)

- **Procédure d'analyse**

Une solution mère de colorant rouge-Bezaktiv à une concentration de 1000 ppm a été préparée. Des dilutions successives ont permis d'obtenir des solutions expérimentales aux concentrations souhaitées. Les solutions de concentrations connues (2–50 ppm) ont été mélangées avec 30mg de Lemna minor brute ou activée dans un agitateur à bain-marie thermostaté, en ajustant le pH dans différentes valeurs de 2 à 12. Ces mélanges ont servi aux expériences d'adsorption en mode discontinu. Les mesures de pH ont été réalisées à l'aide d'un pH-mètre (modèle ST7300, JENWAY). La concentration résiduelle du colorant a été déterminée par spectrophotométrie UV/VIS (modèle ST7300, Perkin-Elmer) après une durée d'adsorption de 0 à 150 minutes, en utilisant une longueur d'onde λ = 524 nm.

La quantité de colorant adsorbée à l'équilibre, notée q (en mg/g), a été calculée à l'aide de l'équation (1) :

$$q_t = \frac{(C_i - C_t)}{m} \times V \qquad (1)$$

Avec :

C_i, C_t et C_e : représentent respectivement les concentrations initiales (en mg/L), à l'instant tt et à l'équilibre du colorant ;

V : Volume de solution (L) ;

m : la masse de l'adsorbant sec utilisé (g).

Le taux d'élimination (R%) a été évalué à l'aide de l'équation (2) :

$$\boldsymbol{R}(\%) = \frac{(\boldsymbol{C_i - C_e})}{\boldsymbol{ci}} \times \mathbf{100}$$

2- Étude cinétique de l'adsorption du colorant rouge-Bezaktiv par Lemna minor (LM)

L'étude de l'adsorption à l'équilibre pour l'élimination du colorant BRSM, à partir d'une concentration initiale de 40 ppm, révèle des performances différentes entre le charbon activé à l'acide phosphorique (ALM-P) et celui activé à l'acide citrique (ALM-C), tous deux issus de Lemna minor (LM). Les résultats, présentés dans la **figure III.9**, montrent également que le LM non traité présente une efficacité d'adsorption faible.

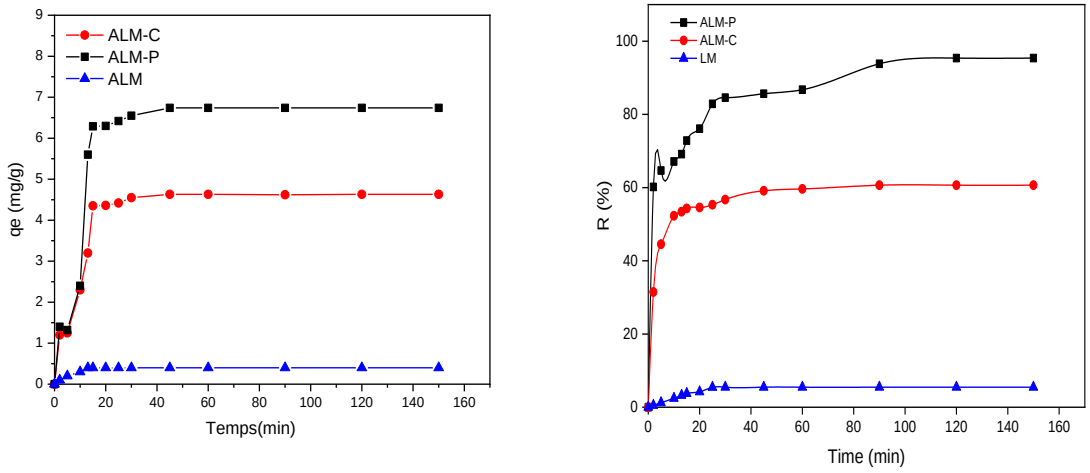

Figure III. 10. Cinétique d'adsorption du colorant rouge-Bezaktiv par Lemna minor brute (LM) et activées (ALM).

Dès les premières minutes (15min), Lemna minor activé avec l'acide phosphorique (l'ALM-P) démontre une adsorption supérieure, avec 6,29 mg/g de colorant adsorbé, soit plus de 78 % d'élimination. En comparaison, Lemna minor activée avec l'acide citrique (l'ALM-C) n'adsorbe que 4,35 mg/g (54 % d'efficacité).

Cette efficacité initiale est attribuée au volume poreux élevé et à la distribution homogène des tailles de pores de l'ALM-P, favorisant une fixation rapide des molécules de colorant. À 45 minutes, l'ALM-P améliore encore son efficacité (6,74 mg/g, soit 84,20 %), tandis que l'ALM-C atteint 4,63 mg/g (57,93 %). Les données confirment que l'ALM-P surpasse systématiquement l'ALM-C, grâce à sa surface spécifique plus large et à sa structure mésoporeuse, facilitant la diffusion et l'adsorption du colorant. À l'inverse, les pores plus étroits et restreints de l'ALM-C limitent sa capacité d'adsorption.

A l'équilibre, l'adsorption est atteinte vers 90 minutes : l'ALM-P présente une élimination de 85,05 % (6,80 mg/g), tandis que l'ALM-C se stabilise à 4,68 mg/g (58,53 %). Ces valeurs soulignent le potentiel supérieur de l'ALM-P, lié à ses propriétés de surface et à sa structure poreuse optimisées. En revanche, le Lemna minor non activée n'élimine que 5 % du colorant, confirmant l'importance de l'activation chimique.

Le traitement acide élimine d'une maniéré significatives les impuretés, les oxydes et les contaminants de surface, améliorant l'adhésion, la mouillabilité et la réactivité. Dans cette étude, l'acide citrique (pKa = 3,06) et l'acide phosphorique (pKa = 2,12) ont été utilisés pour activer le Lemna minor. L'efficacité de l'ALM-P s'explique par l'acidité plus élevée de l'acide phosphorique, permettant une élimination importante des contaminants colmatant les pores.

Le **tableau III.3**, montre les performances d'adsorption élevée de Lemna minor activée avec l'acide phosphorique (l'ALM-P) sur le colorant rouge-Bezaktiv à 16,86 mg/g, surpassant les autres adsorbants testés comme les noyaux de dattes et les graines d'hévéa pour différents colorants.

Tableau III. 5: Comparaison des capacités d'adsorption des colorants par des adsorbants

Adsorbants	Colorants	q_{max} (mg/g)	Ref
Carbon (noyaux de dattes)	Éosine jaune	0.16	[20]
Lemna minor	Bleu de méthylène	1.14 (Naturelle, non activée)	[4]
Boue rouge	Rouge Congo	7.08	[21]
Graine d'hévéa	Rouge Congo	9.82	[22]
Lemna minor	Bleu de méthylène	11.49 (Vivante, non activée)	[23]
Lemna minor	Rouge-Bezaktiv	16.86 (ALM-P) 7.69 (ALM-C)	[24]

Modélisation cinétique de l'adsorption

Afin d'élucider le mécanisme d'adsorption du colorant, les paramètres cinétiques ont été déterminés en analysant les données expérimentales à l'aide des modèles cinétiques suivants :

- **Modèle de pseudo-premier ordre (PPO)**

$$\mathrm{Ln}(q_e - q_t) = \mathrm{Ln}q_e - k_f \times t$$

- **Modèle de pseudo-second ordre (PSO)**

$$\frac{t}{q_t} = \frac{1}{k_s . q_e^2} + \frac{t}{q_e}$$

Avec :

q_t : Quantité de colorant adsorbée à un temps donné **(mg·g⁻¹)**,

q_e : Capacité d'adsorption à l'équilibre **(mg·g⁻¹)**,

kr: Constante cinétique du premier ordre **(min⁻¹)**,

ks : Constante cinétique du seconde ordre **(g·mg⁻¹·min⁻¹)**,

t : Temps de contact **(min)**.

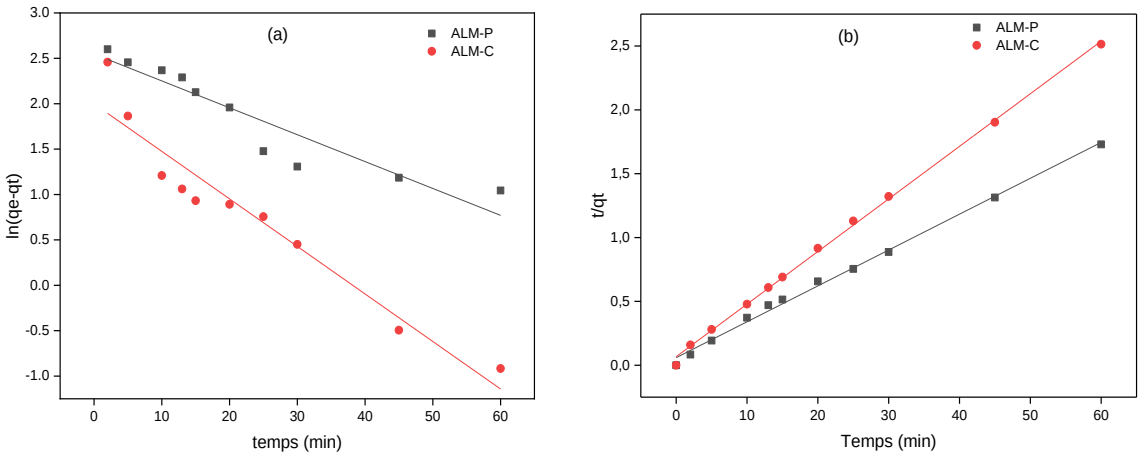

Figure III. 11. Courbes cinétiques de l'adsorption du colorant sur ALM-P et ALM-C (a) PPO et (b) PSO

D'après les résultats de la **figure III.10**, le modèle de pseudo-second ordre (PSO) s'avère meilleure que le modèle de pseudo-premier ordre (PPO) pour décrire les données expérimentales d'adsorption du colorant, comme le résume le **tableau III.4**. Les coefficients de corrélation (R^2) obtenus avec le PSO sont significativement supérieurs à ceux du PPO ($R^2 \geq 0{,}99$) pour le PSO contre ($R^2 \geq 0{,}93$) pour le PPO, confirmant un ajustement plus précis aux données expérimentales. De plus, les capacités d'adsorption à l'équilibre (q_e) calculées par le modèle PSO présentent une excellente concordance avec les valeurs expérimentales mesurées.

Tableau III. 6: Modèles PSO et PPO pour l'adsorption sur ALM-P et ALM-C.

Échantillons	Pseudo-Premier-ordre		Pseudo-second-ordre	
	K_1(min^{-1})	R^2	K_2(mg/g/min)	R^2
ALM-P	0.03	0.93	0.01	0.99
ALM-C	0.06	0.96	0.03	0.99

3- Effet du pH

Le pH constitue un paramètre déterminant dans l'étude de l'élimination des molécules colorantes, influençant simultanément les propriétés de surface des matériaux adsorbants et le degré d'ionisation des molécules de colorant. Les ajustements du pH initial ont été réalisés à l'aide de solutions d'acide chlorhydrique ou d'hydroxyde de sodium à 0,1 M. La **figure III.11,** présente l'évolution de l'adsorption du colorant rouge-Bezaktiv en fonction du pH, mettant en évidence deux comportements distincts pour les adsorbants ALM-P et ALM-C.

L'étude révèle que le pH affecte significativement l'efficacité d'adsorption, avec une diminution progressive lorsque le pH augmente. Les valeurs maximales d'adsorption (77,65% pour ALM-P et 45,42% pour ALM-C) sont obtenues à pH 2,0. Ce phénomène s'explique par la protonation des groupes carboxyles en milieu acide, favorisant la formation de liaisons hydrogène avec les atomes d'oxygène du colorant rouge-Bezaktiv et renforçant ainsi l'affinité des molécules pour la surface adsorbante.

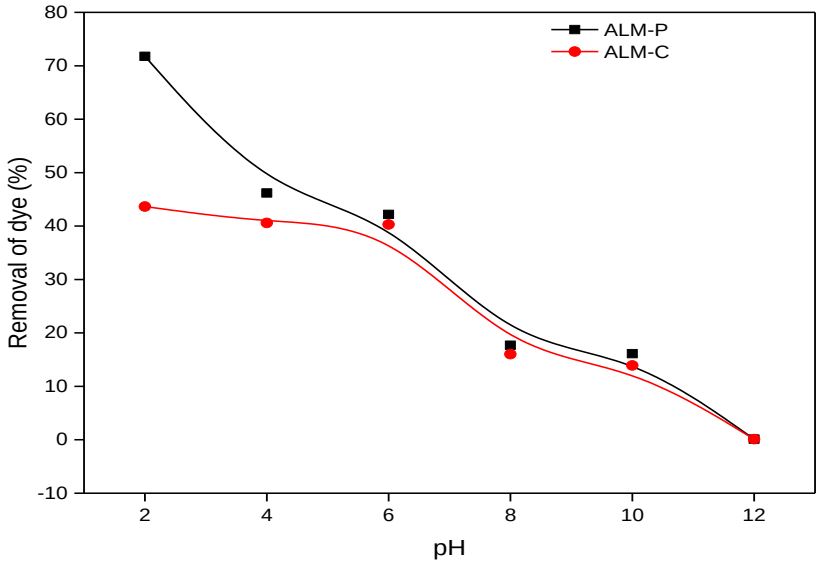

Figure III. 12. Adsorption du colorant sur Lemna minor (P,C) en fonction du pH initial

La détermination du point de charge nulle (pH_{PZC} à 5,4 pour ALM-P et 5,2 pour ALM-C (**Figure III. 12)**, a permis d'expliquer les mécanismes d'interaction. Lorsque le pH est inférieur à ces valeurs critiques, la surface des adsorbants acquiert une charge positive, facilitant l'adsorption du colorant anionique par attraction électrostatique. La protonation des groupements de surface réduit la charge négative résiduelle, amplifiant ces interactions électrostatiques.

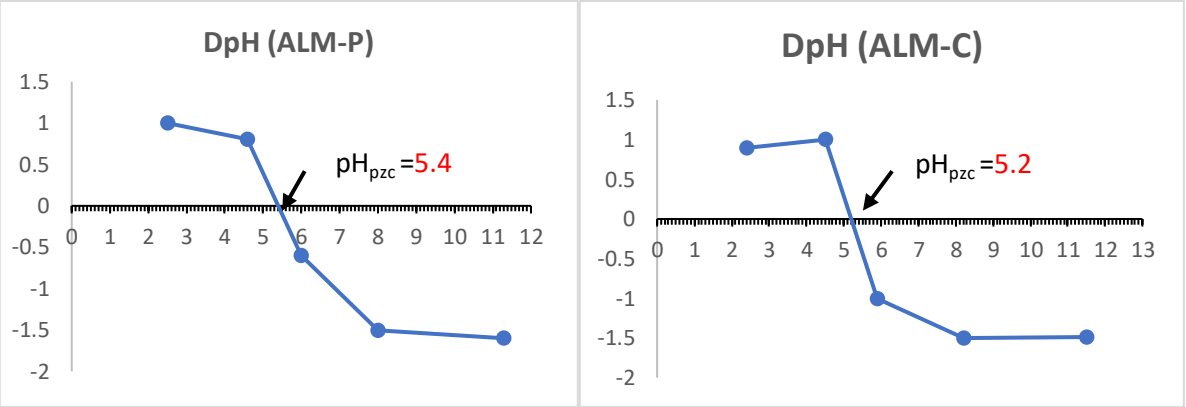

Figure III. 13. Détermination du point zéro charge (pH_{pzc}) pour ALM-(P,C)

4-Effet de la concentration initiale du colorant sur l'adsorption

Pour évaluer l'impact de la concentration initiale du colorant sur l'adsorption, une gamme de concentrations (2 à 50 ppm) a été testée, comme illustré dans la **figure III.13.** Les résultats montrent que la quantité de colorant rouge-Bezaktiv adsorbée par le matériau activé à l'acide (ALM-P) augmente de 6,66 mg/g à 16,68 mg/g avec l'élévation de la concentration initiale. En comparaison, le charbon activé chimiquement (ALM-C) présente une augmentation plus modeste de sa capacité d'adsorption, passant de 6,66 mg/g à 7,64 mg/g dans les mêmes conditions. Cette tendance suggère que des concentrations initiales élevées renforcent les interactions entre la surface de l'adsorbant et les molécules de colorant, améliorant le transfert de masse du colorant vers l'adsorbant. Ces résultats soulignent l'efficacité supérieure de l'ALM-P, dont la structure poreuse et la surface spécifique optimisées favorisent une adsorption accrue à fortes concentrations, contrairement à l'ALM-C dont la capacité reste limitée.

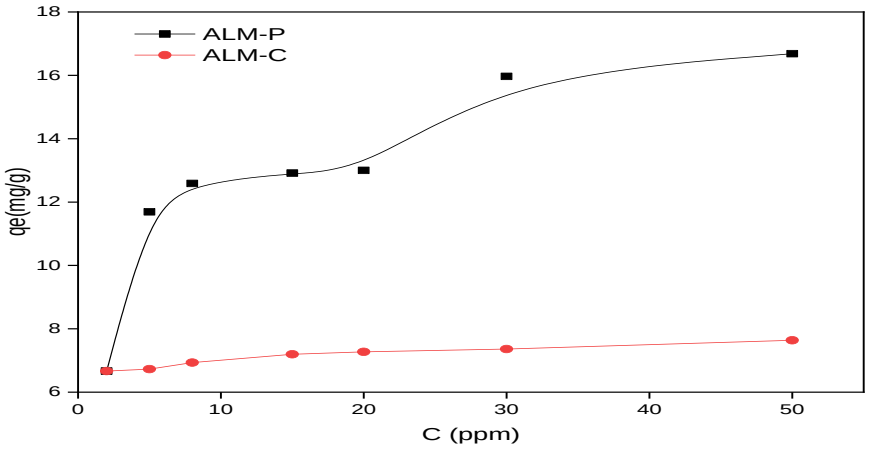

Figure III. 14. Adsorption du colorant sur ALM-(P,C) en fonction de la concentration initiale.

À des concentrations initiales plus élevées en colorant, la capacité d'adsorption s'améliore généralement, car plus de molécules de colorant sont disponibles pour interagir avec la surface de l'adsorbant. Cependant, lorsque la concentration dépasse un seuil critique, un effet de saturation peut réduire l'efficacité de l'adsorption. Ce phénomène se produit lorsque les sites de fixation actifs de l'adsorbant sont progressivement occupés, atteignant un état où peu de sites restent accessibles aux molécules de colorant supplémentaires.

En conséquence, la surface de l'adsorbant ne peut plus accueillir de nouvelles molécules, entraînant une diminution progressive de l'efficacité d'élimination due à la saturation des sites. Cette limitation est caractéristique des systèmes atteignant un équilibre d'adsorption, où l'excès de colorant persiste en solution, la capacité d'adsorption étant dictée par le nombre fini de sites actifs disponibles à la surface.

5- Isothermes d'adsorption

Les modèles de Langmuir et Freundlich sont les équations les plus couramment utilisées pour représenter les données d'adsorption. Elles sont exprimées par les relations suivantes :

- **Isotherme de Langmuir**

$$\frac{C_e}{q_e} = \frac{1}{q_m K_L} + \frac{1}{q_m} C_e$$

- **Isotherme de Freundlich**

$$Lnq_e = LnK_F + \frac{1}{n} LnC_e$$

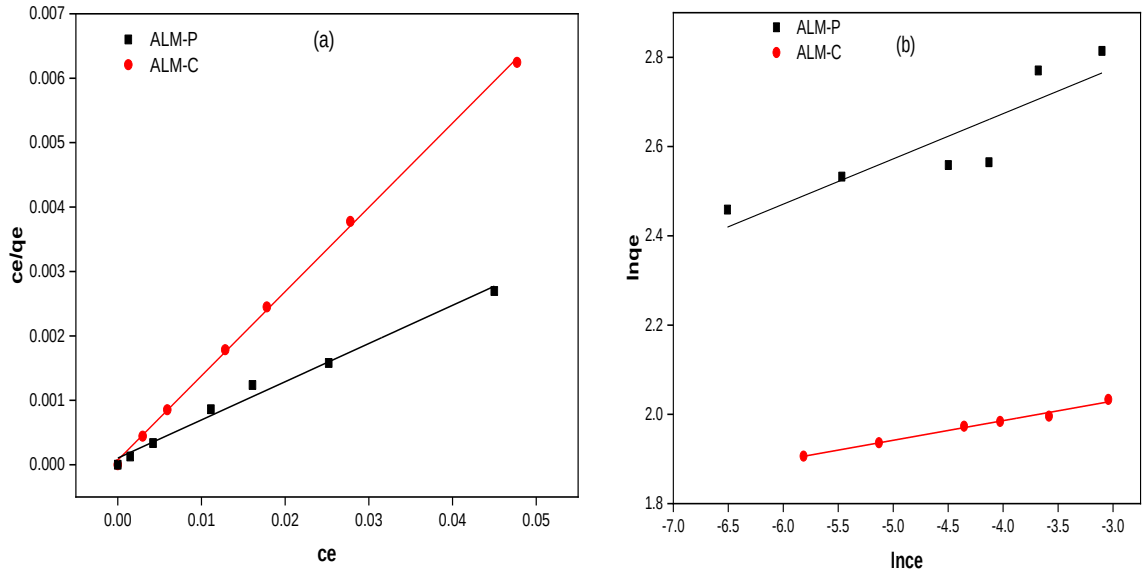

Figure III. 15. Modèle de Langmuir(a), modèle de Freundlich (b).

Tableau III. 7: Paramètres d'adsorption obtenus par les modèles de Langmuir et Freundlich

Isotherm	Parameters	ALM-P	ALM-C
Experiment	q_e (mg. g^{-1})	16.68	7.64
Langmuir	q_{max} (mg. g^{-1})	16.86	7.65
	k_L ($L.mg^{-1}$)	0.574	1.817
	R^2	0.994	0.998
Freundlich	K_F (mg. g^{-1})	21.74	8.688
	1/n	0.101	0.044
	R^2	0.886	0.994

L'excellente linéarité observée pour le modèle de Langmuir (**Figure III. 14. (a))**, montrée par les paramètres présentés dans le **tableau III.5**, témoigne de l'adéquation remarquable de ce modèle avec les données expérimentales d'adsorption du colorant BRSM sur les charbons activés ALM (traités respectivement à l'acide phosphorique et citrique).

Le coefficient de détermination élevé ($R^2 \approx 0,99$) confirme que le processus d'adsorption s'effectue principalement selon un mécanisme de monocouche sur une surface homogène. Cette observation implique que chaque molécule de colorant rouge-Bezaktiv vient occuper un site actif spécifique à la surface des matériaux ALM, minimisant ainsi les interactions intermoléculaires entre espèces adsorbées. Ce comportement est en parfaite conformité avec les postulats fondamentaux du modèle de Langmuir, qui suppose une adsorption en monocouche sur des sites énergétiquement équivalents et en l'absence d'interactions entre molécules adsorbées. La validité de ce modèle est étayée par plusieurs éléments : (1) la valeur quasi-unité du coefficient R^2 qui en valide statistiquement l'applicabilité, (2) la structure mésoporeuse des charbons ALM compatible avec la formation d'une monocouche, et (3) les analyses de caractérisation (BET, MEB) confirmant l'homogénéité de surface.

Ces résultats suggèrent que les sites d'adsorption présentent une affinité comparable pour le colorant et que la capacité maximale (q_m) correspond bien à la saturation complète de l'ensemble des sites disponibles.

6- Paramètres thermodynamiques

Une analyse thermodynamique a été réalisée à partir de données expérimentales issues d'études antérieures sur l'effet de la température de la solution. Les paramètres thermodynamiques, notamment l'énergie libre standard (ΔG°), l'enthalpie standard (ΔH°) et l'entropie standard (ΔS°), ont été calculés à l'aide des équations suivantes :

$$\mathbf{Ln}\ K_L = \frac{\mathbf{\Delta S}}{\mathbf{R}} - \frac{\mathbf{\Delta H}}{\mathbf{RT}}$$

Où :

R : Constante des gaz parfaits **(8,314 J/mol· K) ;**

T : Température **(K) ;**

K_L : Coefficient de distribution, défini par :

$$\mathbf{k_L(mL/g)} = \frac{\mathbf{C_i - C_e}}{\mathbf{C_e}} \times \frac{\mathbf{V}}{\mathbf{m}}$$

Avec :

C_i et **C_e** : Concentrations initiale et à l'équilibre du colorant rouge-Bezaktiv **($mg \cdot L^{-1}$).**

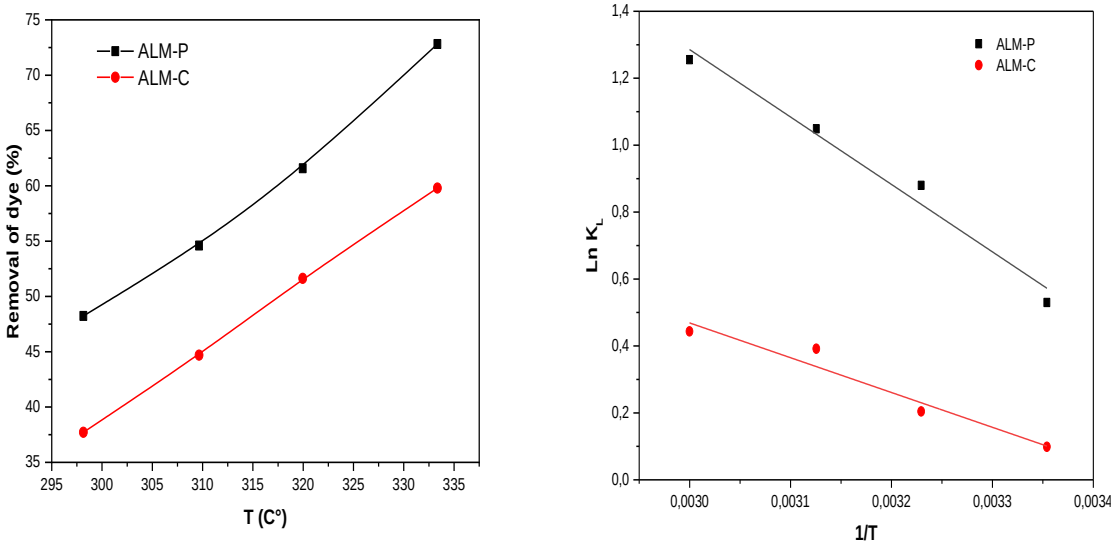

Figure III. 16. Courbe de Van't Hoff pour l'adsorption du colorant sur ALM-P et ALM-C

Tableau III. 8: Données thermodynamiques de l'adsorption du colorant sur Lemna minor

	ΔH° (KJ/mol)	ΔS° (J/mol)	R^2	ΔG° (KJ/mol)			
				298.1 K	309.6 K	319.9K	333.3 K
ALM-P	9.646	37.194	0.98	-1.44	-1.87	-2.25	-2.75
ALM-C	8.64	29.83	0.97	-0.24	-0.57	-0.87	-1.26

Les valeurs négatives de ΔG° présentées dans le **tableau III.6**, à toutes les températures testées confirment que le processus d'adsorption est spontané pour ALM-P et ALM-C, avec une tendance nette à l'augmentation de l'efficacité d'adsorption à des températures élevées. Les valeurs positives de ΔH°, caractéristiques d'un comportement endothermique, indiquent qu'une absorption de chaleur est nécessaire pour faciliter l'adsorption du colorant rouge-Bezaktiv sur ALM-P et ALM-C. Cela implique qu'une élévation de la température améliore la capacité d'adsorption.

Par ailleurs, les valeurs positives de ΔS° suggèrent une augmentation du désordre à l'interface solide-liquide, probablement due à l'interaction et à l'alignement des molécules de colorant sur la surface de l'ALM activé. ALM-P présente une spontanéité et des tendances endothermiques plus marquées que ALM-C, avec une ΔS° plus élevée (37,194 J/mol·K) et des ΔG° plus négatifs sur l'ensemble des températures.

7- Mécanisme d'adsorption

La **figure III.16**, illustre de manière détaillée les interactions entre les molécules du colorant rouge-Bezaktiv et le Lemna minor (LM) traité à l'acide phosphorique (ALM-P). Cette représentation met en évidence les mécanismes moléculaires, tels que les liaisons hydrogène et les interactions électrostatiques, qui favorisent l'adsorption du rouge-Bezaktiv sur la surface de Lemna minor activée a l'acide phosphorique (ALM-P).

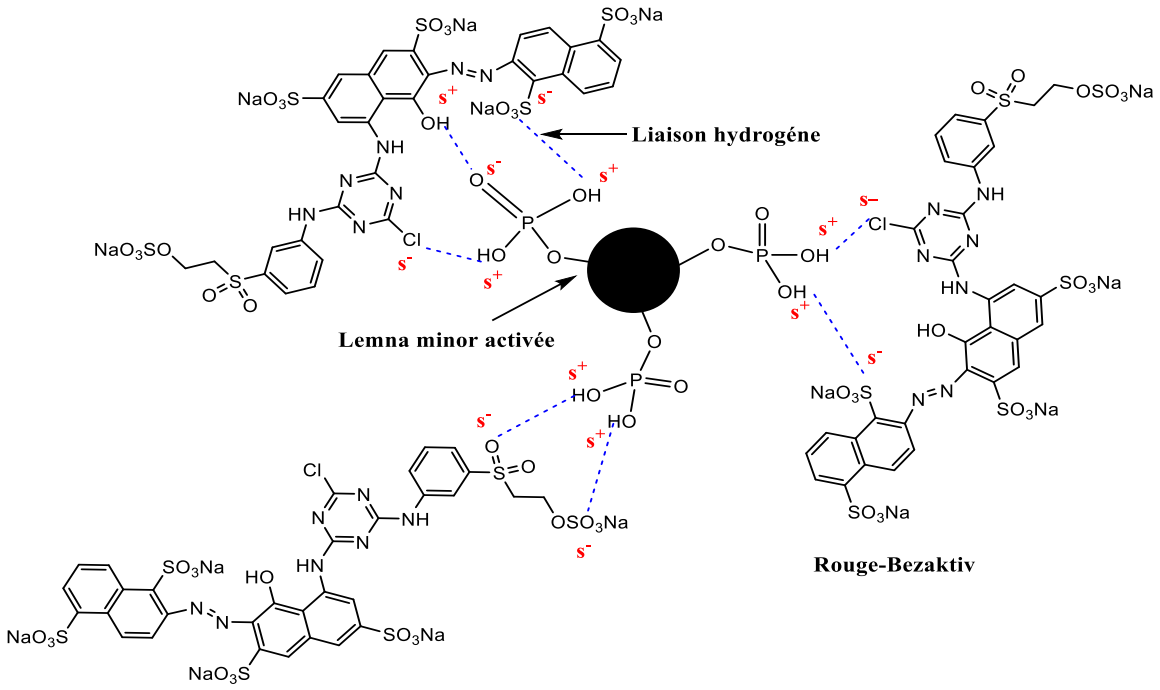

Figure III. 17. Représentation de mécanisme réactionnel entre les groupements fonctionnels de l'ALM-P et les sites réactifs du colorant rouge-Bezaktiv.

Le mécanisme d'adsorption met en évidence des interactions par liaisons hydrogène multiples entre les molécules de rouge-Bezaktiv et la surface de la Lemna minor activée avec l'acide phosphorique (ALM-P) (**Figure III. 18**). Le colorant rouge-Bezaktiv possède plusieurs groupes fonctionnels, notamment des groupes sulfonates (SO_3Na et SO_4Na), hydroxyle (–OH) et chlorure (Cl). Les atomes d'oxygène de ces groupes fonctionnels agissent comme accepteurs de liaisons hydrogène, permettant aux molécules de colorant de former des liaisons hydrogène stables avec des groupes spécifiques de la surface la Lemna minor activée avec l'acide phosphorique (ALM-P).

Sur la surface d'ALM-P, les groupes hydroxyle (–OH) et phosphoryle (P=O) agissent comme sites actifs impliqués dans la formation de liaisons hydrogène, facilitant la formation de liaisons avec les atomes d'oxygène des groupes sulfonate, hydroxyle et chlorure du rouge-Bezaktiv. Ces liaisons hydrogène stabilisent les molécules de rouge-Bezaktiv à la surface d'ALM-P, améliorant leur rétention en renforçant l'interaction entre le colorant et l'ALM-P. Ainsi, les liaisons hydrogène jouent un rôle clé dans l'ancrage du rouge-Bezaktiv à l'ALM-P, conduisant à une stabilité accrue de l'adsorption du colorant. En complément des liaisons hydrogène, les interactions électrostatiques contribuent significativement à l'adsorption du rouge-Bezaktiv sur ALM-P, particulièrement à des pH faibles. Lorsque le pH de la solution diminue, la concentration en ions hydrogène (H^+) augmente. Ce milieu favorise la protonation des groupes

hydroxyle (–OH) de la surface d'ALM-P, conférant à celle-ci une charge positive. La surface protonée d'ALM-P est alors attirée électrostatiquement par les groupes sulfonate chargés négativement du rouge-Bezaktiv.

Cette attraction électrostatique rapproche et aligne les molécules du rouge-Bezaktiv avec la surface d'ALM-P, facilitant la formation de liaisons hydrogène supplémentaires et stabilisant davantage l'adsorption. La synergie entre liaisons hydrogène et interactions électrostatiques assure une rétention efficace du colorant sur la surface d'ALM-P, en particulier sous conditions acides où la protonation amplifie l'affinité globale de liaison.

8- Performance d'ALM-P sur divers colorants anioniques

Les courbes présentées ci-dessous (**Figure III. 17)**, illustrent la cinétique d'adsorption des colorants anioniques Orange et Jaune (Bezaktiv) sur la plante de ALM-P.

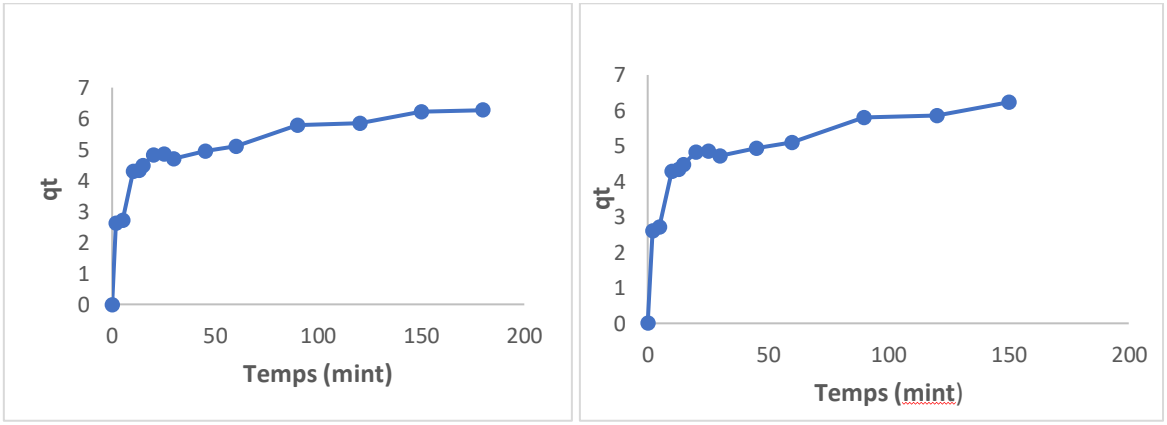

Figure III. 19. Cinétique d'adsorption des colorants (Orange et Jaune) Bezaktiv.

On observe dans les deux cas une adsorption rapide durant les premières minutes de contact, atteignant plus de 70 % de la capacité totale d'adsorption au cours des vingt premières minutes. Cette phase rapide peut être attribuée à la disponibilité initiale des sites actifs à la surface de l'adsorbant. Par la suite, la vitesse d'adsorption diminue progressivement, traduisant une saturation progressive des sites disponibles, jusqu'à atteindre un équilibre après environ 120 à 150 minutes. La comparaison entre les deux courbes montre une capacité d'adsorption légèrement plus élevée pour le colorant Jaune- Bezaktiv par rapport au Orange-Bezaktiv, ce qui pourrait être lié à des différences dans leurs structures moléculaires ou leurs affinités avec les groupes fonctionnels présents à la surface de l'adsorbant.

Les résultats obtenus montrent que Lemna minor activée avec l'acide phosphorique (ALM-P) possède une capacité d'adsorption significative vis-à-vis de plusieurs colorants anioniques de type Bezaktiv, notamment le rouge, mais également l'orange et le jaune. Cette efficacité vis-à-vis de différents types de colorants confirme la polyvalence de ce bio-adsorbant, ce qui le rend prometteur pour le traitement d'eaux usées contenant un large éventail de colorants anioniques. Cette aptitude à capter divers chromophores renforce l'intérêt environnemental de LM comme solution durable dans le domaine de la dépollution industrielle.

9- Conclusion

Les matériaux activés issus de Lemna minor (LM) ont été synthétisés avec succès via deux traitements acides distincts, produisant des adsorbants économiques, écologiques et faciles à préparer. Ces matériaux, désignés sous le nom Lemna minor activée avec l'acide phosphorique (ALM-P), présentent des propriétés de surface améliorées et une surface spécifique élevée, témoignant d'un potentiel d'adsorption accru. L'étude a identifié des conditions optimales pour l'élimination maximale des colorants, incluant une dose de30 mg de Lemna minor activée avec l'acide phosphorique, un pH de 2 pour la solution colorante et un temps d'adsorption de 90 minutes.

L'analyse cinétique a révélé que le modèle pseudo-secondaire décrit précisément la dynamique d'adsorption, tandis que l'isotherme de Langmuir s'ajuste le mieux aux données d'équilibre, indiquant une capacité d'adsorption maximale en monocouche de 16,86 mg g^{-1} pour le colorant rouge-Bezaktiv. Ces résultats confirment que le processus d'adsorption est principalement gouverné par des interactions chimiques homogènes à la surface de l'ALM-P.
En conclusion, cette recherche démontre que Lemna minor, transformés en ALM-P, constituent un adsorbant performant et durable pour l'élimination des colorants synthétiques en milieu aqueux. Leur efficacité, couplée à leur faible coût de production et à leur origine biosourcée, positionne ce matériau comme une solution prometteuse pour la dépollution des eaux industrielles. Ces travaux ouvrent des perspectives concrètes pour l'intégration de biomatériaux activés dans des technologies de purification de l'eau, alignées sur les principes de la chimie verte et de l'économie circulaire.

Au regard des conclusions tirées de cette recherche, il est évident que Lemna minor, une plante aquatique à croissance rapide et abondamment présente, constitue une matière première privilégiée pour la création de matériaux adsorbants de haute efficacité. L'utilisation de l'acide phosphorique et de l'acide citrique pour une activation chimique a conduit à la création de

surfaces fonctionnelles riches et de structures mésoporeuses propices à l'adsorption de colorants comme le rouge-Bezaktiv. Ce traitement acide a prouvé l'efficacité du charbon actif obtenu, notamment celui activé par l'acide phosphorique, tant sur le plan de la vitesse que de la capacité d'adsorption maximale.

Réduction Catalytique du 4-Nitrophénol

Ce chapitre expose les observations expérimentales liées à la transformation catalytique du 4-nitrophénol (4-NP) en 4-aminophénol (4-AP), en utilisant le poly(aniline-co-o-toluidine) comme catalyseur solide. Une étude approfondie a été menée afin d'examiner l'influence des conditions opératoires sur la performance de la réaction, tout en mettant l'accent sur les caractéristiques physico-chimiques du copolymère, telles que sa conductivité électrique, sa surface réactive, ainsi que sa résistance thermique. Ces paramètres incluent :

- L'effet de temps de contacte (0–60 min), analysé pour identifier la cinétique de réduction et le temps nécessaire à l'atteinte de l'équilibre.
- L'effet de la concentration initiale du 4-NP (5,10 et 15ppm).
- L'effet de la masse de catalyseur (4,10, et 20 mg), pour déterminer son impact sur l'efficacité d'élimination du polluant.
- L'effet de la température, afin d'étudier l'évolution des mécanismes de réduction catalytique en fonction des conditions thermiques.

La réduction catalytique du 4-nitrophénol (4-NP) a été étudiée selon le modèle de pseudo-premier ordre en fonction des paramètres opératoires (température, masse, concentration et temps).

Cette approche permet de clarifier les mécanismes réactionnels et d'optimiser les conditions opératoires de la réduction catalytique.

1. Détermination des paramètres spectroscopiques du 4-Nitrophénol

➢ Détermination de la courbe d'étalonnage du 4-Nitrophénol (4-NP)

Les préparations des solutions étalons du 4-NP ont été réalisées à partir d'une solution mère de concentration connue 40 mg/L. Ces solutions étalons, diluées à différentes concentrations (5,10 ,15, et 20 mg/L), ont permis d'établir une courbe d'étalonnage reliant l'absorbance mesurée à la concentration du 4-NP. Les lectures d'absorbance ont été effectuées à l'aide d'un spectrophotomètre UV/VIS réglé sur une longueur d'onde optimale de 400 nm, spécifique au maximum d'absorption du 4-NP.

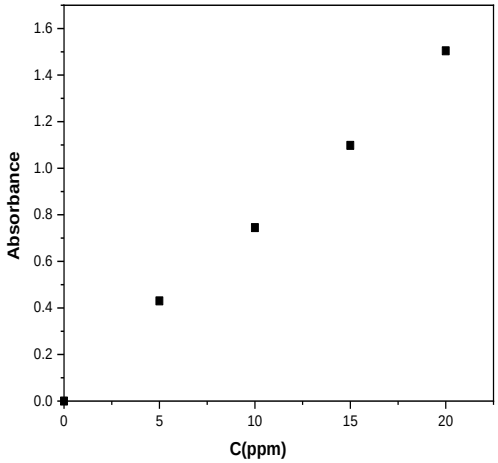

Figure III. 20. Courbe d'étalonnage du 4-nitrophénol

2. Procédure d'analyse

Afin d'évaluer l'activité catalytique, des solutions de 4-nitrophénol aux concentrations de 2, 10 et 15 ppm ont été préparées dans un volume fixe de 10mL. Le catalyseur, doté de propriétés magnétiques, a été mis en suspension sous agitation à l'aide d'un barreau agitateur en verre, assurant une homogénéité du mélange. Après un prémélange de 5 minutes, une masse de 10 mg de catalyseur a été ajoutée au système réactionnel. La réaction a été poursuivie pendant une durée de 60 minutes à température ambiante. Une diminution progressive de la teinte jaune caractéristique du 4-nitrophénol a été observée, traduisant l'avancement de la réaction de réduction. L'évolution de la réaction a été suivie en mesurant l'absorbance à 400 nm, correspondant à la disparition du 4-NP et à la formation du 4-AP. Les mesures de pH ont été réalisées à l'aide d'un pH-mètre (modèle ST7300, JENWAY).

La concentration résiduelle du 4-NP a été déterminée par spectrophotométrie UV/VIS (modèle ST7300, Perkin-Elmer).

3. Étude cinétique de la réduction du 4-NP par le nanocomposite

L'effet de la concentration initiale du 4-nitrophénol (4-NP) sur sa transformation catalytique en 4-aminophénol (4-AP) à l'aide du catalyseur $NiFe_2O_4$/Poly [o-toluidine + aniline] (POAT) a été étudié. Les résultats montrent que la réactivité du système est fortement influencée par la quantité de substrat. À faible concentration (2 ppm), la réduction est très efficace, avec un ratio $C_t/C_\circ$ de 0,631 après une heure de réaction, traduisant une bonne accessibilité des centres catalytiques. À 10 ppm, une baisse modérée de l'activité est notée ($C_t/C_\circ$ = 0,77), en

raison d'une concurrence importante pour les sites actifs. À 15 ppm, la réaction est nettement ralentie (C_t/C_o = 0,878), ce qui laisse penser à une saturation du catalyseur ou à des limitations dues au transfert de matière (**Figure III.19**)

La **figure III. 20**, présente l'évolution spectroscopique au cours de la réaction de réduction du 4-nitrophénol (4-NP). À l'état initial (temps = 0 minute), le pic d'absorbance à 400 nm atteint son intensité maximale, correspondant à la concentration initiale du 4-NP. Au cours de la réaction, on observe une diminution progressive de l'intensité de ce pic à 400 nm, parallèlement à l'émergence et à l'augmentation d'un pic à 318 nm. Ces modifications spectrales témoignent de la transformation cinétique du 4-NP en 4-aminophénol (4-AP), confirmant l'avancement de la réduction.

Conditions expérimentales : Volume de solution = 10 mL, Température ambiante (25 °C), pH = 7,43, Concentrations initiales du 4-NP (2, 10 et 15 ppm), Masse du catalyseur = 10 mg.

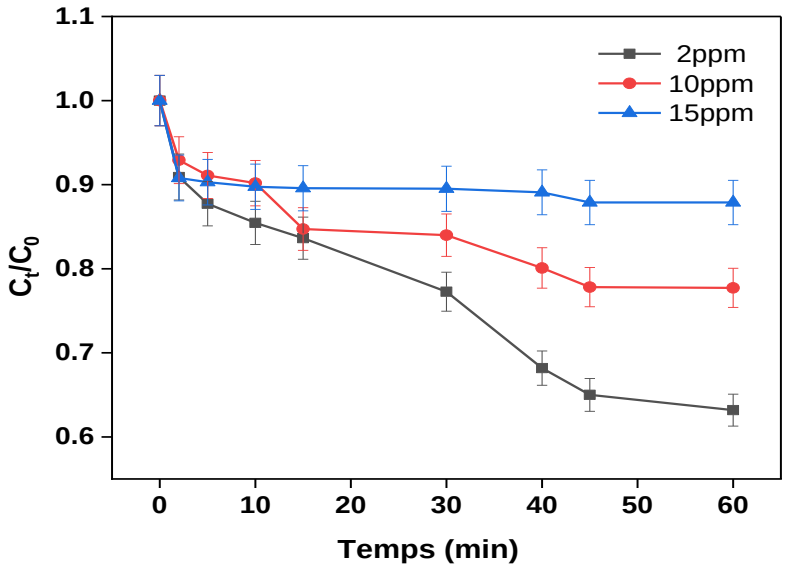

Figure III. 21. Effet de la concentration du 4-NP sur la réduction.

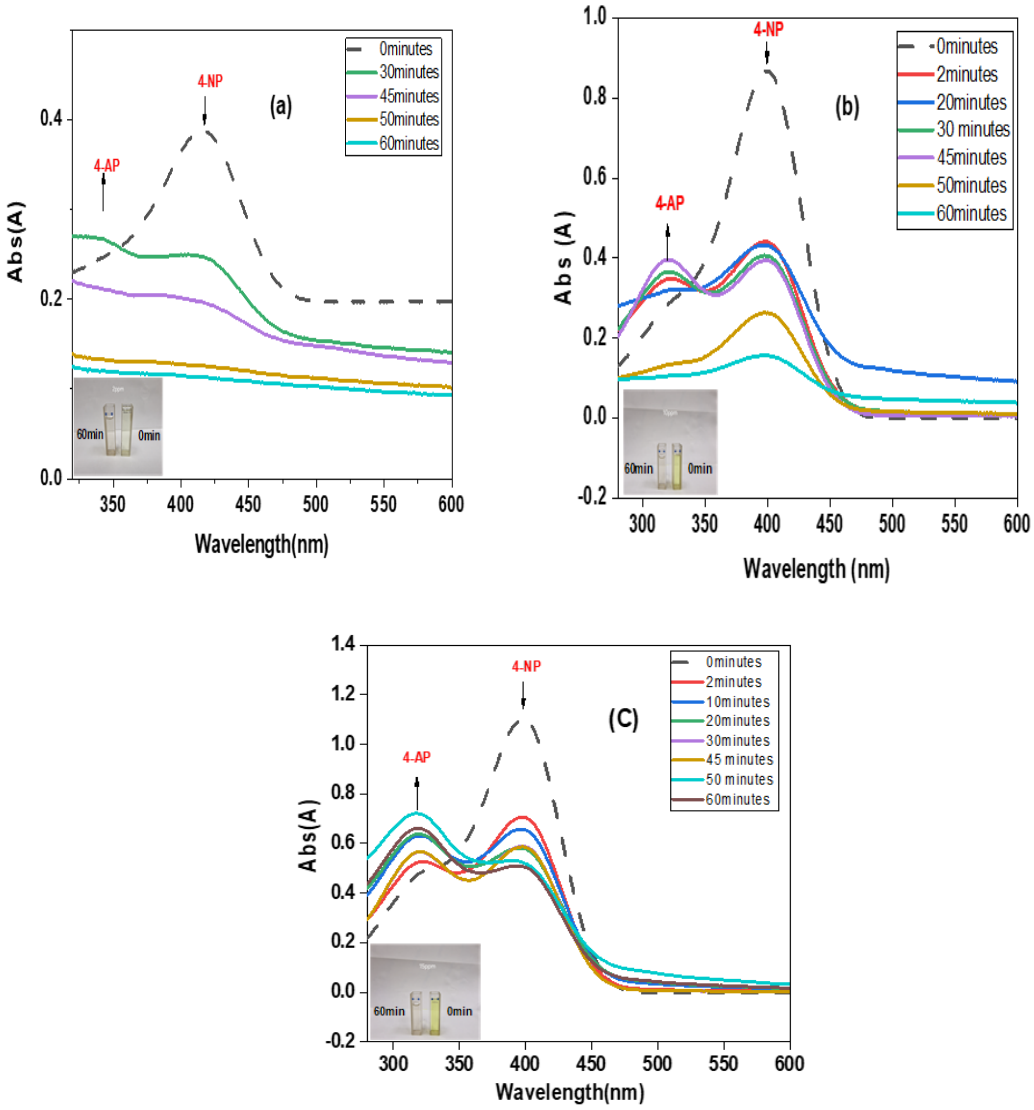

Figure III. 22. Spectres UV-visible de la réduction du 4-NP en 4-AP à (a) 2 ppm, (b) 10 ppm et (c) 15 ppm

Le rapport entre la concentration de 4-NP à un temps t (C_t) et sa concentration initiale à t_0 (C_o) est équivalent au rapport des valeurs d'absorbance correspondantes A_t/A_o mesurées à une longueur d'onde de 400 nm. Sur la base de cette relation, l'équation cinétique régissant le processus de réduction peut être exprimée par l'équation de pseudo premier ordre :

$$-Ln(C_t/C_0) = -ln(A_t/A_o) = K_{app}\, t$$

La constante apparente de vitesse (K_{app}) est déterminée à partir de la pente de la courbe linéaire représentant ln (C_t/C_0) en fonction du temps de réaction. La **figure III.21,** met en évidence une relation linéaire entre ln (A_t/A_o) et le temps, confirmant que la réduction du 4-nitrophénol (4-NP) catalysée par le $NiFe_2O_4$/POAT suit une cinétique de pseudo-premier ordre.

Les constantes apparentes de vitesse (K_{app}) ont été calculées à partir des pentes des droites correspondantes :

- 2 ppm: $K_{app} = 1{,}16 \times 10^{-2}$ min^{-1}, $R^2 = 0{,}98$
- 10 ppm: $K_{app} = 3{,}5 \times 10^{-3}$ min^{-1}, $R^2 = 0{,}96$
- 15 ppm: $K_{app} = 5{,}44 \times 10^{-4}$ min^{-1}, $R^2 = 0{,}94$

Ces résultats révèlent une variation significative de la vitesse de réduction avec l'augmentation de la concentration initiale. Cette diminution de K_{app} aux concentrations élevées pourrait s'expliquer par :

- Une compétition importante pour les sites actifs à la surface du catalyseur, réduisant l'accessibilité des molécules de 4-NP.
- Des modifications des interactions moléculaires entre le 4-NP et la surface catalytique, influençant l'adsorption et l'activation des réactifs.

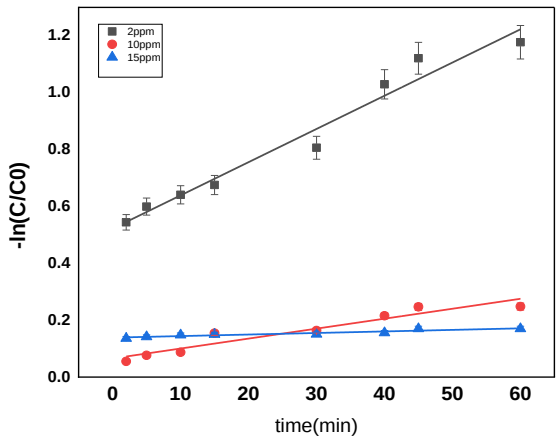

Figure III. 23. Vitesse de réduction du 4-nitrophénol ($m_{NiFe_2O_4/POAT}$ =10 mg)

4. Effet de la quantité du catalyseur

La **figure III.22**, analyse l'impact de la quantité de catalyseur $NiFe_2O_4$/PAOT sur la dégradation du 4-nitrophénol (4-NP), testée à des concentrations initiales de 2, 10 et 15 ppm avec des doses catalytiques de 5, 10 et 20 mg. L'augmentation de la masse de catalyseur réduit le rapport C_t/C_o (concentration résiduelle/concentration initiale), reflétant une meilleure efficacité de réduction. La solution à 2 ppm montre la réduction la plus marquée ($C_t/C_o = 0{,}545$ à 20 mg), suivie des solutions à 10 ppm ($C_t/C_o = 0{,}59$) et 15 ppm ($C_t/C_o = 0{,}78$) à la même dose. Cependant, l'efficacité diminue aux concentrations élevées, nécessitant des doses catalytiques plus importantes pour une dégradation optimale à des niveaux de polluant plus élevés. Ces résultats confirment l'effet favorable de l'augmentation de la dose catalytique sur l'efficacité de réduction, particulièrement à faible concentration en polluant (4-NP).

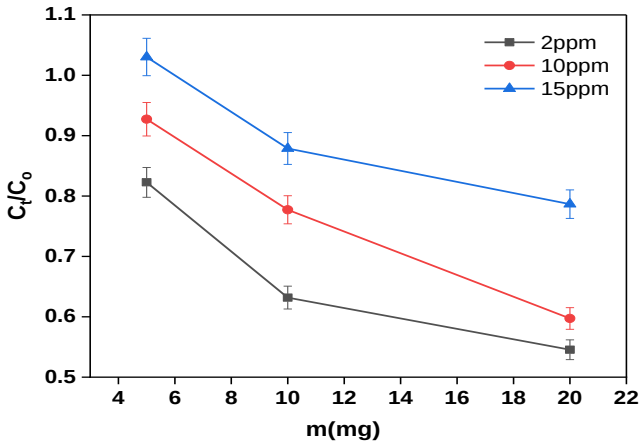

Figure III. 24. Effet de la dose (NiFe2O4 /PAOT) sur la réduction de (4NP), (m=5, 10 et 20 mg)

5. Effet de la température

La **figure III.23,** analyse l'effet de la température (37°C ; 50°C) sur la réduction du 4-NP catalysée par le $NiFe_2O_4$/POAT. À 37°C, l'efficacité maximale est observée à 2 ppm (64%), mais chute à 38% et 37% pour 10 ppm et 15 ppm. À 50°C, l'efficacité s'élève à 64% (2 ppm), 63% (10 ppm) et 61% (15 ppm), révélant une activation thermique du catalyseur. Cette amélioration est attribuée à l'augmentation de l'énergie cinétique des réactifs et à l'optimisation du transfert d'électrons, étapes limitantes à basse température. Ces données soulignent que 50°C est une condition optimale pour maximiser la réduction du 4-NP, indépendamment de la concentration initiale, dans le système catalytique étudié.

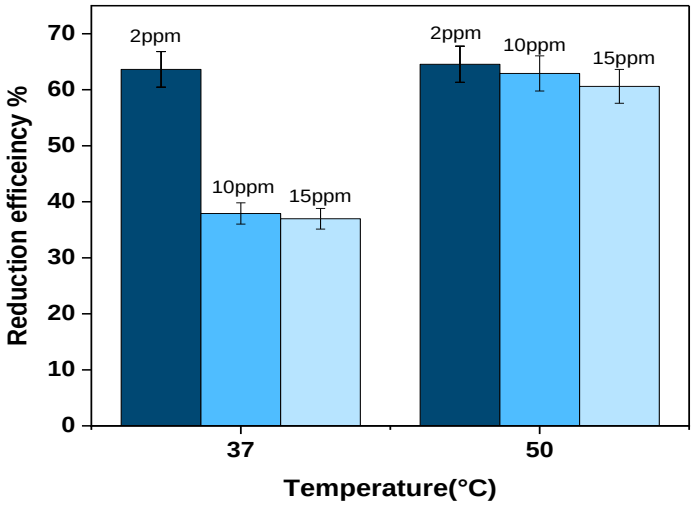

Figure III. 25. Effet de la température sur la réduction du 4NP, T = (37 et 50 °C)

6. Détermination de l'énergie de gap

La **figure III. 24,** illustre l'énergie de gap optique (E) du $NiFe_2O_4$, obtenue en traçant $[F(R)\cdot E]^2$ en fonction de l'énergie des photons (E, en eV) et en extrapolant la portion linéaire de la courbe jusqu'à son intersection avec l'axe des énergies. D'après la figure, l'énergie de gap calculée pour le $NiFe_2O_4$ est d'environ 1,66 eV, ce qui concorde avec les valeurs antérieurement rapportées dans la littérature **[25],** confirmant ainsi la fiabilité de ce résultat.

Après modification avec du POAT, l'énergie de gap diminue à environ 1,24 eV (**Figure III.24**), indiquant que le matériau composite $NiFe_2O_4$/POAT présente une capacité améliorée à absorber des photons de plus basse énergie. Cette réduction de l'énergie de bande gap énergétique accroît la sensibilité du catalyseur à la lumière visible, le rendant ainsi plus efficace pour des applications photocatalytiques et renforçant son efficacité globale dans les processus de dépollution environnementale.

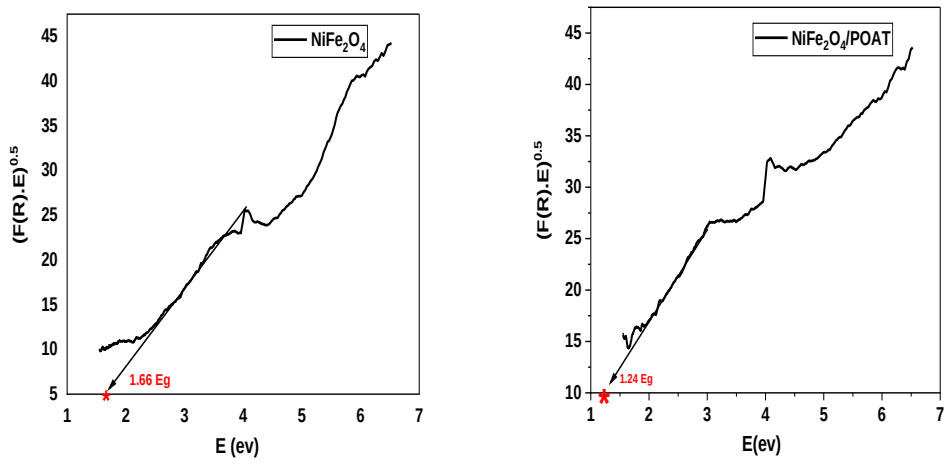

Figure III. 26. Gap énergétique du $NiFe_2O_4$ et du $NiFe_2O_4$/POAT

7. Mécanisme de réduction catalytique du 4-nitrophénol (4-NP) en 4-aminophénol (4-AP)

Le nanocomposite $NiFe_2O_4$/POAT, issu de la combinaison de nickel ferrite et du copolymère poly(aniline-co-o-toluidine), démontre une performance catalytique élevée pour la conversion du 4-nitrophénol (4-NP) en 4-aminophénol (4-AP) sous éclairage à lumière visible (**Figure III.25**). Ce comportement catalytique repose sur une interaction synergique entre le caractère semi-conducteur du $NiFe_2O_4$ et la conductivité électronique du POAT. L'intégration du polymère réduit l'énergie de bande de 1,66 eV (matériau seul) à 1,24 eV (système hybride), améliorant ainsi la capacité du matériau à absorber le spectre visible.

Le copolymère POAT, constitué par les deux polymères d'aniline et d'o-toluidine, joue le rôle d'un donneur d'électrons via ses cycles redox, transférant ces électrons vers les centres catalytiquement actifs du $NiFe_2O_4$ (notamment les cations Ni^{2+} et Fe^{3+}), où ils peuvent être temporairement piégés. Les molécules de 4-NP sont adsorbées en surface grâce à des interactions π-π entre les cycles aromatiques du substrat et la structure conjuguée du polymère.

Le processus de réduction s'initie par l'attaque du groupe nitro ($-NO_2$) du 4-NP par les électrons transférés, suivant une séquence réactionnelle : transformation en nitroso (-NO), puis en hydroxylamine (-NHOH), pour aboutir à l'aminophénol ($-NH_2$). À chaque étape, les protons (H^+) présents dans le milieu interviennent pour stabiliser les espèces intermédiaires.

La bonne mobilité électronique assurée par la conductivité du POAT, combinée à la structure spinelle du $NiFe_2O_4$, qui favorise la circulation des électrons à travers ses sites métalliques, limite la recombinaison des paires électron-trou. Cette efficacité se traduit par une conversion complète en une heure, (1) la décoloration progressive de la solution (du jaune vers l'incolore), indiquant la disparition du groupe chromophore nitro, et (2) l'évolution du spectre UV-visible, marquée par la diminution du pic à 400 nm (associé au 4-NP) et l'apparition simultanée d'un nouveau pic à **318** nm, correspondant au 4-AP.

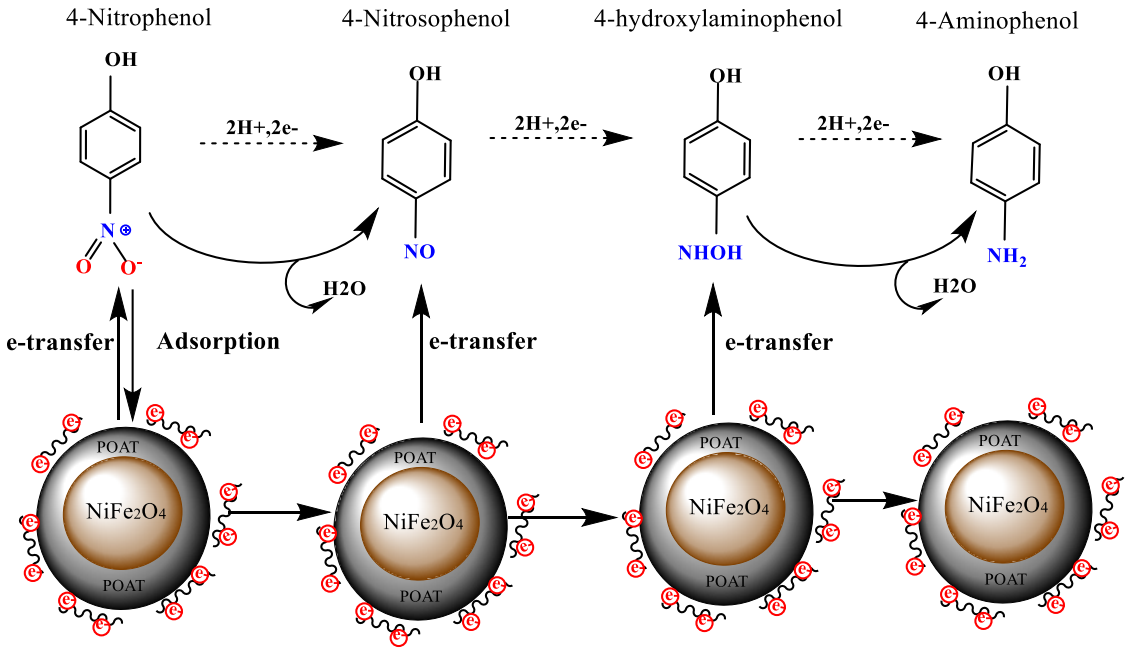

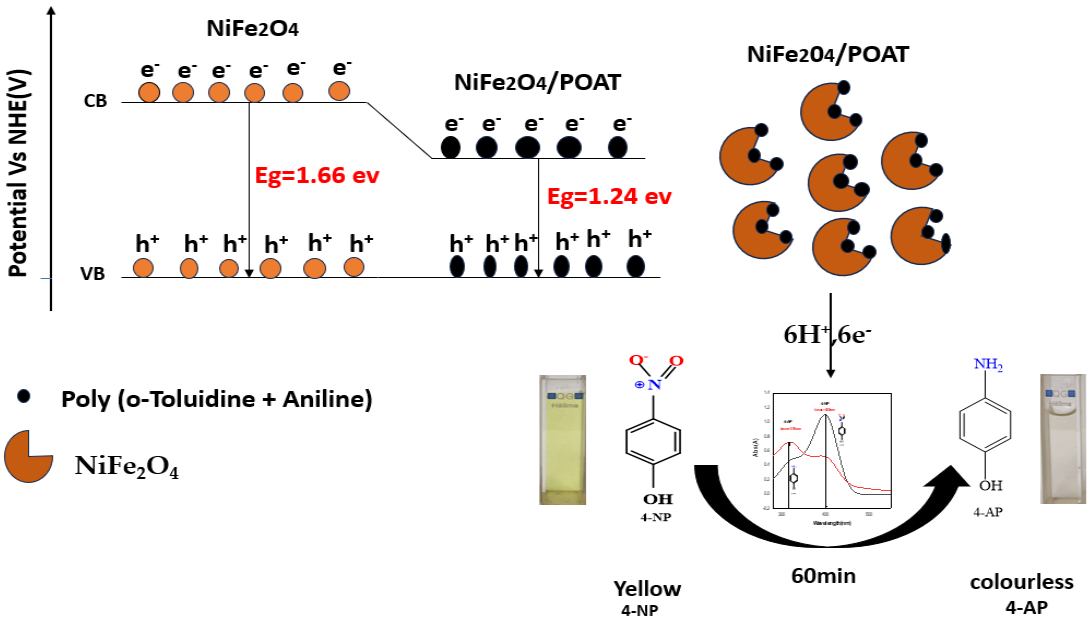

Figure III. 27. Mécanisme proposé de la réduction du 4-nitrophénol en 4-aminophénol à la surface du catalyseur

Le copolymère conducteur poly(aniline-co-o-toluidine) intervient de manière essentielle en agissant comme donneur d'électrons durant la réaction de réduction du 4-nitrophénol (4-NP), tandis que la ferrite de nickel ($NiFe_2O_4$) agit comme vecteur de transfert électronique. Le processus réactionnel suit une séquence en deux temps :

Étape 1 : Le groupe nitro ($-NO_2$) est d'abord réduit en une espèce intermédiaire de type nitroso (-NO), par transfert de deux électrons et de deux protons :

$$-NO_2 + 2e^- + 2H^+ \rightarrow -NO + H_2O$$

Étape 2 : L'intermédiaire nitroso subit ensuite une réduction plus poussée en groupe amine ($-NH_2$), avec intervention de quatre électrons et de quatre protons supplémentaires :

$$-NO + 4e^- + 4H^+ \rightarrow -NH_2 + H_2O$$

La transformation globale du 4-nitrophénol en 4-aminophénol peut être représentée par l'équation suivante :

$$C_6H_4(NO_2)\,OH + 6e^- + 6H^+ \rightarrow C_6H_4(NH_2)\,OH + 2H_2O$$

8. Optimisation du catalyseur

La **figure III.26**, présente la réduction catalytique du 4-nitrophénol (4-NP) en 4-aminophénol (4-AP) dans des conditions optimales, mise en évidence par les spectres d'absorption UV-visible, avec 20 mg de $NiFe_2O_4$/POAT comme catalyseur à une température de 50 °C. La recherche a été effectuée en modifiant les concentrations initiales de 4-NP (2 ppm,

10 ppm et 15 ppm), avec des observations effectuées à deux moments : t = 0 min et t = 60 min. Dès le début de la réaction (t = 0 min), chaque concentration a présenté un pic d'absorption à 400 nm, typique de l'ion (NO_2), qui est la forme prédominante du 4-NP dans un environnement alcalin.

La force d'absorption s'est accrue en proportion de la concentration initiale du 4-NP, atteignant un pic pour la solution à 15 ppm. Une baisse notable de l'absorbance à 400 nm a été notée pour toutes les concentrations après une heure, attestant de la transformation du 4-NP en 4-AP. Les taux de diminution calculés étaient de 85,83% (2 ppm), 95% (10 ppm) et 99% (15 ppm), mettant en évidence l'efficacité du catalyseur $NiFe_2O_4$/POAT dans cette procédure. Ces résultats attestent d'une forte performance catalytique, avec une vitesse de réaction augmentée à des concentrations initiales supérieures, entraînant une conversion presque complète du 4-NP en 60 minutes.

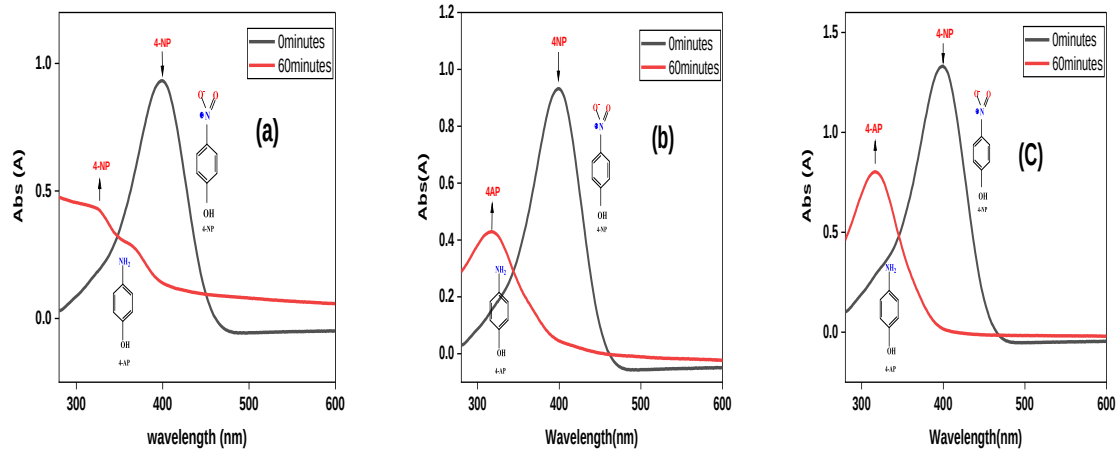

Figure III. 28. Évolution des spectres d'absorption UV-visible de la réduction du 4-NP ((a) 2 ppm, (b) 10 ppm, et (c) 15 ppm)

Tableau III. 9: Comparaison des catalyseurs dans la littérature pour la réduction du 4-NP

Catalyseurs	Réduction R %	Temps (min)	Concentration	Energie de gap (ev)	Agent de réduction	Ref.
$NiFe_2O_4$	75	120	10 ppm	1.58	___	[26]
$Ni_{0.7}Cu_{0.3}Fe_2O_4$	82	120	10 ppm	1.48	___	[26]
$NiZnFe_2O_4$/CQDs	96	20s	_____	1.87	$NaBH_4$	[27]
TiO $_2$/CoFe $_2O_4$	95	35	10 ppm	3.2	$NaBH_4$	[28]
$CuFe_2O_4$	95	40s	0.005 ppm	___	$NaBH_4$	[29]

$NiFe_2O_4$ /RGO	100	30	0.036 M	____	$NaBH_4$	[27]
rGO/Cu-BDC MOF	44.67	8	0.04 mM	____	$NaBH_4$	[30]
Bi_2S_3@Fe_3O_4	98	29	0.1 mM	2.72	$NaBH_4$	[31]
g-C_3N_4/Bi_2S_3	60	60	0.125 mM	___	$NaBH_4$	[31]
Bi_2S_3 NSs	70	60	0.125 mM	___	$NaBH_4$	[32]
CuO/kaolinNC-1	99	12	20ppm	___	$NaBH_4$	[33]
BiFeO3	96	4.5	20 ppm	2.2	$NaBH_4$	[34]
$NiFe_2O_4$/POAT	85 95 99	60	2 ppm 10 ppm 15 ppm	1.24	___	[35]

Le **tableau III. 7**, montre l'efficacité et les conditions d'utilisation de différents catalyseurs employés pour la réduction du 4-nitrophénol (4-NP), un polluant environnemental nocif. Le $NiFe_2O_4$ traité avec du polyaniline (POAT) se distingue par des performances remarquables, avec des efficacités de réduction de 85 %, 95 % et 99 % pour des concentrations respectives de 2 ppm, 10 ppm et 15 ppm en 60 minutes.

En comparaison avec d'autres catalyseurs mentionnés dans les publications citées dans le **tableau III. 7**, le $NiFe_2O_4$/POAT montre des bénéfices notables. Même si des matériaux catalyseurs comme le $NiFe_2O_4$/RGO et le Bi_2S_3@Fe_3O_4 parviennent à une réduction presque totale, le $NiFe_2O_4$/POAT conserve une performance élevée et stable face à des concentrations changeantes, mettant en évidence sa solidité et son aptitude à réduire les polluants sous lumière visible dans les systèmes de traitement des eaux usées. Contrairement à de nombreux catalyseurs nécessitant du $NaBH_4$ comme agent réducteur, cette étude élimine l'utilisation de produits chimiques toxiques et coûteux, faisant de $NiFe_2O_4$/POAT une alternative écologique et économique. Globalement, ce travail contribue au développement de systèmes catalytiques verts et innovants, ouvrant la voie à une adoption plus large dans les efforts de dépollution environnementale.

9. Détermination du nombre de cycles du nanocomposite $NiFe_2O_4$/PAOT

Le **tableau III.8** révèlent que le catalyseur $NiFe_2O_4$/PAOT présente, lors du premier cycle, un taux de réduction élevé (91 %), confirmant son efficacité initiale pour la conversion du 4-NP. Toutefois, une chute significativement marquée de son activité est observée lors des cycles ultérieurs : l'efficacité passe à (71 %), au deuxième cycle, puis s'effondre à ~38 % au troisième cycle. Au quatrième cycle, le catalyseur ne dégrade plus qu'environ 9 % du 4-NP. Cette tendance indique que, bien que le catalyseur présente une activité catalytique initiale

prometteuse, celle-ci se dégrade progressivement. Cette diminution pourrait résulter d'une désactivation progressive des sites actifs.

Tableau III. 10: Cycle de réduction catalytique de 4NP

Cylcle	Réduction du 4NP en %
1	91
2	71
3	38
4	9

10. Conclusion.

Cette étude démontre l'efficacité des nanocomposites $NiFe_2O_4$/PAOT pour éliminer le 4-nitrophénol (4-NP) des solutions aqueuses. Le catalyseur a démontré une efficacité de réduction de 85% à une concentration de 2 ppm, indiquant sa performance efficace à de faibles niveaux de polluants. À des concentrations de 10 ppm et de 15 ppm, les efficacités de réduction étaient notables, atteignant respectivement 95 % et 99 %.

La constance des performances à différentes concentrations met en évidence l'adaptabilité des nanocomposites $NiFe_2O_4$/PAOT dans la gestion efficace de différentes charges polluantes. L'énergie de la bande interdite observée de 1,24 eV renforce l'attrait du catalyseur en indiquant une forte capacitée d'absorption de la lumière visible. Cette caractéristique rend le nanocomposite particulièrement approprié pour les applications photo-catalytiques, facilitant l'activation par la lumière naturelle du soleil ou par des sources artificielles de lumière visible, réduisant ainsi considérablement la dépendance à l'égard des systèmes coûteux basés sur les UV et améliorant l'efficacité énergétique.

L'utilisation de la lumière visible présente un avantage significatif pour l'assainissement de l'environnement, en améliorant à la fois l'aspect pratique et la rentabilité du processus. Le nanocomposite $NiFe_2O_4$/PAOT présente une efficacité de réduction élevée et un potentiel d'application important dans le traitement des eaux usées. L'activité de la lumière visible et la dégradation efficace des polluants aromatiques dangereux en font une solution durable et efficace pour le nettoyage des sources d'eau contaminées.

En se basant sur les résultats, le nanocomposite $NiFe_2O_4$/PAOT a prouvé son efficacité exceptionnelle dans la réduction catalytique du 4-nitrophénol, tout en respectant les critères de durabilité et réutilisabilité.

Références

1. A. K. Tolkou, E. K. Tsoutsa, G. Z. Kyzas and I. A. Katsoyiannis, *Environ. Sci. Pollut. Res*., 2024, **31**, 14662–14689.

2. N. V. Sych, S. I. Trofymenko, O. I. Poddubnaya, M. M. Tsyba, V. I. Sapsay, D. O. Klymchuk and A. M. Puziy, *Appl. Surf. Sci*., 2012, **261**, 75–82.

3. A. O. Cardoso Juarez, E. Ivan Ocampo Lopez, M. K. Kesarla and N. K. R. Bogireddy, *ACS Omega*, 2024, **9**, 33335–33350.

4. M. F. Imron, A. R. Ananta, I. S. Ramadhani, S. B. Kurniawan and S. R. S. Abdullah, *Environ. Technol. Innov*., 2021, **24**, 101921.

5. M. A. Fathy, A. H. Kamel and S. S. M. Hassan, *RSC Adv*., 2022, **12**, 7433–7445.

6. E. A. Al-Maliky, H. A. Gzar and M. G. Al-Azawy, IOP Conf. Ser. Mater. *Sci. Eng*., 2021, **1184**, 012004.

7. L. B. L. Lim, N. Priyantha, C. M. Chan, D. Matassan, H. I. Chieng and M. R. R.Kooh, Arab. *J. Sci. Eng*., 2014, **39**, 6757–6765.

8. M. Danish, R. Hashim, M. N. M. Ibrahim and O. Sulaiman, *J. Anal. Appl. Pyrolysis*, 2013, **104**, 418–425.

9. V. K. Gupta, M. R. Ganjali, A. Nayak, B. Bhushan and S. Agarwal, *Chem. Eng. J*., 2012, **197**, 330–342.

10. H. Liu, P. Dai, J. Zhang, C. Zhang, N. Bao, C. Cheng and L. Ren, *Chem. Eng. J*., 2013, **228**, 425–434.

11. J. Yang and K. Qiu, *Chem. Eng. J*., 2011, **167**, 148–154.

12. J. Fan, J. Zhang, C. Zhang, L. Ren and Q. Shi, *Desalination*, 2011, **267**, 139–146.

13. F. J. García-Mateos, J. M. Rosas, R. Ruiz-Rosas, J. Rodríguez-Mirasol and T. Cordero, Carbon N. Y., 2022, **200**, 134–148.

14. L. Ren, J. Zhang, Y. Li and C. Zhang*, Chem. Eng*. J., 2011, **168**, 553–561.

15. L**.** Wang, J. Zhang, R. Zhao, Y. Li, C. Li and C. Zhang, *Bioresour. Technol.*, 2010, **101**, 5808–5814.

16. A. G. Ramu, S. Salla, S. Chandrasekaran, P. Silambarasan, S. Gopi, S. Seo, K. Yun and D. Choi, *Environ. Pollut.*, 2021, **270**, 116063.

17. O. Baytar, A. Ekinci, Ö. Şahin and A. Akdag, *ChemistrySelect*, 2024, **9**, e202304491.

18. F. D. Koca and B. Şahin, *Inorg. Nano-Metal Chem*., 2024, 1–7.

19. M. Shabani, E. Saebnoori, S. A. Hassanzadeh-Tabrizi and H. R. Bakhsheshi-Rad, J. *Mater. Eng. Perform*., 2023, **32**, 2165–2182.

20. N. Abdus-Salam, A. V. Ikudayisi-Ugbe and F. A. Ugbe*, Chem. Data Collect*., 2021, **31**, 100626.

21. A. TOR and Y. Cengeloglu, *J. Hazard. Mater*., 2006, **138**, 409–415.

22. M. A. Zulfikar, H. Setiyanto, Rusnadi and L. Solakhudin, Desalin. *Water Treat*., 2015, **56**, 2976–2987.

23. R. M. Reema, P. Saravanan, M. D. Kumar and S. Renganathan, Sep. *Sci. Technol*., 2011, **46**, 1052–1058.

24. G. B. Stambouli, B. Benguella, B. Makhoukhi, M. S. El-ouchdi and A. H. Kamel, *Anal. Methods*, 2025, **17**, 2134–2143.

25. W. Xu, R. Qin, G. Cao, Y. Qiang, M. Lai and Y. Lu, *Environ. Pollut*., 2024, **360**, 124602.

26. P. Azhagapillai, K. Gopalsamy, I. Othman, S. Salman Ashraf, F. Banat and M. Abu Haija, Mater. *Sci. Energy Technol*., 2024, **7**, 195–204.

27. S. Naghash-Hamed, N. Arsalani and E. Sharifi As, *Nano-Structures & Nano-Objects*, 2023, **35**, 101002.

28. M. Khatamian, B. Divband and A. Jodaei, Mater. *Chem. Phys*., 2012, **134**, 31–37.

29. J. Feng, L. Su, Y. Ma, C. Ren, Q. Guo and X. Chen, *Chem. Eng*. J., 2013, **221**, 16–24.

30. A. A. Yadav, Y. M. Hunge, S. Majumder, A.-H. I. Mourad, M. M. Islam, T. Sakurai and S.-W. Kang, *J. Colloid Interface Sci*., 2025, **677**, 161–170.

31. N. Kurnaz Yetim, N. Aslan and M. M. Koç, *J. Environ. Chem. Eng*., 2020, **8**, 104258.

32. D. Ayodhya and G. Veerabhadram, *Environ. Technol*., 2021, **42**, 826–841.

33. Z. G. Asmare, B. A. Aragaw and M. Atlabachew, *ACS Omega*, 2024, **9**, 48014–48031.

34. S. Parida, B. Sarangi, J. Nanda and B. Pany, *Inorg. Chem. Commun*., 2024, **170**, 113344.

35. G. B. Stambouli, B. Benguella, M. Benamar and A. H. Kamel, *Environ. Sci. Adv*., 2025, **4**, 1684–1698.

Conclusion Générale

Aujourd'hui, la pollution des eaux industrielles, notamment par les composés organiques persistants comme les colorants synthétiques et les dérivés nitroaromatiques, représente une problématique environnementale considérable. Face à ce défi, cette recherche a choisi de développer et d'évaluer deux méthodes distinctes mais convergentes, dans le but de proposer des solutions pratiques, écologiques et financièrement accessibles pour la dépollution des environnements aquatiques.

La stratégie initiale consiste à utiliser la biomasse de Lemna minor, une plante aquatique qui pousse rapidement et abondamment présente, comme ressource première pour la fabrication de charbons actifs. En utilisant des méthodes d'activation chimique simples et respectueuses de l'environnement, nous avons réussi à convertir cette plante en un matériau adsorbant efficace, doté d'une surface spécifique importante et d'une porosité qui favorise l'adsorption des colorants. L'analyse des processus d'interaction entre le colorant et le substrat a révélé un phénomène d'adsorption chimique spécifique, adapté par les caractéristiques de la surface du matériau, l'acidité de la solution et le temps de contact. Ces résultats valident l'idée de valorisent des ressources naturelles peu exploitées pour la création d'adsorbants écologiques et performants dans le traitement des effluents colorés.

Simultanément, une autre méthode a été élaborée en se basant sur la réduction catalytique pour la réduction des composés aromatiques nocifs, notamment le 4-nitrophénol. Dans cette optique, on a procédé à la synthèse de nanocomposites magnétiques à partir de ferrites de nickel, qui ont ensuite été modifiés grâce à un polymère conducteur copolymérisé dérivé de l'aniline et de l'o-toluidine. Cette association confère au matériau des caractéristiques électroniques améliorées, une stabilité structurelle renforcée et une réactivité sous lumière visible permettant une activation catalytique efficace à l'aide de sources lumineuses ambiantes. Les tests de décomposition ont montré une conversion efficace du contaminant en un composé moins notif, soulignant l'énorme potentiel de ces nanomatériaux pour des applications spécifiques de dépollution, tout en simplifiant leur récupération grâce à leurs propriétés magnétiques.

L'intérêt de fusionner des ressources renouvelables et des progrès en matière de nanotechnologie pour faire face aux défis de la pollution industrielle est mis en évidence par la combinaison de ces deux approches - l'adsorption à l'aide d'un biomatériau fonctionnalisé et la catalyse via un nanocomposite activable par lumière. Ces approches, combinées, démontrent la capacité à élaborer des processus intégrés, ajustables en fonction des types de polluants, qui allient efficacité, durabilité et conformité aux normes environnementales contemporaines.

Ces recherches contribuent significativement à l'enrichissement des technologies actuelles de traitement des eaux usées, en apportant des solutions innovantes et efficaces basées sur des matériaux à haute performance. Elles permettent non seulement d'optimiser les procédés existants, mais aussi de proposer des alternatives écologiquement durables et économiquement. À travers l'intégration de matériaux catalytiques tel que $NiFe_2O_4$ modifié par le poly(aniline-co-o-toluidine) ou biosorbants comme Lemna minor, ces travaux ouvrent la voie à des applications à grande échelle dans le domaine de la purification de l'eau, notamment dans les stations de traitement municipales et les installations industrielles. En outre, les résultats obtenus démontrent un fort potentiel de mise en œuvre dans des contextes variés, y compris en milieu rural ou dans les zones à ressources limitées, où des solutions efficaces, peu coûteuses et faciles à déployer sont particulièrement nécessaires.

Perspectives sur l'adsorption

Dans un objectif d'expansion scientifique, diverses orientations de recherche peuvent être envisagées :

- Extension de la gamme des polluants visés : Même si cette recherche s'est focalisée sur un colorant anionique particulier, l'utilisation des charbons activés issus de Lemna minor pourrait être étendue à d'autres catégories de polluants organiques (comme les pesticides et les résidus médicaux) ou inorganiques (tels que les métaux lourds comme le Cd, Pb et Ni). Une analyse systématique de l'adsorption de plusieurs contaminants aiderait à comprendre davantage les interactions sur les sites actifs du Lemna minor.

- Amélioration du processus de synthèse Sur le plan technique, optimiser les conditions d'activation pourrait encore améliorer les performances de Lemna minor. L'étude d'autres activateurs (tels que l'acide tartrique, l'acide oxalique ou des bases plus faibles), ainsi que l'expérimentation de nouvelles techniques (activation par micro-ondes, ultrasons ou plasma froid) pourrait favoriser la création de porosités adaptées à des molécules de diverses tailles. Une étude sur le couplage chimio-thermique ou la carbonisation maîtrisée dans une atmosphère inerte serait aussi pertinente.

- Incorporation dans des systèmes de traitement en temps réel. L'application à grande échelle de ces adsorbants dans des dispositifs de filtration continue (colonnes statiques, lits fluidisés ou cartouches) constitue une phase indispensable. Il serait judicieux de reproduire les conditions d'opération des effluents industriels réels (fluctuation du flux, présence de sels, interférence d'autres composés organiques) pour apprécier les performances des matériaux dans des environnements complexes.

Perspective sur la réduction

Les perspectives présentées ci-dessous visent à proposer de nouvelles orientations de recherche permettant d'améliorer et d'élargir les applications de $NiFe_2O_4$ recouvert par le poly(aniline-co-o-toluidine) :

- Élargissement aux contaminants émergents, bien que le $NiFe_2O_4$/PAOT ait montré une efficacité remarquable pour la réduction du 4-NP, il serait pertinent d'explorer son potentiel vis-à-vis d'autres polluants organiques émergents, tels que les perturbateurs endocriniens (bisphénol A, hormones synthétiques) ou les antibiotiques. Cela permettrait de tester la polyvalence du catalyseur dans des contextes environnementaux plus complexes.

- Collaboration avec des agents photosensibles, l'intégration de photosensibilisateurs tels que des nanoparticules d'argent ou des colorants organiques pourrait augmenter l'absorption visible et optimiser les performances photo-catalytiques, en particulier sous la lumière naturelle. Cela faciliterait l'association de la réduction catalytique et de la photodégradation pour des processus mixtes plus performants.

- Exploration du doping métallique ou non-métallique, l'enrichissement du $NiFe_2O_4$ avec d'autres ions métalliques (tels que Mg^{2+}, Zn^{2+}) ou non-métalliques (comme le N, le S) pourrait transformer la structure électronique de ce matériau et augmenter sa capacité réactive. Ces ajustements pourraient ouvrir la voie à la conception d'une nouvelle génération de catalyseurs multifonctionnels.

- Simulation et modélisation à l'échelle moléculaire, l'application de modèles DFT (Density Functional Theory) faciliterait une meilleure compréhension des processus de transfert d'électrons entre le catalyseur et le 4-NP, tout en permettant l'identification des sites actifs au niveau atomique. Cela orienterait la conception rationnelle de catalyseurs optimisés.

Publications

Analytical Methods

ROYAL SOCIETY OF CHEMISTRY

PAPER

View Article Online
View Journal

Cite this: DOI: 10.1039/d4ay02206h

Physicochemical properties of mesoporous acid activated materials from *Lemna minor* for Bezaktiv Red S-MAX dye removal

Ghizlène Boudghene Stambouli,*[ab] Belkacem Benguella,[a] Benamar Makhoukhi,[a] Mohamed Said El-ouchdi[a] and Ayman H. Kamel *[bc]

Lemna minor, a cheap and easily accessible substance, was utilized to create activated carbon through acid activation [with H_3PO_4 (ALM-P) and citric acid (ALM-C)]. Brunauer–Emmett–Teller (BET) analysis reveals that the *L. minor* activated materials (LACs) had a surface area of 208.54 $m^2\ g^{-1}$ and 216.11 $m^2\ g^{-1}$ after H_3PO_4 and citric acid activation, respectively. The presence of rich hydroxyl, carboxyl, amide, and phosphate functional groups on the surface of LACs is revealed by Fourier transform infrared spectroscopy (FTIR). This enables easy Bezaktiv dye, type Red S-MAX (BRSM), binding to the surface through strong chemisorptive bonds or ion exchange. With a maximal mono-layer adsorption capacity (q_m) of 16.86 and 7.69 mg g^{-1} at 25 °C, the pseudo-second-order model and Langmuir isotherm provided a good description of the kinetic and equilibrium data. The adsorption was caused in part by the intra-particle diffusion mechanism. With negative $\Delta G°$ and positive $\Delta H°$ values, the adsorption process was spontaneous and endothermic. Under optimum conditions of pH 3.0 and 25 °C, the maximum % removal for BRSM (90 mg L^{-1}) was reported to be 77.65% within 90 min. These indicated that dye-contaminated water might be treated with the inexpensive LACs as a possible adsorbent.

Received 6th December 2024
Accepted 3rd February 2025

DOI: 10.1039/d4ay02206h

rsc.li/methods

1. Introduction

Technological and industrial advancements continued to increase, creating a significant problem for wildlife and plant life, leading to environmental pollution. Water pollution has emerged as the most severe form of pollution due to industrial discharges, posing a critical environmental challenge. Among the major sources of pollution are those stemming from the textile industry, as they release over one million cubic meters of wastewater annually.[1] In fact, the dyeing and treatment of textile fibers involve the consumption of substantial volumes of water and chemicals, ultimately leading to the discharge of 17% to 20% of the total dye content into the environment at the conclusion of the dyeing process.[2] These dyes are hazardous not only to human health but also to the environment, as they exhibit short-term toxicity, are occasionally carcinogenic, and possess intricate chemical structures that make them poorly biodegradable, conferring a persistent nature upon them.[3]

Adsorption is considered a promising approach due to its material reusability, low operating costs, enhanced selectivity for certain metals of interest, and quick operation times.[4] Researchers have effectively used a variety of adsorbents to remove pollutants from aqueous media, such as wheat husk,[5] treated alga (*Oedogonium hatei*),[6] hen feathers,[7] and activated materials (ACs). Because of their numerous functional groups on the surface, chemical stability, huge specific surface area, and highly porous structure, ACs are among the most effective adsorbents for extracting heavy metals from wastewater.[8] It appears promising to manufacture ACs with high mesoporosity for large molecule absorption using inexpensive and readily available materials for applications such as battery capacitors, catalytic supports, biomedical engineering, and adsorbents for bulky pollutants.[9] One of the best and least expensive activation techniques for creating mesoporous ACs is acid activation. The acid-activated ACs can accomplish a number of goals, including low activation temperature, high ion-exchange capacity, thermal and chemical stability, and high meso-porosity.[10] Acid-activated materials have thus extensively removed dyes from water. Biomass sources containing cellulose, hemicellulose, or lignin can serve as precursors for ACs.[11] Various renewable and affordable biomass sources, including lotus stalk,[11] cotton stalk,[12] water hyacinth,[13] *Enteromorpha prolifera*,[14] maize stalks,[15] and plant leftovers,[16] have been effectively used to prepare ACs. Under ideal growing conditions, duckweed, or *Lemna minor*, can treble its mass in just one week. Duckweed (*Lemna minor*) is a globally available aquatic plant that thrives in diverse freshwater environments, particularly in nutrient-rich

[a]*Inorganic Chemistry and Environment Laboratory, University of Tlemcen, P. O. Box 119, 13000 Tlemcen, Algeria. E-mail: ghizoustambouli@gmail.com*

[b]*Department, College of Science, University of Bahrain, Sakhir 32038, Kingdom of Bahrain. E-mail: ahkamel76@sci.asu.edu.eg*

[c]*Department of Chemistry, Faculty of Science, Ain Shams University, Cairo 11566, Egypt*

water. Its rapid growth, accessibility, and ability to be harvested with minimal resources make it a viable material for resource-limited communities. Beyond its rapid growth, duckweed is rich in lignocellulosic content, enabling its transformation into high-performance adsorbents for environmental applications. Furthermore, its cultivation aligns with sustainable practices, offering dual benefits in water quality improvement and pollutant remediation. Overgrowth of *L. minor* can result in negative consequences such as obstructed flood drains, hindrances to land navigation, and secondary pollutants linked to its debris. Reasonable harvesting and use of such aquatic plants are required to prevent these drawbacks. Lead, nickel, cadmium, copper, and chromium were among the heavy metals that have been eliminated using duckweed.[17,18] Additionally, cellulose, lipids, lignin, pentosan, pectin, and minerals are present in *L. minor*.[17] Consequently, *L. minor* presents itself as a promising low-cost precursor for the synthesis of ACs because of its lignin-cellulose structure, thereby enhancing the adsorption process's economic feasibility. Furthermore, there is not much information in the literature regarding mesoporous activated carbon made from *L. minor*. In order to increase the specific surface area and mesoporosity of activated carbon, *L. minor* – a possible low-cost precursor – and a modified chemical activation method using H_3PO_4 were coupled. Chemical activation with phosphoric acid and citric acid is a well-established method for developing high-performance adsorbents. Phosphoric acid promotes microporosity and introduces phosphate groups, while citric acid contributes mesoporosity and carboxylic functional groups. This dual activation approach has been shown to enhance the adsorption efficiency of various organic and inorganic pollutants, making it a suitable choice for the remediation of hazardous dyes.

The main goal of this work is to use citric and H_3PO_4 as activating agents to make ACs from *L. minor* that have a lot of surface functional groups, a large mesopore volume, and a large surface area. The acid activated *L. minor* is characterized using N_2 adsorption, scanning electron microscopy (SEM) and Fourier transform infrared spectroscopy (FTIR). The adsorption capacity of these adsorbents and their suitability for the removal of Bezaktiv Red S-MAX (BRSM) from an aqueous solution were examined. Optimization of the adsorption process in terms of temperature effect, the effect of pH, contact time, the amount of the adsorbent and the initial BRSM concentration was also performed. We examined the equilibrium and kinetic data to understand the adsorption kinetics, isotherms, thermodynamic characteristics, and mechanism of BRSM adsorption on LACs.

2. Experimental

2.1. Materials and apparatus

The macrophyte biomass for *L. minor* was collected from a natural lake in El-Fayoum city, Egypt. It was transported to Algeria in an ice box and then stored in a refrigerator at 4 °C until use. 20 g of *L. minor* sample was air dried in the sun after being washed three times with distilled water. Before being used, these *L. minor* samples, which were the raw, non-living biomass, were sieved to a size of 2.0 mm. In the pre-treatment phase, distilled water was also used to prepare all of the experimental solutions at ambient temperature and an agitation rate of 150 rpm. Finally, the *L. minor* samples that had all been pre-treated were dried in an oven for 10 h at 70 °C. Commercial Bezaktiv dye, type Red S-MAX (BRSM) (molecular formula $C_{31}H_{19}ClN_7Na_5O_{19}S_6$, 1136.28 g mol^{-1}), is very reactive and widely used in the textile industry.[19] It was supplied by SOITEX Company (Tlemcen-Algeria). All other chemicals were purchased from Sigma Aldrich (Saint Louis, USA) and were used as received without prior treatment.

The FTIR spectrum was recorded using a spectrometer (L160000A, PerkinElmer, USA) between wave numbers 400 and 4000 cm^{-1}. Using a surface area analyser (V350, Alliance, USA) and the manufacturer's software, the surface area S_{BET} and the total pore volume V_{tot} of the ALMs were calculated. SEM analysis (TM-1000, HITACHI, Japan) was performed to examine the surface texture and porosity development.

2.2. Activation of *Lemna minor*

The activation process using a combination of phosphoric acid and citric acid was optimized based on their complementary effects. Phosphoric acid enhances microporosity and introduces phosphate functional groups, while citric acid contributes carboxylic functional groups for improved adsorption interactions. A concentration of 0.1 M was selected to achieve effective activation without compromising the structural integrity of the activated carbon. The method was adapted from previous studies.[10] In brief, a quantity of 20 g of LM was treated with 1000 mL of 0.1 M of phosphoric acid or citric acid for 3 hours under stirring at 300 rpm to obtain ALM-P or ALM-C, respectively. The samples were then dried in an oven at 50° for 24 hours, crushed and sieved to be finally used in absorption experiments.

2.3. Adsorption experiments

A stock solution of 1000 mg L^{-1} of the red dye was prepared. Additional dilution produced experimental solutions with the required concentration. The experimental solutions of known concentrations (2–50 mg L^{-1}) were mixed with 0.03 g L^{-1} of either LM or ALM in a temperature-controlled water bath shaker within a pH range of 2.0–12.0. This was done for the batch adsorption experiments. A pH meter (ST7300, JENWAY, UK) was used for all pH measurements. A UV/VIS spectrophotometer (ST7300, PerkinElmer, UK) was used to measure the dye concentration in the supernatant liquids after they were adsorbed for 5–150 min at a wavelength $\lambda = 524$ nm. The dye uptake at the equilibrium q (mg g^{-1}) was calculated using eqn (1) as follows:

$$q_t(\text{mg g}^{-1}) = \frac{(C_i - C_t)}{W} \times V \quad (1)$$

The removal percentage (R%) was evaluated using eqn (2):

$$\text{Adsorption (\%)} = \frac{C_i - C_e}{C_i} \times 100 \quad (2)$$

where C_i, C_t and C_e (mg L^{-1}) are dye concentrations at the initial stage, time t and equilibrium, respectively; V and W are the liquid volume (L) and the dried used adsorbent weight (g), respectively.

3. Results and discussion

The yield of activated materials was calculated based on the dry weight of the raw *Lemna minor* and the final dry weight of ALM-P and ALM-C after activation. The yield was 40% for ALM-P and 35% for ALM-C, reflecting the effectiveness of the phosphoric acid and citric acid activation processes. These values align with typical yields reported for lignocellulosic precursors in chemical activation studies. Elemental analysis of raw *Lemna minor* revealed a composition of 45% carbon, 5% hydrogen, 40% oxygen, and 1% nitrogen. The high carbon content confirms its suitability as a precursor for producing activated materials. Furthermore, the difference in yields between ALM-P and ALM-C can be attributed to the varying effects of the activation agents on the structural and chemical properties of the raw material.

3.1 FTIR spectroscopy

To learn more about the functional groups involved in the bioaccumulation of BRSM dye, FTIR analysis was performed on the *L. minor* plant sample. The chemical groups on the LM's surface and the type of binding that occurs between the adsorbent and the dye were both revealed by the FTIR investigations. An important band at 3419.7 cm^{-1} was seen in the FTIR study (Fig. 1), which points to the stretching vibration of O–H groups in carboxylic groups in duckweed. The spectrum at 1651.5 represents the carboxyl groups. The peaks at 1444.4 cm^{-1} and 1632.3–598.1 cm^{-1} are attributed to C–O stretching and O–H bending.[20] For ALM-P samples, the phosphonate group was thought to be represented by the P–OH stretching at 1086.5 cm^{-1} and the P=O stretching of the absorption bands, which were observed at 1409.6 cm^{-1}.[21] For ALM-C samples, the stretching vibration of the C=O group shifts from 1651.5 to 1735 cm^{-1}, confirming the esterification of the carboxyl group in LM samples. The presence of the carboxyl group, which promotes the buildup of BRSM dye, is evident in the adsorbent's FTIR examination. A decrease in pH causes the carboxyl groups on the adsorbent to be undissociated. Therefore, there is a possibility of hydrogen bonding or electrostatic interactions at low pH values, which makes it easier for a negatively charged anionic dye to bind.

3.2 SEM analysis of *L. minor*

The SEM images of LMs and ALMs are displayed in Fig. 2. The LMs' surface morphology showed a big, accessible surface area with a fluffy, irregularly porous structure. We collected and examined data on nitrogen adsorption and desorption to elucidate the mechanisms of adsorption ability and selectivity. The significant adsorption capacity of type IV, with a small hysteresis loop (H3 type) at a high relative P/P^0 (>0.6), indicated the development of a meso-porous (D_P = 7.5 nm) structure for the ALMs. As acid catalysts, H_3PO_4 or citric acid break bonds and create crosslinks through cyclization or condensation when mixed with organic species to make phosphate and phosphate bridges. Once cleaned with deionized water, it occupies space, preventing the particle from contracting during the carbonization process, and eventually reveals a porous structure.[22] The larger dye molecules diffuse into the pores more easily due to the ALM's higher mesoporosity and larger average pore diameter.[23] ALM-P has a larger mesoporous area compared to ALM-C, despite being made under the same activation conditions. These include ACs from lotus stalk (74.4%),[24] herb residues (82.3%),[25] loosestrife (83.3%),[26] lignin (76.0%),[27] cattail fiber (78.1%),[28] and *Polygonum orientale* Linn. (82.5%).[29]

3.3 BET analysis

For a comprehensive analysis of mesoporous acid-activated carbon derived from ALM for removing Bezaktiv Red S-MAX

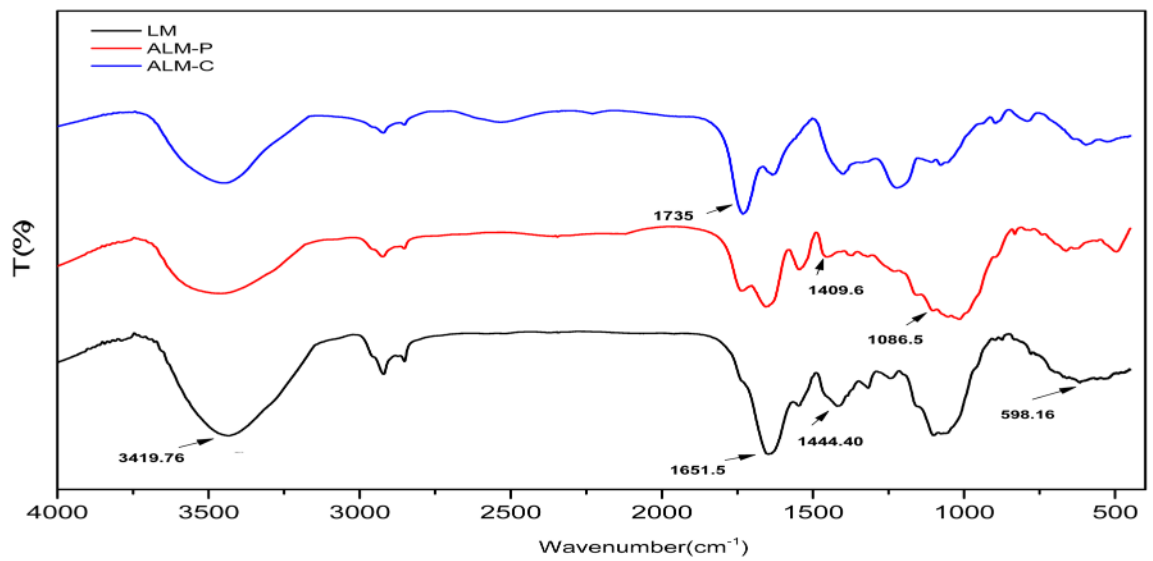

Fig. 1 FTIR spectra of LM and ALM.

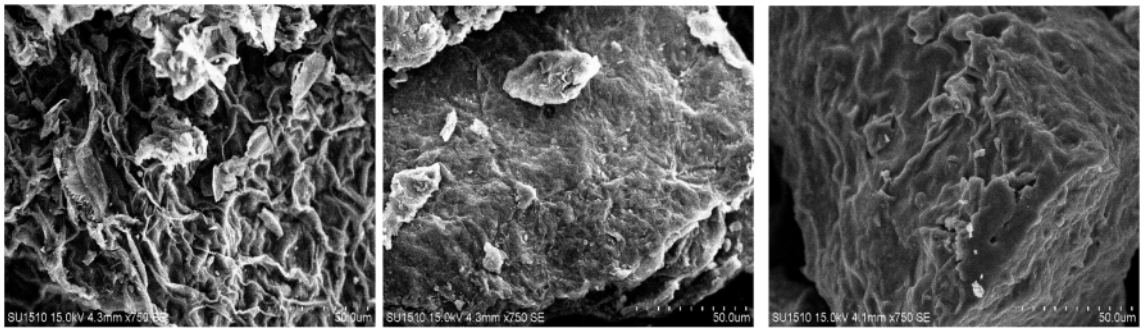

Fig. 2 SEM images of LM (a), (b) ALM-P, and (c) ALM-C.

dye, the BET analysis provides key insights into the material's structure and potential adsorption efficiency (Table 1). The total pore volume is a critical factor in determining the material's capacity to accommodate dye molecules within its structure. For untreated ALM, it exhibits a relatively low pore volume of 0.02 $cm^3\ g^{-1}$, indicating that the untreated carbon has limited internal voids, likely due to the lack of activation. For ALM treated with citric acid (ALM-C), the acid activation step significantly increases the total pore volume to 0.15 $cm^3\ g^{-1}$. This increase suggests the development of a porous structure, enhancing the material's ability to capture and hold dye molecules. Further chemical activation using H_3PO_4 increases the pore volume to 0.2 $cm^3\ g^{-1}$. This is the highest value among the three samples, implying that chemical activation creates even more accessible voids for dye molecules, potentially improving the adsorption capacity.

The average pore diameter gives insight into the types of pores formed, which affects the material's suitability for specific adsorbates. An average pore diameter of 35 nm places the untreated carbon in the mesoporous to macroporous range, which is suitable for larger molecules but may not be efficient for dye molecules, which are typically smaller. Phosphoric acid activation reduces the average pore diameter to 4 nm, entering the lower mesoporous range. This is more appropriate for adsorbing medium-sized dye molecules, providing a balance between accessible pore volume and pore size. Citric acid activation reduces the average pore diameter further to 2.3 nm, close to the microporous range. Smaller pores are advantageous for adsorbing smaller molecules but may hinder dye diffusion if the pore entrances become restrictive.

The specific surface area is crucial for adsorption capacity, as a larger surface area allows more interaction points for dye molecules. The ALM shows a specific surface area of 73.2 $m^2\ g^{-1}$, which is relatively low and limits its adsorption efficiency. Acid activation with citric acid (ALM-C) increases the surface area to 208.51 $m^2\ g^{-1}$, which is slightly lower than that achieved through H_3PO_4 activation (216.11 $m^2\ g^{-1}$). This increase suggests that acid treatment successfully removes impurities and opens up more adsorption sites, potentially boosting dye removal efficiency. Acid treatment using H_3PO_4 exhibits a higher specific surface area than using citric acid. This can be attributed to the specific structural changes or partial pore collapse during activation.

In conclusion, phosphoric acid promotes the development of a hierarchical pore structure, predominantly micropores, while citric acid enhances mesoporosity and introduces carboxyl functional groups. The synergy between these acids leads to improved adsorption capacity for organic pollutants, as observed in this study.

3.4 Dye adsorption using ALM-P

Several factors were investigated in this study, including contact time, initial pH effect, initial dye concentration, and temperature effect.

3.4.1 Kinetics study. The equilibrium adsorption study for Bezaktiv Red S-MAX (BRSM) dye removal, starting from a 40 mg per L concentration, reveals performance differences between phosphoric acid-activated carbon (ALM-P) and citric acid-activated carbon (ALM-C), both derived from *Lemna minor* (LM). The results, plotted in (Fig. 3), also highlight that untreated LM shows negligible adsorption efficiency.

Initially, after 15 minutes, ALM-P demonstrates superior performance by adsorbing 6.29 mg g^{-1} of dye, translating to over 78% dye removal. Comparatively, ALM-C captures 4.35 mg g^{-1}, achieving a 54% removal rate. This early efficacy is likely due to ALM-P's higher pore volume and well-distributed pore size, which favor rapid dye molecule uptake. At 45 minutes,

Table 1 BET analysis of both treated and untreated *L. minor*

Type of adsorbent	Total pore volume ($cm^3\ g^{-1}$)	Average pore diameter (nm)	Specific surface area ($m^2\ g^{-1}$)
ALM	0.02	35	73.2
ALM-P	0.15	4	216.11
ALM-C	0.2	2.3	208.51

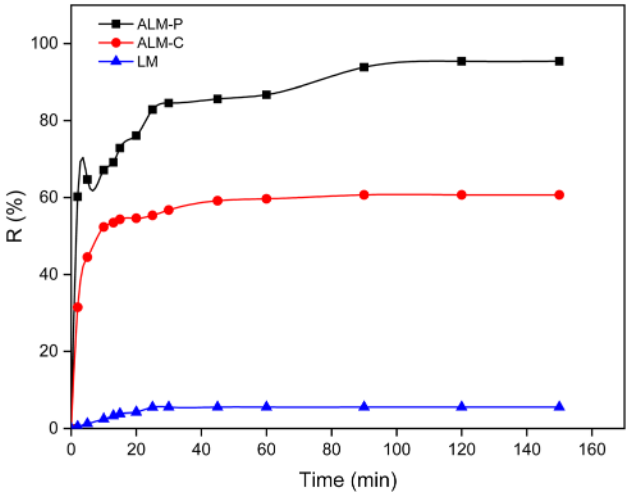

Fig. 3 Adsorption of Bezaktiv-Red dye onto LM and ALM as a function of time.

ALM-P further improves, adsorbing 6.74 mg g^{-1} (84.20% efficiency), while ALM-C reaches 4.63 mg g^{-1} (57.93% efficiency). The data show that ALM-P consistently outperforms ALM-C in dye uptake, likely due to its larger specific surface area and mesoporous design, which supports efficient dye diffusion and adsorption. ALM-C's structure, with smaller and more restricted pores, limits this rate. The materials reach equilibrium at around 90 minutes: ALM-P achieves 85.05% removal (6.80 mg g^{-1}), while ALM-C stabilizes at 4.68 mg g^{-1} (58.53%). These values confirm ALM-P's superior adsorption potential, attributed to its advantageous pore and surface characteristics. In comparison, unmodified LM removes only 5% of the dye, reinforcing the effectiveness of the acid-activated materials. In summary, ALM-P shows a higher adsorption yield for BRSM dye, indicating that acid activation optimizes its mesoporous properties, making it a more efficient adsorbent than ALM-C in both initial and equilibrium stages.

Acid treatment can effectively remove impurities, oxides, and other contaminants from the material's surface, enhancing properties such as adhesion, wettability, and reactivity with other substances. In this study, citric acid ($pK_a = 3.06$) and phosphoric acid ($pK_a = 2.12$) were used to activate *Lemna minor* (LM) to observe the differences in adsorption efficiency. The results indicated that phosphoric acid (ALM-P) enhanced adsorption more effectively than citric acid. This increased performance could be attributed to the higher acidity of phosphoric acid, which likely removed surface contaminants that could obstruct the material's pores, thereby improving adsorption potential through enhanced surface accessibility and structural changes. While this study primarily focused on adsorption capacity, it also aimed to address environmental concerns by examining waste reduction possibilities. Comparative adsorption capacities for different adsorbents are presented in Table 2, showing the high adsorption performance of ALM-P for Bezaktiv Red dye at 16.86 mg g^{-1}, outperforming other tested adsorbents like date palm seeds[30] and rubber seeds[32] for different dyes.

3.4.2 Adsorption kinetics model. In order to express the dye adsorption mechanism, kinetic parameters are determined by analyzing adsorption experimental data using the following kinetic model equations.

PFO (pseudo-first order rate equation):

$$\ln (q_e - q_t) = \ln q_e - k_f \times t \quad (3)$$

PSO (pseudo-second order rate equation):

$$\frac{t}{q_t} = \frac{1}{k_s \times q_e^2} + \frac{t}{q_e} \quad (4)$$

q_t: amount of adsorbate adsorbed at a specific time (mg g^{-1}), q_e: adsorption capacity at equilibrium (mg g^{-1}), k_f: constant of the PFO (min^{-1}), K_s: constant of the PSO (g mg^{-1} min^{-1}), and t: contact time (min).

According to Fig. 4, the PSO is more suitable than the PFO for experimental data of dye adsorption (Table 3). High correlation coefficients obtained employing the PSO are better than those obtained employing the PFO ($R^2 \geq 0.99$ for PSO and $R^2 \geq 0.93$ for PFO). The calculated equilibrium adsorption capacity is comparable to experimental data, which implies that the adsorption of BRSM dye onto the two samples is chemical (chemisorption), featuring valence forces due to electron exchange between the adsorbent and sorbate. In chemisorption, the adsorption capacity is proportional to the number of occupied active sites on the adsorbent surface.[34]

3.5 Effect of pH

The pH level plays a critical role in the study of dye molecule removal, as it significantly influences both the surface characteristics of the adsorbent material and the ionization process of the dye molecules. To achieve the desired initial pH values of the solution, adjustments were made using 0.1 M hydrochloric acid or sodium hydroxide solutions. The experimental data for

Table 2 Comparison of the sorption capacity of dyes

Adsorbents	Adsorbed dyes	q_{max} (mg g^{-1})	Ref.
Carbon (date palm seeds)	Eosin yellow	0.16	30
L. minor	Methylene blue	1.14	20
Red mud	Congo red	7.08	31
Rubber seed	Congo red	9.82	32
L. minor	Methylene blue	11.49	33
L. minor	Bezaktiv-Red	16.86 (ALM-P) 7.69 (ALM-C)	This work

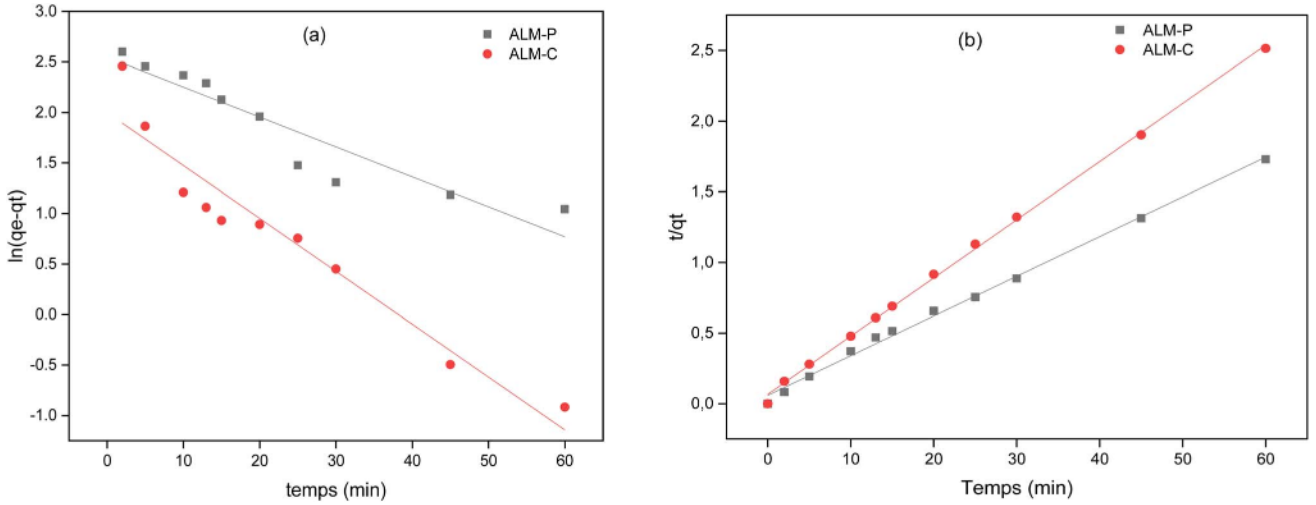

Fig. 4 Kinetic plots for the adsorption of dye onto ALM-P and ALM-C: (a) pseudo-first-order and (b) pseudo-second-order.

Table 3 PSO and PFO models for adsorption onto ALM-P and ALM-C

	Pseudo-first-order		Pseudo-second-order	
Samples	K_1 (min^{-1})	R^2	K_2 (mg g^{-1} min)	R^2
ALM-P	0.03	0.93	0.01	0.99
ALM-C	0.06	0.96	0.03	0.99

dye removal as a function of pH were analyzed using a linear regression model for ALM-P and a piecewise linear model for ALM-C. These models were selected based on the observed trends in removal efficiency across the pH range. Fig. 5 illustrates the variation in BRSM dye adsorption from an aqueous solution across a range of pH values. In this study, two distinct trends emerged for BRSM adsorption onto ALM-P and ALM-C under varying pH conditions. The solution pH notably impacts dye recovery and concentration, as it leads to the formation of soluble dye complexes, which unfortunately remain stable in aqueous media. Adsorption experiments using *Lemna minor* (*L. minor*) were conducted across a broad pH range (2.0–12.0), with the results depicted in Fig. 5. Observations indicate that dye adsorption decreases as the initial pH of the solution increases. Notably, maximum adsorption was achieved at a low pH of 2.0, reaching 77.65% for ALM-P and 45.42% for ALM-C. This behavior can be attributed to the protonation of the carboxyl groups present on the adsorbent surfaces (ALM-P and ALM-C) at lower pH levels. In a protonated state, these groups may form hydrogen bonds with the oxygen atoms in BRSM dye molecules, enhancing the affinity of the dye for the ALM surface through hydrogen bonding interactions.

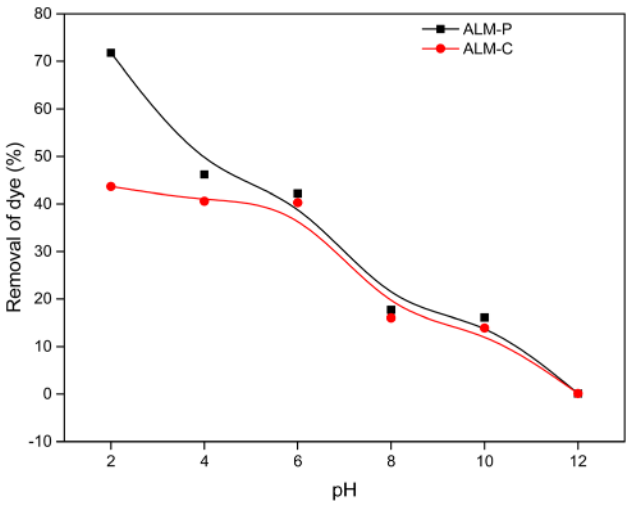

Fig. 5 Adsorption of dye onto *Lemna minor* in relation to initial pH.

The point of zero charge (pH_{pzc}) of ALM-P and ALM-C was determined to be 5.4 and 5.2, respectively. When the pH of the solution falls below these values, the ALM-P and ALM-C surfaces acquire a positive charge. This positively charged surface promotes the adsorption of the anionic dye (BRSM) due to increased electrostatic attraction. Additionally, if the surface is protonated, reducing its net negative charge, electrostatic attractions between the positively charged adsorbent surface and negatively charged dye molecules are likely to occur, further facilitating adsorption. Thus, the observed increase in adsorption at low pH is primarily driven by these protonation and electrostatic effects, both of which enhance the interaction between the dye molecules and the adsorbent material.

In conclusion, for ALM-P, the removal efficiency exhibits a linear trend across the pH range (2–12), highlighting the material's robustness and stable adsorption performance under varying pH conditions. In contrast, ALM-C shows a distinct piecewise trend: a baseline removal of ~40% at pH < 6, followed by a linear decrease at higher pH values. This behavior reflects the influence of surface functional groups and their ionization states, which are governed by the activation method. The strong performance of ALM-P can be attributed to its high mesoporosity and the presence of phosphate groups that provide consistent adsorption capabilities.

3.6 Dye concentration effect

To assess how varying initial dye concentrations affect adsorption, a range of concentrations from 2 to 50 mg L^{-1} was applied, as depicted in Fig. 6. The results show that the quantity of BRSM dye adsorbed by the acid-activated material (ALM-P) increases from 6.66 mg g^{-1} to 16.68 mg g^{-1} as the initial dye concentration rises. In comparison, chemically activated carbon (ALM-C) shows a more modest increase in adsorption capacity, from 6.66 mg g^{-1} to 7.64 mg g^{-1}, with increasing dye concentration. This trend suggests that higher initial dye concentrations strengthen the interactions between the adsorbent surfaces and dye molecules, enhancing the mass transfer of the dye to the adsorbent.

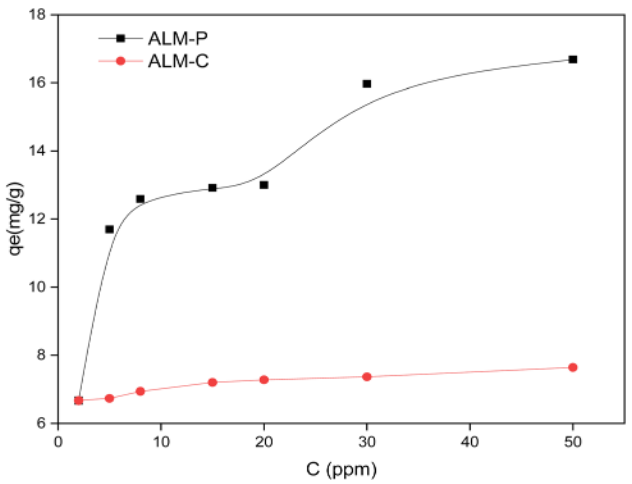

Fig. 6 Adsorption of dye onto *Lemna minor* as a function of concentration.

At higher initial dye concentrations, adsorption capacity generally improves because more dye molecules are available to interact with the adsorbent surface. However, as the concentration reaches a high threshold (such as above 90 mg L^{-1}), a saturation effect may begin to limit adsorption efficiency. This occurs when the adsorbent's available binding sites become progressively occupied, eventually reaching a point where fewer sites remain accessible to additional dye molecules. Consequently, the adsorbent surface can no longer accommodate as many dye particles, resulting in a gradual decrease in removal efficiency as binding sites are maxed out. This saturation is characteristic of systems where adsorption equilibrium is reached, and excess dye molecules remain in solution due to the finite number of active sites on the adsorbent surface.

3.7 Isotherm adsorption

Langmuir and Freundlich isotherms are the most used equations to represent adsorption data, represented by the following equations:

$$\frac{C_e}{q_e} = \frac{1}{q_m K_L} + \frac{1}{q_m} C_e \quad (5)$$

$$\ln q_e = \ln K_F + \frac{1}{n} \ln C_e \quad (6)$$

C_e: equilibrium dye concentration (mg L^{-1}), q_e: equilibrium dye adsorbed quantity (mg g^{-1}), K_L: Langmuir adsorption constant (L mg^{-1}), q_m: the maximum dye adsorbed quantity, k_F: Freundlich adsorption constant, and n: Freundlich energetic parameter.

The Langmuir isotherm's high linearity, shown in (Fig. 7) and supported by the parameters in Table 4, shows the strong fit of the Langmuir model to the adsorption data for BRSM dye

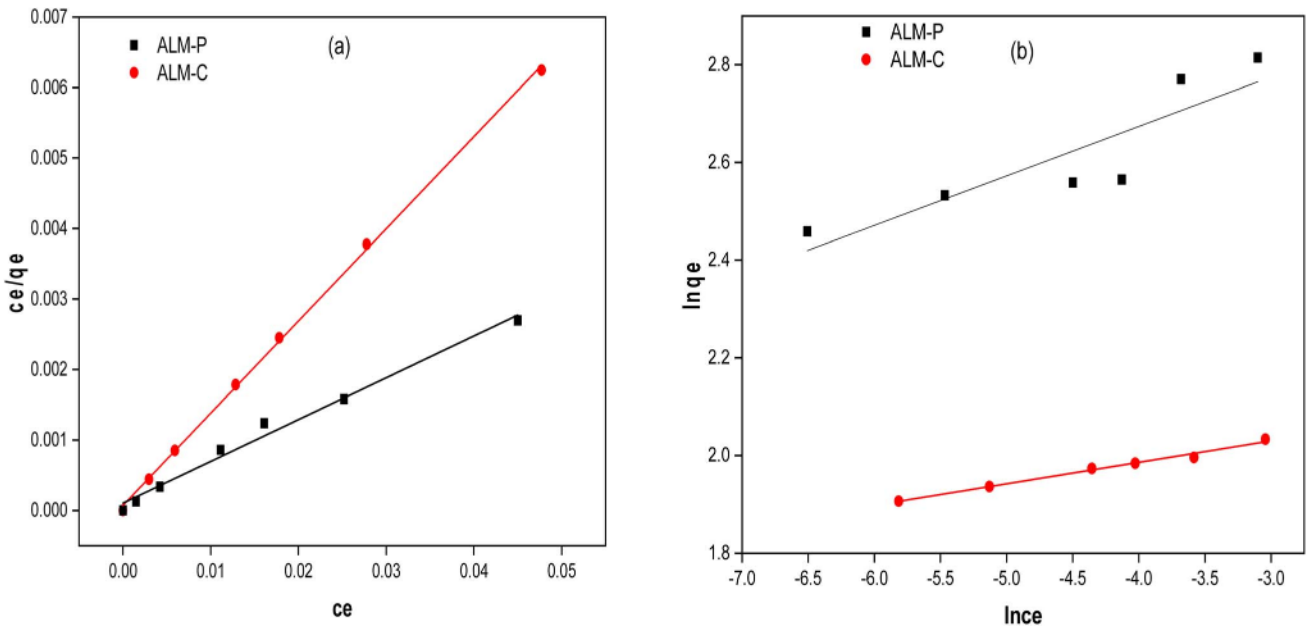

Fig. 7 (a) Langmuir and (b) Freundlich model plots.

Table 4 Parameters obtained from Langmuir and Freundlich models

Isotherm	Parameters	ALM-P	ALM-C
Experiment	q_e (mg g^{-1})	16.68	7.64
Langmuir	q_{max} (mg g^{-1})	16.86	7.65
	k_L (L mg^{-1})	0.574	1.817
	R^2	0.994	0.998
Freundlich	K_F (mg g^{-1})	21.74	8.688
	$1/n$	0.101	0.044
	R^2	0.886	0.994

onto LM-activated carbon (ALM) with phosphoric acid and citric acid. With an R^2 value near unity (0.99), this model suggests that dye adsorption occurs primarily as a monolayer on a homogeneous adsorbent surface. In this context, each BRSM dye molecule likely occupies an individual site on the activated surface of ALM, which minimizes interaction between dye molecules, aligning with Langmuir's assumptions of monolayer coverage.

3.8 Thermodynamic parameters

Utilizing the experimental data from previous research on the effect of solution temperature, thermodynamic analysis was performed. The following formulae can be used to compute the thermodynamic parameters, which are standard free energy ($\Delta G°$), standard enthalpy ($\Delta H°$), and standard entropy ($\Delta S°$):

$$\ln K_L = \frac{\Delta S}{S} - \frac{\Delta H}{RT} \quad (7)$$

where R (8.314 J mol^{-1} K^{-1}): the gas constant, T: the temperature (K) and K_L: the distribution coefficient that can be calculated as:

$$k_L(\text{ml g}^{-1}) = \frac{C_i - C_e}{C_e} \times \frac{V}{m} \quad (8)$$

C_0 and C_e: initial and equilibrium BRSM dye concentrations (mg L^{-1}), respectively (Table 5).

The thermodynamic study was conducted at temperatures of 298.1 K, 309.6 K, 319.9 K, and 333.3 K. These temperatures were selected to encompass a range of conditions, including ambient temperature (298.1 K) and higher temperatures that may be encountered in practical applications or controlled experimental environments. This approach ensures a comprehensive analysis of the adsorption process over varying thermal conditions.

As shown in Fig. 8, the negative values of $\Delta G°$ across all tested temperatures confirm that the adsorption process is spontaneous for both ALM-P and ALM-C, with a clear trend of

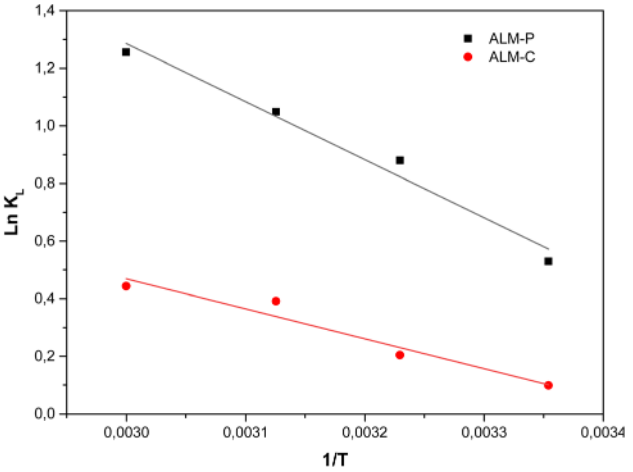

Fig. 8 Van't Hoff plot for the sorption of dye onto ALM-P and ALM-C.

increasing adsorption efficiency at elevated temperatures. The positive $\Delta H°$ values, indicative of endothermic behavior, reveal that heat absorption is required to facilitate the adsorption of BRSM dye onto both ALM-P and ALM-C, meaning that increasing the temperature enhances adsorption capacity. Moreover, the positive $\Delta S°$ values suggest increased disorder at the solid–liquid interface, which could be due to the dye molecules interacting and aligning on the surface of activated ALM. ALM-P exhibits higher spontaneity and endothermic tendencies than ALM-C, with a higher $\Delta S°$ (37.194 J mol^{-1} K^{-1}) and $\Delta G°$ values more negative across temperatures, suggesting that phosphoric acid activation may provide a more favorable adsorption surface compared to citric acid activation. This difference implies that ALM-P has a structurally optimized surface with greater affinity for BRSM dye molecules, possibly due to the enhanced pore structure and surface chemistry, which promote effective dye interaction.

The selected temperature range allowed for the evaluation of the adsorption process across varying thermal conditions. The negative values of $\Delta G°$ observed at all temperatures confirm the spontaneity of the adsorption process, with increased spontaneity at higher temperatures due to the more negative $\Delta G°$ values. This suggests that adsorption onto ALM-P and ALM-C is thermodynamically favorable and enhanced by increasing temperature.

3.9 Adsorption mechanism

Fig. 9 provides a detailed illustration of the interactions between Bezaktiv Red S-Max (BRSM) dye molecules and LM

Table 5 Thermodynamic data for adsorption of dye onto *L. minor*

	$\Delta H°$ (kJ mol^{-1})	$\Delta S°$ (J mol^{-1})	R^2	$\Delta G°$ (kJ mol^{-1})			
				298.1 K	309.6 K	319.9K	333.3 K
ALM-P	9 646	37 194	0.98	−1.44	−1.87	−2.25	−2.75
ALM-C	8.64	29.83	0.97	−0.24	−0.57	−0.87	−1.26

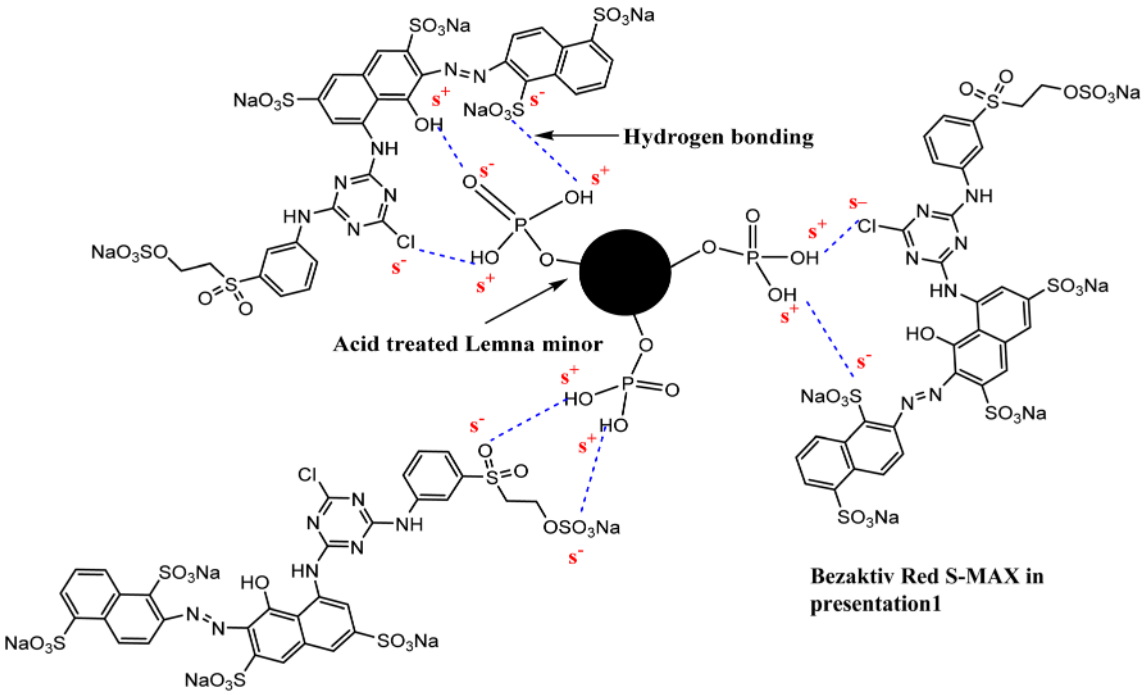

Fig. 9 Proposed adsorption mechanism of BRSM dye on ALMP.

treated with phosphoric acid (ALM-P). This graphic emphasizes the molecular mechanisms of hydrogen bonding and electrostatic interactions that facilitate the adsorption of BRSM onto ALM-P.

The adsorption mechanism shows multiple hydrogen-bonding interactions occurring between BRSM molecules and the ALM-P surface. BRSM dye contains several functional groups, including sulfonate groups (SO_4Na and SO_3Na), hydroxyl (–OH), and chloride (Cl) groups. The oxygen atoms within these functional groups can serve as hydrogen bond acceptors, allowing the dye molecules to form stable hydrogen bonds with specific groups on the ALM-P surface, and on the ALM-P surface, the hydroxyl (–OH) and phosphoryl (P═O) groups act as hydrogen donors, facilitating bond formation with the oxygen atoms of BRSM's sulfonate, hydroxyl, and chloride groups. This hydrogen bonding stabilizes the BRSM molecules on the ALM surface, enhancing their retention by reinforcing the binding interaction between the dye and the ALM-P. Thus, hydrogen bonds play a vital role in anchoring BRSM to ALM-P, leading to improved dye adsorption stability. In addition to hydrogen bonding, electrostatic interactions contribute significantly to BRSM dye adsorption on ALM-P, particularly at lower pH levels. As the solution's pH decreases, the concentration of hydrogen ions (H^+) in the medium increases. This environment favors the protonation of ALM-P's surface hydroxyl (–OH) groups, imparting a positive charge to the surface. The protonated ALM-P surface is then attracted to the negatively charged sulfonate groups of BRSM, fostering a strong electrostatic attraction between the ALM-P and BRSM molecules. This electrostatic attraction promotes the proximity and alignment of BRSM with ALM-P, facilitating additional hydrogen bonding and further stabilizing the adsorption. By combining hydrogen bonding and electrostatic interactions, this mechanism ensures efficient dye retention on the ALM-P surface, especially under acidic conditions that enhance protonation and, therefore, the overall binding affinity.

4. Conclusions

Activated materials derived from *Lemna minor* (LM) waste were successfully synthesized using two distinct acid treatments, resulting in adsorbents that are cost-effective, eco-friendly, and simple to produce. These ALM-P-based materials demonstrate enhanced surface properties and a high specific surface area, reflecting significant improvements in their adsorption potential. The study found that the ideal conditions for maximum dye removal include a dose of 0.03 g of ALM-P, a dye solution pH of 2, and an adsorption time of 90 minutes. Kinetic analysis suggests that the pseudo-second-order (PSO) model accurately describes the adsorption kinetics, while the Langmuir isotherm provides the best fit for equilibrium data, indicating a maximum monolayer adsorption capacity of 16.86 mg g^{-1} for BRSM dye. Based on these results, ALM-P shows strong potential as an effective adsorbent for removing synthetic dyes from aqueous solutions, positioning it as a promising material for water purification applications.

Data availability

The data supporting this article have been included in the main manuscript.

Author contributions

All authors listed have made a substantial, direct, and intellectual contribution to the work and approved it for publication.

Conflicts of interest

The authors declare that the research was conducted in the absence of any commercial or financial relationships that could be construed as a potential conflict of interest.

References

1 B. T. Eddine and M. M. Salah, *Int. J. Energy Environ. Eng.*, 2012, **3**, 17.
2 M. Hassaan and A. el Nemr, *Am. J. Environ. Sci. Eng.*, 2017, **1**, 64–67.
3 C. Visvanathan, R. Ben Aim and K. Parameshwaran, *Crit. Rev. Environ. Sci. Technol.*, 2000, **30**, 1–48.
4 A. K. Giri, R. Patel and S. Mandal, *Chem. Eng. J.*, 2012, **185–186**, 71–81.
5 V. K. Gupta, R. Jain and S. Varshney, *J. Hazard. Mater.*, 2007, **142**, 443–448.
6 V. K. Gupta, A. Rastogi and A. Nayak, *J. Colloid Interface Sci.*, 2010, **342**, 533–539.
7 V. K. Gupta, A. Mittal, L. Kurup and J. Mittal, *J. Colloid Interface Sci.*, 2006, **304**, 52–57.
8 L. Mouni, D. Merabet, A. Bouzaza and L. Belkhiri, *Desalination*, 2011, **276**, 148–153.
9 M. Al Bahri, L. Calvo, M. A. Gilarranz and J. J. Rodriguez, *Chem. Eng. J.*, 2012, **203**, 348–356.
10 N. V. Sych, S. I. Trofymenko, O. I. Poddubnaya, M. M. Tsyba, V. I. Sapsay, D. O. Klymchuk and A. M. Puziy, *Appl. Surf. Sci.*, 2012, **261**, 75–82.
11 H. Liu, P. Dai, J. Zhang, C. Zhang, N. Bao, C. Cheng and L. Ren, *Chem. Eng. J.*, 2013, **228**, 425–434.
12 K. Li, Z. Zheng and Y. Li, *J. Hazard. Mater.*, 2010, **181**, 440–447.
13 Y. Huang, S. Li, J. Chen, X. Zhang and Y. Chen, *Appl. Surf. Sci.*, 2014, **293**, 160–168.
14 Y. Li, Q. Du, X. Wang, P. Zhang, D. Wang, Z. Wang and Y. Xia, *J. Hazard. Mater.*, 2010, **183**, 583–589.
15 Y. Huang, S. Li, J. Chen, X. Zhang and Y. Chen, *Appl. Surf. Sci.*, 2014, **293**, 160–168.
16 J. Yang and K. Qiu, *Chem. Eng. J.*, 2011, **167**, 148–154.
17 Y. Tang, L. Chen, X. Wei, Q. Yao and T. Li, *J. Hazard. Mater.*, 2013, **244–245**, 603–612.
18 S. X. Li, Z. Feng-Ying, H. Yang and N. Jian-Cong, *J. Hazard. Mater.*, 2011, **186**, 423–429.
19 M. Daoud, O. Benturki, Z. Kecira, P. Girods and A. Donnot, *J. Mol. Liq.*, 2017, **243**, 799–809.
20 M. F. Imron, A. R. Ananta, I. S. Ramadhani, S. B. Kurniawan and S. R. S. Abdullah, *Environ. Technol. Innov.*, 2021, **24**, 101921.
21 L. B. L. Lim, N. Priyantha, C. M. Chan, D. Matassan, H. I. Chieng and M. R. R. Kooh, *Arab. J. Sci. Eng.*, 2014, **39**, 6757–6765.
22 M. Danish, R. Hashim, M. N. M. Ibrahim and O. Sulaiman, *J. Anal. Appl. Pyrolysis*, 2013, **104**, 418–425.
23 V. K. Gupta, M. R. Ganjali, A. Nayak, B. Bhushan and S. Agarwal, *Chem. Eng. J.*, 2012, **197**, 330–342.
24 H. Liu, P. Dai, J. Zhang, C. Zhang, N. Bao, C. Cheng and L. Ren, *Chem. Eng. J.*, 2013, **228**, 425–434.
25 J. Yang and K. Qiu, *Chem. Eng. J.*, 2011, **167**, 148–154.
26 J. Fan, J. Zhang, C. Zhang, L. Ren and Q. Shi, *Desalination*, 2011, **267**, 139–146.
27 J. M. Rosas, R. Ruiz-Rosas, J. Rodríguez-Mirasol and T. Cordero, *Carbon N. Y.*, 2012, **50**, 1523–1537.
28 L. Ren, J. Zhang, Y. Li and C. Zhang, *Chem. Eng. J.*, 2011, **168**, 553–561.
29 L. Wang, J. Zhang, R. Zhao, Y. Li, C. Li and C. Zhang, *Bioresour. Technol.*, 2010, **101**, 5808–5814.
30 N. Abdus-Salam, A. V. Ikudayisi-Ugbe and F. A. Ugbe, *Chem. Data Collect.*, 2021, **31**, 100626.
31 R. M. Reema, P. Saravanan, M. D. Kumar and S. Renganathan, *Sep. Sci. Technol.*, 2011, **46**, 1052–1058.
32 M. A. Zulfikar, H. Setiyanto and L. Solakhudin, *Desalin. Water Treat.*, 2015, **56**, 2976–2987.
33 A. Tor and Y. Cengeloglu, *J. Hazard. Mater.*, 2006, **138**, 409–415.
34 M. el A. Zennaki, L. Tennouga and S. Balkaid, *J. Macromol. Sci., Part B:Phys.*, 2024, **63**, 314–332.

Environmental Science Advances

ROYAL SOCIETY OF CHEMISTRY

PAPER

View Article Online
View Journal

Cite this: DOI: 10.1039/d5va00128e

Polymer-enhanced nickel ferrite catalyst for the efficient reduction of 4-nitrophenol as a hazard pollutant

Ghizlene Boudghene Stambouli,[ab] Belkacem Benguella,[b] Makhoukhi Benamar[b] and Ayman H. Kamel *[ac]

The synthesized nickel ferrite ($NiFe_2O_4$)/poly(aniline-*co*-*o*-toluidine) (PAOT) nanocomposite was successfully characterized using XRD, FTIR, SEM, and EDX, confirming the formation of a stable spinel structure with uniform particle distribution (32–68 nm). The material exhibited a low bandgap energy of 1.24 eV and retained magnetic properties, enabling easy recovery and reuse for up to four cycles. The catalytic activity of the $NiFe_2O_4$/PAOT nanocomposite was evaluated for the visible-light-assisted reduction of 4-nitrophenol (4-NP) without external reducing agents. The catalyst achieved reduction efficiencies of 85.83% at 2 ppm, 95% at 10 ppm, and 99% at 15 ppm within 60 min, with improved performance at higher catalyst dosages and temperatures (*e.g.*, 50 °C with 20 mg). Kinetic analysis revealed pseudo-first-order behavior. Compared to other reported catalysts, $NiFe_2O_4$/PAOT offers green synthesis, high efficiency, magnetic recoverability, and operational simplicity, making it a promising material for sustainable wastewater treatment.

Received 9th May 2025
Accepted 26th August 2025

DOI: 10.1039/d5va00128e

rsc.li/esadvances

Environmental significance

The presence of 4-nitrophenol (4-NP) in wastewater poses a significant environmental and health hazard due to its toxicity, persistence, and resistance to conventional degradation methods. This study introduces a highly efficient and sustainable approach for 4-NP reduction using $NiFe_2O_4$/POAT nanocomposite catalysts, which demonstrate exceptional catalytic performance under visible light conditions. The low bandgap energy (1.24 eV) enhances electron transfer, enabling effective degradation of pollutants without reliance on UV irradiation, making the process more energy-efficient. Furthermore, the magnetic properties of the catalyst allow for easy recovery and reuse, reducing secondary waste generation and operational costs. With a 95% reduction efficiency within one hour and reusability over multiple cycles, $NiFe_2O_4$/POAT offers a scalable and environmentally friendly alternative for wastewater treatment. These findings contribute to the development of sustainable catalytic systems that align with green chemistry principles, paving the way for improved strategies in water purification and environmental remediation.

Introduction

Globally, the development of new and creative solutions for the effective treatment of wastewater that contains harmful organic contaminants is very important.[1,2] Water is one of the primary components that sustain life on Earth. Every day, water is used for various purposes and is essential to every bodily function. Numerous things contribute to water contamination, such as agriculture, industry, and urbanization. Agricultural and industrial operations result in water contamination from fertilizers, chemicals, pesticides, heavy metals, diseases, *etc.* The health of both humans and animals is now at risk due to such activities.[3]

Aromatic nitrophenols, including 4-nitrophenol, are significant contributors to water pollution due to their extensive use in industries such as pesticides, fertilizers, dyes, paper, and plasticizers production. Additionally, they serve as precursors in the synthesis of paracetamol in the pharmaceutical industry. These nitrophenols are highly toxic, with exposure linked to carcinogenic effects in humans and other living organisms. The World Health Organization (WHO) and the U.S. Environmental Protection Agency (EPA) classify 4-nitrophenol (4-NP) as a highly toxic substance. To safeguard public health, regulations like the Mexican NOM-127-SSA1-19 945 set its permissible concentration in drinking water at 1 μg L^{-1}.[4] Prolonged or high exposure to 4-NP can impair the nervous system and reduce the blood's oxygen-carrying capacity. Inhalation of 4-NP may result in respiratory issues, including throat and lung irritation, coughing, and shortness of breath, along with systemic effects such as nausea, weakness, rapid heart rate, disorientation, and fever.

[a]*Chemistry Department, College of Science, University of Bahrain, Sakhir 32038, Kingdom of Bahrain. E-mail: ahkamel76@sci.asu.edu.eg; amohamed@uob.edu.bh*
[b]*Inorganic Chemistry and Environment Laboratory, University of Tlemcen, P. O. Box 119, 13000 Tlemcen, Algeria*
[c]*Department of Chemistry, Faculty of Science, Ain Shams University, Cairo 11566, Egypt*

Severe exposure can lead to collapse or even fatal outcomes. These compounds are highly soluble and persist at high concentrations in industrial wastewater, posing significant environmental challenges. As a result, the removal of nitrophenols from wastewater is essential.

To overcome these limitations, magnetic ferrite-based nanomaterials, particularly nickel ferrite ($NiFe_2O_4$), have emerged as promising alternatives. Ferrites exhibit superior redox properties, high surface area, low band gap energy, and excellent magnetic separability, which significantly enhance their catalytic performance while enabling easy post-treatment recovery using an external magnetic field.[5–7] Ferrites have also shown potential in applications such as dye degradation, sensing, drug delivery, and water splitting, demonstrating their multifunctionality and stability.[8,9]

Several remediation methods, including, catalytic reduction,[10] adsorption,[11] photodegradation,[12] and membrane filtration,[13] have been employed. However, these approaches often suffer from high costs and limited removal efficiency.

In catalytic decomposition, traditional catalysts like, carbon nanotubes,[14] activated carbon,[15] oxides,[16] and microporous polymers[17] have been widely utilized. However, these materials present a significant limitation in practical applications due to challenges in separating them from the treated water. This issue becomes particularly problematic in large-scale systems. The incomplete removal of these conventional catalysts from the processed solution can result in their buildup in the environment, potentially causing secondary pollution and introducing new environmental contaminants. The issue has been effectively addressed with the development of magnetic nanocatalysts, which have garnered significant research attention for reducing organic contaminants from wastewater. These materials offer unique advantages, such as a low band gap energy, high reduction capacity, and effortless separation using an external magnetic field. This minimizes the risk of secondary pollution, overcoming the limitations of traditional catalysts that are difficult to separate from contaminated solutions. Recent research has demonstrated that $NiFe_2O_4$ nanostructures can effectively catalyze the reduction of nitroaromatic compounds such as 4-NP under visible light or mild reaction conditions.[18,19] However, bare ferrite nanoparticles often suffer from agglomeration, poor dispersibility in aqueous systems, and reduced active site accessibility, which limit their catalytic efficiency.[20] To address this, researchers have begun incorporating conductive polymers—such as polyaniline (PANI), polypyrrole (PPy), and their derivatives—onto ferrite surfaces to form hybrid nanocomposites with enhanced performance.[7,20] They have been utilized in diverse applications, including dye degradation, electrochemical sensors, cancer treatment, drug delivery, gas sensing, and water splitting, owing to their high surface area and stability. Jiang *et al.* (2025) demonstrated high catalytic performance using core–shell magnetic heterojunctions for 4-NP reduction under visible light.[21] Similarly, Chen *et al.* (2025) reported a bifunctional $NiFe_2O_4$@graphene nanocomposite with enhanced stability and reusability.[22] Their potential for nitro compound removal in wastewater treatment makes them an attractive choice.

Moreover, there is growing interest in enhancing the performance of these magnetic nano-catalyst by incorporating conductive polymers like polyaniline (PANI)[23] and polypyrrole (PPy).[24] These polymers contribute additional benefits, including a low gap energy, flexibility, robust mechanical strength, and distinctive electrical properties, along with functional groups such as –NH. Several studies have highlighted that conductive polymer coatings not only reduce particle agglomeration but also improve charge carrier separation and redox kinetics, especially in ferrite-based nanocomposites.[25,26] These ferrite–polymer nanocomposites benefit from improved electrical conductivity, enhanced charge separation, redox tunability, and better stability in aqueous environments. In particular, polymers like poly(aniline-*co*-*o*-toluidine) (PAOT) possess –NH and $-CH_3$ functional groups that enhance electron delocalization and create strong interfacial interactions with ferrite nanoparticles. Such synergy facilitates electron transfer processes crucial to catalytic reduction reactions.[19,20]

Magnetic ferrite-based systems such as $NiFe_2O_4$ have been extensively utilized in various domains including dye degradation,[27] electrochemical sensors,[28] cancers treatment,[29] drug delivery,[30] gas sensing[31] and water splitting,[32] owing to their stability, high surface area, and electron transfer capabilities.

Despite their potential, $NiFe_2O_4$-based polymer nanocomposites remain underexplored for catalytic detoxification of 4-NP. Previous studies have largely focused on either bare ferrites or composites with conventional polymers. Furthermore, detailed mechanistic studies on the role of polymer-ferrite interfacial bonding, surface charge modulation, and catalyst recyclability in enhancing 4-NP reduction remain scarce. While magnetic $NiFe_2O_4$ nanoparticles have shown promise in pollutant degradation, there remains a significant gap in understanding how copolymer-functionalization, particularly with PAOT, can be leveraged to maximize their performance in wastewater treatment applications. No comprehensive studies have yet reported the synthesis, stability, and catalytic behavior of $NiFe_2O_4$/PAOT nanocomposites toward 4-NP reduction under mild conditions.

In this study, a $NiFe_2O_4$/PAOT nanocomposite was developed by first synthesizing $NiFe_2O_4$ nanoparticles and subsequently modifying them with poly(aniline-*co*-*o*-toluidine) (PAOT). The $-CH_3$ group in the *o*-toluidine aromatic ring enhances electron density, facilitating strong interactions between nickel ferrite molecules and the polymer.[33,34] These non-covalent interactions, particularly between the hydrogen of the metal complex and the electron-rich *o*-toluidine ring, contribute to the nanocomposite's enhanced stability. The use of magnetic metal ferrites, particularly nickel ferrite combined with poly(aniline-*co*-*o*-toluidine), offers notable advantages such as cost-effectiveness, high reduction efficiency, and straightforward preparation, making them highly suitable catalysts for the reduction of 4-nitrophenol. These catalysts have demonstrated significant effectiveness in addressing the challenges associated with 4-nitrophenol reduction. Furthermore, this approach highlights the potential of ferrite-poly(aniline-*co*-*o*-toluidine) composites synthesized through chemical polymerization,

which, to the best of our knowledge, remain relatively underutilized for this application.

Experimental

Chemicals and apparatus

All chemicals were utilized as received without additional purification. Ferric chloride hexahydrate ($FeCl_3 \cdot 6H_2O$, 97%) and nickel chloride hexahydrate ($NiCl_2 \cdot 6H_2O$) were sourced from Sigma-Aldrich, USA. Ammonium persulfate ($(NH_4)_2S_2O_8$), aniline ($C_6H_5NH_2$), and *o*-toluidine (C_7H_9N) were also obtained from the same supplier. Sodium hydroxide (NaOH) and hydrochloric acid (HCl) were procured from Merck, Germany. 4-Nitrophenol ($C_6H_5NO_3$) was acquired from, FLUKA Chemika, Switzerland. All reagents were of analytical grade. Ultrapure water was used for all solution preparations. Both stock and diluted, 4-NP solutions were stored in dark, airtight containers to avoid degradation.

For the instruments, FTIR spectrometer (Sp-3-300, Pye-Unicam, UK) was recorded between wave numbers of 200 and 4000 cm^{-1}. XRD analysis (ULTIMA IV, Rigaku, JAPAN), SEM analysis (JSM-IT800, JEOL Ltd, JAPAN) to examine the surface texture and porosity development, EDX analysis (JSM-IT800, JEOL Ltd, JAPAN), UV-Vis-NIR spectrophotometer (UV-3600, SHIMASZU, JAPAN), UV-visible spectrophotometer (GENESYS 10S, USA).

Synthesis of nano-sized nickel ferrite ($NiFe_2O_4$)

At room temperature (22 ± 2 °C), a solution was prepared using ferric and nickel chloride in a 2 : 1 molar ratio and stirred continuously for 30 min. A 2.0 M sodium hydroxide (NaOH) solution was then gradually introduced at a controlled rate of 1.0 mL min^{-1} until the pH of the mixture reached.[35] The reaction led to the formation of a brown precipitate (Scheme 1), which was subsequently heated to 100 °C while being stirred for one hour. The mixture was then left to mature overnight. The precipitate was thoroughly washed with distilled water until the filtrate reached a neutral pH of 7. The obtained residue was dried at 110 °C for six hours, transforming into a deep dark powder, which was then subjected to calcination at 600 °C for five hours. The final product was ground and stored in a desiccator for further use.

Synthesis of $NiFe_2O_4$/PAOT nanocomposite

Nickel ferrite-based polymer nanocomposites were synthesized through a chemical polymerization process (Scheme 2). Initially, 4.5 g of $NiFe_2O_4$ nanoparticles were dispersed in a solvent mixture containing 20 mL of chloroform and 30 mL of double-distilled water. This dispersion was subjected to ultrasonic treatment for 1 hour at room temperature (22 ± 2 °C). Concurrently, 0.05 moles of both aniline and *o*-toluidine monomers were dissolved in 200 mL of 1.0 M hydrochloric acid and stirred continuously for 30 min. The nanoparticle dispersion was then combined with the monomer solution and further sonicated for 30 minutes. Polymerization was initiated by the dropwise addition of 20 mL of a 0.1 M aqueous ammonium persulfate (APS) solution at a controlled rate of 0.5 mL min^{-1} using a peristaltic pump, while sonication continued for an additional hour. A gradual change to a black coloration was observed during the process.[36] The reaction mixture was left undisturbed overnight. The resulting nickel ferrite-poly(aniline-*co*-*o*-toluidine) composite was separated by vacuum filtration, thoroughly washed with double-distilled water and methanol, and subsequently dried at 60 °C. The final dried product was finely ground into powder for further use.

Catalytic reduction of nitrophenol

The reduction efficiency of the synthesized nanocomposites was evaluated using the batch equilibrium method. A series of 4-

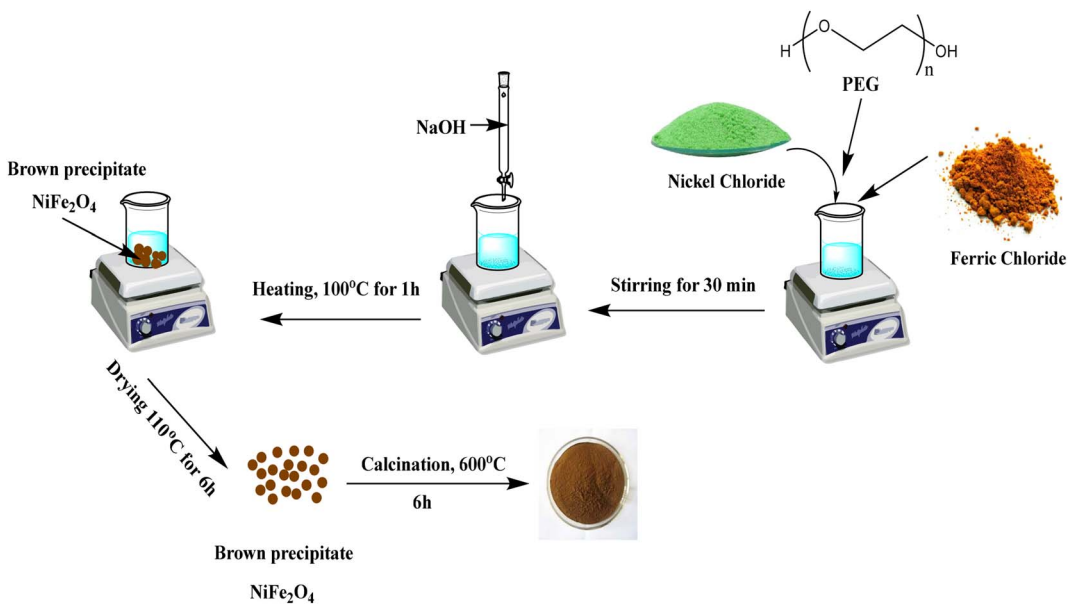

Scheme 1 Schematic representation the preparation of $NiFe_2O_4$ nanoparticles.

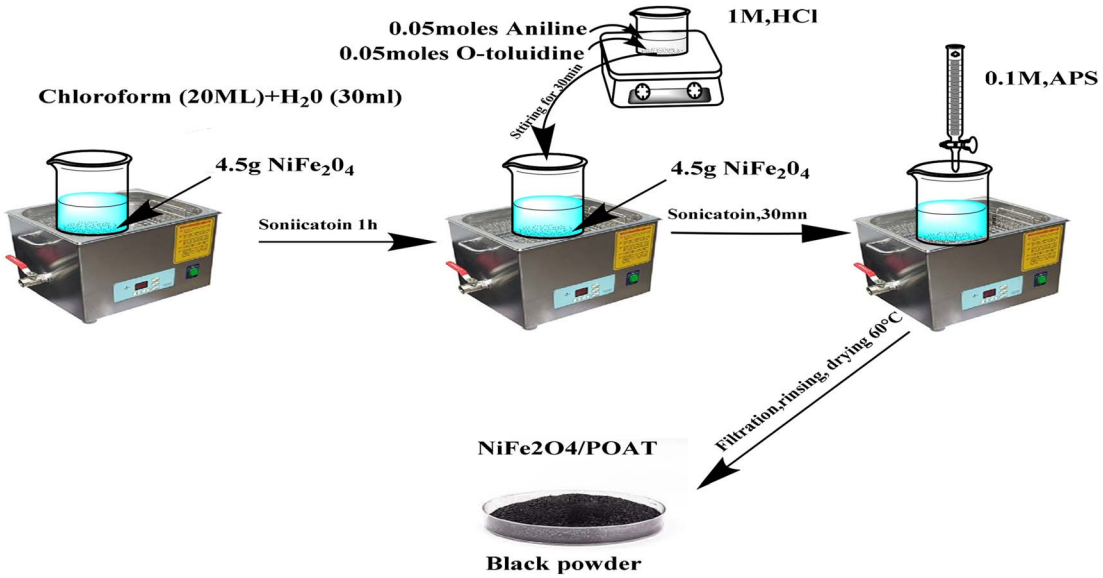

Scheme 2 Schematic representation the preparation of $NiFe_2O_4$/PAOT nanocomposite.

nitrophenol (4-NP) solutions with concentrations of 2, 10, and 15 ppm were prepared. Varying amounts (5, 10, and 20 mg) of the $NiFe_2O_4$/PAOT nanocomposite were dispersed in 10 mL of the prepared 4-NP aqueous solution, maintaining a pH of 7.43. The reaction mixtures were allowed to interact for durations ranging from 2 to 60 minutes at a constant temperature of 25 °C. After the reaction, the $NiFe_2O_4$/PAOT catalyst was separated by centrifugation, with additional recovery facilitated using a magnetic bar. The conversion of 4-nitrophenol (4-NP) to 4-aminophenol (4-AP) was quantitatively analyzed using spectrophotometry. The maximum absorption wavelength (λ_{max}) was recorded at 400 nm for 4-NP and 318 nm for 4-AP.

Results and discussion

Characterization of the nanomaterial composite

Fourier transform infra-red (FT-IR) spectroscopy. Fig. 1 presents the FTIR spectra of $NiFe_2O_4$ nanoparticles post-calcination and the $NiFe_2O_4$/PAOT nanocomposite after copolymerisation. The IR spectrum of calcined $NiFe_2O_4$ (ref. 37) nanoparticles shows a thin, broad band at about 3440 cm^{-3}. This band shows the O–H stretching and vibrational modes of the water that is adsorbed in the KBr pellet manufacturing process. The asymmetric stretching vibrations of the adsorbed carbonate groups account for two additional bands located between 1632 and 1382 cm^{-1}. The characteristic bands seen at 585–453 cm^{-3} are caused by the intrinsic stretching vibrations of the Fe–O and Ni–O bonds in the spinel structure. The spectra of calcinated $NiFe_2O_4$ nanoparticles exhibit no additional peaks.[38] On the other hand, the infrared spectrum of the $NiFe_2O_4$/poly(aniline-*co*-*o*-toluidine) composite shows a broad band in the 3384–3230 cm^{-3} range. This band is due to N–H stretching, which is made wider by hydrogen bonding. A band seen between 2920 and 2852 cm^{-3} shows the stretching vibrations of the $-CH_3$ group in the toluidine moiety. The bands observed in the 1587–1485 cm^{-1} region are attributed to the stretching vibrations of N–H and C=N. Bands present in the 1149–1006 cm^{-1} range are linked to the bending of the C–H plane. Finally, the metal–oxygen vibrations in the spinel crystal lattice are linked to two separate bands that span from 572 to 415 cm^{-3}.

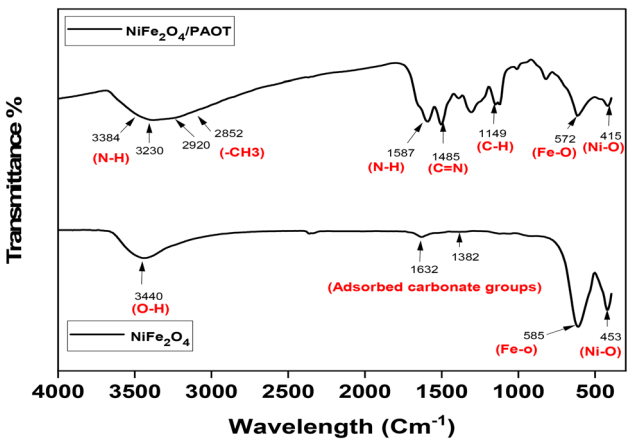

Fig. 1 FTIR spectra of $NiFe_2O_4$ nanoparticles and $NiFe_2O_4$/PAOT nanocomposite.

SEM microscopic analysis. The unique morphological features of $NiFeO_4$ are revealed by the SEM image Fig. 2(a), which emphasises homogeneous particle distribution and nanoscale structure. The distribution of the particle sizes is rather uniform and homogeneous, ranging from roughly 45 nm to 56 nm. This nanoscale size can increase the material's surface area, which is essential to its catalytic and magnetic capabilities. High-quality $NiFeO_4$ synthesis is demonstrated by the tightly packed particle arrangement with little agglomeration. Applications like adsorption, catalytic reduction, and other environmental cleanup procedures benefit from this morphology.[39]

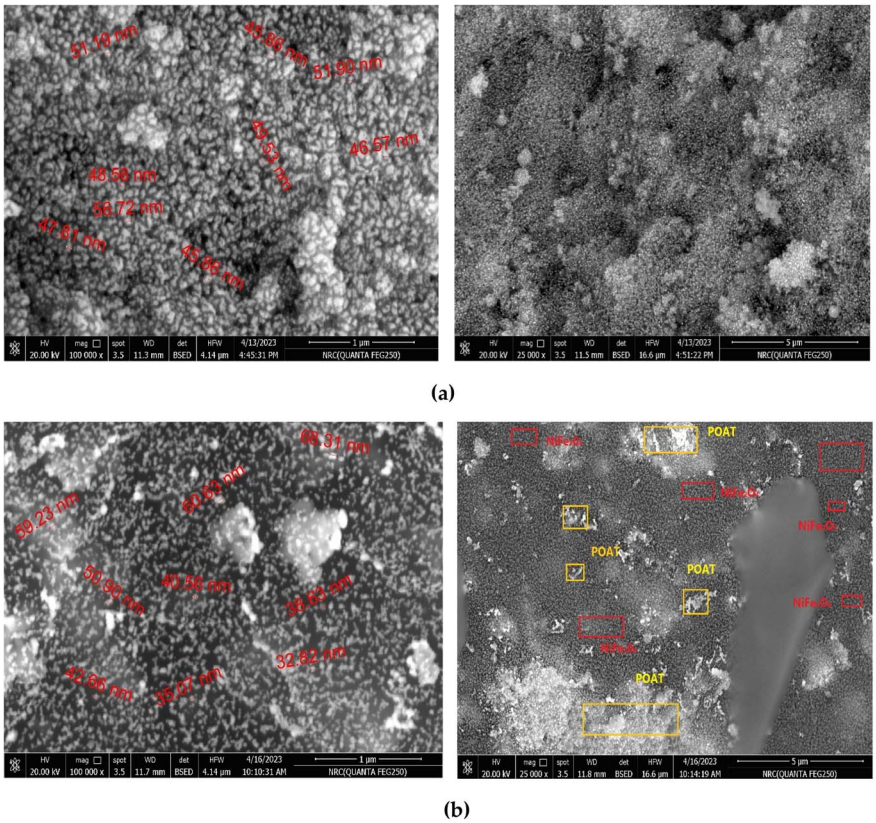

Fig. 2 SEM images of (a) $NiFe_2O_4$, and (b) $NiFe_2O_4$ coated with poly[*co*-*o*-toluidine + aniline].

The SEM image in Fig. 2(b), recorded at a scale of 1 μm, shows the structural and morphological changes in $NiFe_2O_4$ coated with poly(*o*-toluidine-*co*-aniline), resulting from the presence of the polymer.[40] The histograms in Fig. 3 shows the particle sizes vary from about 32 nm to 68 nm, suggesting that the polymer coating causes variations in the distribution. The polymer produces a smoother and more cohesive surface morphology, and the image shows a rather uniform dispersion of particles. The polymer's presence is probably what improves material stability and decreases particle aggregation. While preserving the fundamental nanoscale characteristics of $NiFeO_4$, this coating adds novel surface characteristics that are beneficial for catalytic and environmental applications.

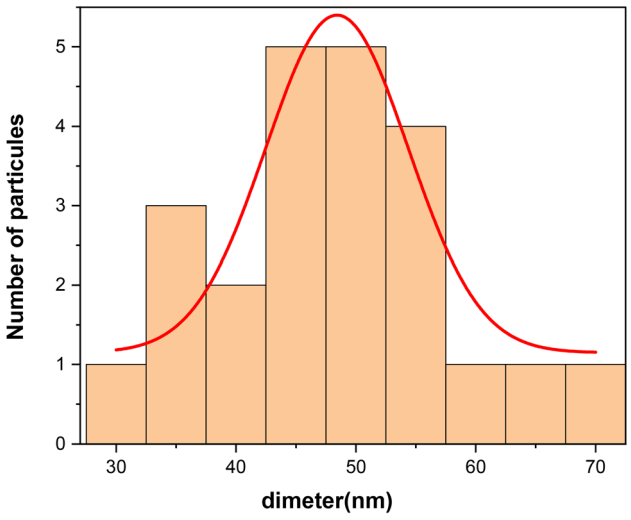

Fig. 3 Particle size distribution histogram of $NiFe_2O_4$ and $NiFe_2O_4$ coated with poly(aniline-*co*-*o*-toluidine) based on SEM analysis.

EDX spectrum. The EDX analysis in Fig. 4 showed that the synthesis and surface modification went well by confirming the elemental makeup of $NiFe_2O_4$ and its polymer-coated form. Following the expected spinel structure, the analysis found that $NiFe_2O_4$ is mostly made up of oxygen, iron, and nickel. Iron had the highest weight percentage (62.71%), indicating its dominant presence in the structure, but oxygen had the lowest weight percentage (26.15%) due to its lower atomic mass. The expected stoichiometric ratio was met by the smaller amounts of nickel (11.13% by weight). Iron and oxygen have modest error margins, indicating accurate measurements. Because lighter elements like carbon and nitrogen were incorporated from the polymer layer, the atomic percentages of metal elements in the polymer-coated $NiFe_2O_4$ sample fell. Furthermore, trace levels of chlorine were found, indicating the presence of small amounts of residual contaminants. The results showed that the polymer coating changed the surface by adding lighter parts while keeping the spinel structure of the core material.

Powder X-ray diffraction (XRD) analysis. The synthesized materials were subjected to analysis of their structural

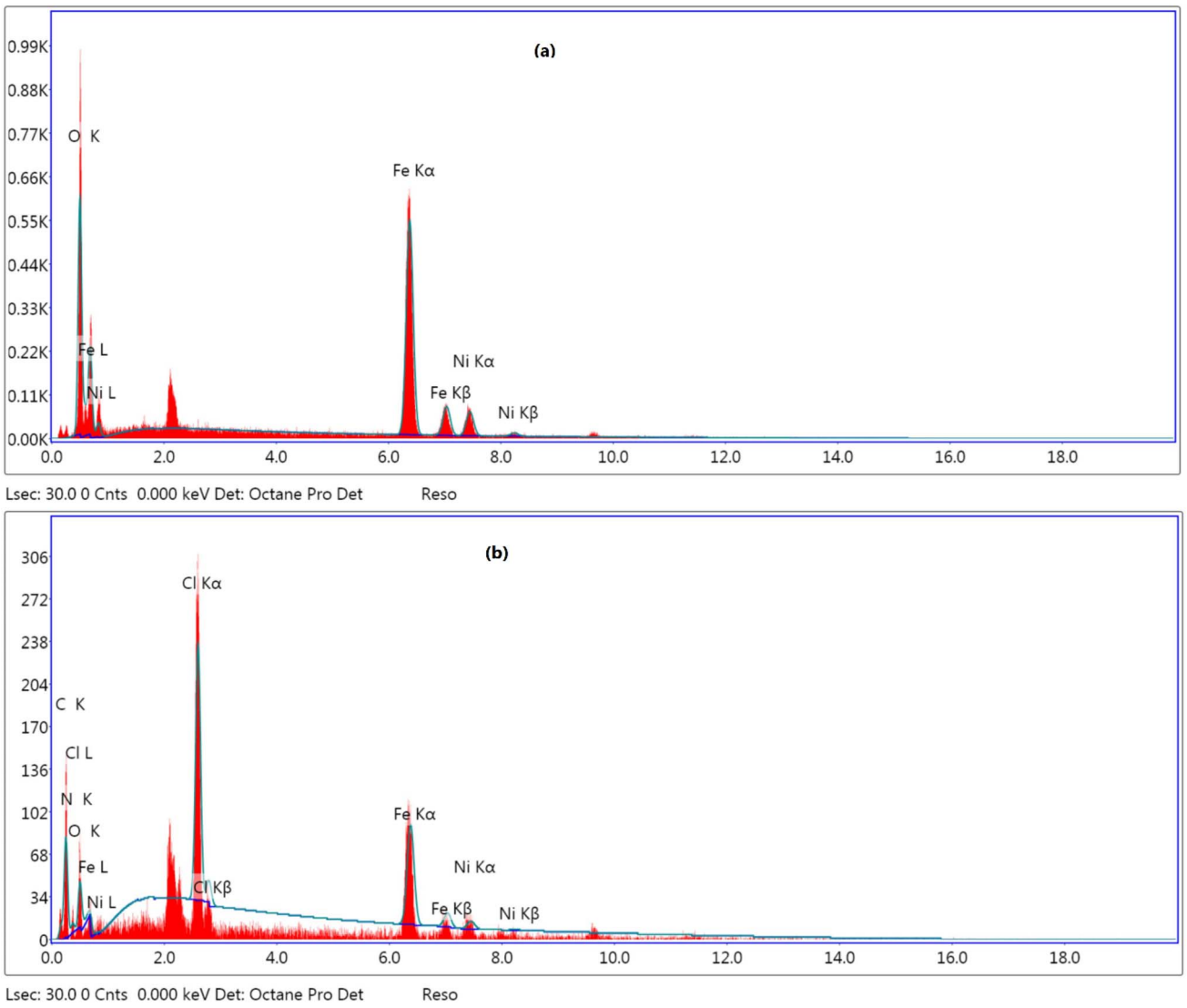

Fig. 4 (a) EDX of $NiFe_2O_4$ (a), (b) EDX spectrum of $NiFe_2O_4$ coated with poly(aniline-*co*-*o*-toluidine).

properties through X-ray diffraction (XRD). XRD patterns for $NiFe_2O_4$ nanoparticles[37] and $NiFe_2O_4$/PAOT nanocomposites were acquired using a powder X-ray diffractometer (PANalytical, Almelo, Netherlands) with CuKα radiation ($\lambda = 0.154$ nm) across a scanning range of 10° to 70°. The diffraction patterns, in accordance with the JCPDS standard (card no. 10-0325), confirmed the formation of a cubic spinel crystal structure, as depicted in Fig. 5.[36,37] No further peaks suggesting the presence of impurities like NiO or FeO_3 were detected. Polymer-enhanced nickel ferrite catalysts for the efficient reduction of 4-nitrophenol pollutants. Seven important diffraction peaks were found at 2, values of 30.24°, 35.48°, 36.94°, 43.06°, 53.80°, 57.20°, and 62.88°, corresponding to the crystal planes (311), (220), (222), (422), (511), (400), and (440). The XRD pattern of $NiFe_2O_4$/PAOT nanocomposites was mostly the same as that of pure $NiFe_2O_4$ nanoparticles, with the addition of a broad diffraction band seen between $2\theta = 15°$ and 25.[36] This was because the PAOT copolymer matrix is amorphous in Fig. 5.[36] The observed decrease in diffraction peak intensities in the nanocomposite relative to the pure $NiFe_2O_4$ nanoparticles suggests that PAOT was successfully integrated onto the $NiFe_2O_4$ surface while maintaining its crystalline structure. The average particle sizes of $NiFe_2O_4$ and $NiFe_2O_4$/PAOT were estimated using Scherrer's equation.

$$D = (K\lambda)/(\beta\cos\theta) \quad (1)$$

The Scherrer equation defines D as the crystallite size, λ as the wavelength of the X-ray radiation (CuKα, 0.154 nm), θ as the Bragg diffraction angle (in radians), and β as the full width at half maximum (FWHM) of the most intense XRD peak, particularly for the (311) plane. The value of the Scherrer constant (k) was set at 0.9. The calculation method yielded estimated average crystallite sizes of 12.3 nm for $NiFe_2O_4$ nanoparticles and 16.7 nm for $NiFe_2O_4$/PAOT nanocomposites.[36]

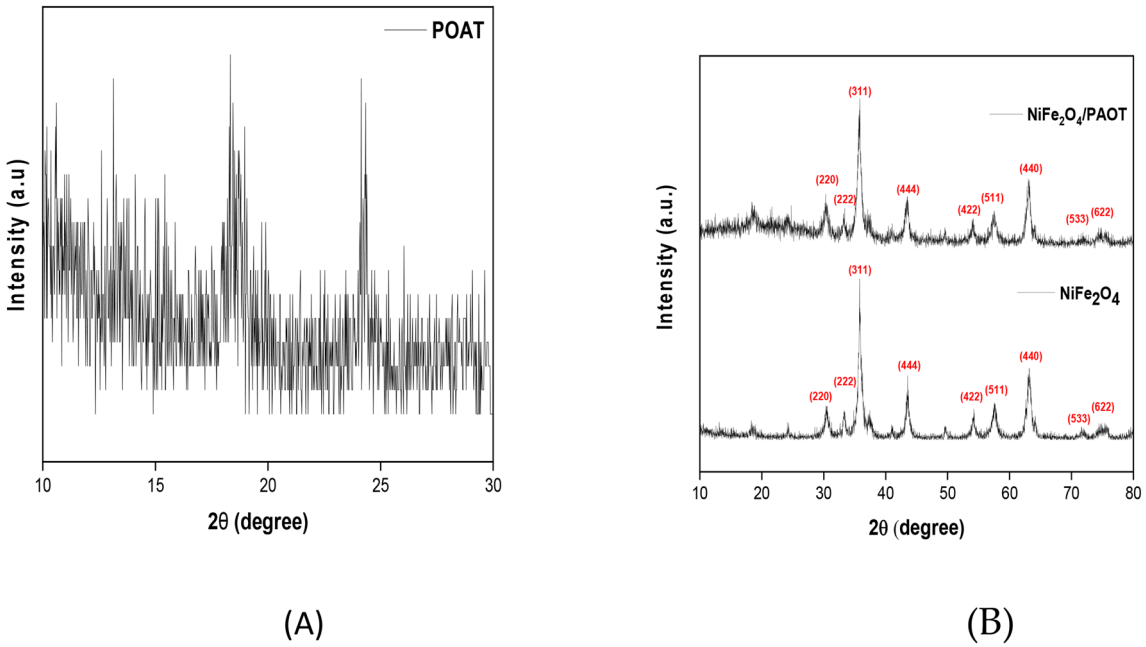

Fig. 5 XRD patterns of (A) PAOT, and (B) $NiFe_2O_4$ nanoparticles and $NiFe_2O_4$/PAOT nanocomposite.

In both the bare $NiFe_2O_4$ and the $NiFe_2O_4$/PAOT nanocomposite, additional diffraction peaks are observed in the high-angle region between 70° and 80° (2θ). These peaks correspond to the (533) and (622) crystallographic planes of the spinel $NiFe_2O_4$ phase, in agreement with the standard JCPDS card no. 10-0325. The presence of these reflections in both samples confirms that the crystalline spinel structure of $NiFe_2O_4$ is retained after polymer coating. The PAOT modification does not introduce new crystalline peaks in this range, indicating that the polymer layer is amorphous in nature and does not alter the fundamental crystal lattice of the ferrite core.

Catalytic degradatoin of 4-nitrophenol (NP). The process of catalytic reduction stands as the most effective method for converting hazardous nitrophenols, exemplified by 4-nitrophenol (4-NP), into benign aminophenols. Solutions that incorporate 4-NP display an absorbance peak within the range of 300 to 400 nm, with distinct absorption maxima identified at 400 nm for 4-NP and at 318 nm for 4-aminophenol (4-AP), as illustrated in Fig. 6. Upon the introduction of $NiFe_2O_4$ coated with poly[*o*-toluidine + aniline], the solution exhibited a discernible colour transition from dark yellow to light yellow within a span of 60 min.

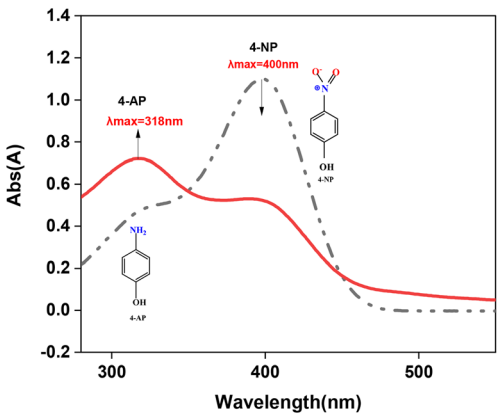

Fig. 6 Absorption peaks of 4-nitrophenol and 4-aminophenol in UV-Vis spectrum.

Solutions with concentrations of 2, 10, and 15 ppm were employed to investigate the catalytic reduction of 4-NP in 10 mL. Due to the magnetic properties of the materials, we implemented a glass stirrer to ensure homogenous suspension agitation. 10 mg of the catalyst was introduced after five minutes of continuous agitation, and the mixture was stirred for an additional 60 min at room temperature thereafter. The darker yellow colouration progressively dissipated during this period. Molecular absorption spectroscopy was employed to monitor the absorbance at 400 nm in order to ascertain the conversion of 4-NP to 4-AP. The relative concentration of 4-NP was then calculated using the following formula:[41]

$$C_t/C_0 = I_t/I_0 \quad (2)$$

The C_0 (mg L^{-1}) value shows how much 4-NP was in the solution before the catalyst was added. The C_t (mg L^{-1}) value shows how much 4-NP was still in the solution at a certain time after the catalyst was added. I_0 and I_t represent the absorbance intensities of 4-NP measured at 400 nm at $t = 0$ (prior to the addition of the catalyst) and at any later reaction time, respectively. The intensities were presumed to have a direct correlation with the concentration of 4-NP in the reaction system.

Effect of 4-NP concentration. The catalytic reduction of 4-nitrophenol (4-NP) to 4-aminophenol (4-AP) was examined using $NiFe_2O_4$ coated with poly[*o*-toluidine + aniline]. The study was conducted at initial concentrations of 2 ppm, 10 ppm, and

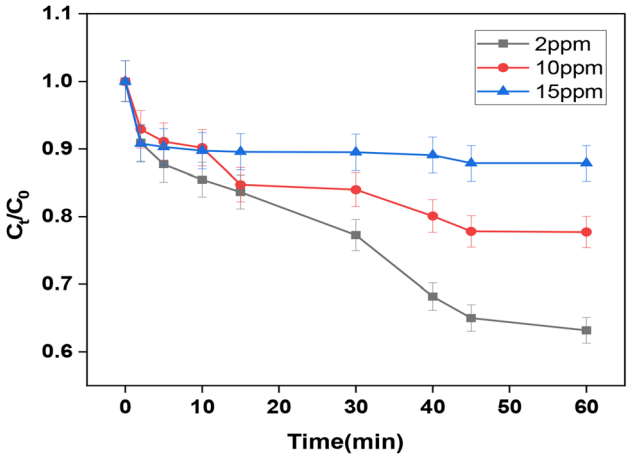

Fig. 7 Effect of $C_{NiFe_2O_4/PAOT}$ on the reduction of (4-NP) [$V_{solution}$ = 10 mL, T = 25 °C, pH = 7.43, [4-NP] = 2, 10, 15 ppm; m = 10 mg].

15 ppm over a reaction period of 60 min using a catalyst dosage of 10 mg, as shown in Fig. 7. At a starting concentration of 2 ppm, the reduction happened faster, as shown by a steeper drop in the C_t/C_0 ratio to 0.631. This means that the catalyst was more effective at lower substrate concentrations. At 10 ppm, the reaction rate exhibited a moderate level, with a more gradual decline in C_t/C_0 relative to 2 ppm, reaching a value of 0.77, indicating a reduction in catalytic activity with increasing concentration. At a concentration of 15 ppm, the reaction progressed most slowly and exhibited the lowest reduction efficiency at equilibrium. After 60 min, the C_t/C_0 ratio was 0.878. Since the catalyst dose was only 10 mg, higher concentrations of 4-NP may stop the reaction. This is probably because the active site is full or there are problems with mass transfer.

The $NiFe_2O_4$/POAT catalyst's conduction band acts as an electron source, allowing interactions between active electrons (e^-) and 4-NP. These interactions help reduce the $-NO_2$ group to $-NH_2$ by moving electrons and protons around. $NiFe_2O_4$/POAT has a low energy band gap, which makes it easier for 4-NP to turn into 4-AP. This is done by efficiently moving electrons between the catalyst and the pollutant, which speeds up the reaction. The polymer layer enhances electron mobility between the catalyst and 4-NP, thereby increasing its catalytic activity. However, this enhancement decreases when the system is saturated or overloaded, resulting in a decline in catalytic efficiency.[42]

Fig. 7 illustrates the spectral evolution of the 4-NP reduction reaction. At 0 minutes, the absorbance peak at 400 nm reaches its maximum, signifying the initial concentration of 4-NP. During the reaction, the peak at 400 nm diminishes progressively, whereas the peak at 318 nm rises, indicating the transformation of 4-NP to 4-AP. At 2 ppm, the absorbance curve drops more quickly at 400 nm than at 10 ppm and 15 ppm. This means that the reaction happens faster at lower concentrations. The observed trends indicate that $NiFe_2O_4$/POAT shows superior catalytic performance at lower concentrations, as diminished competition for active sites enhances electron transfer and reaction advancement.

Fig. 8 illustrates the time-dependent UV-visible spectral changes during the catalytic reduction of 4-nitrophenol (4-NP) to 4-aminophenol (4-AP) using $NiFe_2O_4$/PAOT nanocomposites at initial concentrations of (a) 2 ppm, (b) 10 ppm, and (c) 15 ppm. At the start of the reaction (t = 0 min), a strong absorbance peak is observed at 400 nm in all spectra, corresponding to the 4-nitrophenolate ion. As the reaction proceeds, the intensity of this peak gradually decreases, indicating the progressive consumption of 4-NP. Simultaneously, a new peak appears around 318 nm, which corresponds to the formation of 4-aminophenol (4-AP), the final reduction product. The rate of peak reduction is more rapid at lower concentrations (2 ppm), suggesting enhanced catalytic activity due to reduced competition for active sites. At higher concentrations (10 and 15 ppm), the peak reduction is slower, indicating a concentration-dependent reaction rate. The spectral shift and disappearance of the 400 nm peak, accompanied by the emergence of the 318 nm band, provide clear evidence for the successful transformation of 4-NP into 4-AP, demonstrating the efficiency of $NiFe_2O_4$/PAOT as a visible-light-responsive catalyst under ambient conditions.

Kinetics of the reduction process of nitrophenol. The reduction rate of nitrophenol can be analyzed using a pseudo-first-order kinetic model, as described in prior studies.[43] For the 4-nitrophenol (4-NP) reduction process, the ratio of the concentration of 4-NP at any time t (C_t) to its initial concentration at t = 0 (C_0) is equivalent to the ratio of the corresponding absorbance values A_t/A_0 measured at a wavelength of 400 nm. Based on this relationship, the kinetic equation governing the reduction process can be expressed bu eqn (3):[44]

$$-\ln(C_t/C_0) = -\ln(A_t/A_0) = K_{app}t \quad (3)$$

The apparent rate constant (K_{app}) can be calculated from the slope of the linear graph of $\ln(C_t/C_0)$ *versus* reaction time. Fig. 9 demonstrates a linear relationship between $\ln(A_t/A_0)$ and time, confirming that the reduction of 4-NP using $NiFe_2O_4$/POAT followed pseudo-first-order kinetics. Furthermore, the catalytic reduction of 2-NP with $NiFe_2O_4$/POAT was also examined. Fig. 9 illustrates that the linear trend of $\ln(A_t/A_0)$ against time also suggests that the reduction of 2-NP adhered to pseudo-first-order kinetics. The apparent rate constants (K_{app}) are calculated based on the slopes of the corresponding lines. At 2 ppm ($K_{app} = 1.16 \times 10^{-2}$ min^{-1}, $R^2 = 0.98$), 10 ppm ($K_{app} = 3.5 \times 10^{-3}$ min^{-1}, $R^2 = 0.96$), 15 ppm ($K_{app} = 5.44 \times 10^{-4}$ min^{-1}, $R^2 = 0.94$) dependency on concentration: the reduction rate exhibits significant variation as initial concentrations increase. This change could be caused by differences in how easy it is to get to active sites on the catalyst or by changes in how the 4-NP molecules interact with the surface of the catalyst.

Effect of the catalyst dose. Fig. 10 shows how the amount of $NiFe_2O_4$/PAOT catalyst affects the breakdown of 4-nitrophenol (4-NP). This evaluation was conducted at various initial concentrations (2 ppm, 10 ppm, and 15 ppm) with catalyst amounts of 5 mg, 10 mg, and 20 mg. An increase in catalyst mass led to a decrease in the C_t/C_0 ratio (where C_t denotes the remaining 4-NP concentration and C_0 is the initial

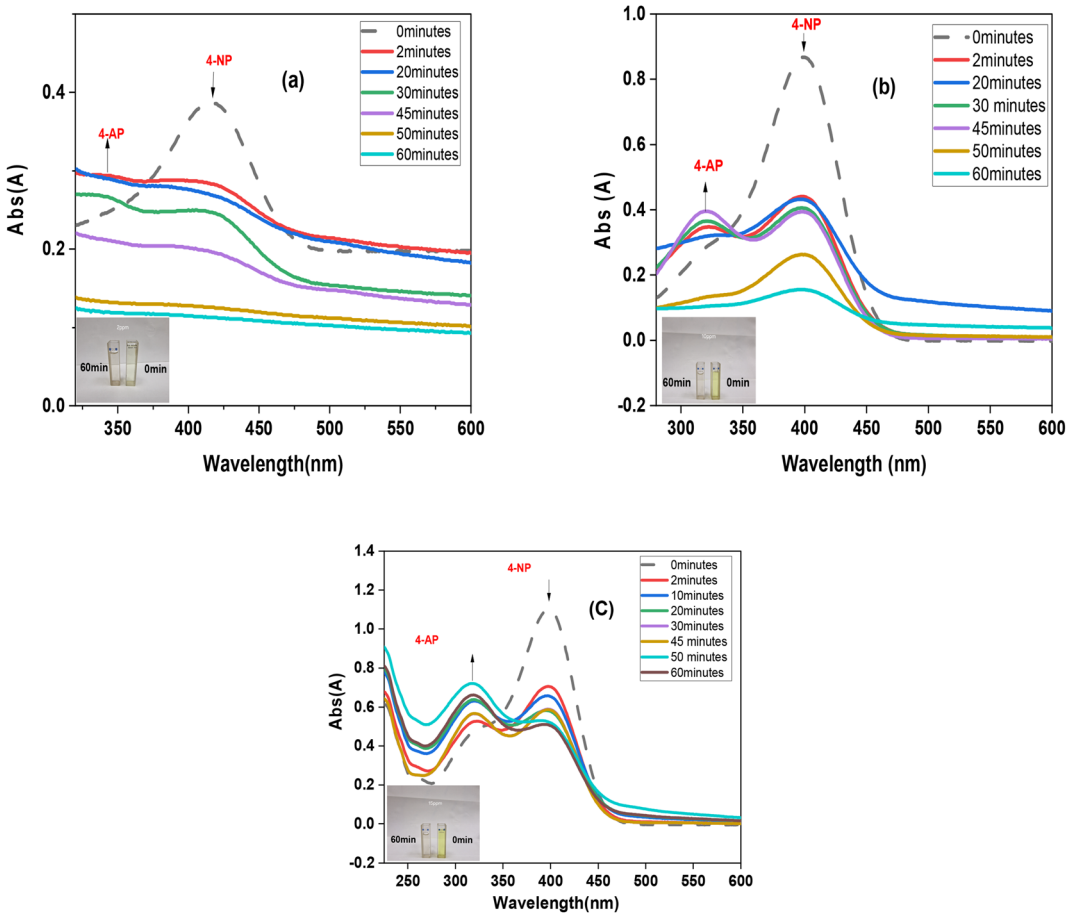

Fig. 8 UV-visible spectra of the reduction reaction of 4-NP to 4-AP at (a) 2 ppm, (b) 10 ppm, and (c) 15 ppm.

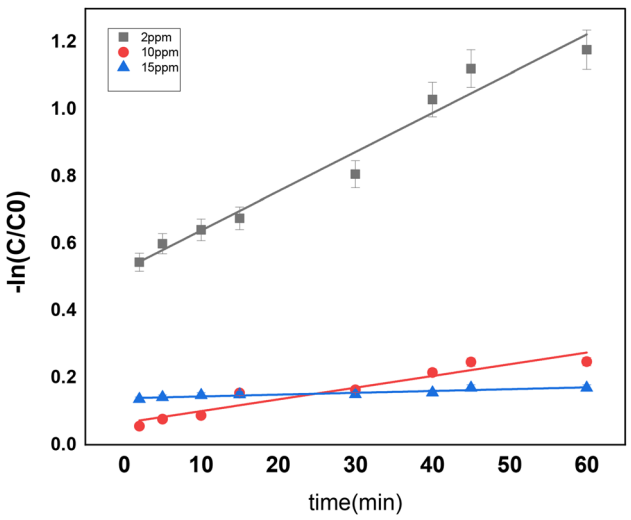

Fig. 9 Rate of reduction of 4-nitrophenol at different concentrations using 10 mg of $NiFe_2O_4$/POAT.

concentration), suggesting enhanced reduction efficiency. The 2 ppm solution exhibited the most notable reduction, with the C_t/C_0 ratio dropping to 0.545 at 20 mg of catalyst, indicating a highly effective degradation process. A comparable trend was noted for the 10 ppm and 15 ppm solutions, with the C_t/C_0 ratio reducing to 0.59 and 0.78, respectively, at 20 mg of catalyst. Nonetheless, the degree of reduction appeared to diminish at elevated concentrations, indicating that a larger catalyst dosage is necessary for efficient reduction as pollutant levels rise. The findings highlight that increasing the catalyst dose improves

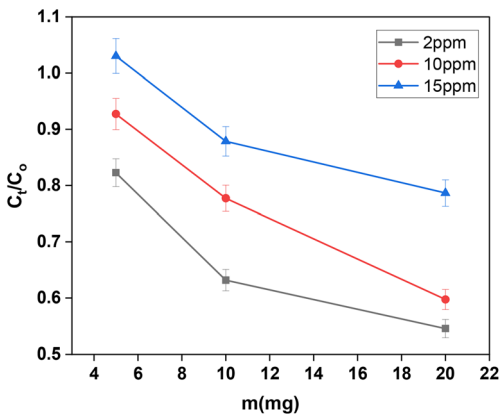

Fig. 10 Effect of dose ($NiFe_2O_4$/PAOT) on the reduction of (4-NP): $V_{solution} = 10$ mL, $T = 25$ °C, pH = 7.43, [4-NP] = 2, 10, 15 ppm, $m = (5, 10, 20)$ mg.

reduction efficiency, with a more pronounced effect observed at lower pollutant concentrations. At higher concentrations, the efficiency gain diminishes, highlighting the importance of optimizing catalyst dosage based on pollutant levels for maximum effectiveness.[45]

Temperature effect. The reduction efficiency of 4-nitrophenol (4-NP) was assessed at two temperatures, 37 °C and 50 °C, employing $NiFe_2O_4$/POAT as a catalyst, as illustrated in Fig. 11. The findings demonstrate that temperature significantly influences the reduction process. At 37 °C, the reduction efficiency is comparatively lower, with 2 ppm reaching a maximum efficiency of over 64%. In contrast, higher concentrations of 10 ppm and 15 ppm yield efficiencies of 38% and 37%, respectively. At 50 °C, the efficiency reduction markedly enhances, achieving 64% for 2 ppm, 63% for 10 ppm, and 61% for 15 ppm, indicating a more effective catalytic process. Elevated temperatures augment the kinetic energy of reactant molecules, facilitating their interaction with the active electrons of $NiFe_2O_4$/POAT. Moreover, increased temperatures may enhance the electron transfer process from 4-NP to 4-AP, which is a vital component of the reduction mechanism. The findings indicate that the reduction of 4-NP is influenced by temperature, with elevated temperatures enhancing catalytic performance. The results suggest that 50 °C may be an optimal temperature for maximizing reduction efficiency under the specified reaction conditions.[46,47]

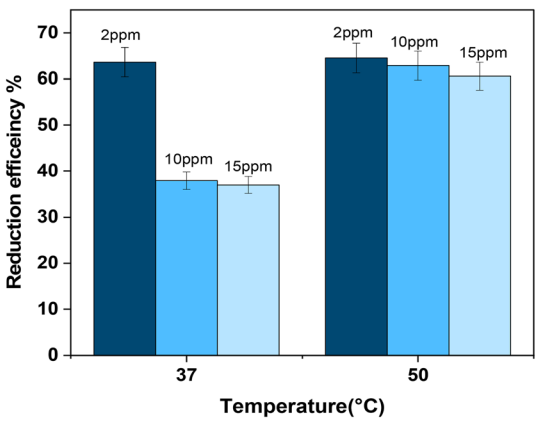

Fig. 11 Effect of temperature on the reduction of 4-NP [$V_{solution}$ = 10 mL, T = (37, 50) °C, pH = 7.43, [4-NP] = 2, 10, 15 ppm].

Catalyst optimization. The UV-visible absorption spectra illustrate the catalytic reduction of 4-NP to 4-AP under optimal conditions, utilising 20 mg of $NiFe_2O_4$/POAT as a catalyst at 50 °C, as shown in Fig. 12. The research was carried out using various initial concentrations of 4-NP (2 ppm, 10 ppm, and 15 ppm) and documented at two time points: t = 0 min and t = 60 min. At the initiation of the reaction (t = 0 min), all samples exhibited a pronounced absorption peak at 400 nm, indicative of the nitrophenolate ion, which represents the characteristic form of 4-NP under alkaline conditions. The absorbance intensity exhibited an increase corresponding to higher concentrations of 4-NP, with the maximum observed for the 15 ppm solution. Following a 60 minute period, a notable decrease in absorbance at 400 nm was recorded across all concentrations, validating the conversion of 4-NP to 4-AP. The calculated percentage reductions were 85.83% for 2 ppm, 95% for 10 ppm, and 99% for 15 ppm, highlighting the effectiveness of $NiFe_2O_4$/POAT in the reduction process. The results show that the catalyst does a good job of helping to change 4-NP. The higher the starting concentration, the faster the reaction goes, and within 60 minutes, almost all the 4-NP has been changed.

The data in Table 1 highlights the efficiency and operating conditions of various catalysts used for the reduction of 4-nitrophenol (4-NP), a hazardous environmental pollutant. Among them, $NiFe_2O_4$ modified with polyaniline (POAT) exhibited exceptional performance, achieving reduction efficiencies of 85%, 95%, and 99% for 2 ppm, 10 ppm, and 15 ppm concentrations, respectively, within 60 minutes. Compared to other reported catalysts, $NiFe_2O_4$/POAT demonstrates significant advantages. While catalysts like $NiFe_2O_4$/RGO and Bi_2S_3@Fe_3O_4 achieved near-complete reduction, $NiFe_2O_4$/POAT maintains consistently high efficiency across varying concentrations, highlighting its robustness and suitability for visible light-driven pollutant reduction in wastewater treatment applications. Unlike many catalysts that require $NaBH_4$ as

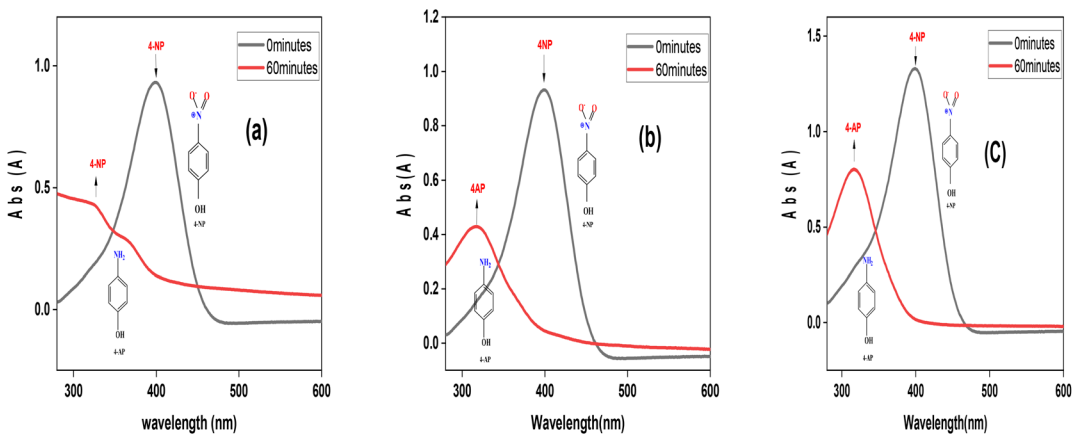

Fig. 12 The UV-Vis absorption spectra change for the reduction process of 4-NP for: (a) 2 ppm, (b) 10 ppm, and (c) 15 ppm.

Table 1 Comparison of previously reported catalysts for 4-nitrophenol reduction

Catalysts	Reduction efficiency (%)	Time (min)	Concentration	Gap energy (eV)	Reducing agent	Ref.
$NiFe_2O_4$	75	120	10 ppm	1.58	—	48
$Ni_{0.7}Cu_{0.3}Fe_2O_4$	82	120	10 ppm	1.48	—	48
$NiZnFe_2O_4$/CQDs	96	20 s	—	1.87	$NaBH_4$	33
$TiO_2/CoFe_2O_4$	95	35	10 ppm	3.2	$NaBH_4$	49
$CuFe_2O_4$	95	40 s	0.005 ppm	—	$NaBH_4$	50
$NiFe_2O_4$/RGO	100	30	0.036 M	—	$NaBH_4$	33
rGO/Cu-BDC MOF	44.67	8	0.04 mM	—	$NaBH_4$	51
$Bi_2S_3@Fe_3O_4$	98	29	0.1 mM	2.72	$NaBH_4$	52
g-C_3N_4/Bi_2S_3	60	60	0.125 mM	—	$NaBH_4$	53
Bi_2S_3 NSs	70	60	0.125 mM	—	$NaBH_4$	53
CuO/kaolinNC-1	99	12	20 ppm	—	$NaBH_4$	47
$BiFeO_3$	96	4.5	20 ppm	2.2	$NaBH_4$	54
$NiFe_2O_4$/POAT	85	60	2 ppm	1.24	—	This work
	95		10 ppm			
	99		15 ppm			

a reducing agent, this study eliminates the use of toxic and expensive chemicals, making $NiFe_2O_4$/POAT an eco-friendly and cost-effective alternative. Its alignment with green chemistry principles minimizes environmental risks and operational costs. Additionally, the lower energy band gap (1.24 eV) enhances electron transfer and catalytic activity, offering advantages over alternatives such as $NiZnFeO_4$/CQDs (1.87 eV), $TiO_2/CoFe_2O_4$ (3.2 eV), and $Bi_2S_3@Fe_3O_4$ (2.72 eV). While catalysts like $CuFe_2O_4$ achieve rapid reduction in 40 seconds, the scalability and stability of $NiFe_2O_4$/POAT over a practical 60 minute timeframe make it more suitable for industrial and real-world wastewater treatment applications. This study presents $NiFe_2O_4$/POAT as a scalable, efficient, and economically viable solution for 4-NP reduction, addressing both environmental and toxicological concerns. Its ability to function without a conventional reducing agent marks a significant step toward sustainable water treatment technologies. Overall, this work contributes to the advancement of green and innovative catalytic systems, paving the way for broader adoption in environmental remediation efforts.

Reusability of $NiFe_2O_4$/PAOT nanocomposite. The usability of $NiFe_2O_4$/PAOT nanocomposite was examined to determine whether the catalyst could be used for repeated reduction of 4-NP in successive cycles. Every cycle was carried out as described above. An external magnet bar was used to separate the catalyst from the test solution at the end of each cycle. After dipping the catalyst in 50 mL of 40 ppm NaOH for one hour, it was repeatedly cleaned with methanol and distilled water until the pH reached about 7, at which point it was dried. Sequential cycles were performed using the regenerated catalyst. eqn (3) (ref. 55) was used to determine the decreasing efficiency for % 4-NP after each cycle:

$$\text{Reduction efficiency (\%)} = ((C_0 - C_{eq})/C_0) \times 100 \quad (4)$$

From Fig. 13, it can be observed that in the first cycle, the catalyst achieves a high reduction efficiency of around 91%, indicating its initial effectiveness in reducing 4-NP. However, as the cycles progress, the reduction in efficiency significantly decreases. In the second cycle, the efficiency drops to approximately 71%, and by the third cycle, it further decreases to around 38%. By the fourth cycle, the catalyst only degrades to a minimal amount of 4-NP (~9%). The drastic decline in the fourth cycle is attributed to severe catalyst deactivation after repeated use. Several factors may contribute to this behavior: (i) partial loss of catalyst mass during recovery despite magnetic separation, (ii) surface fouling by strongly adsorbed intermediates or by-products that block active sites, (iii) structural or morphological changes during repeated reaction-regeneration cycles (including polymer detachment and reduced conductivity), and (iv) agglomeration of magnetic nanoparticles, which decreases the active surface area and dispersion in solution. While the $NiFe_2O_4$/PAOT nanocomposite shows strong catalytic activity in the initial runs, these cumulative effects limit its long-term reusability—a challenge similarly reported for ferrite–polymer composites in previous studies.[56,57]

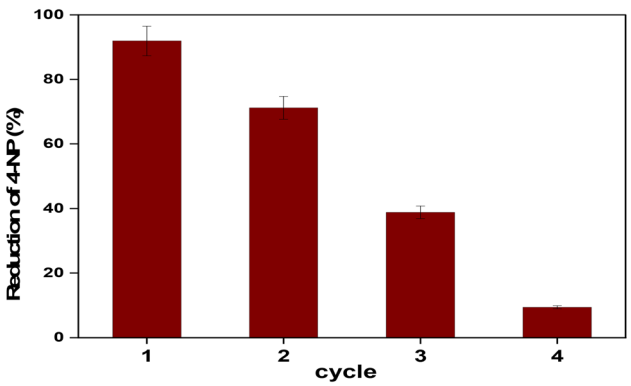

Fig. 13 Reusability of the $NiFe_2O_4$/POAT catalyst for 4-NP reduction.

Mechanism of catalytic reduction of 4-nitrophenol. The catalytic reduction of 4-nitrophenol (4-NP) to 4-aminophenol (4-AP) using $NiFe_2O_4$/POAT composite operates through an electron-driven mechanism facilitated by enhanced charge carrier dynamics.[58] $NiFe_2O_4$ represented by (Fig. 14), a ferrite

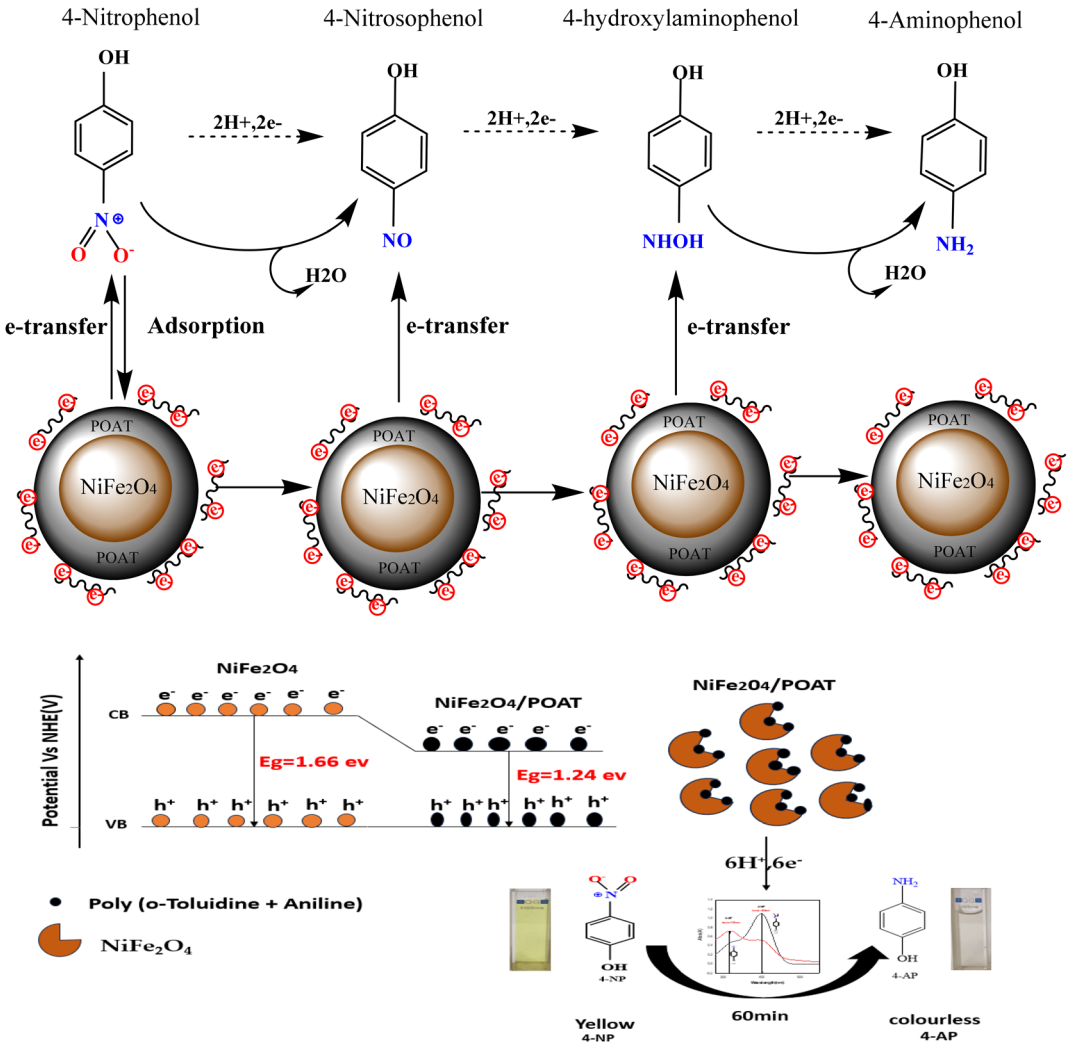

Fig. 14 Proposed mechanism of 4-nitrophenol reduction to 4-aminophenol on the catalyst surface.

material with a bandgap of 1.66 eV, absorbs visible light, generating electron–hole pairs. The incorporation of POAT into $NiFe_2O_4$ reduces the bandgap to 1.24 eV, leading to improved electron mobility and charge separation efficiency. During the reaction, electrons from the conduction band (CB) of $NiFe_2O_4$/POAT are transferred to the nitro group ($-NO_2$) of 4-NP, initiating a stepwise reduction process. The reaction proceeds through intermediate species, including nitroso (–NO) and hydroxylamine (–NHOH), ultimately yielding 4-aminophenol (4-AP) as the final product. Protons from the reaction medium combine with these electrons to complete the reduction. The composite's improved electron transport properties minimize recombination of charge carriers, ensuring a continuous supply of electrons for the reaction. The transformation is evidenced by a color change in the solution from yellow (indicating 4-NP) to colourless (indicating 4-AP). This change is further verified using UV-visible spectroscopy, which shows the disappearance of the characteristic absorption peak of 4-NP at 400 nm, and the appearance of a new peak at 318 nm. The reaction is completed within 60 min, demonstrating the superior catalytic efficiency of the $NiFe_2O_4$/POAT composite.

The 4-nitrophenol (4-NP) molecules are drawn to the surface of $NiFe_2O_4$ due to aromatic interactions: π–π stacking between the aromatic ring of 4-NP and the catalytic surface enhances adsorption. The copolymer poly(aniline-*co*-*o*-toluidine) acts as a source of electrons due to its electroactive nature. The copolymer has good electronic conductivity, which facilitates the transfer of electrons. Thanks to the oxidation/reduction cycles of the aniline and *o*-toluidine units, the polymer provides the necessary electrons for the catalytic reduction process (4-NP to 4-AP). $NiFe_2O_4$ plays the role of a semiconductor here, facilitating the migration of electrons from the copolymer to 4-nitrophenol. The Ni^{2+} and Fe^{3+} ions in the $NiFe_2O_4$ structure provide active sites that promote electron transfer and reduction reactions. The poly(aniline-*co*-*o*-toluidine) transfers electrons to the metal ions (Ni^{2+}/Fe^{3+}) on the surface of $NiFe_2O_4$. Once activated, $NiFe_2O_4$ transfers electrons to 4-nitrophenol, the band gap energy of $NiFe_2O_4$/POAT nanocomposites is low (1.24 eV) enough to excite electrons from the valence band to the conduction band. This is the main reason that facilitates the transfer of electrons from the $NiFe_2O_4$/POAT

nanocomposites to 4-nitrophenol, which is reduced to 4-aminophenol.

The conductive polymer, poly[aniline-*co*-*o*-toluidine], plays a crucial role in providing electrons for the reduction of 4-NP, $NiFe_2O_4$ facilitates electron transfer from first step: reduction of $–NO_2$ to a nitroso (–NO) intermediate[58] eqn (5), second step, reduction of –NO to an amine ($–NH_2$) eqn (6) and conversion of 4-NP to 4-aminophenol (4-AP) is represented as eqn (7).

$$–NO_2 + 2e^- + 2H^+ \rightarrow –NO + H_2O \quad (5)$$

$$–NO + 4e^- + 4H^+ \rightarrow –NH_2 + H_2O \quad (6)$$

$$C_6H_4(NO_2)OH + 6e^- + 6H^+ \rightarrow C_6H_4(NH_2)OH + 2H_2O \quad (7)$$

Conclusion

This study demonstrates the efficiency of $NiFe_2O_4$/PAOT nanocomposites in removing 4-nitrophenol (4-NP) from aqueous solutions. The catalyst demonstrated a reduction efficiency of 85% at a concentration of 2 ppm, indicating its effective performance at low pollutant levels. At concentrations of 10 ppm and 15 ppm, the reduction efficiencies were notable, achieving 95% and 99%, respectively. The consistent performance across varying concentrations highlights the adaptability of $NiFe_2O_4$/PAOT nanocomposites in effectively managing different pollutant loads. The observed bandgap energy of 1.24 eV enhances the catalyst's appeal by indicating a strong capacity for visible light absorption. This characteristic renders the nanocomposite especially appropriate for photocatalytic applications, facilitating activation by natural sunlight or artificial visible light sources, thereby significantly decreasing dependence on costly UV-based systems and enhancing energy efficiency. Leveraging visible light presents a significant advantage for environmental remediation, enhancing both the practicality and cost-effectiveness of the process. The $NiFe_2O_4$/PAOT nanocomposite exhibits high reduction efficiency and significant potential for application in wastewater treatment. The visible light activity and efficient reduction of hazardous aromatic pollutants make it a sustainable and effective solution for cleaning contaminated water sources.

Author contributions

All authors listed have made a substantial, direct, and intellectual contribution to the work and approved it for publication.

Conflicts of interest

The authors declare that the research was conducted in the absence of any commercial or financial relationships that could be constructed as a potential conflict of interest.

Data availability

Data supporting the findings of this study are available within the article.

References

1 A. Gholami, S. B. Mousavi, S. Z. Heris and M. Mohammadpourfard, Nitrate removal performance of a novel magnetic chitosan-based nanocomposite: modeling and optimization using response surface methodology, *Biomass Convers. Biorefin.*, 2024, **14**, 17481–17497.
2 R. Das, V. S. Sypu, H. K. Paumo, M. Bhaumik, V. Maharaj and A. Maity, Silver decorated magnetic nanocomposite (Fe_3O_4@PPy-MAA/Ag) as highly active catalyst towards reduction of 4-nitrophenol and toxic organic dyes, *Appl. Catal. B Environ.*, 2019, **244**, 546–558.
3 S. Z. Heris, M. Etemadi, S. B. Mousavi, M. Mohammadpourfard and B. Ramavandi, Preparation and characterizations of TiO_2/ZnO nanohybrid and its photocatalytic activity for degradation of organic dyes, *J. Photochem. Photobiol., A*, 2023, **443**, 114893.
4 X. Kong, H. Zhu, C. Chen, G. Huang and Q. Chen, Insights into the reduction of 4-nitrophenol to 4-aminophenol on catalysts, *Chem. Phys. Lett.*, 2017, **684**, 148–152.
5 Y. Shen, L. Zhang, Q. Li and X. Wang, *J. Phys. Chem. Solids*, 2022, **167**, 110783.
6 M. R. Kumar, A. S. Sekhar and S. J. Patel, *Results Chem.*, 2023, **5**, 100963.
7 S. Balgude, K. Patil, S. Moharil, M. Puranik, S. Kadam, P. Lokhande, S. Patange and P. More, *Chem. Select*, 2022, **7**, e202200221.
8 R. K. Raval and P. D. Patel, *J. Phys. Chem. Solids*, 2021, **148**, 109700.
9 S. Singh, V. K. Gupta and P. Ghosh, *RSC Adv.*, 2020, **10**, 42766–42776.
10 Z.-F. Jiang, F.-M. Tian, K.-M. Fang, Z.-G. Wang, L. Zhang, J.-J. Feng and A.-J. Wang, Atomically dispersed ternary FeCoNb active sites anchored on N-doped honeycomb-like mesoporous carbon for highly catalytic degradation of 4-nitrophenol, *J. Colloid Interface Sci.*, 2025, **677**, 718–728.
11 X. Zhang, F. Wei and S. Wang, Adsorption and catalytic degradation by $CoFe_2O_4$ coated on metal–organic framework for the removal of 4-nitrophenol and 2,4-dichlorophenol, *Sep. Purif. Technol.*, 2025, **354**, 129458.
12 S. Taghavi Fardood, F. Moradnia and T. M. Aminabhavi, Green synthesis of ZnO nanoparticles using Sargassum muticum aqueous extract and their photocatalytic degradation of methylene blue, *Environ. Pollut.*, 2024, **358**, 124534.
13 X. Liao, X. Wang, L. Zheng, Y. Hu, A. Wu and G. Li, A novel risk assessment model of urban gas pipeline network in expansions by integrating the OPA method and GraphSAGE algorithm, *Process Saf. Environ. Prot.*, 2024, **182**, 1227–1236.
14 Y. Yan, J. Miao, Z. Yang, F. X. Xiao, H. B. Yang, B. Liu and Y. Yang, Carbon nanotube catalysts: recent advances in synthesis, characterization and applications., *Chemical Society Reviews*, 2015, **44**(10), 3295–3346.
15 C. Ge, F. Shu, X. Guo, H. Jiao, D. Shi, C. Du, X. Guo, Q. Zhang, W. Wu, Y. Jin and B. Jiang, Comparison of Pd nanoparticle-decorated softwood and hardwood activated carbon in

catalytic reduction of high-concentrated industrial 4-nitrophenol, *Sep. Purif. Technol.*, 2024, **343**, 127149.
16 H. H. Shanaah, E. F. H. Alzaimoor, S. Rashdan, A. A. Abdalhafith and A. H. Kamel, Development of a novel potentiometric sensor for the determination of ketotifen fumarate in pharmaceutical formulations, *Sustainability*, 2023, **15**, 7336.
17 A. H. Kamel, H. S. M. Abd-Rabboh and A. Hefnawy, Molecularly imprinted polymer-based electrochemical sensors for monitoring the persistent organic pollutants chlorophenols, *RSC Adv.*, 2024, **14**, 20163–20181.
18 H. M. Al-Harbi, R. Kumar, M. A. Gondal and S. Al-Sayari, *Surf. Interfaces*, 2022, **33**, 102189.
19 A. Kumar, S. Sharma and V. Singh, *J. Mater. Sci.: Mater. Electron.*, 2024, **35**, 1636.
20 L. Zhao, F. Chen and M. Liu, *Inorg. Chem. Commun.*, 2024, **170**, 113170.
21 Z.-F. Jiang, F.-M. Tian, K.-M. Fang, Z.-G. Wang, L. Zhang, J.-J. Feng and A.-J. Wang, Atomically dispersed ternary FeCoNb active sites anchored on N-doped honeycomb-like mesoporous carbon for highly catalytic degradation of 4-nitrophenol, *J. Colloid Interface Sci.*, 2025, **677**, 718–728.
22 Y. Chen, H. Zhang, L. Chen, G. Fan and Y. Long, Efficient removal of 4-nitrophenol from aqueous solution using a novel magnetic biochar composite: Adsorption and catalytic degradation performance, *Sep. Purif. Technol.*, 2025, **353**, 128437.
23 A. Ammara, S. Noreen, S. Ali, S. Jamil, S. Bibi, M. J. Latif and S. R. Khan, Synthesis and characterization of chitosan-based nanocomposite for efficient removal of heavy metals from wastewater, *Polym. Bull.*, 2024, **81**, 15153–15182.
24 J. Mahmood, N. Arsalani, S. Naghash-Hamed, Z. Hanif and K. E. Geckeler, Preparation and characterization of hybrid polypyrrole nanoparticles as a conducting polymer with controllable size, *Sci. Rep.*, 2024, **14**, 11653.
25 S. S. M. Hassan, A. H. Kamel, A. A. Hassan, H. A. El-Naby, M. A. Al-Omar and A. Y. A. Sayed, *Molecules*, 2020, **25**(12), 2721.
26 A. H. Kamel, A. A. Hassan, H. H. El-Shalakany and M. A. Al-Omar, Synthesis and characterization of chitosan-based nanocomposite for efficient removal of heavy metals from wastewater, *Nanomaterials*, 2020, **10**(3), 586.
27 D. M. Dotzauer, S. Bhattacharjee, Y. Wen and M. L. Bruening, Nanoparticle-containing membranes for the catalytic reduction of nitroaromatic compounds, *Langmuir*, 2009, **25**(3), 1865–1871.
28 S. S. M. Hassan, A. H. Kamel and M. A. Fathy, A novel screen-printed potentiometric electrode with carbon nanotubes/polyaniline transducer and molecularly imprinted polymer for the determination of nalbuphine in pharmaceuticals and biological fluids, *Anal. Chim. Acta*, 2022, **1227**, 340239.
29 M. N. Ahmed, H. Khan, L. Islam, M. H. Alnasir, S. N. Ahmed, M. T. Qureshi and M. Y. Khan, Investigating nickel ferrite (NiFe2O4) nanoparticles for magnetic hyperthermia applications, *Journal of Materials and Physical Sciences*, 2023, **4**(1), 32–45.
30 Q. Qi, H. Zhang, M. Liu, S. Qi, Z. Huo, Y. Ma, Z. Zhang, Y. Lu, X. Qi, S. Han and G. Wang, Multifunctional nanoplatform for targeted cancer therapy and imaging, *Cancer Nanotechnol.*, 2023, **14**(1), 46.
31 S. Z. Heris, M. Etemadi, S. B. Mousavi, M. Mohammadpourfard and B. Ramavandi, Preparation and characterizations of TiO_2/ZnO nanohybrid and its photocatalytic activity for degradation of organic dyes, *J. Photochem. Photobiol., A*, 2023, **443**, 114893.
32 M. R. Gholipour, C. T. Dinh, F. Béland and T. O. Do, Nanostructured photocatalysts for solar hydrogen production, *Nanoscale*, 2015, **7**(18), 8187–8208.
33 S. Naghash-Hamed, N. Arsalani and E. Sharifi As, Synthesis of novel nano-structured materials for environmental applications, *Nano-Struct. Nano-Objects*, 2023, **35**, 101002.
34 S. Sambhudevan, Green Synthesis of Metal Nanoparticles for Catalytic Applications, *Chem. Pap.*, 2021, **75**, 3697–3710.
35 S. S. M. Hassan, A. H. Kamel, A. A. Hassan, A. E.-G. E. Amr, H. A. El-Naby and E. A. Elsayed, Development of Nanomaterial-Based Sensors for Environmental Monitoring, *Nanomaterials*, 2020, **10**, 254.
36 M. A. Fathy, A. H. Kamel and S. S. M. Hassan, Fabrication of Molecularly Imprinted Electrochemical Sensors for Pharmaceutical Analysis, *RSC Adv.*, 2022, **12**, 7433–7445.
37 O. Baytar, A. Ekinci, Ö. Şahin and A. Akdag, Synthesis of Novel Compounds with Potential Biological Activity, *ChemistrySelect*, 2024, **9**(8), e202304491.
38 A. G. Ramu, S. Salla, S. Chandrasekaran, P. Silambarasan, S. Gopi, S. Seo, K. Yun and D. Choi, Environmental Applications of Nanomaterials: A Review, *Environ. Pollut.*, 2021, **270**, 116063.
39 F. D. Koca and B. Şahin, Green Synthesis of $NiFe_2O_4$ Nanoparticles and Evaluation of Their Photocatalytic Activities, *Inorg. Nano-Met. Chem.*, 2024, **1**, 1–7.
40 M. Shabani, E. Saebnoori, S. A. Hassanzadeh-Tabrizi and H. R. Bakhsheshi-Rad, Synthesis and Characterization of TiO_2/ZnO Nanohybrid and Its Photocatalytic Activity for Degradation of Organic Dyes, *J. Mater. Eng. Perform.*, 2023, **32**, 2165–2182.
41 L. Sabaghzadeh, A. Tadjarodi, N. Steinfeldt and J. Strunk, Facile Synthesis of MFe_2O_4/RGO (M = Ni, Co) Nanocomposites and Their Application in the Reduction of 4-Nitrophenol, *Iran. J. Sci.*, 2024, **48**, 357–372.
42 P. Wang, D. Li, L. Wang, S. Guo, Y. Zhao, H. Shang, D. Wang and B. Zhang, Heteroatom-Doped Noble Carbon-Tailored Pd Nanoparticles for Efficient Catalytic Degradation of 4-Nitrophenol, *Chem. Eng. J.*, 2024, **495**, 153631.
43 D. M. Dotzauer, S. Bhattacharjee, Y. Wen and M. L. Bruening, Nanoparticle-Containing Membranes for the Catalytic Reduction of Nitroaromatic Compounds, *Langmuir*, 2009, **25**, 1865–1871.
44 J. Feng, L. Su, Y. Ma, C. Ren, Q. Guo and X. Chen, $CuFe_2O_4$ Magnetic Nanoparticles: A Simple and Efficient Catalyst for the Reduction of Nitrophenol, *Chem. Eng. J.*, 2013, **221**, 16–24.
45 Y. Chen, H. Zhang, L. Chen, G. Fan and Y. Long, Efficient Removal of 4-Nitrophenol from Aqueous Solution Using

a Novel Magnetic Biochar Composite: Adsorption and Catalytic Degradation Performance, *Sep. Purif. Technol.*, 2025, **353**, 128437.

46 A. O. Cardoso Juarez, E. I. Ocampo Lopez, M. K. Kesarla and N. K. R. Bogireddy, *ACS Omega*, 2024, **9**, 33335–33350.

47 Z. G. Asmare, B. A. Aragaw and M. Atlabachew, Facile Synthesis of Natural Kaolin-Based CuO Catalyst: An Efficient and Eco-Friendly Catalyst for the Reduction of 4-Nitrophenol, *ACS Omega*, 2024, **9**(49), 48014–48031.

48 P. Azhagapillai, K. Gopalsamy, I. Othman, S. Salman Ashraf, F. Banat and M. Abu Haija, Photocatalytic Reduction of 4-Nitrophenol over Eco-Friendly $Ni_xCu_xFe_2O_4$ Without an Additional Reducing Agent in Water, *Mater. Sci. Energy Technol.*, 2024, **7**, 195–204.

49 M. Khatamian, B. Divband and A. Jodaei, Synthesis and Characterization of TiO_2/ZnO Nanohybrid and Its Photocatalytic Activity for Degradation of Organic Dyes, *Mater. Chem. Phys.*, 2012, **134**, 31–37.

50 J. Feng, L. Su, Y. Ma, C. Ren, Q. Guo and X. Chen, $CuFe_2O_4$ Magnetic Nanoparticles: A Simple and Efficient Catalyst for the Reduction of Nitrophenol, *Chem. Eng. J.*, 2013, **221**, 16–24.

51 A. A. Yadav, Y. M. Hunge, S. Majumder, A.-H. I. Mourad, M. M. Islam, T. Sakurai and S.-W. Kang, Catalytic Degradation of 4-Nitrophenol in Polluted Water by Three-Dimensional Co_3O_4 Nanostructures, *J. Colloid Interface Sci.*, 2025, **677**, 161–170.

52 N. Kurnaz Yetim, N. Aslan and M. M. Koç, Synthesis and Characterization of TiO_2/ZnO Nanohybrid and Its Photocatalytic Activity for Degradation of Organic Dyes, *J. Environ. Chem. Eng.*, 2020, **8**, 104258.

53 D. Ayodhya and G. Veerabhadram, Catalytic Degradation of 4-Nitrophenol in Polluted Water by Three-Dimensional Co_3O_4 Nanostructures, *Environ. Technol.*, 2021, **42**, 826–841.

54 S. Parida, B. Sarangi, J. Nanda and B. Pany, Effect of Co^{2+} Doping on Structural, Optical, and Magnetic Properties of $NiFe_2O_4$ Nanoparticles, *Inorg. Chem. Commun.*, 2024, **170**, 113344.

55 G. B. Stambouli, B. Benguella, B. Makhoukhi, M. S. El-ouchdi and A. H. Kamel, Physicochemical properties of mesoporous acid activated materials from Lemna minor for Bezaktiv Red S-MAX dye removal, *J. Anal. Methods*, 2025, **17**, 2134–2143.

56 F. F. Alharbi, S. Gouadria, M. Abdullah, A. G. Abid, F. Mehar-un-Nisa, H. M. T. Farid and S. Aman, Development of High-Performance Alloys for Aerospace Applications, *JOM*, 2024, DOI: **10.1007/s11837-024-06964-x**.

57 T. L. Lambat, P. V. Ledade, J. K. Gunjate, V. R. Bahekar, S. H. Mahmood and S. Banerjee, Recent Developments in the Organic Synthesis Using Nano-$NiFe_2O_4$ as Reusable Catalyst: A Comprehensive Synthesis & Catalytic Reusability Protocol, *Results Chem.*, 2023, **6**, 101176.

58 T. K. Das and N. C. Das, Advances on Catalytic Reduction of 4-Nitrophenol by Nanostructured Materials as Benchmark Reaction, *Int. Nano Lett.*, 2022, **12**, 223–242.

RSC Advances

REVIEW

View Article Online
View Journal | View Issue

Cite this: *RSC Adv.*, 2025, **15**, 6875

Metal oxides and their composites for the remediation of organic pesticides: advanced photocatalytic and adsorptive solutions

Ayman H. Kamel, *[ab] Hisham S. M. Abd-Rabboh, [c] Ahmed Abd El-Fattah, [ad] Ghizlene Boudghene Stambouli[ae] and Lina Adeida[ae]

Metal oxide nanoparticles and their composites have garnered significant attention in water treatment and environmental cleanup due to their unique physicochemical properties. These materials exhibit distinct crystalline structures, tunable morphologies, large surface areas, versatile surface chemistry, and widespread availability. These features make nanostructured metal oxides and their composites highly effective for the selective removal of organic pollutants from the environment, either by adsorption or photodegradation. This article focuses on recent advances, challenges, and opportunities in the use of metal oxides and their composites for the targeted removal of organic contaminants, including insecticides, phenolic compounds, organic dyes, and similar pollutants. The discussion encompasses a broad range of metal oxides and their composites, highlighting their diverse structural, crystallographic, and morphological characteristics that influence their adsorption and photocatalytic performance. Emphasis is placed on the photocatalytic and adsorptive capabilities of these materials, including their photo-stimulation properties and mechanisms. Metal oxides are highlighted as outstanding photocatalysts due to their high photodegradation efficiency, cost-effective synthesis methods, and optimized bandgap engineering. This review serves as a valuable resource for researchers exploring the photocatalytic and adsorptive applications of metal oxide-based materials, particularly in the remediation of hazardous organic pollutants such as pesticides.

Received 16th November 2024
Accepted 22nd December 2024

DOI: 10.1039/d4ra08149h

rsc.li/rsc-advances

[a]*Department of Chemistry, College of Science, University of Bahrain, Zallaq P. O. Box 32038, Bahrain. E-mail: ahmohamed@uob.edu.bh*

[b]*Department of Chemistry, Faculty of Science, Ain Shams University, Cairo 11566, Egypt. E-mail: ahkamel76@sci.asu.edu.eg*

[c]*Chemistry Department, Faculty of Science, King Khalid University, Abha 61413, Saudi Arabia*

[d]*Department of Materials Science, Institute of Graduate Studies and Research, Alexandria University, Alexandria 21526, Egypt*

[e]*Department of Chemistry, Inorganic Chemistry and Environment Laboratory, University of Tlemcen, P. O. Box 119, 13000 Tlemcen, Algeria*

Ayman H. Kamel

Prof. Kamel has completed his PhD degree from Ain Shams University, Cairo, Egypt with a focus on the fabrication and characterization of electrochemical sensors for environmental, biomedical and pharmaceutical analysis. Prof. Kamel has published over 137 research articles in well reputed high impact factor international journals. He is also the author of several book chapters. He serves as guest editor, member, referee, and reviewer for many international renowned scientific journals. He has successfully completed several research projects as Principal Investigator. Professor Ayman H. Kamel is a leading figure in the field of sensors and their applications. His research primarily focuses on developing novel sensor technologies and exploring their potential applications in various fields such as healthcare, environmental monitoring, and industrial automation. Prof. Kamel has made significant contributions to the development of sensors with improved sensitivity, selectivity, and reliability. His work often involves interdisciplinary collaboration, combining principles from fields such as materials science, electrical engineering, and chemistry to advance sensor technology. One of his notable achievements is in the area of biomedical sensors, where he has worked on developing sensors for early disease detection, monitoring of physiological parameters, and drug delivery systems. These sensors have the potential to revolutionize healthcare by providing real-time monitoring and personalized treatment options.

1. Introduction

Wastewater contains a variety of substances, including those that are organic (such as pathogens), inorganic (such as heavy metal ions, metal oxides, metal complexes, salts, and other inorganic substances), and nutrient- and agricultural-runoff-related. Organic pollutants are attracting a lot of interest due to their (a) varied applications and subsequent discharge to terrestrial and aquatic bodies; (b) prolonged persistence; (c) high resistance to degradation; and (d) considerable health and environmental consequences.[1] About 85–90% of all fresh water is used for irrigation of agricultural land in Africa and Asia.[2] Agriculture continues to be the predominant user of global freshwater resources, representing approximately 70% of total withdrawals, with variations observed across regions due to differing irrigation practices.[3] The issue of pesticide contamination remains a critical challenge, as residues from agricultural runoff continue to impact major rivers and aquatic ecosystems worldwide.[4] The two issues underscore the critical necessity for sustainable water management practices within the agricultural sector.[5]

Pesticides are the main cause of organic pollutants in water bodies. Pesticides primarily enter the aquatic system from (a) personal usage, (b) pesticide production industry effluents, and (c) the agriculture sector, where they are heavily used for pest management to protect crops from pest damage. Insecticides, herbicides, fungicides, rodenticides, and plant growth regulators are examples of pesticides. Uncontrolled and excessive pesticide usage contaminates water (agricultural runoff) and is harmful to aquatic life and human health. The current WHO guidelines for drinking water quality specify that acceptable levels of pesticides depend on individual compounds.[6] For instance, guideline values are derived based on toxicity and potential exposure. The maximum acceptable values for individual pesticides often fall within 0.1 μg L^{-1} to 1 μg L^{-1} for specific compounds, with stricter limits for more hazardous pesticides. For total pesticides, the cumulative limit generally aligns with 0.5 μg L^{-1}, but this varies depending on local regulations and risk assessments.[6] Pesticides that are used in excess of the allowed amount can have harmful effects on human health, including endocrine, gastrointestinal, neurological, respiratory, reproductive, and dermatological issues.[7] Contaminated water contributes to scarcity because it becomes unusable for domestic, agricultural, or industrial purposes, reducing the overall accessible water supply. This exacerbates water scarcity, especially in regions where clean water resources are already limited. Water demand has increased because of rising population, economic development, urbanization, dynamic changes in lifestyle, attitudes about water use, and rapid industrialization.[8] Water scarcity is a danger in many parts of the world, and many people are unable to meet their basic needs. As a result, much effort has been made to conserve water and remove toxins from wastewater so that it can be used for domestic and agricultural purposes. The removal of various types of organic pollutants from wastewater using cost-effective and ecologically friendly approaches is a hot topic. The study of the interaction between organic contaminants in water and the materials that may be used to remove or degrade them quickly and cheaply is becoming increasingly important for technological application in this context.

The transition metal oxide nanoparticles are appealing candidates for the adsorption process because of their exceptional surface properties, microstructural features, and large surface area.[9] The increased surface area and active sites make adsorption events simpler. Nanoscale properties, such as high surface-to-volume ratios and increased active sites, enhance adsorption kinetics by providing more interaction points for pollutant molecules. Thermodynamically, the high surface energy at the nanoscale facilitates stronger binding interactions, leading to favorable adsorption equilibria. In order to remove organic contaminants from wastewater, nanoparticles have superior adsorption capability than their bulkier cousins. Metal oxide nanoparticles, either alone or in combination, have demonstrated tremendous promise recently as highly selective adsorbents for the quick and effective removal of organic contaminants from wastewater.[10]

2. Pesticide: risks and benefits

Pesticides are lethal chemical or biological substances that are released into the environment to reduce, eliminate, or control the population of insects, weeds, rodents, fungi, and other pests.[11] The main sources of pesticides in the environment are forestry and agriculture. Even though it is well known that a growing world population needs greater global food production, it is desirable for the pesticide to kill the target organisms to reduce the impact of weed species on both humans and the environment. On the other hand, these organic pollutants could destroy the ecosystem's flora and wildlife if they are applied improperly. In addition, humans and other living things are more negatively impacted by the widespread use of these dangerous chemical pesticides.

Hazardous pesticides are widely used against various organisms. Among them, 80% of pesticide applications are targeted at insect control, followed by 15% for herbicide use and 1% for treating plant fungal diseases, with the remaining 4% used for other purposes. When categorizing the types of pesticides by frequency of use, insecticides constitute 47.5%, herbicides 29.5%, fungicides 17.5%, and other chemicals 5.5%. This discrepancy likely arises from differences in classification—one based on the purpose of application and the other on the types of pesticides sold or applied.[12] The long-term consequences of pesticides and the influence of hazardous chemicals released into water bodies are well known to environmental specialists and farmers.[13] In the past 50–60 years, there has been a rise in the incidence of cancer and chronic diseases because chemical pesticides act as catalysts for carcinogens.[14]

Hazardous chemical pollutants accumulated in the soil have been reduced using treatment techniques like leaching and landfilling. On the other side, the soil remediation process takes a long time and is expensive. To safeguard farmland and limit the use of harmful pesticides, organic waste/earthworm techniques and manure as a soil amendment are required.

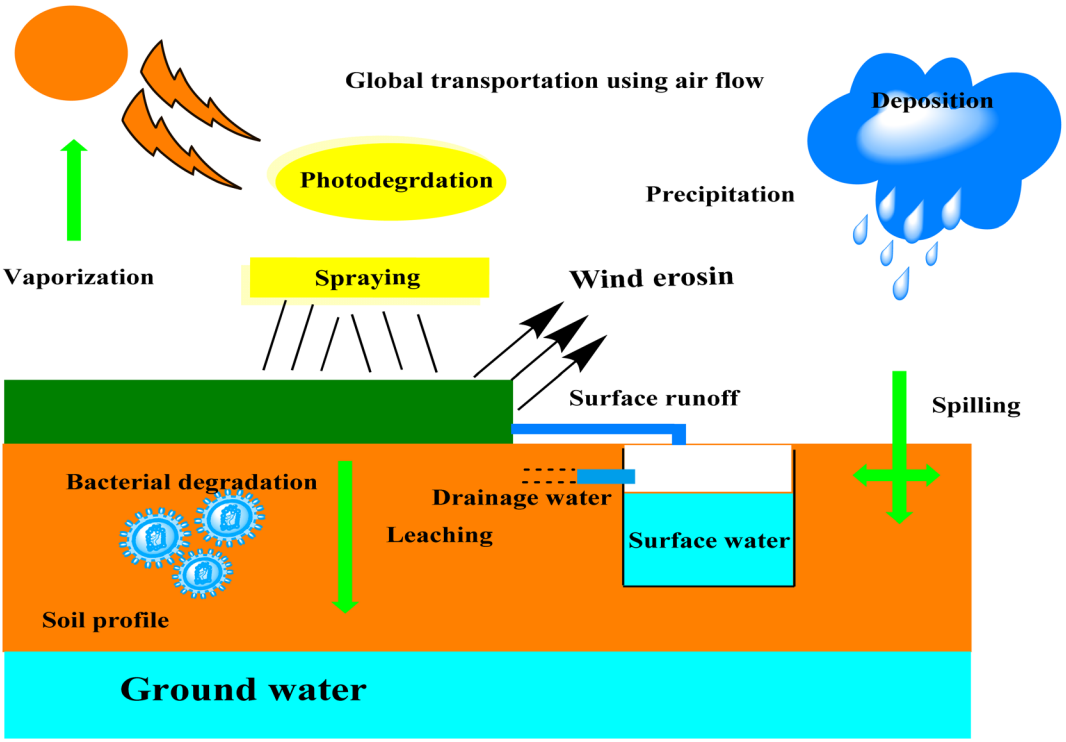

Fig. 1 Different stages of pesticide cycle that reach the ground and surface water.

Numerous beneficial bacteria can create surfactants.[15] On the other hand, more research approaches are needed to address environmental and procedural problems that need in-depth examination to broaden their scope. In recent years, bioremediation techniques, such as the use of microorganisms and metabolic enzymes to break down pesticides and change them into another form through sludge formation, have become less toxic.[16] But many defaulters nevertheless restrict their regular use in a hazardous environment and environmental restoration.[17]

Due to the existence of pesticide toxins and their impact on water quality and agricultural soils through their use, which may be damaging to all forms of life, the problem of pollution is a cause of concern for many developing and developed countries. Although a larger dose of a pesticide can injures humans more than the intended pest, humans can be killed in a variety of ways with very tiny quantities.[18]

Inhibiting sex hormones, impairing ovarian function, and damaging endocrine glands are all fatal impacts of pesticides.[19] Due to their heightened biological function and quick toxicity, pesticides are categorized as being extremely damaging, highly poisonous, and moderately dangerous. The compounds dimethoate, quinalphos, and dichloro-diphenyl-trichloroethane are all a little dangerous. Malathion is a very dangerous substance. Atrazine and other carbamates are unlikely to present a serious concern.[20] If toxic pesticides are misused, agricultural producers are particularly vulnerable to their negative effects.[21] Pesticides tend to settle as sediments, which can turn agricultural soils into a source of organochloride pollutants that can spread and volatilize and pose a risk to the surfaces of soil and water (Fig. 1).[22]

Pesticides can kill and injure soil-dwelling microorganisms, particularly when these substances are employed improperly or excessively, which causes chemical compounds to accumulate in the soil.[23] These chemicals may take several years to break down. Incomplete knowledge exists regarding how pesticides affect soil microorganisms. Numerous studies have shown that pesticides harm soil microorganisms and biochemical processes, whereas other studies have shown that microorganisms break down and absorb pesticide residues.[24]

Pesticides have different impacts on different types of soil microorganisms depending on their stability, concentration, and toxicity, as well as several environmental factors.[24] It is challenging to make definitive judgements about the relationship between pesticides and soil ecology due to the intricate interactions between the variables. The overall metabolic systems governing the nutrition cycle may become compromised by prolonged pesticide use.[24] Additionally, herbicides like triclopyr affect the soil's ability to convert ammonia to nitrite.[25] The ability to measure changes in the various settings of pesticide-treated soil would be greatly enhanced by improved operational allocations of bacterial taxonomic groups.[25] Water serves as a binder, making it simple for pesticides to penetrate moist soil.[26] The amount of pesticide that affects the soil varies according to soil humidity, temperature, sunshine, plants, and physiological features of the soil.[9]

3. Pesticides classifications

Based on their composition, level of toxicity, and intended use, pesticides are classified. The most common technique for classifying pesticides is based on the chemical properties of the

Table 1 Classification of organic pesticides based on their origin[2,9,10]

Origin	Source	Class	Example	Feature
Organic	Natural	Plants phytochemical	Essential oil, plant extracts, and leftover oilseed cakes	Low toxicity, limited persistent in environment, and complicated structures that prevent resistance in pests
	Synthetic	Pyrethroids	Phenthion, diazinon, cypermethrin, deltamethrin, cyfluthrin, and cypermethrin	Effect the sodium channel in insects resulting in paralysis of the organism, highly toxic to insects and fish but less to mammals, unstable upon the exposure of light, and commonly used in food
		Organophosphates	Aldrin, dieldrin, glyphosate, and chlorpyrifos	Cause paralysis resulting in death, and dominant for variety of pests
		Carbamates	Deltamethrin, cypermethrin, fenvalerate, permethrin, cyfluthrin, cyhalothrin, cypermethrin, and carbofuran	Effect the nerve of the pests resulting in poisoning and death, and low pollution caused upon degradation
		Organochlorine	Chlorothalonil and endrin aldehyde	Used for insects, long persistent in environment, and affect the nerve system causing paralysis and death of the pests

pesticide (Table 1) and the characteristics of the target (Table 2). Based on their chemical makeup, pesticides are classified as organochlorines, organophosphorus, carbamates, pyrethrins, and pyrethroids (Table 3). Most insecticides used nowadays are organic and include both synthetic and plant-specific pesticides.[27] Based on the structure, toxicity, and functional categories of pesticides; more groupings are created. Pesticides are used in several ways to prevent the spread of pests or manage their numbers. Some herbicides are used to prevent plant growth, while others have effective photosynthetic control.[28] Nearly all insecticides have the potential to significantly impact the ecosystem. They pose a serious risk to the ecosystem.[28] Fungi and their spores are killed or have their growth slowed by substances referred to as fungicides.[29] Fungicide misuse, storage, and release into moving water all present significant contamination risks.[30]

4. Overview of water cleanup methods

Organic dyes, insecticides, medicines, fertilizers, surfactants, and other chemicals can be found in a wide variety of products. Conversely, excessive use, environmental discharge or disposal, and inadequate treatment contaminate water sources and have detrimental effects on our ecosystem, including humans. As a result, it has proven difficult to eliminate organic pollutants from wastewater. There were numerous efforts made to eliminate or degrade organic pollutants from the water. Utilizing a range of physical, chemical, and biological methods, organic pollutants, and the breakdown products they produce are eliminated or reduced from the aquatic environment (Fig. 2). These techniques are used individually or in combination with others to detoxify contaminated wastewater. Adsorption, membrane filtration, biological degradation, photocatalytic degradation, nanofiltrations, oxidation, reverse osmosis, UV radiation, and other techniques are used to disinfect water.[31,32] The greatest techniques for eliminating pesticides, beta blockers, and medications have been discovered to be chemical oxidation processes such as ozonation (O_3), UV photolysis, and photo-Fenton processes.[33] Among other biological processes, membrane filtration remediation (MFR), activated sludge, and aeration methods were superior at removing endocrine distributing chemicals (EDCs) [*i.e.* endocrine-disrupting chemicals (EDCs) are compounds that interfere with the hormonal systems of organisms, potentially causing adverse developmental, reproductive, neurological, and immune effects].[34] With the activated sludge technique, surfactants, EDCs, and personal care products (PCPs) can be effectively eliminated.[35] Reviewing the importance of employing metal oxide nanocomposites in water remediation is the main goal of this article. The field of wastewater photocatalysis using photocatalyst nanocomposite is driven by ultraviolet (UV) and visible light. Using different kinds of organic waste, full studies showed that photocatalysis led to complete and efficient degradation and the creation of less harmful, eco-friendly products.[36] Toxic byproducts, however, may have been produced because of partial breakdown.[36] Adsorption and photocatalysis are economically scalable due to their reliance on abundant and inexpensive materials (*e.g.*, activated carbon, metal oxides). For instance, the use of sunlight in photocatalysis reduces energy costs, while adsorption processes benefit from renewable or waste-derived adsorbents like biochar.

Recent studies have highlighted the effectiveness of metal oxide nanostructures, particularly TiO_2–ZnO composites, in treating water contaminated with persistent organic pollutants.[37] Exposed to visible light, these nanostructures show significantly higher degradation rates than conventional methods, a critical advancement that could favor their use under ambient light conditions.[37] This research demonstrates how optimizing the structure and porosity of composites can accelerate degradation processes, reducing energy demands and enhancing water purification efficiency under natural conditions.[38]

Table 2 Classification of pesticides based on target[3,5,11]

Class	Example	Target pests	
Acaricides	Bifonazole	Mites	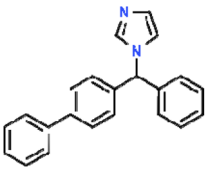
Avicides	Avitrol (4-amino pyridine)	Birds	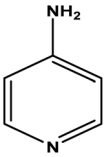
Fungicides	Azoxystrobin	Fungi	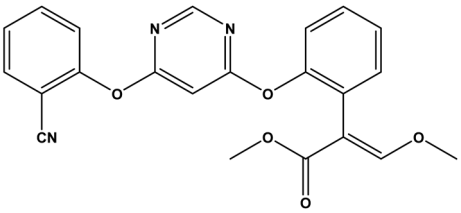
Herbicides	Atrazine	Weeds	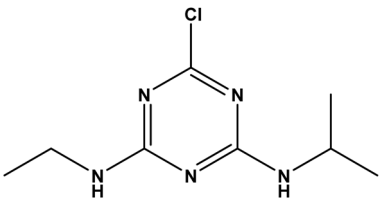
Insecticides	Aldicarb	Insects	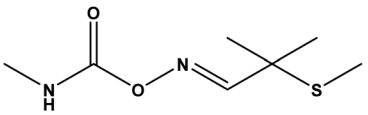
Larvicides	Methoprene	Larvae	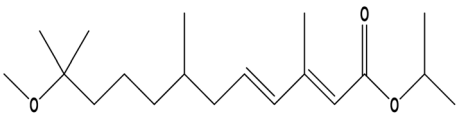
Molluscicides	Metaldehyde	Snail	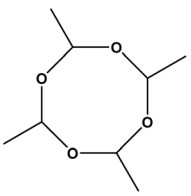
Nematicides	Aldicarb	Nematodes	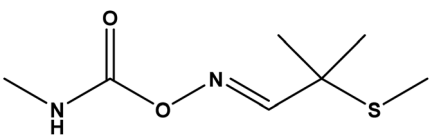
Ovicides	Benzoxazine	Egg – prevents hatching of egg in insects and mites	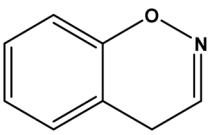

Table 2 (*Contd.*)

Class	Example	Target pests	
Piscicides	Rotenone	Fishes	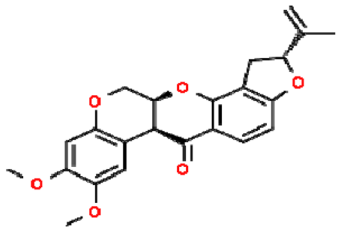
Repellents	Methiocarb	Insects	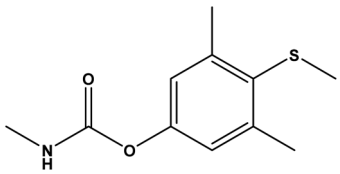
Rodenticides	Warfarin	Rodents	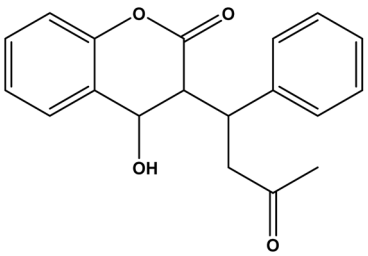
Termiticides	Fipronil	Kills termites	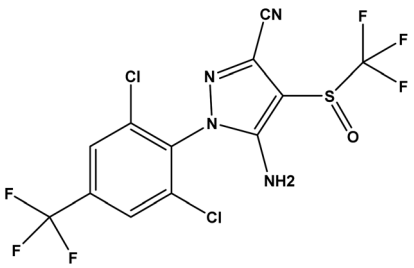

5. Metal oxides-based nanostructured materials

Metal oxide nanoparticles have been studied in a variety of applications, including energy storage, catalysis, electrochemistry, lubrication, sensors, coatings, environmental remediation, and others.[39,40] The surface properties, microstructural features, and high surface area of transition metal oxide nanoparticles make them suitable candidates for the adsorption process.[41] Adsorption is aided by the active sites and large surface area. When the size of materials is lowered from bulk to nano, the surface-to-volume ratio increases rapidly.[42] When it comes to removing organic pollutants from wastewater, nanoparticles have a better adsorption capability than their bulkier counterparts. Activated carbon derived from biomass, as well as novel forms of carbon such as graphene, carbon nanotubes, fibers, and others, displayed good organic pollutant adsorption capabilities in wastewater.[43] Metal oxide nanoparticles have lately shown significant promise as highly selective adsorbents for the quick and effective removal of organic pollutants from wastewater,[44] either as single materials or as composites. Transition metal oxides and their composites have excellent photocatalytic activity for destroying organic pollutants.[45] Wide band gap semiconductors with non-toxicity and water stability for photocatalytic oxidation/degradation of organic pollutants are made from metal oxide-based nanomaterials with well-controlled structural, crystalline, and surface characteristics. Recent advancements in metal oxide nanostructures research have significantly boosted their adsorption and photocatalytic capabilities. For instance, a 2023 study demonstrated that TiO_2 and ZnO nanoparticles, modified with rare-earth dopants, offer increased active sites, allowing for more intensive interactions with pollutants and thereby enhancing degradation efficiency in diverse settings.[46] Adjusting morphology and composition makes these metal oxides particularly promising for use under various environmental conditions.[1]

Table 3 Classification of pesticides based on their chemical makeup[14–16]

Category	Name	Chemical structure
Organophosphorous	Phenthion	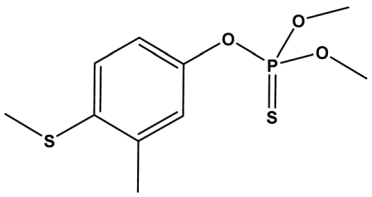
	Diazinon	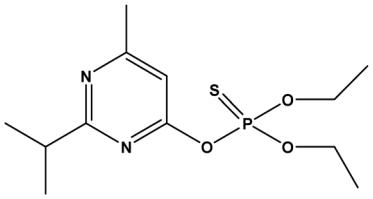
	Glyphosate	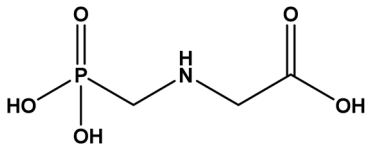
	Dichlorvos	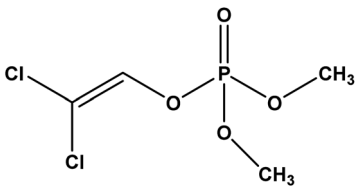
	Acephate	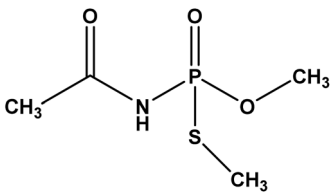
	Parathion	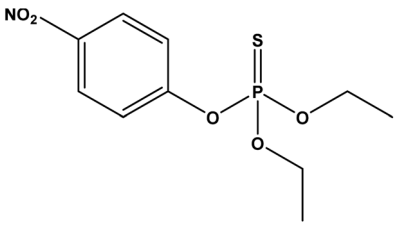
Organochlorine	Aldrin	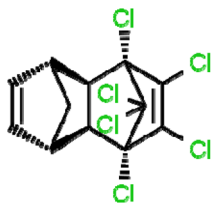
	Dieldrin	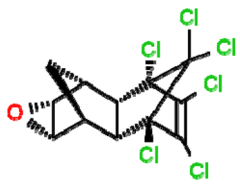
	Cypermethrin	

Table 3 (*Contd.*)

Category	Name	Chemical structure
Carbamates	Chlorpyrifos	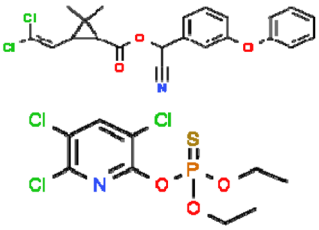
	Cyfluthrin	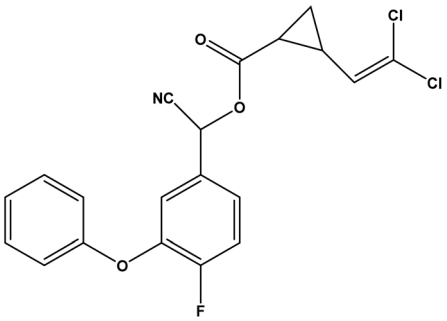
	Chlorothalonil	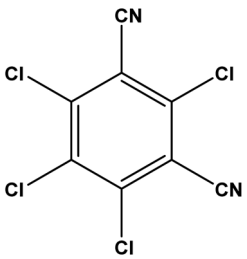
	Endrin	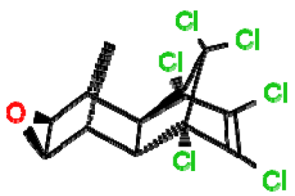
	Carbaryl	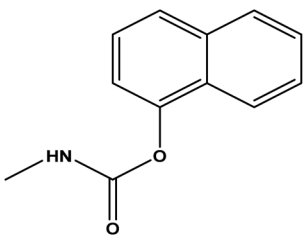
	Carbofuran	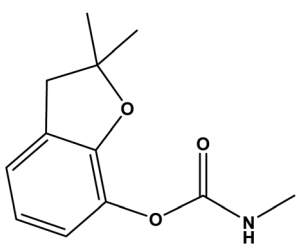
	Methomyl	

Table 3 (*Contd.*)

Category	Name	Chemical structure
		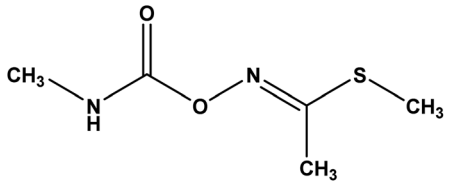
	Aldicarb	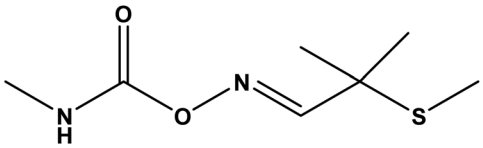
	Oxamyl	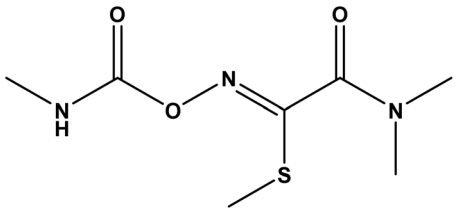
	Terbufos	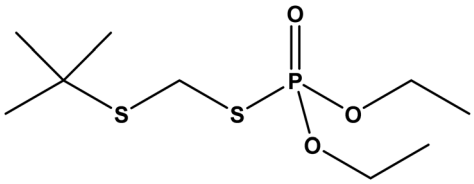
	Carbosulfan	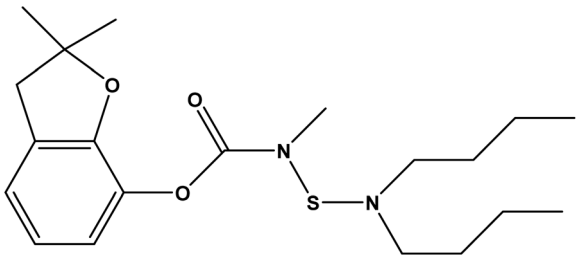
	Carbamic acid	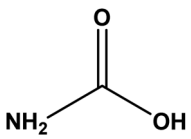

Photo-degradation has long been seen to be one of the most environmentally friendly ways to remove organic pollutants from water.[47] It has several advantages, including the use of renewable energy (solar energy) and the conversion of organic contaminants into non-toxic molecules and gases.[48] Metal oxide semiconductors only use a small fraction of the solar spectrum, specifically UV light (5% of the solar spectrum),[49] which is a major limitation of the photocatalytic process. This disadvantage can be solved through band gap engineering of metal oxide nanoparticles, which comprises chemical and structural changes, heteroatom doping, and nanocomposites.

The best photocatalysts absorb the visible spectrum efficiently, delay hole and electron pair recombination, and perform well as photocatalysts.[50] Metal oxide nanoparticles, such as iron oxides, Al_2O_3, TiO_2, CuO, ZnO, CeO_2, and others, have attracted interest as adsorbents and photocatalysts.[51,52] For enhancing performance efficiency and selectivity, porous materials-supported metal oxides, magnetic metal oxides, metal–metal oxides, graphene–metal oxides, and other metal oxide-based nanocomposites have all been explored.[53,54] The size, texture, and surface characteristics of these nanomaterials influence the adsorption events.[37,39,41,44] Various morphologies

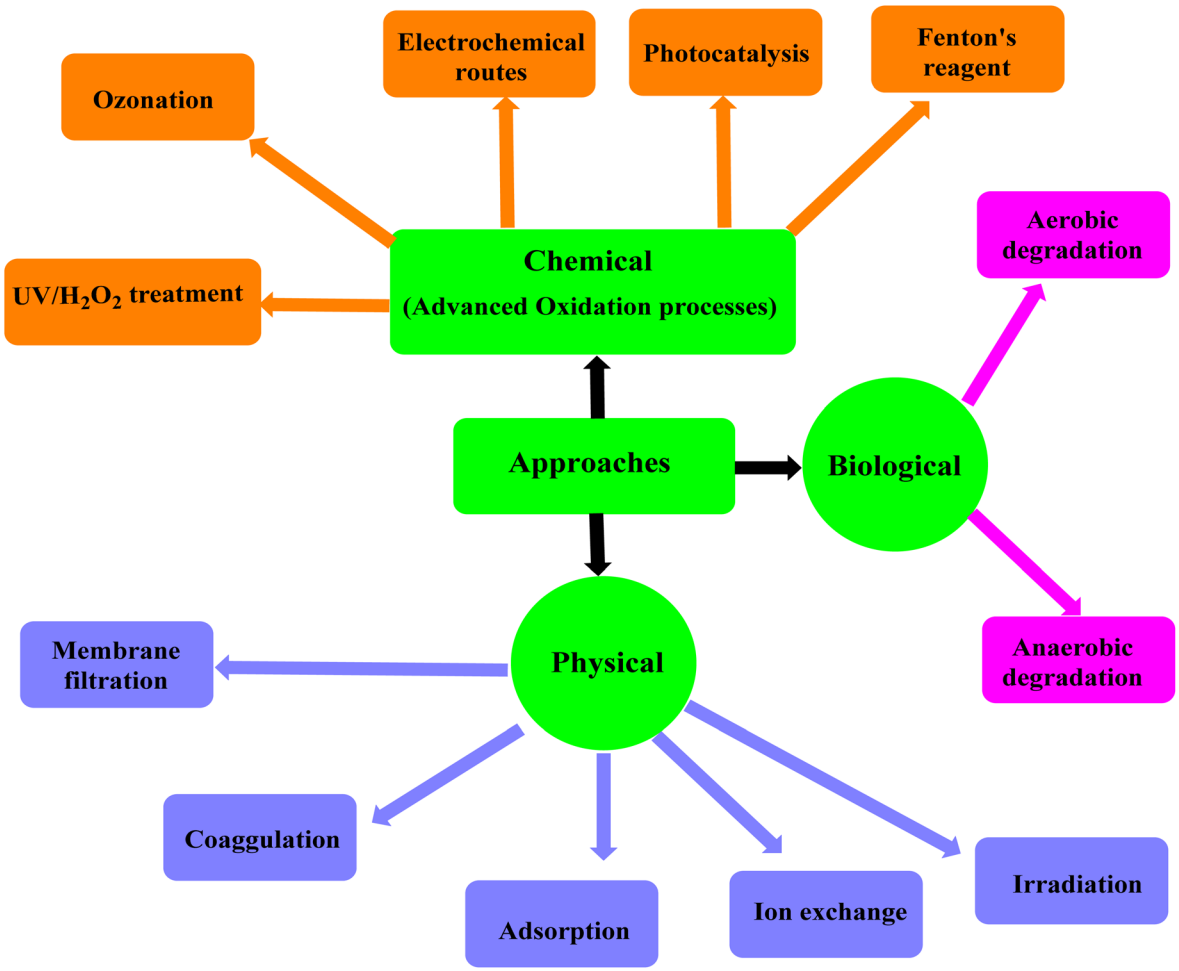

Fig. 2 Chemical, biological, and physical approaches to remove or degrade the organic pollutants in the wastewater.

of nanoparticles provide distinct crystal facets as active sites on the surface of materials for adsorption and photocatalytic applications. Bhatti *et al.*[55] examined the effect of ZnO nanoparticle shape on the photocatalytic degradation of methyl orange dye. This research examines the structural, crystalline, and surface properties of a variety of metal oxide nanoparticles and their nanocomposites for wastewater treatment *via* adsorption and photocatalytic destruction of organic pollutants.

Metal oxide nanostructures have been shown to be effective and flexible in cleaning up the environment, which shows how useful they could be. However, it is also important to think about how safe they are for the environment and how easily they can be recycled for long-term use. Metal oxide nanoparticles, when released into the environment, may present significant risks to aquatic organisms and soil ecosystems because of their elevated reactivity and durability. To address these risks, approaches like surface functionalization and the addition of biocompatible coatings have been investigated, leading to a decrease in toxicity and environmental impact. Additionally, the ability to recycle these materials presents a considerable benefit. For example, magnetic iron oxide nanoparticles can be efficiently retrieved from treated water through the application of external magnetic fields, allowing for their reuse across several cycles with negligible efficiency loss. Research indicates that doped metal oxides or composite structures enhance photocatalytic performance while also improving material stability, thereby supporting their reusability. Highlighting these features promotes a comprehensive understanding of the advantages and obstacles associated with the large-scale implementation of metal oxide nanostructures for water treatment.

6. Photocatalytic degradation of pesticides using metal oxide nanoparticles

The photocatalytic activity of metal oxide nanoparticles is attributed to their semiconducting properties, which enable efficient absorption of light and generation of electron–hole pairs. These properties are critical in driving the redox reactions required for environmental cleanup. These nano particles have an effective and selective photocatalytic activity due to their superconducting nature, which has been exploited in various

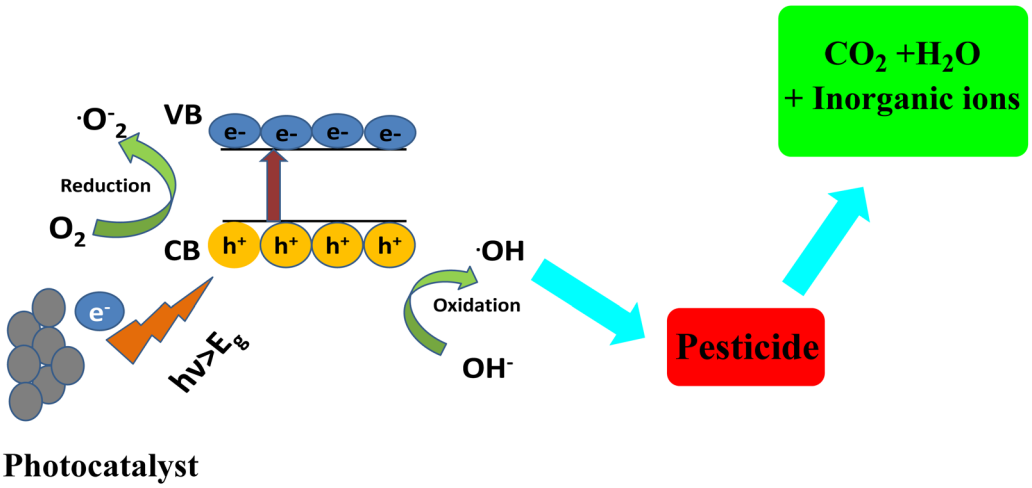

Fig. 3 Photocatalytic degradation of pesticides using photocatalysts.

research projects for pesticide sensing and remediation.[56] Metal oxide nano particles such as silica (SiO_2), zinc oxide (ZnO), titanium oxide (TiO_2), and iron oxide (Fe_2O_3 or Fe_3O_4) have been utilized to detect, degrade, and remove pollutants from various sources.[57,58] The photocatalyst produces pairs of electrons and holes when it absorbs ultraviolet (UV) radiation from sunshine or artificially irradiated light sources (such as fluorescent lamps). When exposed to light radiation, the electron in the semiconductor catalyst's valence band becomes excited. This excited electron's extra energy aids in its transition to the catalyst's conduction band, where it leaves a positive hole behind. The result is the creation of the negative electron (e^-) and positive hole (h^+) pair. The term "photoexcitation" refers to this stage of the semiconductor catalyst. The "bandgap" energy is the difference in energy between the conduction band and the valence band. Fig. 3 illustrates the photocatalytic degradation of pesticides using the photo catalysts.

A recent analysis of the photocatalytic performance of metal oxide composites revealed that incorporating metals like silver and copper into structures such as CuO and Fe_2O_3 extends the lifetime of electron–hole pairs.[59,60] This feature is crucial because it supports more efficient pesticide degradation under visible light exposure. The study showcased significant improvements in breaking down compounds like diazinon and

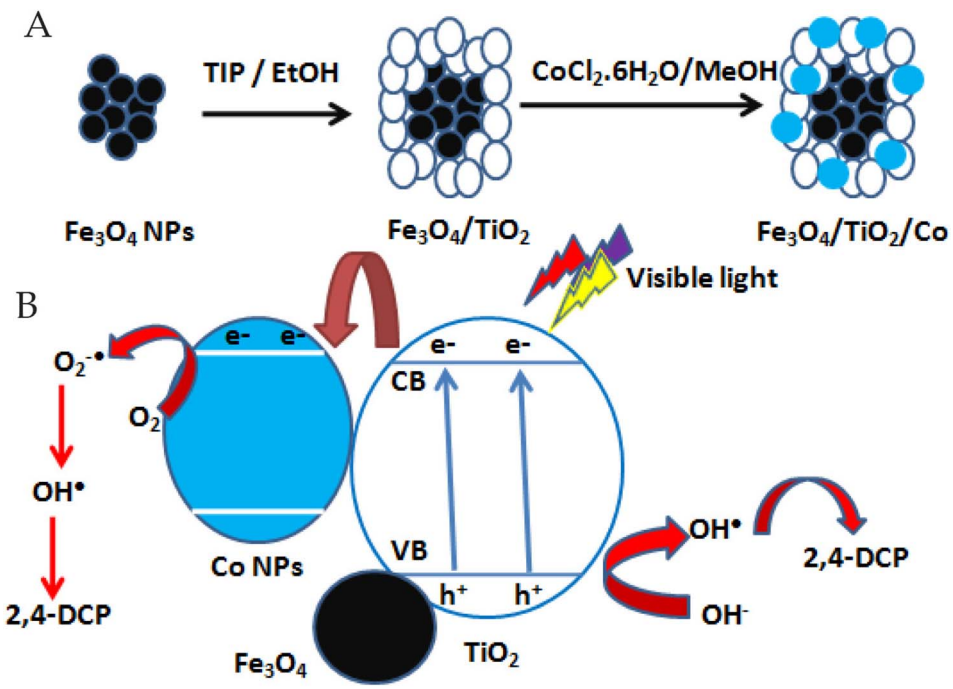

Fig. 4 2,4-Dichlorophenol degradation *via* photo-reactive TiO_2 nanoparticles, (A) preparation of the photocatalyst; (B) the degredation pathway of 2,4-DCP.[69]

chlorpyrifos, underscoring how these structural modifications contribute to practical, sustainable solutions for environmental cleanup.[61]

6.1 Titanium oxide nanoparticles

TiO_2 has attracted the greatest attention from researchers because its unique characteristics, such as excellent photocatalytic activity across a wide range of pH and temperatures, cost-effectiveness, chemical stability, and non-toxicity.[62] TiO_2 nanoparticles' high surface area for photocatalysis has allowed them to be used at the nanoscale to remediate a variety of pollutants from the environment.[63] With a bandgap of 3.2 eV, TiO_2's photocatalytic activity is limited to the UV range.[64] On the other hand, dye sensitization and surface modification of TiO_2 nanoparticles with other metal oxides, non-metals, or carbon-based compounds help to extend the photocatalytic activity of nanoparticles to the visible range.[65] TiO_2 nanoparticles were used as a photocatalyst to degrade chlorpyrifos in water.[66] The photocatalyst was subjected to UV rays to produce pesticide degradation, and it was discovered that as the illumination period was increased, the photo-degradation efficiency rose.[66] To increase their photocatalytic activity against several pesticides, TiO_2 nano particles have been treated with various metal ions. The fungicide carbendazim, for example, was destroyed by TiO_2 nanoparticles doped with Fe and Si ions. The doping improved the photocatalytic activity of nanoparticles, resulting in a 98% breakdown of the fungicide in the presence of sunshine.[67] Also, during the advanced oxidation process (AOP), cobalt (Co)-doped TiO_2 nanoparticles were used as a photocatalyst to decompose 2,4-dichlorophenol (DCP).[68,69] DCP was degraded by TiO_2 nanoparticles in visible light because of the doping. They got 30.42% and 57.84% degradation of 2,4-DCP after 180 min irradiation in the presence of pure TiO_2 and ternary nanocomposite containing 2.92 wt% cobalt (Fe_3O_4/TiO_2 nanocomposite (2.92)), respectively. The higher photocatalytic performance of Fe_3O_4/TiO_2 nanocomposite samples was attributed to the high specific surface areas and the enhancing visible light absorption by cobalt.[69] The pathway of 2,4-dichlorophenol degradation was illustrated in Fig. 4.

Recent studies have confirmed the enhanced photocatalytic properties of TiO_2 doped with metals such as silver and iron, especially for degrading persistent organic pollutants like carbendazim,[70] tebuconazole (TEB) and 2,4-dichlorophenoxyacetic acid (2,4-D) pesticides.[71] Doping with silver, for example, has been shown to increase TiO_2's reactivity under visible light, which reduces the energy needed for activation compared to pure TiO_2.[71] This is particularly significant because it allows for photocatalytic processes to occur under ambient light, making them more feasible for practical applications, including large-scale pollutant degradation.

Molecularly imprinted TiO_2 photocatalysts were added so that the sol–gel method could be used to selectively remove certain pesticides from water.[72] Using TiO_2 imprinted with the appropriate pesticide target, a notable improvement in photocatalytic performance was confirmed.[73] The comparison with the breakdown of pesticides that were not utilized as a template allowed for the verification of the photodegradation process's selectivity, as seen in Fig. 5.

It was looked into how adding foreign materials, like rare earth, transition, and noble metals, to TiO_2 could increase the bathochromic shift, lower the band gap energy, and make photo-generated electron/hole pairs last longer.[73] Many surface parameters, including area, charge, and acidity, are altered by doping TiO_2, making the resulting material more photocatalytically active when exposed to visible light.[73] To make the rare earth lanthanide ions (La^{3+}, Nd^{3+}, Sm^{3+}, Eu^{3+}, Gd^{3+}, and Yb^{3+})-doped TiO_2 nanoparticles, the sol–gel method was used.[74] These were then tested as photocatalysts for dye remediation.[75] The shape, band gap, and particle size of TiO_2 changed when lanthanides were added to it. This made the photocatalytic performance much better than pure TiO_2. The lowest bandgap,

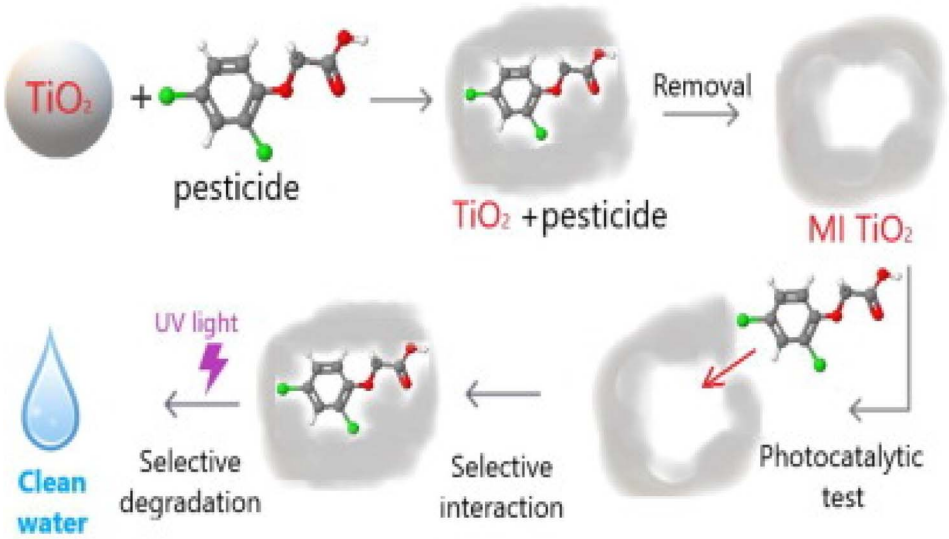

Fig. 5 Preferential removal of pesticides from water by molecular imprinting on TiO_2 photocatalysts.[73]

Table 4 TiO_2 nanomaterials and their composites as photo-catalysts for pesticides degradation

Photo catalyst	Targeted pesticide	Light source	Reaction time	Degradation efficiency (%)	Ref.
TiO_2/Bi_2WO_6 nanostructured hetero-junctions	4-Chlorophenol	Visible	7.5 h	90.5	77
TiO_2/Fe_2O_3 nanocomposite	Diazinon	Visible	45 min	95.1	78
Zn^{2+}-doped TiO_2 nanoparticles	Malathion	UV	81 min	98	79
In and S co-doped TiO_2@rGO	Atrazine	Visible	20 min	99.5	80
SBA-15 loaded with 8–42% TiO_2	Dimethoate	Simulated solar	7 h	100	81

tiniest particle size with the greatest surface area, and pore volume of the lanthanides-doped TiO_2 explained why the Gd^{3+} doping exhibited the highest photocatalytic performance.[76] The nanomaterials based on titanium dioxide and their composites for the photocatalytic destruction of some pesticides are compiled in Table 4.

6.2 Zinc oxide nanoparticles

Because of their distinctive size and high density at the surface's edge points, ZnO nanoparticles have unique chemical and physical properties.[82] These nanoparticles are also known to have high photocatalytic action, which is important for pollutant degradation. The band gap of zinc oxide is 3.25 eV, the same as that of TiO_2 (3–3.25 eV).[83] It is often used in photocatalytic degradation processes to break down organic pollutants in wastewater. Photocatalytic process of zinc oxide and titanium dioxide are very similar. Because of this, ZnO nanoparticles have also been suggested as an alternative to titanium dioxide for cleaning water. ZnO performed better as a photocatalyst when compared to other semiconductors under investigation; this was due to ZnO's ability to absorb a greater portion of the solar spectrum. It was also looked at how to employ ZnO nanoparticles' fluorescence emission properties for the photocatalytic destruction of various organic contaminants.[84] Because ZnO's photocatalytic activity is extremely pH-sensitive and photo-corrosion is facilitated by strongly acidic conditions (pH < 4), its potential is limited in lower pH media.[85] For the purpose of degrading the pesticide diazinon, the photocatalytic activity of nanocrystalline ZnO and commercially available ZnO was evaluated.[86] Nanocrystalline ZnO was found to have better photocatalytic activity than commercial ZnO because of two things: (a) its small crystalline size, which increased the active surface area of the photocatalytic reaction; and (b) the amount of dispersed ZnO particles per volume in the solution, which increased photon absorption for better performance.[86] Using natural sunlight to accelerate the photo-degradation of a variety of pesticides in the leaching water, the $ZnO/Na_2S_2O_8$ nanocomposite was employed as an antioxidant and photosensitizer.[87] Adding $Na_2S_2O_8$ to ZnO made it more effective at oxidation, which cut down on the time needed for photocatalytic pesticide breakdown.[87]

The ZnO–SnO_2 nanorods are a potential material for water purification applications due to its great recyclability and facile remembrance of wasted photocatalysts.[88] Recent studies highlight the potential of ZnO-based photocatalysts for environmental cleanup, particularly when doped with transition metals or combined with nanocomposites.[89] For instance, ZnO doped with $Na_2S_2O_8$ shows enhanced photocatalytic degradation of pesticides like diazinon, especially under natural sunlight in alkaline media, where its stability is higher.[90] In such conditions, the degradation rate can increase by up to 85%, demonstrating a significant improvement over pure ZnO. Similarly,

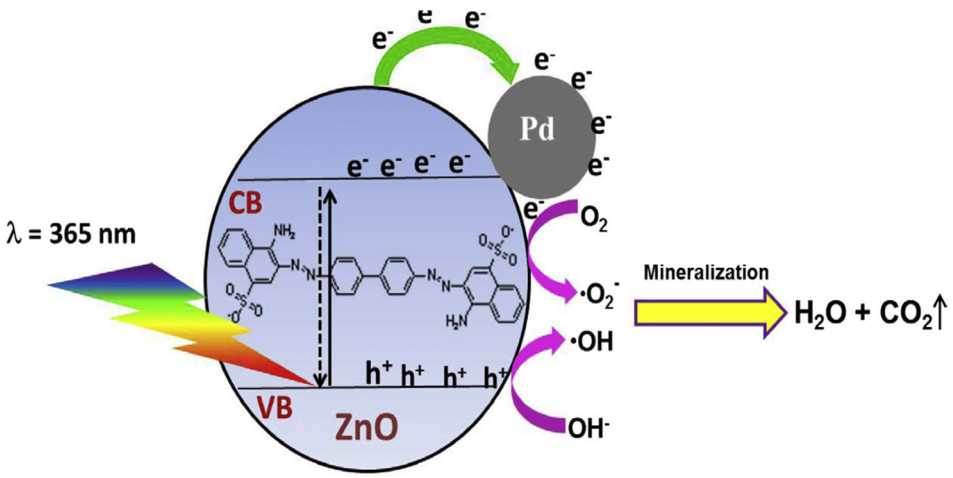

Fig. 6 Schematic diagram illustrating the plausible photocatalytic mechanism for degradation of Congo red dye using the Pd-doped ZnO photocatalyst.[93] Reprinted with permission from Copyright 2016 Elsevier.

Table 5 A summary of the ZnO and their composites that can break down pesticides through photocatalysis

Organic pollutant	ZnO-based nanomaterials	Light source	Degradation efficiency (%)	Ref.
Phenylhydrazine (PHZ)	ZnO supported onto clinoptilolite	UV-vis	69	95
2-Phenylphenol (OPP)	ZnO/TiO_2	UV-vis	100	96
Diazinon	Nanocrystalline ZnO	UV-C	80	97
Azoxystrobin	$ZnO/Na_2S_2O_8$	Sunlight	99	98
Hexaconazole			98	
Kresoximmethyl			100	
Pirimicarb			95	
Propyzamide			97	
Pyrimethanil			96	

doping ZnO with manganese (Mn) improves photocatalytic efficiency by creating surface defects that promote electron–hole separation (ZnO's photocatalytic performance can be significantly improved by increasing its surface area, which reduces defects related to volume and enhances its ability to absorb more light. Studies have shown that doping ZnO with elements like manganese (Mn) or silver (Ag) can further enhance its photocatalytic activity by reducing electron–hole recombination.[91,92] This, in turn, increases the material's efficiency in degrading organic pollutants, making ZnO a more effective photocatalyst under visible light conditions), further boosting its ability to break down organic contaminants. This synergy between ZnO and its dopants or additives promises improved photocatalytic performance, making ZnO an effective solution for large-scale environmental remediation.[86]

Different methods were used to make the Pd-doped ZnO photocatalysts, and their ability to break down Congo red dye varied a lot. These methods included microwave irradiation, borohydride reduction, and photoreduction. Because of the higher doping and good dispersibility of Pd on ZnO, which improved the photodegradation efficiency of organic dye by reducing the recombination of photogenerated electron–hole pairs, the Pd-doped ZnO photocatalyst prepared by the borohydride reduction method exhibited superior photocatalytic activity (Fig. 6).[93] Er-doped ZnO nanoparticles with varying Er concentrations increased photocatalytic activity when exposed to visible light. Adding different amounts of Er to ZnO nanoparticles changed their structure, morphology, band gap, half-life of the photogenerated electron–hole pair, and their ability to absorb visible light. This doped ZnO was used to degrade Red-31 dye.[94] A summary of the ZnO and their composites that can break down pesticides through photocatalysis is shown in Table 5.

6.3 Iron oxide nanoparticles

The n-type semiconductor iron oxide is widely accessible and could break down organic contaminants through photocatalysis.[99] Moreover, the inherent magnetic effect facilitates the material's easy recovery from the aqueous medium, making it a viable photocatalytic material.[99] Fe_2O_3 semiconductors were found to be activated by visible light because of their low band gap energy (2.2 eV).[100] Recent work has shown that gold-doped iron oxide (Fe_2O_3) nanoparticles enhance photocatalytic efficiency for degrading organic dyes. For example, in the degradation of Disperse Blue 79, photocatalytic efficiency improved by 35% when Fe_2O_3 was doped with 1% gold.[101] However, challenges remain, such as the rapid recombination of electron–hole pairs and the need for longer reaction times. These limitations must be addressed to optimize large-scale applications in wastewater treatment and pollutant degradation.

The degrading properties of Fe^{3+} oxides under photocatalysis, including α-Fe_2O_3, γ-Fe_2O_3, α-FeOOH, β-FeOOH, and γ-FeOOH, were examined with the purpose of destroying harmful organic pollutants within the visible spectrum of the sun.[102] Low-band-gap iron oxide nanoparticles can be applied to photocatalytic reactions that occur within the visible portion of the solar spectrum.[103] The quick recombination of the photogenerated electron–hole pair, however, poses a significant obstacle to their viability in photocatalytic uses (Fig. 7).[104]

The recombination events of charge carriers are tuned, and the photocatalytic activity is enhanced through the doping of iron oxide nanostructures with varying metals or metal oxides and the construction of iron oxide-based nanocomposites. When exposed to sunlight, Au–Fe_2O_3 aerogels with different amounts of Au were tested as photocatalysts for breaking down the dye Disperse Blue 79. The metallic gold made Fe_2O_3 more photocatalytic by allowing more photogenerated electrons to build up and delaying the recombination process. So, oxidative species backed by photogenerated charge carriers attacked the azo dye molecules that had stuck to the surface.[105] Iron oxide-based photocatalysts are promising options for the removal of organic pollutants from wastewater due to their high recycling value, inexpensive cost, and practicality. Controlling the size, shape, and surface properties of iron oxide NPs, which play a key role in the detection and destruction of a variety of agrochemicals, can improve the efficacy and specificity of pesticide remediation operations.

6.4 Silica nanoparticles

Silica-based materials have received considerable interest in pesticide degradation owing to their elevated surface area, adjustable porosity, and chemical stability.[106] These characteristics render silica a superior support material for catalytic and photocatalytic applications. Using advanced oxidation processes, different active species, such as titanium dioxide or

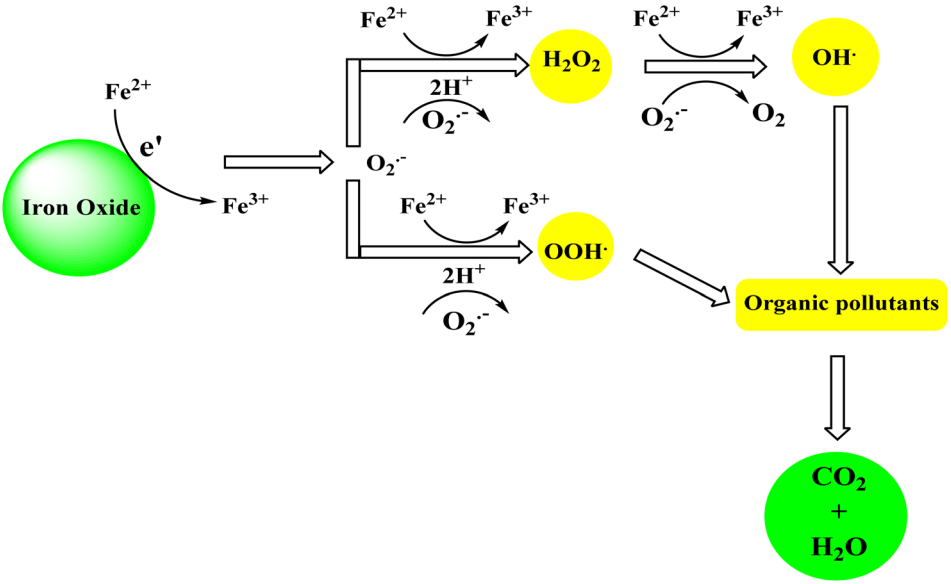

Fig. 7 Photo-degradation pathways for organic pollutants using iron oxide.

transition metal oxides, can be added to silica to make pesticides break down more quickly. Additionally, the biocompatibility and environmental safety of silica make it a favorable choice for sustainable applications. Nonetheless, the application of silica in pesticide degradation presents certain limitations.[107] The synthesis of functionalized silica materials is complex and costly, which may restrict large-scale applications. Silica by itself usually doesn't have much catalytic activity, so it needs to be changed with active agents. If this isn't done properly, it can cause problems for the environment. The regeneration and reuse of silica-based catalysts present challenges, as fouling or activity loss over multiple cycles may diminish their economic viability. Ongoing advancements in material science are enhancing silica's effectiveness in pesticide degradation, despite existing limitations. The integration of nano-engineered features has demonstrated potential in addressing several of these challenges.[108] Recent research highlights the significant role of silica nanoparticles (SiO_2 NPs) in environmental remediation, particularly in the extraction and degradation of pesticides.[109] The unique properties of SiO_2 NPs, such as their high surface area and tunable porosity (microporous, mesoporous, or hollow), make them ideal candidates for sorbent materials in solid-phase extraction (SPE) techniques. For instance, SiO_2 NPs functionalized with *N*-methylimidazole have demonstrated a remarkable ability to adsorb polar pesticides such as sulfonylurea from aqueous samples, with extraction efficiencies reaching up to 85%.[110] Similarly, when co-functionalized with polar cyanopropyltriethoxysilane (CNPrTEOS) and non-polar methyltrimethoxysilane (MTMOS), SiO_2 NPs have been successfully used to extract a variety of organophosphate pesticides, including diazinon, methidathion, and chlorpyrifos, from water samples, achieving extraction efficiencies exceeding 90%.[111] These pesticides were then quantified using high-performance liquid chromatography (HPLC) and gas chromatography-mass spectrometry (GC-MS) for precise analysis. Furthermore, silica molecular imprinted polymers (MIPs) made from SiO_2 NPs have been shown to enhance pesticide extraction, as demonstrated by significant increases in fluorescence or chemiluminescence intensity in response to pesticide concentrations.[112,113]

6.5 Cerium oxide

The potential uses of cerium dioxide (ceria) include fuel cell reformer, hydrocarbon fuel oxidation, and photocatalytic degradation of organic pollutants due to its non-toxicity, high thermal stability, specific chemical reactivity, and rigidity.[114,115] In addition to its exceptional catalytic capabilities, the ceria displays a broad band gap of 3.1 eV.[116] Several organophosphate pesticides have been photodegraded using it.[117,118] The temperature at which ceria is calcined has a significant impact on its photocatalytic capability. Organophosphate pesticides effectively adsorb on the surface of ceria by electrostatic contact with the hydroxyl functions of ceria nanoparticles because of their positive charge on phosphorus. The ceria nanoparticles calcined at a lower temperature effectively adsorb organophosphate insecticides, which photo-catalyzed to break them down.[119] It was shown that CeO_2–Fe_2O_3 composites were magnetically separable and could break down organophosphate insecticides quickly.[120] The CeO_2–Fe_2O_3 composite that was calcined at a temperature of 300–400 °C demonstrated the maximum degrading efficiency and kept its good magnetic characteristics, enabling simple separation. The CeO_2–Fe_2O_3 site was calcined at a temperature greater than 500 °C, which greatly reduced its surface area, active surface sites, and pore volume while concurrently increasing its crystallinity. At high calcination temperatures, these modifications decreased the photocatalytic activity of the CeO_2–Fe_2O_3 composite. When compared to commercially available CeO_2 nanoparticles, one-dimensional CeO_2 nanotubes (CeO_2-NT) with a hollow interior

demonstrated improved photocatalytic degradation of phenols.[121] Researchers found that the CeO_2 nanotubes' higher photocatalytic activity compared to the nanoparticles was since the photocatalytic behavior of ceria changes depending on its shape. It was shown that the CuO–CeO_2 catalyst could degrade methyl orange dye more effectively in the microwave, both with and without H_2O_2.[122] The process of organic pollutants photodegradation is accelerated by the hydroxyl radicals generated by H_2O_2. Rhodamine B dye was degraded by CeO_2–Y_2O_3 binary metal oxide nanostructures with a changeable molar ratio under UV-visible light, and the degradation efficiency was 98%.[123] The photocatalytic degradation of the CeO_2–Y_2O_3 nanocomposites was much better than that of the CeO_2 and Y_2O_3 components alone. Increased oxygen vacancies and a large active surface area were credited with the improved photocatalytic activity. The higher pH and H_2O_2 speeds up the photodegradation reactions by removing electrons from the conduction band and making more hydroxyl radicals.[123]

6.6 Copper oxides

With band gap energy of about 1.4 eV, copper oxides are cheap, widely accessible and environmentally benign p-type semiconductor materials.[124] CuO's tiny band gap makes it possible to absorb visible light, which is necessary for photocatalytic activation. There are two main types of copper oxide: CuO and Cu_2O. CuO has been discovered to have better photocatalytic activity than Cu_2O. The narrow bandgap energy, which promotes recombination of these pairs, hinders the photogenerated electron–hole pairs' potential for photocatalytic applications. Copper oxide nanoparticles have recently been functionalized or doped with different metal oxides (like TiO_2, ZnO, SiO_2, *etc.*), MoS_2, ionic liquids, reduced graphene oxide, and other things to make them better photocatalytic.[125] These modifications have changed the electronic structure, light absorption characteristics, and charge transport characteristics.[126]

The hierarchical 3D metal oxide–CuO nanostructures containing ZnO and Fe_3O_4 improved the photocatalytic properties for the breakdown of Congo red dye under solar light.[127] This might be because the n-type (ZnO/Fe_3O_4) and p-type (CuO) semiconductors have better charge separation at the p–n junction, which is where the two types of semiconductors meet (Fig. 8).[127] The band gap of pure CuO nanowires was changed by making hetero-architectural composites of Fe_3O_4–CuO (1.7 eV) and ZnO–CuO (1.5 eV), which have lower band gap energies than pure Fe_3O_4 (2.19 eV) and ZnO (3.34 eV), respectively.[128]

Doping ZnO with CuO leads to stoichiometric deficiencies and structural flaws in the nanomaterial. These flaws change the band gap energy and make the CuO–ZnO nanocomposite more photocatalytic. Additionally, the presence of exogenous electron acceptors—specifically, H_2O_2, peroxomonosulfate, and

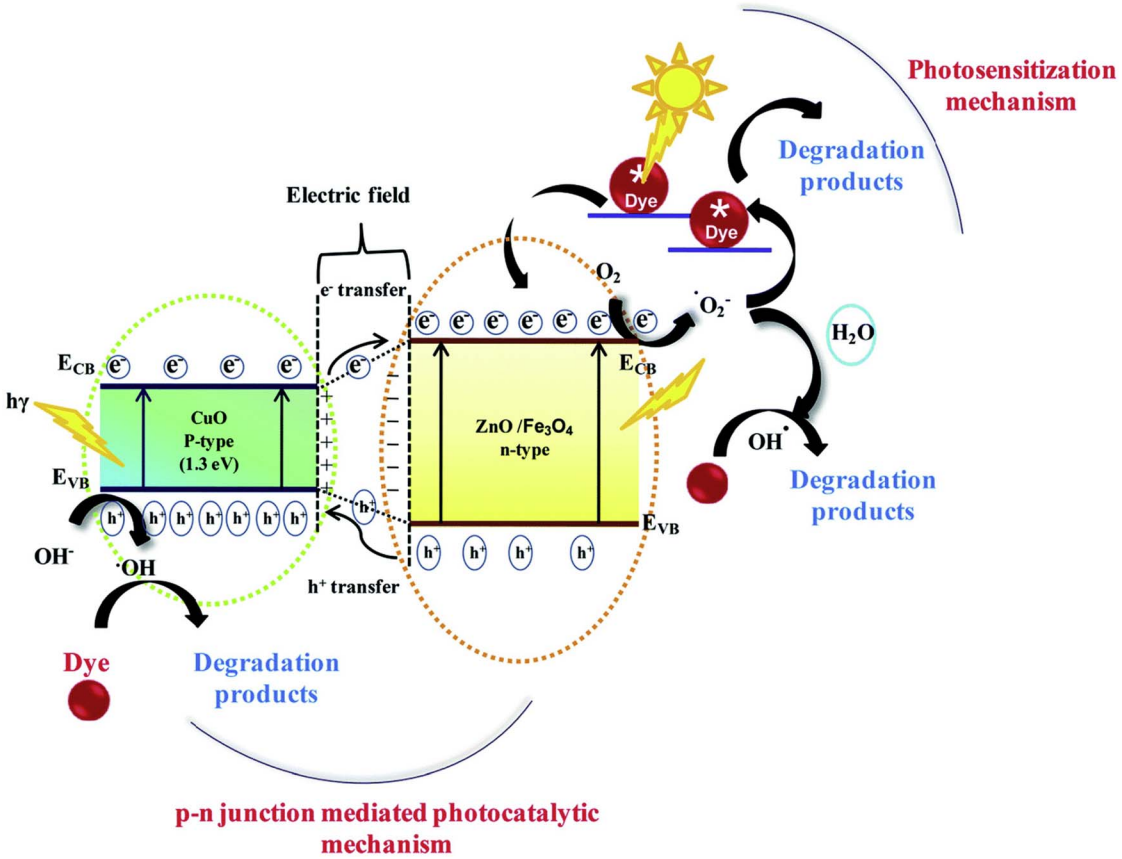

Fig. 8 Photocatalytic degradation pathway under the solar light irradiation using the p–n heterojunctions (ZnO–CuO or Fe_3O_4–CuO).[127] Copyright 2016 Elsevier.

peroxodisulfate—improved the photocatalytic degradation of textile dyes.[129] When exposed to visible light, the p–n junction-type semiconductor CuO–TiO_2 displayed good photocatalytic activity and broke down the azo dyes on the CuO–TiO_2–zeolite. Under visible light, CuOTiO_2–zeolite breaks down 90% of the methylene blue dye in 60 minutes, while zeolite, TiO_2–zeolite, and CuO–zeolite could remove 79.1%, 84.1%, and 85.2% of the dye, respectively, under the same circumstances. The photocatalytic activity under visible light exposure was boosted by bandgap engineering, active surface area-driven suppression of charge carrier recombination, and improved interfacial charge transfer.

6.7 Other metal oxides

Different metal oxides and their composites have also been able to photocatalytically degrade a variety of organic contaminants. The large band gap (3.6 eV) of the n-type semiconductor SnO_2 favors many photocatalytic processes.[130] Functionalizing SnO_2 with MgO prevented the recombination of photogenerated electrons and holes, enhancing the SnO_2–MgO nanocomposite's photocatalytic abilities. SnO_2–MgO nanocomposites have demonstrated the ability to photocatalytically degrade textile colorant compounds.[131]

It was shown that the hetero-structure of Fe_2O_3–WO_3, WO_3–TiO_2, and MoO_3–TiO_2 nanocomposites significantly improved the photocatalytic degradation.[132,133] The photocatalytic properties were improved by the n^+–n heterojunction of the rhombohedral α-Fe_2O_3 nanoparticles that were spread out evenly on the surface of the monoclinic WO_3 structures. The potential energy difference between Fe_2O_3 and WO_3 facilitates the separation of photogenerated charge carriers, which in turn enhances the photocatalytic destruction of organic contaminants (Fig. 9).[132] The p–n heterojunction structure of the Co_3O_4/$BiVO_4$ combination made it last a long time and destroy organic pollutants effectively through photocatalysis.[134] A decrease in the recombination rate of photogenerated charge carriers, according to photoluminescence research,[134] is what led to the increased photocatalytic activity.

Bi_2O_3 is a non-toxic p-type semiconductor with a band gap of 2.8 eV and a greater valence hole oxidation power.[135] It has gotten more attention because it breaks down different dyes. The pharmaceutical component acetaminophen (APAP) has been photodegraded using highly crystalline monodisperse β-Bi_2O_3 nanospheres.[136] A direct-hole oxidation method was suggested to break down APAP. The oxidation process produced comparatively fewer intermediates, which were linked to the high oxidation power of β-Bi_2O_3 nanospheres that had high mineralization efficiency. However, because of the quick recombination of electron–hole pairs produced by visible light, pure Bi_2O_3 exhibits limited photocatalytic efficiency. Adding transition metals or their oxides to Bi_2O_3 made it much better at breaking down organic pollutants through photocatalysis.[136] Matsumura *et al.* studied 2% Ce- and 1.5% Nd-doped Bi_2O_3 nanorods to see how they would break down organic dyes like Acid Yellow 29, Coomassie Brilliant Blue G250, and Acid Green 25.[137] They made it clear that the dopants can easily grab the photogenerated electrons from Bi_2O_3's conduction band. This slows down the recombination process and increases the photocatalytic activity of the nanomaterials.

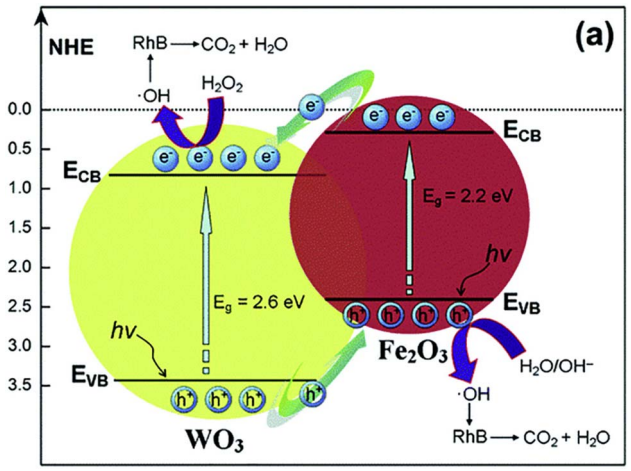

Fig. 9 Mechanism pathway of light-induced charge separation in the Fe_2O_3–WO_3 nanocomposite and photo-degradation of Rhodamine B.[132] Copyright 2014 Royal Society of Chemistry.

7. Pesticides adsorption using metal oxide nanoparticles

Adsorption is the physicochemical surface interaction between the adsorbate and the adsorbent.[138] Temperature, adsorbent–adsorbate interaction forces, medium pH, the presence of foreign components, concentration, and other parameters all affect the adsorption process.[139] Adsorbents should have a large surface area, adequate textural and surface characteristics, and sufficient mechanical stability to remove pesticides from wastewater quickly and efficiently.[140] Organic contaminants in wastewater act as adsorbates, slowly absorbing on adsorbent surfaces until an equilibrium between adsorbent and adsorbate is achieved.[141] Adsorption isotherms of many forms have been created to better understand the adsorption mechanism. Adsorption can be classified as chemisorption or physisorption depending on how they interact with the adsorbates.[141]

In physisorption, a physical interaction through which adsorbable molecule (the adsorptive) is adsorbed onto (surface physisorption) or into (intercalation) the metal oxide and their composites (adsorbent), through van der Waals forces, hydrogen bonding, or dipole–dipole attraction.[141] It falls into three general categories. The most well-known is pure physical adsorption, which is represented as full adsorbate recovery either with an increase in temperature or a drop in the concentration of the surrounding medium. It is a low-temperature phenomenon since the interaction forces get less as the temperature rises.[142] The second category, active adsorption, is characterized by complex formation leading to a partial recovery of the adsorbate. It is a high-temperature process that breaks down complexes above a particular temperature, after which they reach equilibrium.[143] The third

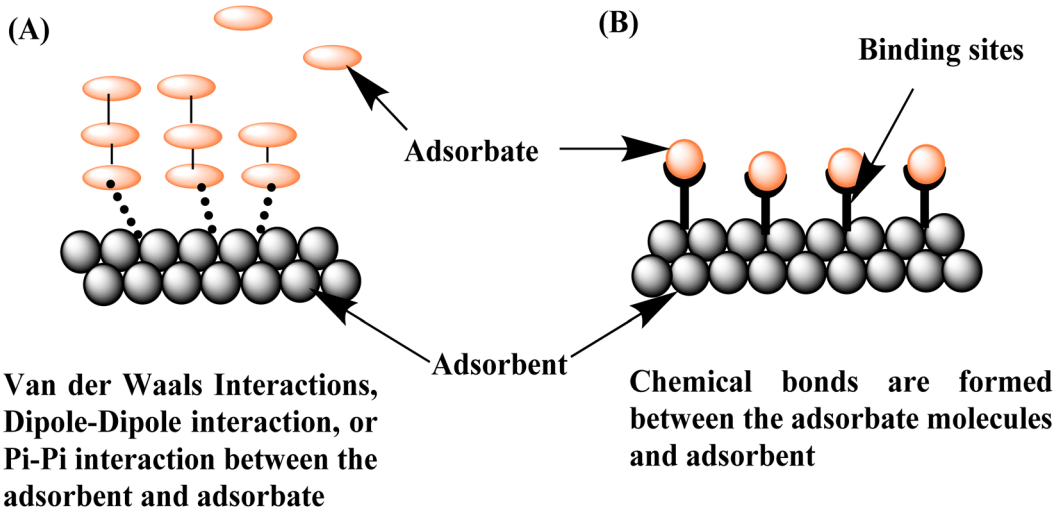

Fig. 10 The adsorption process in: (A) multiple layers (physisorption); and (B) single (chemisorption).

Table 6 Iron oxide-based nanomaterials and their composites as adsorbents for the removal of some pesticides

Adsorbent	Structure	Pesticide	Adsorption removal (%)	Ref.
Fe_3O_4@nSiO_2@mSiO_2	Core–shell microspheres	DDT	97%	159
MWCNTs/iron oxide/β-CD	Magnetic microspheres	*p*-Nitrophenol	69.6%	160
Mg/Al double layered hydroxide	Nanocrystalline particles	Humic acid	98.8	161
		Fulvic acid	97.6	

category is solution, in which the adsorbate is lost through diffusion and is not recovered in the adsorbent core. Chemisorption, in contrast to physisorption, is an adsorption process in which a modifying molecule (the adsorptive) and a surface (the adsorbent) make a chemical connection.[144] Chemisorption occurs either by radical processes or by ionic phenomena.[145] For further explanation, adsorption details are explained in Fig. 10 in both single and multiple-layer models.

The combination of various materials with diameters in the nanoscale range is called a nanocomposite. Combining the qualities of various materials to create a unique nanomaterial with enhanced and better chemical and physical capabilities is the goal of creating nanocomposites. The characteristics of the raw materials and the nanocomposites are very different. In comparison to conventional composite materials, nanocomposites have a huge surface area and a great surface-to-volume ratio.[146] In the realm of environmental studies, these composite materials have garnered interest, particularly for the removal of pesticides from various samples.[147] The main cause of this is the variety and special qualities that the nanomaterials provide, helping with the pesticide removal process. A nanotube is a long, hollow, tubular nanomaterial with a diameter that typically ranges in nanometers and a length that can vary from nm to mm. Because of their high aspect ratio and huge surface area, nanotubes can be used as effective adsorbents for a variety of chemicals. For a variety of uses, different materials, including enzymes, medications, hormones, and nucleic acids, have been entrapped in the lumen of these nanotubes and bonded to their surface. Because of their special qualities and vast surface area, carbon nanotubes (CNTs) and halloysite nanotubes (HNTs) have garnered a lot of interest in the field of environmental remediation.

7.1 Iron oxides

Among the elements that are most prevalent in the crust of the earth is iron. It has a wide range of oxidation states and is quite reactive. The oxidation state and chemical composition of iron determine the crystalline and structural characteristics of iron oxide nanoparticles. The major oxide forms of iron are magnetite (Fe_3O_4), maghemite (γ-Fe_2O_3), and hematite (α-Fe_2O_3).[148] The commonly utilized iron oxide nanoparticles, magnetite, include two separate forms of iron in distinct oxidation states: Fe^{2+} and Fe^{3+}. Iron oxide particles' nano-dimension offers super-paramagnetism and a high surface-area-to-volume ratio. Iron oxide nanoparticles have gotten a lot of attention for a wide range of uses because they are easy to make and change the surface of, they are easy to find, they have unique properties at the nanoscale level, they can separate magnetically, and they are not toxic.[149] For the adsorption of organic contaminants, iron oxide nanoparticles in their pure, doped, and composite forms have been widely employed.[150] After organic pollutants were adsorbed, separating the spent adsorbent from the wastewater has proven to be a significant challenge that calls for energy-intensive procedures like centrifugation. Even so, spent iron oxide-based adsorbents (after removing organic contaminants) are easily separated

Table 7 Titanium dioxide and their composites as adsorbents for the removal of pesticides from the wastewater

Adsorbent	Structure	Pesticides	Adsorbent amount	Contact time	Adsorption removal (%)	Ref
Nano-PP/TiO_2	Nano-polypropylene–titanium dioxide	Malathion	0.5 g L^{-1}	52 min	96	166
Cellulose/PANI/TiO_2	Cellulose/polyaniline/TiO_2 photocomposites	Acetamiprid	—	—	99	167
Nano-PP/TiO_2	Nano-polypropylene–titanium dioxide	Organophosphorous	2.25 g L^{-1}	32.2 min	69.3	168
Fe_3O_4@SiO_2@MOF/TiO_2 nanocomposite	Magnetic metal–organic framework–titanium dioxide nanocomposite	Fungicides (triadimenol, hexaconazole, diniconazole, myclobutanil, and tebuconazole)	—	—	93–95	169

when there is an outside magnetic field.[151] Iron oxide nanoparticles and their composites are therefore becoming more and more popular for use in wastewater treatment applications.[151]

Iron oxide (magnetite) nanoparticles were used to effectively remove chlorinated pesticides such as dieldrin, 2,4-dichlorophenoxyacetic acid (2,4-D), 2,4,5-trichlorophenoxyacetic acid (2,4,5-T), lindane (1,2,3,4,5,6-hexachlorocyclohexane), and hexachlorocyclohexane (α-HCH and γ-HCH) from the polluted water.[152,153] Their chemical structure determines how they adsorb on the iron oxide nanoparticles. Adding surfactants or surface-acting agents to the surface of iron oxide nanoparticles can make them better at absorbing things and being selective.[154] Much work has recently been done on the surface functionalization of iron oxide nanoparticles using a variety of organic species and functionalities, including polyacrylic acid, glutamic acid, organosilane, and so forth. An easy-to-use and practical method for separating used adsorbents must be combined with adsorption properties. The magnetic core of Fe_3O_4, the layer of nonporous silica ($nSiO_2$), and the layer of mesoporous silica ($mSiO_2$) on the outside of the magnetic mesoporous Fe_3O_4@$nSiO_2$@$mSiO_2$ nanoparticles showed a high rate of adsorption and the ability to remove the pesticide DDT.[155]

The immobilized Fe_2O_3 NPs considerably improved palygorskite's ability to retain phenarimol. According to Ouali *et al.*,[156] the material's adsorption capacity demonstrated stability over a two-week period, suggesting a wider application of this material for the long-term elimination of fenarimol. Using a similar strategy, iron oxide nanoparticles (NPs) trapped in mesoporous silica have been used to extract glyphosate from water. Immobilization significantly increased the magnetic adsorbent's surface area and porosity.[157] Fan *et al.*, used Fe_3O_4 nanoparticles and a simple, quick, and sensitive liquid–liquid extraction method to get rid of pyrethroid pesticides from tap, pond, river, and lake water, among others. Four types of pyrethroids were eliminated from water samples.[158]

In conclusion, changing the NPs' size, shape, and surface properties—which are important for finding and getting rid of different agrochemicals—can make these methods that use iron oxide NPs for pesticide cleanup more effective and selective. Because of how they are made, iron oxide nanoparticle surface modifications and mixing them with other nanomaterials will speed up the breakdown and removal of pesticides. Table 6 summarizes the performance of iron oxide-based nanomaterials and their composites as adsorbents for the removal of some pesticides.

7.2 Titanium oxide

Due to its favorable zero point charge (pH_{pzc} = 6–6.8), controlled structural and textural features, high surface reactivity, easy synthesis, and abundant availability of precursors, titanium dioxide (titania) nanomaterials have been investigated as an adsorbent.[152] Additionally, titanium functions as a photocatalytic substance to convert dangerous chemical molecules into harmless ones.[162] One of the most important conditions for

Table 8 Zinc oxide and their composites as adsorbents for the removal of pesticides from the wastewater

Adsorbent	Structure	Pesticide	Adsorption removal (%)	Ref.
CPZiONp-composite	Cucumber peels–zinc oxide nanoparticles composite	Metribuzin	66	172
CS–ZnONPs	Chitosan–zinc oxide nanoparticles	Permethrin	99	173
ZnO-Np	Zinc oxide nanoparticles	Simazine	72	174
ZnO-AC	ZnONP-doped activated carbon	Glyphosate	98	175

Table 9 Silicon dioxide and its composites as adsorbents for the removal of pesticides from the wastewater

Adsorbent	Structure	Pesticide	Adsorption removal (%)	Ref.
SiO_2	Silica nanoparticles	Azoxystrobin	95.21	181
SiO_2	Silica nanoparticles	Cypermethrin	88	182
Ni@SiO_2-G	Nickel@silica-graphene nanocomposites	Organothiophosphate	99	183
PAni:PPy@SiO_2	Polyaniline and polypyrrole with silicon dioxide	2,4-Dichlorophenol	97	184

the photodegradation of organic contaminants is their adsorption on the titania surface. The adsorption of organic pollutants facilitates the interface between the pesticide molecules and surface-active species, or photo-excited holes, and this starts the photo-oxidation events.[163] As a result, the adsorption effectiveness of the titania nanostructure controls the photo-degradation of organic contaminants. Titania's surface properties are influenced by the size, shape, crystallinity, and phase composition of the particles, which in turn affect the adsorption and photocatalytic destruction of organic contaminants. After being manufactured using a hydrothermal technique, the hierarchical nanostructured TiO_2, or TiO_2 1D nanorods, TiO_2 3D0D microspheres, and TiO_2 3D1D microspheres, showed morphological feature-dependent photocatalytic degradation of phenol. Compared to the 1D nanostructured equivalent, the organic pollutants degraded more quickly and efficiently in the hierarchical 3D nanostructured TiO_2 due to its larger degree of surface-active sites and desirable band gap energy.[164]

Six organochlorine pesticides were micro-extracted using mesoporous TiO_2 NPs.[165] These are hexachlororbenzene (HCB), *trans*-chlordane, *cis*-chlordane, *o*,*p*-DDT, *p*,*p*-DDT, and mirex. To remove the pesticides, solid-phase micro-extraction fiber was created using the NPs. Additionally, the produced fiber was utilized to find these chemicals in samples of lake and rainwater.[156] This enhanced adsorption is due to surface charge interactions and hydrogen bonding between the titanol groups of the aerogel and molecules' aromatic rings, nitrogen, and oxygen groups. The ability of the titania aerogel to regenerate adsorption sites at higher pH levels indicates its promise as a durable and efficient adsorbent for environmental cleanup.[152] Table 7 shows TiO_2 and their composites as adsorbents for the removal of pesticides from the wastewater.

7.3 Zinc oxides

ZnO NPs have distinct chemical and physical characteristics because of their high density at the surface's edge points and size. Additionally, these NPs have demonstrated strong photocatalytic activity, which is crucial for the breakdown of contaminants. Zinc oxide nanoparticles' surface functionalization improves both their catalytic and sensing capabilities. In a reported research study, it reveals that the adsorption capacity depends not only on the textural features of the material but also on the functionalization of the nanoparticles. It was found that 1-butyl-3-methylimidazolium tetrafluoroborate (BMTF-IL) functionalized zinc oxide nanoparticles show maximum adsorption capacity (148.3 mg g^{-1}) towards naphthalene removal as compared with CTAB functionalized (89.96 mg g^{-1}) and bare ZnO (66.80 mg g^{-1}) nanoparticles.[170]

Using ZnO NPs, permethrin—a neurotoxic insecticide that is frequently used in agriculture—was eliminated from the water sample. To create beads for the effective removal of the pesticide, NPs and chitosan were mixed. At room temperature and neutral pH, the pesticide's maximum removal efficacy (99%) was achieved using 0.5 g of beads. After three cycles, the beads showed themselves to be a promising material for treating water, with a 56% regeneration effectiveness.[171] Table 8 shows ZnO and their composites as adsorbents for the removal of pesticides from the wastewater.

7.4 Silicon dioxide

The spherical, porous particles known as silica nanoparticles (SiO_2 NPs) can be produced chemically or biologically.[176] Depending on the manufacturing conditions, the particles' porosity can be hollow, mesoporous, or microporous.[177] These particles can conjugate with a variety of chemical and biological substances by undergoing physical and chemical modification. Several environmental contaminants have been remedied using these NPs.[178] They have been applied to various pesticide detection, degradation, and extraction processes.

Pesticides have been extracted from a wide range of materials using solid-phase extraction (SPE). Owing to their substantial surface area, SiO_2 NPs are typically employed in the

Table 10 Silicon dioxide and its composites as adsorbents for the removal of pesticides from the wastewater

Adsorbent	Structure	Pesticide	Adsorption removal (%)	Ref.
MgO NPs	Magnesium oxide nanoparticles	Thiamethoxam	60.13	188
		Chlorpyriphos	80.53	
		Fenpropathrin	92.49	
MTBC	Triadimefon & dinotefuran	Triadimefon	86.42	189
		Dinotefuran	87.86	
MgO/Fe_3O_4-synthesized porous carbons	MgO/Fe_3O_4 modified coconut shell biochar	Atrazine	90.24	190
$MgFe_2O_4$	Mesoporous magnesium ferrite	Chlorpyrifos	91	191

production of sorbents for use in SPE techniques. These NPs' effectiveness and pesticide selectivity are increased when their surfaces are modified. SiO_2 NPs were used to extract sulfonylurea from water samples after they were functionalized with *N*-methylimidazole. Functionalization improved the polar pesticide's ability to bind to NP surfaces.[179] SiO_2 nanoparticles have also been used with cyanopropyltriethoxysilane (CNPrTEOS) and non-polar methyltrimethoxysilane (MTMOS) to get rid of organophosphate pesticides like diazinon, methidathion, malathion, chlorpyrifos, dicrotophos, and mathamidophos.[180] GC-MS or HPLC are then used to test the pesticides that were extracted from different sources using SiO_2 NPs. Table 9 shows SiO_2 and their composites as adsorbents for the removal of pesticides from the wastewater.

7.5 Magnesium oxide

It has been demonstrated that MgO nanoparticles are a promising adsorbent for organic pollutants and hazardous substances.[185,186] Magnesium oxide nanoparticles have a high concentration of low-coordinated sites, controlled textural features, are non-toxic, and have structural flaws, all of which increase their potential for adsorption applications. Furthermore, the adsorption of anionic dyes driven by electrostatic attraction was encouraged by the higher pH (12.4) of the zero-point charge (pH_{pzc}) of MgO. Chlorpyrifos (CPF), a persistent pesticide based on organophosphates, was highly adsorbed (3974 mg g^{-1}) into the hierarchical porous microspheres of MgO nanosheets that were made by precipitation and calcination.[187] Table 10 shows SiO_2 and their composites as adsorbents for the removal of pesticides from the wastewater.

7.6 Other metal oxides

A wide range of distinct metal oxide nanomaterials, such as SnO_2, Cu_2O, MoO_3, MoO_2, ThO_2, CeO_2, *etc.*, have been investigated as adsorbents for wastewater cleanup to remove organic contaminants in addition to iron oxides, titania, zinc oxides, and magnesium oxides. Due to their unique chemical and physical properties, as well as their structural flexibility, manganese oxides have attracted a lot of attention.[192] The MnO_2 nanoparticles' negatively charged surface made it easier for cationic contaminants to stick to them, which was especially true when the pH level was high.[193]

$Ni(OH)_2$ and NiO are significant transition metal hydroxides and oxides used in a variety of applications, such as energy storage devices.[194] The geometrical characteristics and chemical makeup of $Ni(OH)_2$ and NiO regulate their adsorption capacity. When used for effective pesticide removal, the chitosan modified AgO nanoparticles absorbed 99% of the permethrin insecticide from the aqueous solution (0.1 mg L^{-1}), 200% more effectively than pure chitosan (49%).[195]

It was shown that the zirconium-based metal–organic frameworks of UiO-67 could adsorptively remove the pesticides glyphosate and glufosinate from an aqueous solution. The presence of Zr–OH groups in large quantities within UiO-67 particles acted as an anchor for the effective adsorption of herbicides such as glyphosate (537 mg g^{-1}) and glufosinate (360 mg g^{-1}).[196]

8. Adsorptive removal *versus* photocatalytic degradation

In water treatment, two commonly employed techniques for removing organic pollutants are photocatalytic degradation and adsorption. Both methods are efficient and straightforward, but photocatalytic degradation is considered more sustainable than adsorption. While adsorption is a rapid, scalable, and cost-effective technique, it has limitations, as it generates waste after contaminants are absorbed. Additional environmental issues related to adsorption include the disposal of spent adsorbents, potential leaching of pollutants, and challenges in reusing adsorbents for future cycles.[180]

In contrast, photocatalytic degradation converts organic pollutants into less harmful substances or intermediates, eventually yielding mineral end products such as water (H_2O) and carbon dioxide (CO_2), thus minimizing waste.[181] Factors that influence photocatalytic efficiency include the photocatalyst's band-gap structure, the light source, and the ability of pollutants to adhere to the photocatalyst's surface. Enhanced adsorption on the photocatalyst surface aids in effective degradation, as it brings the pollutant molecules into close contact with the catalyst, improving photodegradation.

In summary, while adsorption serves as a useful step to facilitate photodegradation, photocatalytic degradation is ultimately a superior approach due to its ability to fully decompose organic pollutants into harmless byproducts. Nonetheless, effective adsorption is essential for achieving optimal photodegradation rates.

9. Linking adsorption and photocatalysis: synergistic approaches for pollutant remediation

Adsorption and photocatalysis are two distinct but complementary methods for effectively cleaning up organic pollutants. Surface interactions, like van der Waals forces, hydrogen bonding, or chemical bonding, characterize adsorption as a passive process that immobilizes pollutants in the adsorbent material. It exhibits energy efficiency and functions effectively across diverse environmental conditions without requiring external activation. Photocatalysis is an active process that uses light energy to excite electrons in semiconductors. This creates reactive species like hydroxyl radicals ($^{\bullet}OH$) and superoxide ions ($O_2^{\bullet-}$), which help break down pollutants into harmless end products. Photocatalysis necessitates specific conditions, including a suitable light source, optimized material properties, and precise environmental parameters.

The strategic combination of the two methods can enhance remediation efficiency. Adsorption serves as a fundamental capture mechanism, concentrating pollutants on the material's surface. This process removes contaminants from the aqueous phase and facilitates their subsequent degradation. Some materials, like TiO_2 composites with lots of surfaces or metal oxides that have been doped in, make it easier for reactive species made during photocatalysis to reach pollutants that have stuck to them. This process leads to the total mineralization of pollutants, which addresses challenges like incomplete degradation and secondary contamination. The interaction between adsorption and photocatalysis highlights their potential in creating multifunctional materials for advanced water treatment technologies. This section will examine the intricacies of photocatalytic mechanisms, developments in materials, and their roles in pollutant remediation.

10. Summary and future perspectives

Water is essential for the survival of all life forms, yet water pollution has escalated into a critical global issue, with contamination levels rising sharply over time. Numerous remediation techniques have been developed to preserve water quality, each tailored to address specific types of contaminants. Among these, metal oxides and their composites play a significant role as both photocatalytic and adsorptive materials in removing organic pollutants from wastewater. This comprehensive review examines the mechanisms of adsorption and photocatalysis in water treatment, focusing on the various structural, chemical, and surface properties of metal oxide nanomaterials that contribute to their high adsorption efficiency. Different adsorptive pathways—such as chemisorption, physisorption, and charge-driven interactions—demonstrate the versatility of these nanomaterials in capturing organic pollutants.

The application of metal oxide-based nanomaterials and their composites, including those for removing dyes and pesticides from wastewater, is discussed in depth. Materials such as graphene–metal oxide nanocomposites, iron oxides, magnesium oxides, titanium oxides, zinc oxides, tungsten oxides, and copper oxides have shown remarkable potential in this field. This analysis highlights the advancements, opportunities, and challenges associated with using these materials for water purification.

Adsorption is a widely recognized method for removing various contaminants, especially organic pollutants, by transferring them from an aqueous phase to a solid adsorbent phase. Although effective, it has limitations, including the generation of secondary pollutants. Adsorbents are employed across many industries; however, improvements in recyclability, adsorption efficiency, and eco-friendly decomposition of adsorbed pollutants are needed. Recently, metal oxide nanostructured materials and their composites have gained significant interest as photocatalytic agents, capable of degrading organic pollutants or converting them into environmentally benign products. For example, graphene–metal oxide composites, CuO, ZnO, MgO, and TiO_2 have demonstrated the ability to break down organic contaminants upon exposure to light, and these materials offer the advantage of reusability. However, challenges remain, particularly in scaling up the use of these materials for industrial applications with high efficiency.

Developing these materials sustainably and cost-effectively while achieving optimal performance under solar light exposure has been a persistent obstacle. Engineering the crystal structure and surface properties to enhance solar absorption efficiency is another critical challenge. Moving forward, the goal is to design advanced materials for sustainable water remediation that achieve zero pollutant discharge. This requires scientific innovation to create materials with a high specific surface area, optimal crystalline structures, and compatibility with environmentally friendly, economically viable manufacturing processes. The development of such "smart" materials is crucial for advancing water treatment technology toward sustainable and effective pollution control.

Adsorbent/photocatalyst regeneration is another crucial element that supports the process's sustainability and economic feasibility, prevents hazardous disposal, and preserves the equilibrium between water treatment and secondary waste management. Although it hasn't been thoroughly studied, the management of secondary trash is something that needs to be taken very seriously. Catalysis is one of the numerous uses for secondary waste, or used adsorbent.[197] As a result, the possibility of less pollution during the creation of metal oxide nanoparticles and their use in water treatment, as well as their use for other purposes, may help make the platform greener. It took a lot of work to develop economically viable, quicker, greener, and more effective methods for the removal or degradation of organic contaminants in a sustainable way and for the resurgence of safe and clean water for humans and other living things.

Data availability

No primary research results, software or code have been included and no new data were generated or analysed as part of this review.

Author contributions

The listed authors contributed to this work as follows: A. H. K. provided the concepts of the work; A. A., L. A., G. B. S. and H. S. M. A. interpreted the results. A. H. K., A. A. and H. S. M. A. prepared the manuscript; A. H. K. performed the revision before submission. All authors have read and agreed to the published version of the manuscript.

Conflicts of interest

The authors declare that there are no conflicts of interest.

Acknowledgements

The author H. S. M. Abd-Rabboh extends his appreciation to the Deanship of Scientific Research at King Khalid University for funding this work through a large Group Project under grant number (RGP.2/122/46).

References

1 G. Devendrapandi, X. Liu, R. Balu, R. Ayyamperumal, M. V. Arasu, M. Lavanya, V. R. M. Reddy, W. K. Kim and P. C. Karthika, *Environ. Res.*, 2024, 118404.
2 M. Wang, B. L. Bodirsky, R. Rijneveld, F. Beier, M. P. Bak, M. Batool, B. Droppers, A. Popp, M. T. van Vliet and M. Strokal, *Nat. Commun.*, 2024, **15**, 880.
3 M. M. Mekonnen, M. M. Kebede, B. W. Demeke, J. A. Carr, A. Chapagain, C. Dalin, P. Debaere, P. D'Odorico, L. Marston, C. Ray and L. Rosa, *Nat. Rev. Earth Environ.*, 2024, **5**, 890–905.
4 P. K. Singh, U. Kumar, I. Kumar, A. Dwivedi, P. Singh, S. Mishra, C. S. Seth and R. K. Sharma, *Environ. Sci. Pollut. Res.*, 2024, **31**, 56428–56462.
5 M. Rastogi, S. M. Kolur, A. Burud, T. Sadineni, M. Sekhar, R. Kumar and A. Rajput, *J. Geogr. Environ. Earth Sci. Int.*, 2024, **28**, 41–53.
6 F. Edition, *WHO Chron.*, 2011, **38**, 104–108.
7 R. Kaur, D. Choudhary, S. Bali, S. S. Bandral, V. Singh, M. A. Ahmad, N. Rani, T. G. Singh and B. Chandrasekaran, *Sci. Total Environ.*, 2024, 170113.
8 N. Talat, *Water Conserv. Glob. Clim. Change*, 2021, pp. 47–71.
9 L. Wang, C. Shi, L. Pan, X. Zhang and J. J. Zou, *Nanoscale*, 2020, **12**, 4790–4815.
10 R. Gusain, K. Gupta, P. Joshi and O. P. Khatri, *Adv. Colloid Interface Sci.*, 2019, **272**, 102009.
11 Y. Abubakar, H. Tijjani, C. Egbuna, C. O. Adetunji, S. Kala, T. L. Kryeziu, J. C. Ifemeje and K. C. Patrick-Iwuanyanwu, *Nat. Remedies Pest Dis. Weed Control*, 2020, pp. 29–42.
12 A. Shattuck, M. Werner, F. Mempel, Z. Dunivin and R. Galt, *Glob. Environ. Change*, 2023, **81**, 102693.
13 M. Tudi, H. Daniel Ruan, L. Wang, J. Lyu, R. Sadler, D. Connell, C. Chu and D. T. Phung, *Int. J. Environ. Res. Public Health*, 2021, **18**, 1112.
14 V. M. Pathak, V. K. Verma, B. S. Rawat, B. Kaur, N. Babu, A. Sharma, S. Dewali, M. Yadav, R. Kumari, S. Singh and A. Mohapatra, *Front. Microbiol.*, 2022, **13**, 962619.
15 K. K. Gautam and V. K. Tyagi, *J. Oleo Sci.*, 2006, **55**, 155–166.
16 S. G. Parte, A. D. Mohekar and A. S. Kharat, *Afr. J. Microbiol. Res.*, 2017, **11**, 992–1012.
17 M. L. Ortiz-Hernández, E. Sánchez-Salinas, E. Dantán-González and M. L. Castrejón-Godínez, *Biodegrad.: Life Sci.*, 2013, **10**, 251–287.
18 A. D. Kumar and N. Reddy, *Adverse Effects of Pesticides*, 2024.
19 R. Kaur, D. Choudhary, S. Bali, S. S. Bandral, V. Singh, M. A. Ahmad, N. Rani, T. G. Singh and B. Chandrasekaran, *Sci. Total Environ.*, 2024, 170113.
20 N. L. Mdeni, A. O. Adeniji, A. I. Okoh and O. O. Okoh, *Molecules*, 2022, **27**, 618.
21 P. G. Bertrand, *Pesticides*, 2019, 1–14.
22 P. M. Njogu, *Assessment Pollution Prediction Environ. Risks*, 2014.
23 O. G. Okon and U. E. Antia, *One Health Implications Agrochemicals*, 2023, pp. 441–460.
24 M. Shahid and M. S. Khan, *Pestic. Biochem. Physiol.*, 2022, **188**, 105272.
25 S. Antunes-Kenyon and G. Kennedy, *Massachusetts Dep. Agric. Resour.*, 2004.
26 D. K. Hazra and A. Purkait, *J. Pharmacogn. Phytochem.*, 2019, **8**, 686–693.
27 N. Chaudhary, K. K. Choudhary, S. Agrawal and M. Agrawal, *Pestic. Crop Prod.*, 2020, 159–180.
28 W. Draber, K. Tietjen, J. F. Kluth and A. Trebst, *Angew. Chem., Int. Ed.*, 1991, **30**, 1621–1633.
29 J. A. Martinez, Natural fungicides obtained from plants, *Fungicides for Plant and Animal Diseases*, ed. D. Dhanasekaran, InTech, 2012, vol. 10, p. 26336, ISBN: 978-953-307-804-5.
30 K. S. Rajmohan, R. Chandrasekaran and S. Varjani, *Indian J. Microbiol.*, 2020, **60**, 125–138.
31 M. L. Chen, X. W. Yao, Z. H. Diao, J. C. Jin, W. Qian, Y. Q. Yi, X. Chen and L. J. Kong, *Sep. Purif. Technol.*, 2023, **327**, 125013.
32 R. Gao, S. H. Gao, J. Li, Y. Su, F. Huang, B. Liang, L. Fan, J. Guo and A. Wang, *Engineering*, 2024, DOI: **10.1016/j.eng.2024.08.022**.
33 N. N. Roslan, H. L. H. Lau, N. A. A. Suhaimi, N. N. M. Shahri, S. B. Verinda, M. Nur, J. W. Lim and A. Usman, *Catalysts*, 2024, **14**, 189.
34 M. H. Shahverdian, F. Delfani, M. Z. Pedram, M. Hosseini, A. Sohani, H. Fazeli and H. Sayyaadi, *Sustainable Technol. Remediation Pollut.*, 2024, pp. 13–28.
35 O. A. Abiodun and O. O. Ayeleru, *Smart Nanomater. Environ. Appl.*, 2025, pp. 487–525.
36 R. Meena, M. M. Abdullah, V. Vasanthakumar, D. Ravichandran and S. Murugesan, *Ionics*, 2024, **30**, 5639–5650.
37 T. H. H. Al-Aqbi, T. Rafique, I. Mazahirul, S. M. H. Gardazi, W. Ahmad, A. Gupta, R. F. Alshehri and M. M. Ali, *Nanomater. Environ. Remediat.*, 2024.

38 Z. H. Diao and W. Chu, *Sci. Total Environ.*, 2021, **754**, 142155.
39 Y. Khan, H. Sadia, S. Z. Ali Shah, M. N. Khan, A. A. Shah, N. Ullah, M. F. Ullah, H. Bibi, O. T. Bafakeeh, N. B. Khedher and S. M. Eldin, *Catalysts*, 2022, **12**, 1386.
40 J. C. Védrine, *ChemSusChem*, 2019, **12**, 577–588.
41 L. Wang, C. Shi, L. Pan, X. Zhang and J. J. Zou, *Nanoscale*, 2020, **12**, 4790–4815.
42 K. V. Kumar, S. Gadipelli, B. Wood, K. A. Ramisetty, A. A. Stewart, C. A. Howard, D. J. Brett and F. Rodriguez-Reinoso, *J. Mater. Chem. A*, 2019, **7**, 10104–10137.
43 M. M. Sabzehmeidani, S. Mahnaee, M. Ghaedi, H. Heidari and V. A. Roy, *Mater. Adv.*, 2021, **2**, 598–627.
44 R. Gusain, K. Gupta, P. Joshi and O. P. Khatri, *Adv. Colloid Interface Sci.*, 2019, **272**, 102009.
45 S. Gautam, H. Agrawal, M. Thakur, A. Akbari, H. Sharda, R. Kaur and M. Amini, *J. Environ. Chem. Eng.*, 2020, **8**, 103726.
46 M. A. Gatou, A. Syrrakou, N. Lagopati and E. A. Pavlatou, *Reactions*, 2024, **5**, 135–194.
47 K. Kaur, R. Badru, P. P. Singh and S. Kaushal, *J. Environ. Chem. Eng.*, 2020, **8**, 103666.
48 A. Saravanan, P. S. Kumar, S. Jeevanantham, S. Karishma, B. Tajsabreen, P. R. Yaashikaa and B. Reshma, *Chemosphere*, 2021, **280**, 130595.
49 N. K. Elumalai, C. Vijila, R. Jose, A. Uddin and S. Ramakrishna, *Mater. Renewable Sustainable Energy*, 2015, **4**, 1–25.
50 R. B. Marcelino and C. C. Amorim, *Environ. Sci. Pollut. Res.*, 2019, **26**, 4155–4170.
51 A. Venkateshaiah, M. Černík and V. V. Padil, *Nanotechnol. Environ. Remediat.*, 2022, pp. 183–213.
52 P. Joshi, K. Gupta, R. Gusain and O. P. Khatri, *Metal Oxide Nanocomposites: Synthesis and Applications*, 2020, pp. 361–397.
53 R. Gusain, K. Gupta, P. Joshi and O. P. Khatri, *Adv. Colloid Interface Sci.*, 2019, **272**, 102009.
54 I. Ali, M. Suhail, E. C. López, R. A. Khattab and H. M. Albishri, *Arabian J. Geosci.*, 2022, **15**, 521.
55 M. A. Bhatti, A. A. Shah, K. F. Almani, A. Tahira, S. E. Chalangar, A. Chandio, O. Nur, M. Willander and Z. H. Ibupoto, *Ceram. Int.*, 2019, **45**, 23289–23297.
56 H. Chawla, S. Garg, J. Rohilla, Á. Szamosvölgyi, A. Efremova, I. Szenti, P. P. Ingole, A. Sápi, Z. Kónya and A. Chandra, *J. Cleaner Prod.*, 2022, **367**, 132923.
57 B. Karthikeyan, G. Gnanakumar and A. T. Alphonsa, *Nano Metal Oxides*, 2023.
58 *Handbook of Green and Sustainable Nanotechnology: Fundamentals, Developments and Applications*, ed. U. Shanker, C. M. Hussain and M. Rani, Springer Nature, 2023.
59 I. Abdelfattah and A. M. El-Shamy, *Sci. Rep.*, 2024, **14**, 27175.
60 A. A. M. Raub, R. Bahru, M. A. Mohamed, R. Latif, M. A. S. M. Haniff, K. Simarani and J. Yunas, *Nanotechnology*, 2024, **35**, 242004.
61 M. Ortiz-Martínez, J. A. Molina González, G. Ramírez García, A. Luna Bugallo, M. A. Justo Guerrero and E. C. Strupiechonski, *Environ. Toxicol. Chem.*, 2024, **43**, 1468–1484.
62 I. Arora, H. Chawla, A. Chandra, S. Sagadevan and S. Garg, *Inorg. Chem. Commun.*, 2022, **143**, 109700.
63 M. M. Mahlambi, C. J. Ngila and B. B. Mamba, *J. Nanomater.*, 2015, **2015**, 790173.
64 K. Nagaveni, M. S. Hegde, N. Ravishankar, G. N. Subbanna and G. Madras, *Langmuir*, 2004, **20**, 2900–2907.
65 A. T. Kuvarega and B. B. Mamba, *Crit. Rev. Solid State Mater. Sci.*, 2017, **42**, 295–346.
66 J. F. Budarz, E. M. Cooper, C. Gardner, E. Hodzic, P. L. Ferguson, C. K. Gunsch and M. R. Wiesner, *J. Hazard. Mater.*, 2019, **372**, 61–68.
67 R. Goswami, B. Kamal and A. Mishra, *Pestic. Bioremediation*, 2022, pp. 281–309.
68 S. N. Hoseini, A. K. Pirzaman, M. A. Aroon and A. E. Pirbazari, *J. Water Process Eng.*, 2017, **17**, 124–134.
69 M. Mehdipour, A. E. Pirbazari and G. Khayati, *Desalin. Water Treat.*, 2019, **155**, 329–340.
70 T. Kaur, A. Sraw, R. K. Wanchoo and A. P. Toor, *Sol. Energy*, 2018, **162**, 45–56.
71 R. de Oliveira and A. C. Sant'Ana, *Chemosphere*, 2023, **338**, 139490.
72 R. Fiorenza, A. Di Mauro, M. Cantarella, C. Iaria, E. M. Scalisi, M. V. Brundo, A. Gulino, L. Spitaleri, G. Nicotra, S. Dattilo and S. C. Carroccio, *Chem. Eng. J.*, 2020, **379**, 122309.
73 M. A. Rauf, M. A. Meetani and S. Hisaindee, *Desalination*, 2011, **276**, 13–27.
74 M. Janus, *Titanium Dioxide*, BoD – Books on Demand, 2017, ch. 2, 9789535134138.
75 D. Madan, K. P. Misra, S. Chattopadhyay and N. Halder, *Ceram. Sci. Eng.*, 2022, pp. 215–234.
76 K. Singh, S. Harish, J. Archana, M. Navaneethan, M. Shimomura and Y. Hayakawa, *Appl. Surf. Sci.*, 2019, **489**, 883–892.
77 M. Sattari, M. Farhadian, A. R. S. Nazar and M. Moghadam, *J. Photochem. Photobiol., A*, 2022, **431**, 114065.
78 S. R. Mirmasoomi, M. M. Ghazi and M. Galedari, *Sep. Purif. Technol.*, 2017, **175**, 418–427.
79 S. Nasseri, M. O. Borna, A. Esrafili, R. R. Kalantary, B. Kakavandi, M. Sillanpää and A. Asadi, *Appl. Phys. A*, 2018, **124**, 329–340.
80 A. H. C. Khavar, G. Moussavi, A. R. Mahjoub, M. Satari and P. Abdolmaleki, *Chem. Eng. J.*, 2018, **345**, 300–311.
81 G. Li, B. Wang, W. Q. Xu, Y. Han and Q. Sun, *Dyes Pigm.*, 2018, **155**, 265–275.
82 S. Raha and M. Ahmaruzzaman, *Nanoscale Adv.*, 2022, **4**, 1868–1925.
83 S. Maiti, S. Pal and K. K. Chattopadhyay, *CrystEngComm*, 2015, **17**, 9264–9295.
84 C. Hariharan, *Appl. Catal., A*, 2006, **304**, 55–61.
85 N. Daneshvar, D. Salari and A. R. Khataee, *J. Photochem. Photobiol., A*, 2004, **162**, 317–322.

86 N. Daneshvar, S. Aber, M. S. Dorraji, A. R. Khataee and M. H. Rasoulifard, *Sep. Purif. Technol.*, 2007, **58**, 91–98.
87 S. Navarro, J. Fenoll, N. Vela, E. Ruiz and G. Navarro, *J. Hazard. Mater.*, 2009, **172**, 1303–1310.
88 E. K. Kirupa Vasam Jino, *Adv. Environ. Technol.*, 2023, **9**, 124–137.
89 F. H. Abdullah, N. A. Bakar and M. A. Bakar, *J. Hazard. Mater.*, 2022, **424**, 127416.
90 N. Daneshvar, S. Aber, M. S. Dorraji, A. R. Khataee and M. H. Rasoulifard, *Sep. Purif. Technol.*, 2007, **58**, 91–98.
91 T. Iqbal, M. Afzal, B. A. Al-Asbahi, S. Afsheen, I. Maryam, A. Mushtaq, S. Kausar and A. Ashraf, *Mater. Sci. Semicond. Process.*, 2024, **173**, 108152.
92 S. M. Hosseini, I. A. Sarsari, P. Kameli and H. Salamati, *J. Alloys Compd.*, 2015, **640**, 408–415.
93 N. Güy, S. Çakar and M. Özacar, *J. Colloid Interface Sci.*, 2016, **466**, 128–137.
94 S. Bhatia, N. Verma and R. K. Bedi, *Opt. Mater.*, 2016, **62**, 392–398.
95 A. Nezamzadeh-Ejhieh and F. Khodabakhshi-Chermahini, *J. Ind. Eng. Chem.*, 2014, **20**, 695–704.
96 A. A. Khodja, T. Sehili, J. F. Pilichowski and P. Boule, *J. Photochem. Photobiol., A*, 2001, **141**, 231–239.
97 N. Daneshvar, S. Aber, M. S. Dorraji, A. R. Khataee and M. H. Rasoulifard, *Sep. Purif. Technol.*, 2007, **58**, 91–98.
98 S. Navarro, J. Fenoll, N. Vela, E. Ruiz and G. Navarro, *J. Hazard. Mater.*, 2009, **172**, 1303–1310.
99 W. Wu, C. Jiang and V. A. Roy, *Nanoscale*, 2015, **7**, 38–58.
100 M. Mishra and D. M. Chun, *Appl. Catal., A*, 2015, **498**, 126–141.
101 C. T. Wang, *J. Non-Cryst. Solids*, 2007, **353**, 1126–1133.
102 P. Hao, G. Wang, J. Wen, X. Li, Y. Suo, H. Zhan, S. Bi and W. Liu, *J. Environ. Chem. Eng.*, 2022, **10**, 107728.
103 N. S. M. Shahrodin, J. Jaafar, A. R. Rahmat, N. Yusof, M. H. Dzarfan Othman and M. A. Rahman, *Micro Nano Syst.*, 2020, **12**, 4–22.
104 N. Arif, M. N. Zafar, M. Batool, M. Humayun, M. A. Iqbal, M. Younis, L. Li, K. Li and Y. J. Zeng, *J. Mater. Chem. C*, 2024, **12**, 12653–12691.
105 V. Selvaraj, T. S. Karthika, C. Mansiya and M. Alagar, *J. Mol. Struct.*, 2021, **1224**, 129195.
106 E. Akhayere, D. Kavaz and A. Vaseashta, *Appl. Sci.*, 2022, **12**, 9279.
107 G. Bapat, C. Labade, A. Chaudhari and S. Zinjarde, *Adv. Colloid Interface Sci.*, 2016, **237**, 1–14.
108 X. P. Kong, B. H. Zhang and J. Wang, *J. Agric. Food Chem.*, 2021, **69**, 6735–6754.
109 D. Rawtani, N. Khatri, S. Tyagi and G. Pandey, *J. Environ. Manage.*, 2018, **206**, 749–762.
110 M. J. Lerma-García, E. F. Simó-Alfonso, M. Zougagh and Á. Ríos, *Talanta*, 2013, **105**, 372–378.
111 W. A. W. Ibrahim, W. N. W. Ismail and M. M. Sanagi, *J. Teknol.*, 2013, **62**, 3.
112 N. Sadegh, A. Asfaram, H. Javadian, H. Haddadi and E. Sharifpour, *J. Chromatogr. B*, 2021, **1171**, 122640.
113 S. B. Al Massati, Synthesis and characterization of molecularly imprinted polymers for the selective extraction of organophosphorus pesticides from vegetable oils, *Doctoral dissertation*, Université Pierre et Marie Curie-Paris VI, 2017.
114 N. Farooq, Z. ur Rehman, M. I. Khan, W. Iman, I. Kanwal, S. Khan, A. Shanableh, S. Manzoor and R. Luque, *Inorg. Chem. Commun.*, 2024, 113086.
115 R. Gusain, K. Gupta, P. Joshi and O. P. Khatri, *Adv. Colloid Interface Sci.*, 2019, **272**, 102009.
116 S. Tsunekawa, J. T. Wang and Y. Kawazoe, *J. Alloys Compd.*, 2006, **408**, 1145–1148.
117 A. Salerno, I. Pitault, T. Devers, J. Pelletier and S. Briançon, *Environ. Toxicol. Pharmacol.*, 2017, **53**, 18–28.
118 R. Fiorenza, S. A. Balsamo, L. D'Urso, S. Sciré, M. V. Brundo, R. Pecoraro, E. M. Scalisi, V. Privitera and G. Impellizzeri, *Catalysts*, 2020, **10**, 446.
119 P. Janos, P. Kuran, M. Kormunda, V. Stengl, T. M. Grygar, M. Dosek, M. Stastny, J. Ederer, V. Pilarova and L. Vrtoch, *J. Rare Earths*, 2014, **32**, 360–370.
120 P. Janoš, P. Kuráň, V. Pilařová, J. Trögl, M. Šťastný, O. Pelant, J. Henych, S. Bakardjieva, O. Životský, M. Kormunda and K. Mazanec, *Chem. Eng. J.*, 2015, **262**, 747–755.
121 M. K. Diallo, *SSRN Electron. J.*, 2022, 4441684.
122 D. Xiong, C. Fei, L. Qizeng and D. Ping, *Catal. Today*, 2014, **226**, 171–178.
123 C. M. Magdalane, K. Kaviyarasu, J. J. Vijaya, B. Siddhardha, B. Jeyaraj, J. Kennedy and M. Maaza, *J. Alloys Compd.*, 2017, **727**, 1324–1337.
124 T. K. Wong, S. Zhuk, S. Masudy-Panah and G. K. Dalapati, *Materials*, 2016, **9**, 271.
125 V. Molahalli, A. Sharma, K. Bijapur, G. Soman, A. Shetty, B. Sirichandana, B. M. Patel, N. Chattham and G. Hegde, *ACS Nano*, 2024, **18**, 33.
126 P. Raizada, A. Sudhaik, S. Patial, V. Hasija, A. A. P. Khan, P. Singh, S. Gautam, M. Kaur and V. H. Nguyen, *Arabian J. Chem.*, 2020, **13**, 8424–8457.
127 D. Malwal and P. Gopinath, *Catal. Sci. Technol.*, 2016, **6**, 4458–4472.
128 A. A. Umar and M. Oyama, *Cryst. Growth Des.*, 2007, **7**, 2404–2409.
129 S. Jung and K. Yong, *Chem. Commun.*, 2011, **47**, 2643–2645.
130 A. Chawla, A. Sudhaik, P. Raizada, A. A. P. Khan, A. Singh, Q. Van Le, T. Ahamad, S. M. Alshehri, A. M. Asiri and P. Singh, *J. Ind. Eng. Chem.*, 2022, **116**, 515–542.
131 N. Bayal and P. Jeevanandam, *Mater. Res. Bull.*, 2013, **48**, 3790–3799.
132 S. Bai, K. Zhang, J. Sun, R. Luo, D. Li and A. Chen, *CrystEngComm*, 2014, **16**, 3289–3295.
133 S. Bai, H. Liu, J. Sun, Y. Tian, S. Chen, J. Song, R. Luo, D. Li, A. Chen and C. C. Liu, *Appl. Surf. Sci.*, 2015, **338**, 61–68.
134 M. Long, W. Cai, J. Cai, B. Zhou, X. Chai and Y. Wu, *J. Phys. Chem. B*, 2006, **110**, 20211–20216.
135 H. Chawla, S. Garg, S. Upadhyay, J. Rohilla, Á. Szamosvölgyi, A. Sapi, P. P. Ingole, S. Sagadevan, Z. Konya and A. Chandra, *Chemosphere*, 2022, **297**, 134122.
136 H. Chawla, A. Chandra, P. P. Ingole and S. Garg, *J. Ind. Eng. Chem.*, 2021, **95**, 1–15.

137 W. Raza, M. M. Haque, M. Muneer, T. Harada and M. Matsumura, *J. Alloys Compd.*, 2015, **648**, 641–650.
138 X. W. Yao, X. Chen, M. L. Chen, N. J. Feng, L. Y. Tong, Y. Q. Yi, W. Qian and Z. H. Diao, *Process Saf. Environ. Prot.*, 2024, **186**, 808–818.
139 R. Natarajan, K. Saikia, S. K. Ponnusamy, A. K. Rathankumar, D. S. Rajendran, S. Venkataraman, D. B. Tannani, V. Arvind, T. Somanna, K. Banerjee and N. Mohideen, *Chemosphere*, 2022, **287**, 131958.
140 M. H. Dehghani, S. Ahmadi, S. Ghosh, M. S. Khan, A. Othmani, W. A. Khanday, Ö. Gökkuş, C. Osagie, M. Ahmaruzzaman, S. R. Mishra and E. C. Lima, *Appl. Surf. Sci. Adv.*, 2024, **19**, 100558.
141 H. H. Shanaah, E. F. Alzaimoor, S. Rashdan, A. A. Abdalhafith and A. H. Kamel, *Sustainability*, 2023, **15**, 7336.
142 L. W. Bruch, M. W. Cole and E. Zaremba, *Phys. Adsorpt. Forces Phenom.*, 2007.
143 D. C. Wang, Y. H. Li, D. Li, Y. Z. Xia and J. P. Zhang, *Renewable Sustainable Energy Rev.*, 2010, **14**, 344–353.
144 M. Králik, *Chem. Pap.*, 2014, **68**, 1625–1638.
145 A. Clark, *Chemisorptive Bond Basic Concepts*, 2012, vol. 32.
146 C. C. Okpala, *Int. J. Eng. Res. Dev.*, 2013, **8**, 17–23.
147 M. H. Dehghani, S. Ahmadi, S. Ghosh, M. S. Khan, A. Othmani, W. A. Khanday, Ö. Gökkuş, C. Osagie, M. Ahmaruzzaman, S. R. Mishra and E. C. Lima, *Appl. Surf. Sci. Adv.*, 2024, **19**, 100558.
148 R. M. Cornell and U. Schwertmann, *Iron Oxides Struct. Prop. React. Uses*, 2003, vol. 664.
149 M. E. McHenry and D. E. Laughlin, *Acta Mater.*, 2000, **48**, 223–238.
150 A. M. Gutierrez, T. D. Dziubla and J. Z. Hilt, *Rev. Environ. Health*, 2017, **32**, 111–117.
151 F. X. Dong, L. Yan, X. H. Zhou, S. T. Huang, J. Y. Liang, W. X. Zhang, Z. W. Guo, P. R. Guo, W. Qian, L. J. Kong and W. Chu, *J. Hazard. Mater.*, 2021, **416**, 125930.
152 R. Gusain, K. Gupta, P. Joshi and O. P. Khatri, *Adv. Colloid Interface Sci.*, 2019, **272**, 102009.
153 P. Kajitvichyanukul, V. H. Nguyen, T. Boonupara, L. A. P. Thi, A. Watcharenwong, S. Sumitsawan and P. Udomkun, *Environ. Res.*, 2022, **212**, 113336.
154 Y. Wang, R. Cheng, Z. Wen and L. Zhao, *Chem. Eng. J.*, 2012, **181**, 823–827.
155 F. Liu, H. Tian and J. He, *J. Colloid Interface Sci.*, 2014, **419**, 68–72.
156 A. Ouali, L. S. Belaroui, A. Bengueddach, A. L. Galindo and A. Peña, *Appl. Clay Sci.*, 2015, **115**, 67–75.
157 S. Fiorilli, L. Rivoira, G. Calì, M. Appendini, M. C. Bruzzoniti, M. Coïsson and B. Onida, *Appl. Surf. Sci.*, 2017, **411**, 457–465.
158 C. Fan, Y. Liang, H. Dong, G. Ding, W. Zhang, G. Tang, J. Yang, D. Kong, D. Wang and Y. Cao, *Anal. Chim. Acta*, 2017, **975**, 20–29.
159 F. Liu, H. Tian and J. He, *J. Colloid Interface Sci.*, 2014, **419**, 68–72.
160 W. Liu, X. Jiang and X. Chen, *Appl. Surf. Sci.*, 2014, **320**, 764–771.
161 L. Fang, J. Hou, C. Xu, Y. Wang, J. Li, F. Xiao and D. Wang, *Appl. Surf. Sci.*, 2018, **442**, 45–53.
162 A. Markowska-Szczupak, M. Endo-Kimura, O. Paszkiewicz and E. Kowalska, *Nanomaterials*, 2020, **10**, 2065.
163 U. Qumar, J. Z. Hassan, R. A. Bhatti, A. Raza, G. Nazir, W. Nabgan and M. Ikram, *J. Mater. Sci. Technol.*, 2022, **131**, 122–166.
164 J. Zhang, G. Xiao, F. X. Xiao and B. Liu, *Mater. Chem. Front.*, 2017, **1**, 231–250.
165 M. Hadei, A. Mesdaghinia, R. Nabizadeh, A. H. Mahvi, S. Rabbani and K. Naddafi, *Environ. Sci. Pollut. Res.*, 2021, **28**, 13055–13071.
166 M. Gholami, Z. Mosakhani, A. Barazandeh and H. Karyab, *J. Environ. Health Sci. Eng.*, 2023, **21**, 35–45.
167 T. Benhalima, M. Mokhtari and H. Ferfera-Harrar, *J. Water Process Eng.*, 2024, **57**, 104670.
168 A. Barazandeh, H. A. Jamali and H. Karyab, *Korean J. Chem. Eng.*, 2021, **38**, 2436–2445.
169 H. Su, Y. Lin, Z. Wang, Y. L. E. Wong, X. Chen and T. W. D. Chan, *J. Chromatogr. A*, 2016, **1466**, 21–28.
170 Y. Kaur, Y. Bhatia, S. Chaudhary and G. R. Chaudhary, *J. Mol. Liq.*, 2017, **234**, 94–103.
171 S. M. Dehaghi, B. Rahmanifar, A. M. Moradi and P. A. Azar, *J. Saudi Chem. Soc.*, 2014, **18**(4), 348–355.
172 A. U. Haq, M. Saeed, M. Muneer, M. A. Jamal, T. Maqbool and T. Tahir, *Sci. Rep.*, 2022, **12**, 5840.
173 S. M. Dehaghi, B. Rahmanifar, A. M. Moradi and P. A. Azar, *J. Saudi Chem. Soc.*, 2014, **18**(4), 348–355.
174 Z. Samuel, M. O. Ojemaye, O. O. Okoh and A. I. Okoh, *Mater. Today Commun.*, 2023, **34**, 105435.
175 K. Sen and N. K. Mondal, *J. Ind. Eng. Chem.*, 2024, **136**, 150–166.
176 L. K. Harada, M. Guilger-Casagrande, T. Germano-Costa, N. Bilesky-José, L. F. Fraceto and R. Lima, *Silicon Adv. Sustainable Agric. Hum. Health*, 2024, pp. 191–208.
177 S. H. Wu, C. Y. Mou and H. P. Lin, *Chem. Soc. Rev.*, 2013, **42**(9), 3862–3875.
178 J. Tejedor, V. H. Guerrero, K. Vizuete and A. Debut, *J. Phys.: Conf. Ser.*, 2022, **2238**, 012005.
179 V. Bueno, *Synthesis, Characterization and Application of Pesticide-Encapsulated Silica Nanoparticles in Agriculture*, McGill University, Canada, 2021.
180 N. Muhamad, W. A. W. Ibrahim and M. M. Sanagi, *J. Teknol.*, 2014, **71**(5), 57–62.
181 F. Malhat, O. I. Abdallah, M. Hussien, A. M. Youssef, F. M. Alminderej and S. M. Saleh, *Coatings*, 2023, **13**(7), 1286.
182 S. N. Ul Ain, M. S. Khan, N. Riaz, A. Khan, A. Sarwar, A. Khalid, A. Jan, Q. Mahmood and A. Al-Harrasi, *ACS Omega*, 2024, **9**(12), 13803–13817.
183 G. Wu, C. Zhang, C. Liu, X. Li, Y. Cai, M. Wang, D. Chu, L. Liu, T. Meng and Z. Chen, *J. Hazard. Mater.*, 2023, **457**, 131788.
184 A. Bekhoukh, M. Kiari, I. Moulefera, L. Sabantina and A. Benyoucef, *Polymers*, 2023, **15**(9), 2032.
185 M. Nagpal and R. Kakkar, *Sep. Purif. Technol.*, 2019, **211**, 522–539.

186 A. Fouda, S. E. D. Hassan, E. Saied and M. F. Hamza, *J. Environ. Chem. Eng.*, 2021, **9**(4), 105346.
187 L. Sharma and R. Kakkar, *ACS Appl. Mater. Interfaces*, 2017, **9**(44), 38629–38642.
188 A. Kar, S. Deole, B. G. Gadratagi, N. Patil, G. Guru-Pirasanna-Pandi, B. Mahapatra and T. Adak, *Environ. Sci. Pollut. Res.*, 2023, **30**(45), 101467–101482.
189 X. Chen, X. W. Yao, Y. Diao, H. Liu, M. L. Chen, N. J. Feng, W. Qian, X. H. Zhou, P. R. Guo, L. J. Kong and Z. H. Diao, *Sep. Purif. Technol.*, 2024, **336**, 126213.
190 L. Y. George, L. Ma, W. Zhang and G. Yao, *Environ. Sci. Eur.*, 2023, **35**(1), 21.
191 L. Sharma and R. Kakkar, *J. Environ. Chem. Eng.*, 2018, **6**(6), 6891–6903.
192 S. Chaudhary, Y. Kaur, A. Umar and G. R. Chaudhary, *J. Mol. Liq.*, 2016, **224**, 1294–1304.
193 A. K. Sharma, R. K. Tiwari and M. S. Gaur, *Arabian J. Chem.*, 2016, **9**, 1755–1764.
194 D. U. Lee, J. Fu, M. G. Park, H. Liu, A. Ghorbani Kashkooli and Z. Chen, *Nano Lett.*, 2016, **16**(3), 1794–1802.
195 M. V. Bagal and S. Raut-Jadhav, in *Handbook of Nanomaterials for Wastewater Treatment*, Elsevier, 2021, pp. 957–1007.
196 F. Fang, Q. Lv, P. Li, Y. Tao, Y. Zhang, Y. Zhou, X. Li and J. Li, *J. Environ. Chem. Eng.*, 2022, **10**(3), 107824.
197 T. Velempini, M. E. H. Ahamed and K. Pillay, *Results Chem.*, 2023, **5**, 100901.

Analytical Methods

ROYAL SOCIETY OF CHEMISTRY

PAPER

View Article Online
View Journal

Cite this: DOI: 10.1039/d4ay02206h

Physicochemical properties of mesoporous acid activated materials from *Lemna minor* for Bezaktiv Red S-MAX dye removal

Ghizlène Boudghene Stambouli,*[ab] Belkacem Benguella,[a] Benamar Makhoukhi,[a] Mohamed Said El-ouchdi[a] and Ayman H. Kamel *[bc]

Lemna minor, a cheap and easily accessible substance, was utilized to create activated carbon through acid activation [with H_3PO_4 (ALM-P) and citric acid (ALM-C)]. Brunauer–Emmett–Teller (BET) analysis reveals that the *L. minor* activated materials (LACs) had a surface area of 208.54 $m^2\ g^{-1}$ and 216.11 $m^2\ g^{-1}$ after H_3PO_4 and citric acid activation, respectively. The presence of rich hydroxyl, carboxyl, amide, and phosphate functional groups on the surface of LACs is revealed by Fourier transform infrared spectroscopy (FTIR). This enables easy Bezaktiv dye, type Red S-MAX (BRSM), binding to the surface through strong chemisorptive bonds or ion exchange. With a maximal mono-layer adsorption capacity (q_m) of 16.86 and 7.69 mg g^{-1} at 25 °C, the pseudo-second-order model and Langmuir isotherm provided a good description of the kinetic and equilibrium data. The adsorption was caused in part by the intra-particle diffusion mechanism. With negative $\Delta G°$ and positive $\Delta H°$ values, the adsorption process was spontaneous and endothermic. Under optimum conditions of pH 3.0 and 25 °C, the maximum % removal for BRSM (90 mg L^{-1}) was reported to be 77.65% within 90 min. These indicated that dye-contaminated water might be treated with the inexpensive LACs as a possible adsorbent.

Received 6th December 2024
Accepted 3rd February 2025

DOI: 10.1039/d4ay02206h

rsc.li/methods

1. Introduction

Technological and industrial advancements continued to increase, creating a significant problem for wildlife and plant life, leading to environmental pollution. Water pollution has emerged as the most severe form of pollution due to industrial discharges, posing a critical environmental challenge. Among the major sources of pollution are those stemming from the textile industry, as they release over one million cubic meters of wastewater annually.[1] In fact, the dyeing and treatment of textile fibers involve the consumption of substantial volumes of water and chemicals, ultimately leading to the discharge of 17% to 20% of the total dye content into the environment at the conclusion of the dyeing process.[2] These dyes are hazardous not only to human health but also to the environment, as they exhibit short-term toxicity, are occasionally carcinogenic, and possess intricate chemical structures that make them poorly biodegradable, conferring a persistent nature upon them.[3]

Adsorption is considered a promising approach due to its material reusability, low operating costs, enhanced selectivity for certain metals of interest, and quick operation times.[4] Researchers have effectively used a variety of adsorbents to remove pollutants from aqueous media, such as wheat husk,[5] treated alga (*Oedogonium hatei*),[6] hen feathers,[7] and activated materials (ACs). Because of their numerous functional groups on the surface, chemical stability, huge specific surface area, and highly porous structure, ACs are among the most effective adsorbents for extracting heavy metals from wastewater.[8] It appears promising to manufacture ACs with high mesoporosity for large molecule absorption using inexpensive and readily available materials for applications such as battery capacitors, catalytic supports, biomedical engineering, and adsorbents for bulky pollutants.[9] One of the best and least expensive activation techniques for creating mesoporous ACs is acid activation. The acid-activated ACs can accomplish a number of goals, including low activation temperature, high ion-exchange capacity, thermal and chemical stability, and high meso-porosity.[10] Acid-activated materials have thus extensively removed dyes from water. Biomass sources containing cellulose, hemicellulose, or lignin can serve as precursors for ACs.[11] Various renewable and affordable biomass sources, including lotus stalk,[11] cotton stalk,[12] water hyacinth,[13] *Enteromorpha prolifera*,[14] maize stalks,[15] and plant leftovers,[16] have been effectively used to prepare ACs. Under ideal growing conditions, duckweed, or *Lemna minor*, can treble its mass in just one week. Duckweed (*Lemna minor*) is a globally available aquatic plant that thrives in diverse freshwater environments, particularly in nutrient-rich

[a]*Inorganic Chemistry and Environment Laboratory, University of Tlemcen, P. O. Box 119, 13000 Tlemcen, Algeria. E-mail: ghizoustambouli@gmail.com*

[b]*Department, College of Science, University of Bahrain, Sakhir 32038, Kingdom of Bahrain. E-mail: ahkamel76@sci.asu.edu.eg*

[c]*Department of Chemistry, Faculty of Science, Ain Shams University, Cairo 11566, Egypt*

water. Its rapid growth, accessibility, and ability to be harvested with minimal resources make it a viable material for resource-limited communities. Beyond its rapid growth, duckweed is rich in lignocellulosic content, enabling its transformation into high-performance adsorbents for environmental applications. Furthermore, its cultivation aligns with sustainable practices, offering dual benefits in water quality improvement and pollutant remediation. Overgrowth of *L. minor* can result in negative consequences such as obstructed flood drains, hindrances to land navigation, and secondary pollutants linked to its debris. Reasonable harvesting and use of such aquatic plants are required to prevent these drawbacks. Lead, nickel, cadmium, copper, and chromium were among the heavy metals that have been eliminated using duckweed.[17,18] Additionally, cellulose, lipids, lignin, pentosan, pectin, and minerals are present in *L. minor*.[17] Consequently, *L. minor* presents itself as a promising low-cost precursor for the synthesis of ACs because of its lignin-cellulose structure, thereby enhancing the adsorption process's economic feasibility. Furthermore, there is not much information in the literature regarding mesoporous activated carbon made from *L. minor*. In order to increase the specific surface area and mesoporosity of activated carbon, *L. minor* – a possible low-cost precursor – and a modified chemical activation method using H_3PO_4 were coupled. Chemical activation with phosphoric acid and citric acid is a well-established method for developing high-performance adsorbents. Phosphoric acid promotes microporosity and introduces phosphate groups, while citric acid contributes mesoporosity and carboxylic functional groups. This dual activation approach has been shown to enhance the adsorption efficiency of various organic and inorganic pollutants, making it a suitable choice for the remediation of hazardous dyes.

The main goal of this work is to use citric and H_3PO_4 as activating agents to make ACs from *L. minor* that have a lot of surface functional groups, a large mesopore volume, and a large surface area. The acid activated *L. minor* is characterized using N_2 adsorption, scanning electron microscopy (SEM) and Fourier transform infrared spectroscopy (FTIR). The adsorption capacity of these adsorbents and their suitability for the removal of Bezaktiv Red S-MAX (BRSM) from an aqueous solution were examined. Optimization of the adsorption process in terms of temperature effect, the effect of pH, contact time, the amount of the adsorbent and the initial BRSM concentration was also performed. We examined the equilibrium and kinetic data to understand the adsorption kinetics, isotherms, thermodynamic characteristics, and mechanism of BRSM adsorption on LACs.

2. Experimental

2.1. Materials and apparatus

The macrophyte biomass for *L. minor* was collected from a natural lake in El-Fayoum city, Egypt. It was transported to Algeria in an ice box and then stored in a refrigerator at 4 °C until use. 20 g of *L. minor* sample was air dried in the sun after being washed three times with distilled water. Before being used, these *L. minor* samples, which were the raw, non-living biomass, were sieved to a size of 2.0 mm. In the pre-treatment phase, distilled water was also used to prepare all of the experimental solutions at ambient temperature and an agitation rate of 150 rpm. Finally, the *L. minor* samples that had all been pre-treated were dried in an oven for 10 h at 70 °C. Commercial Bezaktiv dye, type Red S-MAX (BRSM) (molecular formula $C_{31}H_{19}ClN_7Na_5O_{19}S_6$, 1136.28 g mol^{-1}), is very reactive and widely used in the textile industry.[19] It was supplied by SOITEX Company (Tlemcen-Algeria). All other chemicals were purchased from Sigma Aldrich (Saint Louis, USA) and were used as received without prior treatment.

The FTIR spectrum was recorded using a spectrometer (L160000A, PerkinElmer, USA) between wave numbers 400 and 4000 cm^{-1}. Using a surface area analyser (V350, Alliance, USA) and the manufacturer's software, the surface area S_{BET} and the total pore volume V_{tot} of the ALMs were calculated. SEM analysis (TM-1000, HITACHI, Japan) was performed to examine the surface texture and porosity development.

2.2. Activation of *Lemna minor*

The activation process using a combination of phosphoric acid and citric acid was optimized based on their complementary effects. Phosphoric acid enhances microporosity and introduces phosphate functional groups, while citric acid contributes carboxylic functional groups for improved adsorption interactions. A concentration of 0.1 M was selected to achieve effective activation without compromising the structural integrity of the activated carbon. The method was adapted from previous studies.[10] In brief, a quantity of 20 g of LM was treated with 1000 mL of 0.1 M of phosphoric acid or citric acid for 3 hours under stirring at 300 rpm to obtain ALM-P or ALM-C, respectively. The samples were then dried in an oven at 50° for 24 hours, crushed and sieved to be finally used in absorption experiments.

2.3. Adsorption experiments

A stock solution of 1000 mg L^{-1} of the red dye was prepared. Additional dilution produced experimental solutions with the required concentration. The experimental solutions of known concentrations (2–50 mg L^{-1}) were mixed with 0.03 g L^{-1} of either LM or ALM in a temperature-controlled water bath shaker within a pH range of 2.0–12.0. This was done for the batch adsorption experiments. A pH meter (ST7300, JENWAY, UK) was used for all pH measurements. A UV/VIS spectrophotometer (ST7300, PerkinElmer, UK) was used to measure the dye concentration in the supernatant liquids after they were adsorbed for 5–150 min at a wavelength $\lambda = 524$ nm. The dye uptake at the equilibrium q (mg g^{-1}) was calculated using eqn (1) as follows:

$$q_t(\text{mg g}^{-1}) = \frac{(C_i - C_t)}{W} \times V \quad (1)$$

The removal percentage (R%) was evaluated using eqn (2):

$$\text{Adsorption (\%)} = \frac{C_i - C_e}{C_i} \times 100 \quad (2)$$

where C_i, C_t and C_e (mg L^{-1}) are dye concentrations at the initial stage, time t and equilibrium, respectively; V and W are the liquid volume (L) and the dried used adsorbent weight (g), respectively.

3. Results and discussion

The yield of activated materials was calculated based on the dry weight of the raw *Lemna minor* and the final dry weight of ALM-P and ALM-C after activation. The yield was 40% for ALM-P and 35% for ALM-C, reflecting the effectiveness of the phosphoric acid and citric acid activation processes. These values align with typical yields reported for lignocellulosic precursors in chemical activation studies. Elemental analysis of raw *Lemna minor* revealed a composition of 45% carbon, 5% hydrogen, 40% oxygen, and 1% nitrogen. The high carbon content confirms its suitability as a precursor for producing activated materials. Furthermore, the difference in yields between ALM-P and ALM-C can be attributed to the varying effects of the activation agents on the structural and chemical properties of the raw material.

3.1 FTIR spectroscopy

To learn more about the functional groups involved in the bioaccumulation of BRSM dye, FTIR analysis was performed on the *L. minor* plant sample. The chemical groups on the LM's surface and the type of binding that occurs between the adsorbent and the dye were both revealed by the FTIR investigations. An important band at 3419.7 cm^{-1} was seen in the FTIR study (Fig. 1), which points to the stretching vibration of O–H groups in carboxylic groups in duckweed. The spectrum at 1651.5 represents the carboxyl groups. The peaks at 1444.4 cm^{-1} and 1632.3–598.1 cm^{-1} are attributed to C–O stretching and O–H bending.[20] For ALM-P samples, the phosphonate group was thought to be represented by the P–OH stretching at 1086.5 cm^{-1} and the P=O stretching of the absorption bands, which were observed at 1409.6 cm^{-1}.[21] For ALM-C samples, the stretching vibration of the C=O group shifts from 1651.5 to 1735 cm^{-1}, confirming the esterification of the carboxyl group in LM samples. The presence of the carboxyl group, which promotes the buildup of BRSM dye, is evident in the adsorbent's FTIR examination. A decrease in pH causes the carboxyl groups on the adsorbent to be undissociated. Therefore, there is a possibility of hydrogen bonding or electrostatic interactions at low pH values, which makes it easier for a negatively charged anionic dye to bind.

3.2 SEM analysis of *L. minor*

The SEM images of LMs and ALMs are displayed in Fig. 2. The LMs' surface morphology showed a big, accessible surface area with a fluffy, irregularly porous structure. We collected and examined data on nitrogen adsorption and desorption to elucidate the mechanisms of adsorption ability and selectivity. The significant adsorption capacity of type IV, with a small hysteresis loop (H3 type) at a high relative P/P^0 (>0.6), indicated the development of a meso-porous (D_P = 7.5 nm) structure for the ALMs. As acid catalysts, H_3PO_4 or citric acid break bonds and create crosslinks through cyclization or condensation when mixed with organic species to make phosphate and phosphate bridges. Once cleaned with deionized water, it occupies space, preventing the particle from contracting during the carbonization process, and eventually reveals a porous structure.[22] The larger dye molecules diffuse into the pores more easily due to the ALM's higher mesoporosity and larger average pore diameter.[23] ALM-P has a larger mesoporous area compared to ALM-C, despite being made under the same activation conditions. These include ACs from lotus stalk (74.4%),[24] herb residues (82.3%),[25] loosestrife (83.3%),[26] lignin (76.0%),[27] cattail fiber (78.1%),[28] and *Polygonum orientale* Linn. (82.5%).[29]

3.3 BET analysis

For a comprehensive analysis of mesoporous acid-activated carbon derived from ALM for removing Bezaktiv Red S-MAX

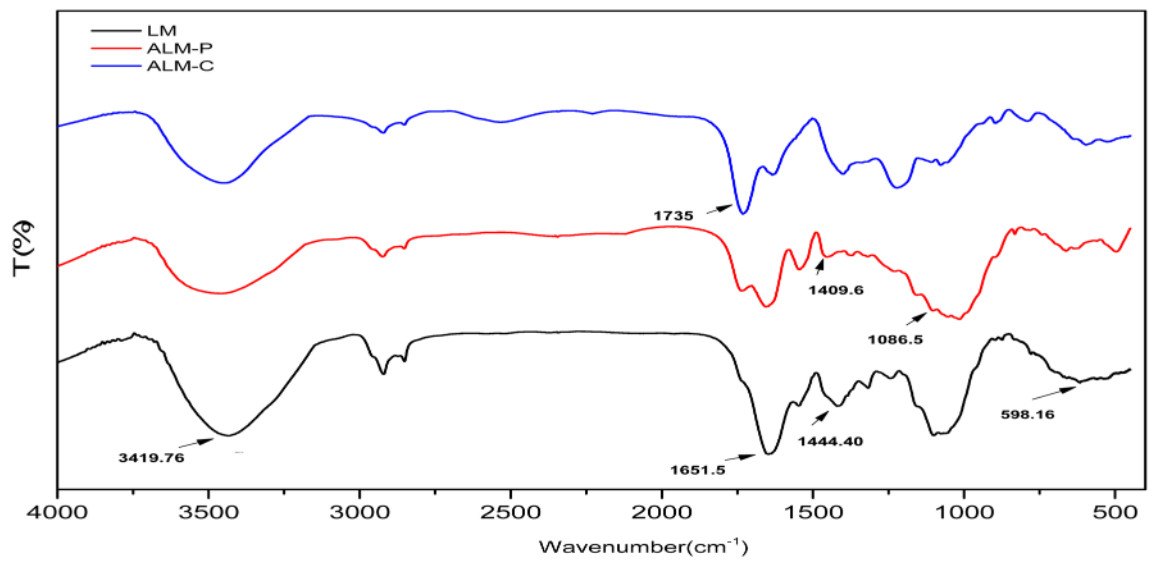

Fig. 1 FTIR spectra of LM and ALM.

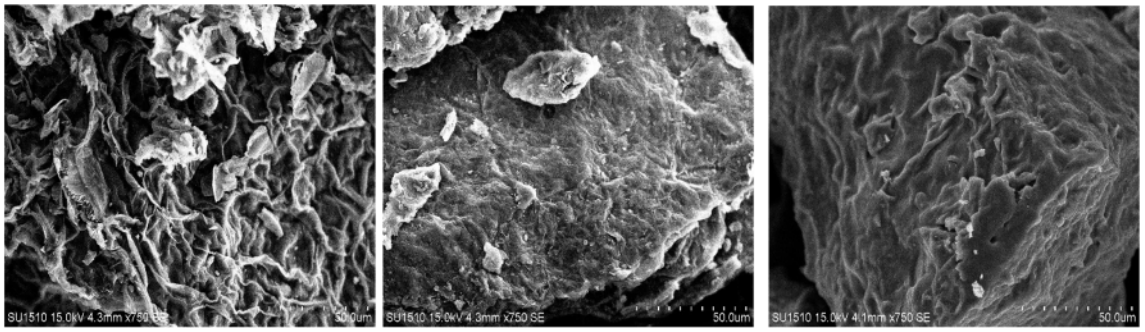

Fig. 2 SEM images of LM (a), (b) ALM-P, and (c) ALM-C.

dye, the BET analysis provides key insights into the material's structure and potential adsorption efficiency (Table 1). The total pore volume is a critical factor in determining the material's capacity to accommodate dye molecules within its structure. For untreated ALM, it exhibits a relatively low pore volume of 0.02 $cm^3\ g^{-1}$, indicating that the untreated carbon has limited internal voids, likely due to the lack of activation. For ALM treated with citric acid (ALM-C), the acid activation step significantly increases the total pore volume to 0.15 $cm^3\ g^{-1}$. This increase suggests the development of a porous structure, enhancing the material's ability to capture and hold dye molecules. Further chemical activation using H_3PO_4 increases the pore volume to 0.2 $cm^3\ g^{-1}$. This is the highest value among the three samples, implying that chemical activation creates even more accessible voids for dye molecules, potentially improving the adsorption capacity.

The average pore diameter gives insight into the types of pores formed, which affects the material's suitability for specific adsorbates. An average pore diameter of 35 nm places the untreated carbon in the mesoporous to macroporous range, which is suitable for larger molecules but may not be efficient for dye molecules, which are typically smaller. Phosphoric acid activation reduces the average pore diameter to 4 nm, entering the lower mesoporous range. This is more appropriate for adsorbing medium-sized dye molecules, providing a balance between accessible pore volume and pore size. Citric acid activation reduces the average pore diameter further to 2.3 nm, close to the microporous range. Smaller pores are advantageous for adsorbing smaller molecules but may hinder dye diffusion if the pore entrances become restrictive.

The specific surface area is crucial for adsorption capacity, as a larger surface area allows more interaction points for dye molecules. The ALM shows a specific surface area of 73.2 $m^2\ g^{-1}$, which is relatively low and limits its adsorption efficiency. Acid activation with citric acid (ALM-C) increases the surface area to 208.51 $m^2\ g^{-1}$, which is slightly lower than that achieved through H_3PO_4 activation (216.11 $m^2\ g^{-1}$). This increase suggests that acid treatment successfully removes impurities and opens up more adsorption sites, potentially boosting dye removal efficiency. Acid treatment using H_3PO_4 exhibits a higher specific surface area than using citric acid. This can be attributed to the specific structural changes or partial pore collapse during activation.

In conclusion, phosphoric acid promotes the development of a hierarchical pore structure, predominantly micropores, while citric acid enhances mesoporosity and introduces carboxyl functional groups. The synergy between these acids leads to improved adsorption capacity for organic pollutants, as observed in this study.

3.4 Dye adsorption using ALM-P

Several factors were investigated in this study, including contact time, initial pH effect, initial dye concentration, and temperature effect.

3.4.1 Kinetics study. The equilibrium adsorption study for Bezaktiv Red S-MAX (BRSM) dye removal, starting from a 40 mg per L concentration, reveals performance differences between phosphoric acid-activated carbon (ALM-P) and citric acid-activated carbon (ALM-C), both derived from *Lemna minor* (LM). The results, plotted in (Fig. 3), also highlight that untreated LM shows negligible adsorption efficiency.

Initially, after 15 minutes, ALM-P demonstrates superior performance by adsorbing 6.29 mg g^{-1} of dye, translating to over 78% dye removal. Comparatively, ALM-C captures 4.35 mg g^{-1}, achieving a 54% removal rate. This early efficacy is likely due to ALM-P's higher pore volume and well-distributed pore size, which favor rapid dye molecule uptake. At 45 minutes,

Table 1 BET analysis of both treated and untreated *L. minor*

Type of adsorbent	Total pore volume ($cm^3\ g^{-1}$)	Average pore diameter (nm)	Specific surface area ($m^2\ g^{-1}$)
ALM	0.02	35	73.2
ALM-P	0.15	4	216.11
ALM-C	0.2	2.3	208.51

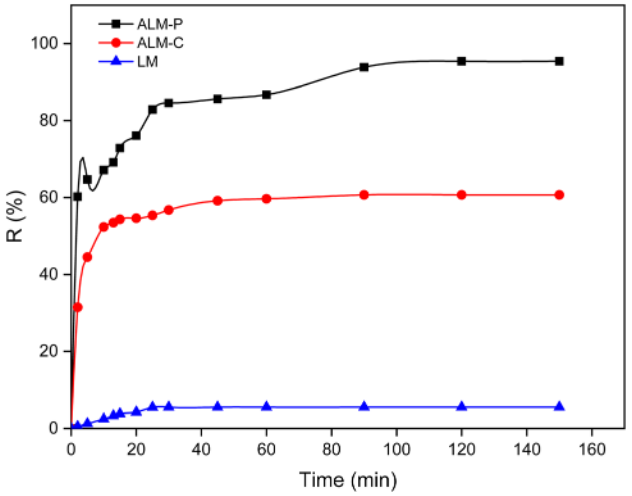

Fig. 3 Adsorption of Bezaktiv-Red dye onto LM and ALM as a function of time.

ALM-P further improves, adsorbing 6.74 mg g^{-1} (84.20% efficiency), while ALM-C reaches 4.63 mg g^{-1} (57.93% efficiency). The data show that ALM-P consistently outperforms ALM-C in dye uptake, likely due to its larger specific surface area and mesoporous design, which supports efficient dye diffusion and adsorption. ALM-C's structure, with smaller and more restricted pores, limits this rate. The materials reach equilibrium at around 90 minutes: ALM-P achieves 85.05% removal (6.80 mg g^{-1}), while ALM-C stabilizes at 4.68 mg g^{-1} (58.53%). These values confirm ALM-P's superior adsorption potential, attributed to its advantageous pore and surface characteristics. In comparison, unmodified LM removes only 5% of the dye, reinforcing the effectiveness of the acid-activated materials. In summary, ALM-P shows a higher adsorption yield for BRSM dye, indicating that acid activation optimizes its mesoporous properties, making it a more efficient adsorbent than ALM-C in both initial and equilibrium stages.

Acid treatment can effectively remove impurities, oxides, and other contaminants from the material's surface, enhancing properties such as adhesion, wettability, and reactivity with other substances. In this study, citric acid ($pK_a = 3.06$) and phosphoric acid ($pK_a = 2.12$) were used to activate *Lemna minor* (LM) to observe the differences in adsorption efficiency. The results indicated that phosphoric acid (ALM-P) enhanced adsorption more effectively than citric acid. This increased performance could be attributed to the higher acidity of phosphoric acid, which likely removed surface contaminants that could obstruct the material's pores, thereby improving adsorption potential through enhanced surface accessibility and structural changes. While this study primarily focused on adsorption capacity, it also aimed to address environmental concerns by examining waste reduction possibilities. Comparative adsorption capacities for different adsorbents are presented in Table 2, showing the high adsorption performance of ALM-P for Bezaktiv Red dye at 16.86 mg g^{-1}, outperforming other tested adsorbents like date palm seeds[30] and rubber seeds[32] for different dyes.

3.4.2 Adsorption kinetics model. In order to express the dye adsorption mechanism, kinetic parameters are determined by analyzing adsorption experimental data using the following kinetic model equations.

PFO (pseudo-first order rate equation):

$$\ln (q_e - q_t) = \ln q_e - k_f \times t \quad (3)$$

PSO (pseudo-second order rate equation):

$$\frac{t}{q_t} = \frac{1}{k_s \times q_e^2} + \frac{t}{q_e} \quad (4)$$

q_t: amount of adsorbate adsorbed at a specific time (mg g^{-1}), q_e: adsorption capacity at equilibrium (mg g^{-1}), k_f: constant of the PFO (min^{-1}), K_s: constant of the PSO (g mg^{-1} min^{-1}), and t: contact time (min).

According to Fig. 4, the PSO is more suitable than the PFO for experimental data of dye adsorption (Table 3). High correlation coefficients obtained employing the PSO are better than those obtained employing the PFO ($R^2 \geq 0.99$ for PSO and $R^2 \geq 0.93$ for PFO). The calculated equilibrium adsorption capacity is comparable to experimental data, which implies that the adsorption of BRSM dye onto the two samples is chemical (chemisorption), featuring valence forces due to electron exchange between the adsorbent and sorbate. In chemisorption, the adsorption capacity is proportional to the number of occupied active sites on the adsorbent surface.[34]

3.5 Effect of pH

The pH level plays a critical role in the study of dye molecule removal, as it significantly influences both the surface characteristics of the adsorbent material and the ionization process of the dye molecules. To achieve the desired initial pH values of the solution, adjustments were made using 0.1 M hydrochloric acid or sodium hydroxide solutions. The experimental data for

Table 2 Comparison of the sorption capacity of dyes

Adsorbents	Adsorbed dyes	q_{max} (mg g^{-1})	Ref.
Carbon (date palm seeds)	Eosin yellow	0.16	30
L. minor	Methylene blue	1.14	20
Red mud	Congo red	7.08	31
Rubber seed	Congo red	9.82	32
L. minor	Methylene blue	11.49	33
L. minor	Bezaktiv-Red	16.86 (ALM-P) 7.69 (ALM-C)	This work

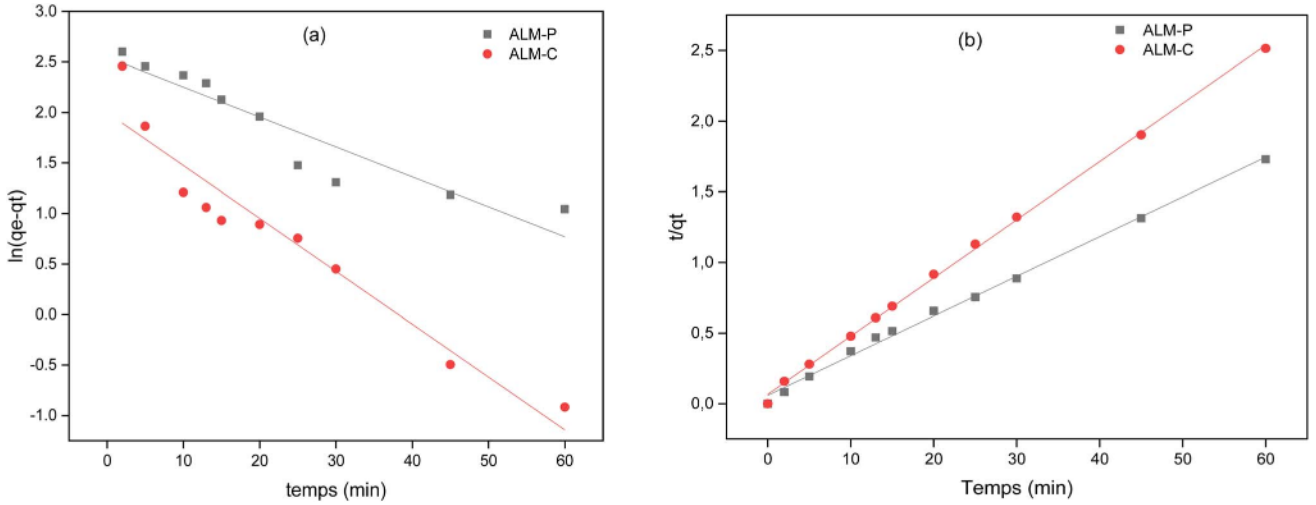

Fig. 4 Kinetic plots for the adsorption of dye onto ALM-P and ALM-C: (a) pseudo-first-order and (b) pseudo-second-order.

Table 3 PSO and PFO models for adsorption onto ALM-P and ALM-C

	Pseudo-first-order		Pseudo-second-order	
Samples	K_1 (min^{-1})	R^2	K_2 (mg g^{-1} min)	R^2
ALM-P	0.03	0.93	0.01	0.99
ALM-C	0.06	0.96	0.03	0.99

dye removal as a function of pH were analyzed using a linear regression model for ALM-P and a piecewise linear model for ALM-C. These models were selected based on the observed trends in removal efficiency across the pH range. Fig. 5 illustrates the variation in BRSM dye adsorption from an aqueous solution across a range of pH values. In this study, two distinct trends emerged for BRSM adsorption onto ALM-P and ALM-C under varying pH conditions. The solution pH notably impacts dye recovery and concentration, as it leads to the formation of soluble dye complexes, which unfortunately remain stable in aqueous media. Adsorption experiments using *Lemna minor* (*L. minor*) were conducted across a broad pH range (2.0–12.0), with the results depicted in Fig. 5. Observations indicate that dye adsorption decreases as the initial pH of the solution increases. Notably, maximum adsorption was achieved at a low pH of 2.0, reaching 77.65% for ALM-P and 45.42% for ALM-C. This behavior can be attributed to the protonation of the carboxyl groups present on the adsorbent surfaces (ALM-P and ALM-C) at lower pH levels. In a protonated state, these groups may form hydrogen bonds with the oxygen atoms in BRSM dye molecules, enhancing the affinity of the dye for the ALM surface through hydrogen bonding interactions.

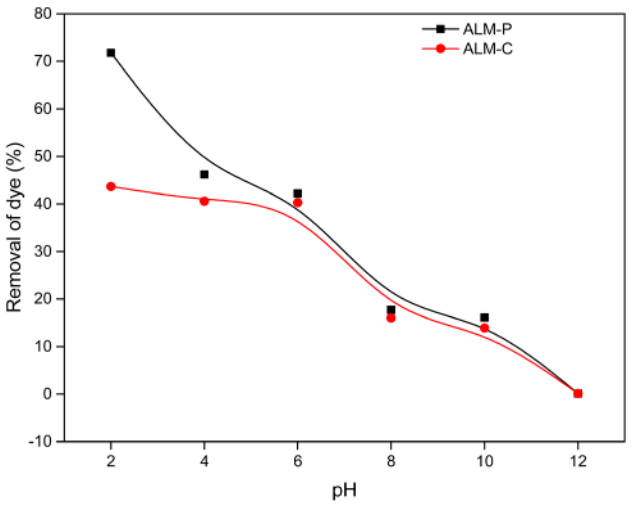

Fig. 5 Adsorption of dye onto *Lemna minor* in relation to initial pH.

The point of zero charge (pH_{pzc}) of ALM-P and ALM-C was determined to be 5.4 and 5.2, respectively. When the pH of the solution falls below these values, the ALM-P and ALM-C surfaces acquire a positive charge. This positively charged surface promotes the adsorption of the anionic dye (BRSM) due to increased electrostatic attraction. Additionally, if the surface is protonated, reducing its net negative charge, electrostatic attractions between the positively charged adsorbent surface and negatively charged dye molecules are likely to occur, further facilitating adsorption. Thus, the observed increase in adsorption at low pH is primarily driven by these protonation and electrostatic effects, both of which enhance the interaction between the dye molecules and the adsorbent material.

In conclusion, for ALM-P, the removal efficiency exhibits a linear trend across the pH range (2–12), highlighting the material's robustness and stable adsorption performance under varying pH conditions. In contrast, ALM-C shows a distinct piecewise trend: a baseline removal of ~40% at pH < 6, followed by a linear decrease at higher pH values. This behavior reflects the influence of surface functional groups and their ionization states, which are governed by the activation method. The strong performance of ALM-P can be attributed to its high mesoporosity and the presence of phosphate groups that provide consistent adsorption capabilities.

3.6 Dye concentration effect

To assess how varying initial dye concentrations affect adsorption, a range of concentrations from 2 to 50 mg L^{-1} was applied, as depicted in Fig. 6. The results show that the quantity of BRSM dye adsorbed by the acid-activated material (ALM-P) increases from 6.66 mg g^{-1} to 16.68 mg g^{-1} as the initial dye concentration rises. In comparison, chemically activated carbon (ALM-C) shows a more modest increase in adsorption capacity, from 6.66 mg g^{-1} to 7.64 mg g^{-1}, with increasing dye concentration. This trend suggests that higher initial dye concentrations strengthen the interactions between the adsorbent surfaces and dye molecules, enhancing the mass transfer of the dye to the adsorbent.

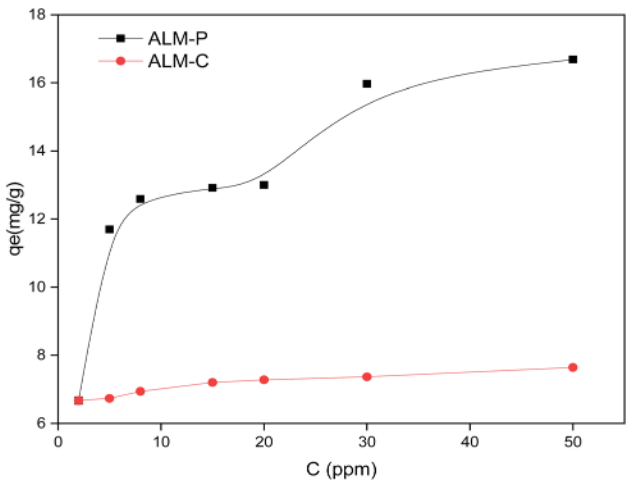

Fig. 6 Adsorption of dye onto *Lemna minor* as a function of concentration.

At higher initial dye concentrations, adsorption capacity generally improves because more dye molecules are available to interact with the adsorbent surface. However, as the concentration reaches a high threshold (such as above 90 mg L^{-1}), a saturation effect may begin to limit adsorption efficiency. This occurs when the adsorbent's available binding sites become progressively occupied, eventually reaching a point where fewer sites remain accessible to additional dye molecules. Consequently, the adsorbent surface can no longer accommodate as many dye particles, resulting in a gradual decrease in removal efficiency as binding sites are maxed out. This saturation is characteristic of systems where adsorption equilibrium is reached, and excess dye molecules remain in solution due to the finite number of active sites on the adsorbent surface.

3.7 Isotherm adsorption

Langmuir and Freundlich isotherms are the most used equations to represent adsorption data, represented by the following equations:

$$\frac{C_e}{q_e} = \frac{1}{q_m K_L} + \frac{1}{q_m} C_e \quad (5)$$

$$\ln q_e = \ln K_F + \frac{1}{n} \ln C_e \quad (6)$$

C_e: equilibrium dye concentration (mg L^{-1}), q_e: equilibrium dye adsorbed quantity (mg g^{-1}), K_L: Langmuir adsorption constant (L mg^{-1}), q_m: the maximum dye adsorbed quantity, k_F: Freundlich adsorption constant, and n: Freundlich energetic parameter.

The Langmuir isotherm's high linearity, shown in (Fig. 7) and supported by the parameters in Table 4, shows the strong fit of the Langmuir model to the adsorption data for BRSM dye

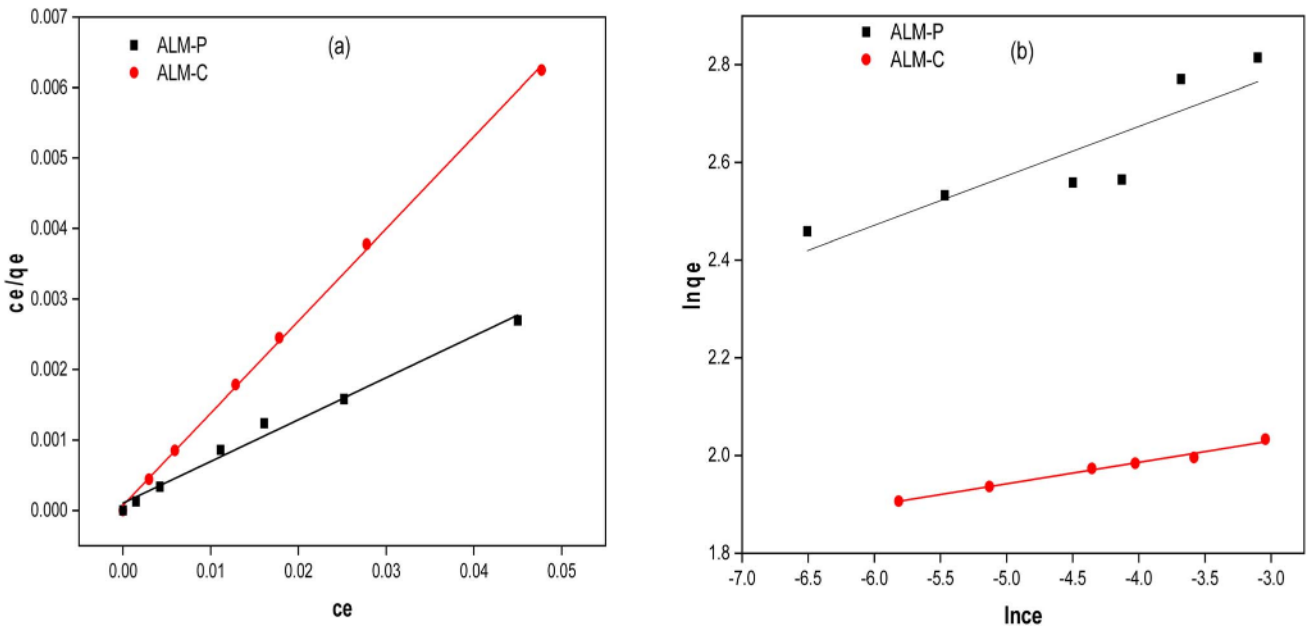

Fig. 7 (a) Langmuir and (b) Freundlich model plots.

Table 4 Parameters obtained from Langmuir and Freundlich models

Isotherm	Parameters	ALM-P	ALM-C
Experiment	q_e (mg g^{-1})	16.68	7.64
Langmuir	q_{max} (mg g^{-1})	16.86	7.65
	k_L (L mg^{-1})	0.574	1.817
	R^2	0.994	0.998
Freundlich	K_F (mg g^{-1})	21.74	8.688
	$1/n$	0.101	0.044
	R^2	0.886	0.994

onto LM-activated carbon (ALM) with phosphoric acid and citric acid. With an R^2 value near unity (0.99), this model suggests that dye adsorption occurs primarily as a monolayer on a homogeneous adsorbent surface. In this context, each BRSM dye molecule likely occupies an individual site on the activated surface of ALM, which minimizes interaction between dye molecules, aligning with Langmuir's assumptions of monolayer coverage.

3.8 Thermodynamic parameters

Utilizing the experimental data from previous research on the effect of solution temperature, thermodynamic analysis was performed. The following formulae can be used to compute the thermodynamic parameters, which are standard free energy ($\Delta G°$), standard enthalpy ($\Delta H°$), and standard entropy ($\Delta S°$):

$$\ln K_L = \frac{\Delta S}{S} - \frac{\Delta H}{RT} \quad (7)$$

where R (8.314 J mol^{-1} K^{-1}): the gas constant, T: the temperature (K) and K_L: the distribution coefficient that can be calculated as:

$$k_L(\text{ml g}^{-1}) = \frac{C_i - C_e}{C_e} \times \frac{V}{m} \quad (8)$$

C_0 and C_e: initial and equilibrium BRSM dye concentrations (mg L^{-1}), respectively (Table 5).

The thermodynamic study was conducted at temperatures of 298.1 K, 309.6 K, 319.9 K, and 333.3 K. These temperatures were selected to encompass a range of conditions, including ambient temperature (298.1 K) and higher temperatures that may be encountered in practical applications or controlled experimental environments. This approach ensures a comprehensive analysis of the adsorption process over varying thermal conditions.

As shown in Fig. 8, the negative values of $\Delta G°$ across all tested temperatures confirm that the adsorption process is spontaneous for both ALM-P and ALM-C, with a clear trend of

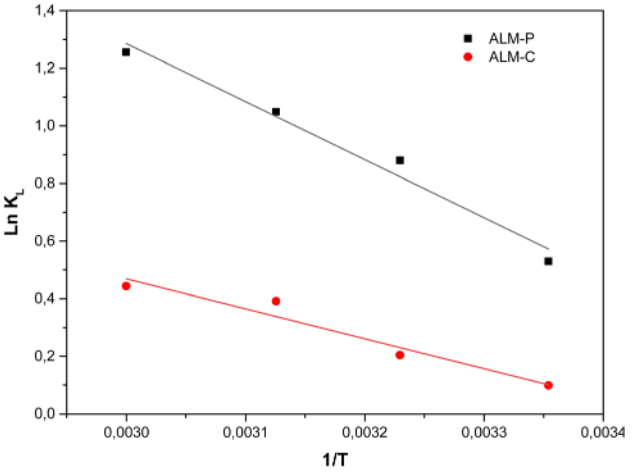

Fig. 8 Van't Hoff plot for the sorption of dye onto ALM-P and ALM-C.

increasing adsorption efficiency at elevated temperatures. The positive $\Delta H°$ values, indicative of endothermic behavior, reveal that heat absorption is required to facilitate the adsorption of BRSM dye onto both ALM-P and ALM-C, meaning that increasing the temperature enhances adsorption capacity. Moreover, the positive $\Delta S°$ values suggest increased disorder at the solid–liquid interface, which could be due to the dye molecules interacting and aligning on the surface of activated ALM. ALM-P exhibits higher spontaneity and endothermic tendencies than ALM-C, with a higher $\Delta S°$ (37.194 J mol^{-1} K^{-1}) and $\Delta G°$ values more negative across temperatures, suggesting that phosphoric acid activation may provide a more favorable adsorption surface compared to citric acid activation. This difference implies that ALM-P has a structurally optimized surface with greater affinity for BRSM dye molecules, possibly due to the enhanced pore structure and surface chemistry, which promote effective dye interaction.

The selected temperature range allowed for the evaluation of the adsorption process across varying thermal conditions. The negative values of $\Delta G°$ observed at all temperatures confirm the spontaneity of the adsorption process, with increased spontaneity at higher temperatures due to the more negative $\Delta G°$ values. This suggests that adsorption onto ALM-P and ALM-C is thermodynamically favorable and enhanced by increasing temperature.

3.9 Adsorption mechanism

Fig. 9 provides a detailed illustration of the interactions between Bezaktiv Red S-Max (BRSM) dye molecules and LM

Table 5 Thermodynamic data for adsorption of dye onto *L. minor*

	$\Delta H°$ (kJ mol^{-1})	$\Delta S°$ (J mol^{-1})	R^2	$\Delta G°$ (kJ mol^{-1})			
				298.1 K	309.6 K	319.9K	333.3 K
ALM-P	9 646	37 194	0.98	−1.44	−1.87	−2.25	−2.75
ALM-C	8.64	29.83	0.97	−0.24	−0.57	−0.87	−1.26

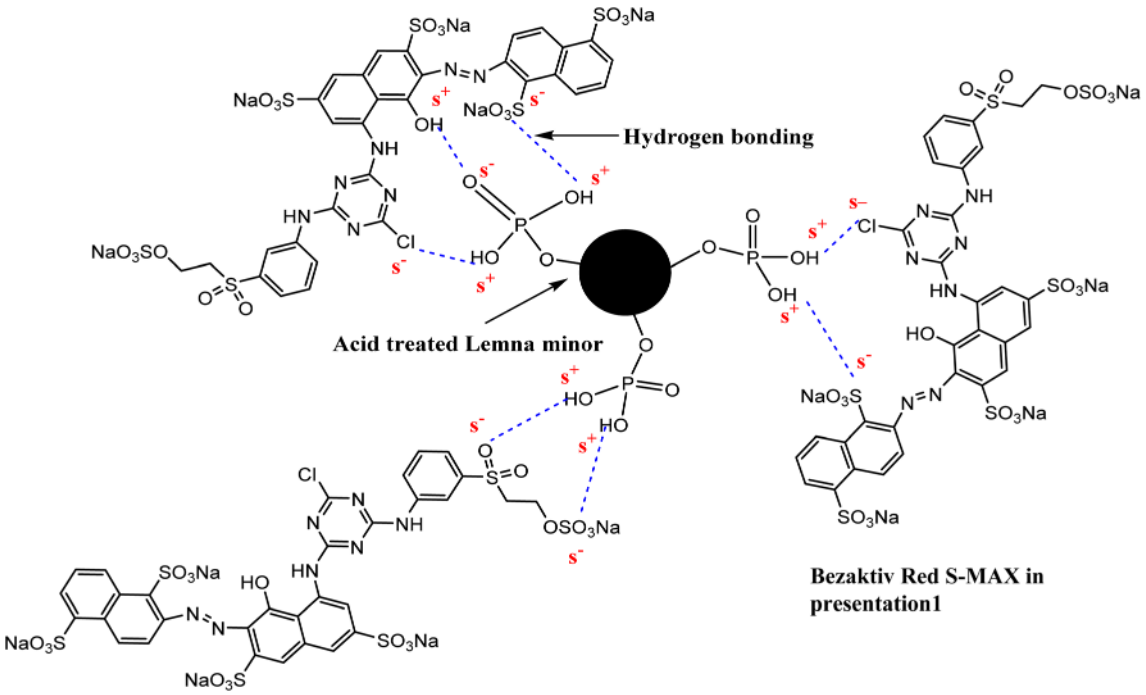

Fig. 9 Proposed adsorption mechanism of BRSM dye on ALMP.

treated with phosphoric acid (ALM-P). This graphic emphasizes the molecular mechanisms of hydrogen bonding and electrostatic interactions that facilitate the adsorption of BRSM onto ALM-P.

The adsorption mechanism shows multiple hydrogen-bonding interactions occurring between BRSM molecules and the ALM-P surface. BRSM dye contains several functional groups, including sulfonate groups (SO_4Na and SO_3Na), hydroxyl (–OH), and chloride (Cl) groups. The oxygen atoms within these functional groups can serve as hydrogen bond acceptors, allowing the dye molecules to form stable hydrogen bonds with specific groups on the ALM-P surface, and on the ALM-P surface, the hydroxyl (–OH) and phosphoryl (P═O) groups act as hydrogen donors, facilitating bond formation with the oxygen atoms of BRSM's sulfonate, hydroxyl, and chloride groups. This hydrogen bonding stabilizes the BRSM molecules on the ALM surface, enhancing their retention by reinforcing the binding interaction between the dye and the ALM-P. Thus, hydrogen bonds play a vital role in anchoring BRSM to ALM-P, leading to improved dye adsorption stability. In addition to hydrogen bonding, electrostatic interactions contribute significantly to BRSM dye adsorption on ALM-P, particularly at lower pH levels. As the solution's pH decreases, the concentration of hydrogen ions (H^+) in the medium increases. This environment favors the protonation of ALM-P's surface hydroxyl (–OH) groups, imparting a positive charge to the surface. The protonated ALM-P surface is then attracted to the negatively charged sulfonate groups of BRSM, fostering a strong electrostatic attraction between the ALM-P and BRSM molecules. This electrostatic attraction promotes the proximity and alignment of BRSM with ALM-P, facilitating additional hydrogen bonding and further stabilizing the adsorption. By combining hydrogen bonding and electrostatic interactions, this mechanism ensures efficient dye retention on the ALM-P surface, especially under acidic conditions that enhance protonation and, therefore, the overall binding affinity.

4. Conclusions

Activated materials derived from *Lemna minor* (LM) waste were successfully synthesized using two distinct acid treatments, resulting in adsorbents that are cost-effective, eco-friendly, and simple to produce. These ALM-P-based materials demonstrate enhanced surface properties and a high specific surface area, reflecting significant improvements in their adsorption potential. The study found that the ideal conditions for maximum dye removal include a dose of 0.03 g of ALM-P, a dye solution pH of 2, and an adsorption time of 90 minutes. Kinetic analysis suggests that the pseudo-second-order (PSO) model accurately describes the adsorption kinetics, while the Langmuir isotherm provides the best fit for equilibrium data, indicating a maximum monolayer adsorption capacity of 16.86 mg g^{-1} for BRSM dye. Based on these results, ALM-P shows strong potential as an effective adsorbent for removing synthetic dyes from aqueous solutions, positioning it as a promising material for water purification applications.

Data availability

The data supporting this article have been included in the main manuscript.

Author contributions

All authors listed have made a substantial, direct, and intellectual contribution to the work and approved it for publication.

Conflicts of interest

The authors declare that the research was conducted in the absence of any commercial or financial relationships that could be construed as a potential conflict of interest.

References

1 B. T. Eddine and M. M. Salah, *Int. J. Energy Environ. Eng.*, 2012, **3**, 17.
2 M. Hassaan and A. el Nemr, *Am. J. Environ. Sci. Eng.*, 2017, **1**, 64–67.
3 C. Visvanathan, R. Ben Aim and K. Parameshwaran, *Crit. Rev. Environ. Sci. Technol.*, 2000, **30**, 1–48.
4 A. K. Giri, R. Patel and S. Mandal, *Chem. Eng. J.*, 2012, **185–186**, 71–81.
5 V. K. Gupta, R. Jain and S. Varshney, *J. Hazard. Mater.*, 2007, **142**, 443–448.
6 V. K. Gupta, A. Rastogi and A. Nayak, *J. Colloid Interface Sci.*, 2010, **342**, 533–539.
7 V. K. Gupta, A. Mittal, L. Kurup and J. Mittal, *J. Colloid Interface Sci.*, 2006, **304**, 52–57.
8 L. Mouni, D. Merabet, A. Bouzaza and L. Belkhiri, *Desalination*, 2011, **276**, 148–153.
9 M. Al Bahri, L. Calvo, M. A. Gilarranz and J. J. Rodriguez, *Chem. Eng. J.*, 2012, **203**, 348–356.
10 N. V. Sych, S. I. Trofymenko, O. I. Poddubnaya, M. M. Tsyba, V. I. Sapsay, D. O. Klymchuk and A. M. Puziy, *Appl. Surf. Sci.*, 2012, **261**, 75–82.
11 H. Liu, P. Dai, J. Zhang, C. Zhang, N. Bao, C. Cheng and L. Ren, *Chem. Eng. J.*, 2013, **228**, 425–434.
12 K. Li, Z. Zheng and Y. Li, *J. Hazard. Mater.*, 2010, **181**, 440–447.
13 Y. Huang, S. Li, J. Chen, X. Zhang and Y. Chen, *Appl. Surf. Sci.*, 2014, **293**, 160–168.
14 Y. Li, Q. Du, X. Wang, P. Zhang, D. Wang, Z. Wang and Y. Xia, *J. Hazard. Mater.*, 2010, **183**, 583–589.
15 Y. Huang, S. Li, J. Chen, X. Zhang and Y. Chen, *Appl. Surf. Sci.*, 2014, **293**, 160–168.
16 J. Yang and K. Qiu, *Chem. Eng. J.*, 2011, **167**, 148–154.
17 Y. Tang, L. Chen, X. Wei, Q. Yao and T. Li, *J. Hazard. Mater.*, 2013, **244–245**, 603–612.
18 S. X. Li, Z. Feng-Ying, H. Yang and N. Jian-Cong, *J. Hazard. Mater.*, 2011, **186**, 423–429.
19 M. Daoud, O. Benturki, Z. Kecira, P. Girods and A. Donnot, *J. Mol. Liq.*, 2017, **243**, 799–809.
20 M. F. Imron, A. R. Ananta, I. S. Ramadhani, S. B. Kurniawan and S. R. S. Abdullah, *Environ. Technol. Innov.*, 2021, **24**, 101921.
21 L. B. L. Lim, N. Priyantha, C. M. Chan, D. Matassan, H. I. Chieng and M. R. R. Kooh, *Arab. J. Sci. Eng.*, 2014, **39**, 6757–6765.
22 M. Danish, R. Hashim, M. N. M. Ibrahim and O. Sulaiman, *J. Anal. Appl. Pyrolysis*, 2013, **104**, 418–425.
23 V. K. Gupta, M. R. Ganjali, A. Nayak, B. Bhushan and S. Agarwal, *Chem. Eng. J.*, 2012, **197**, 330–342.
24 H. Liu, P. Dai, J. Zhang, C. Zhang, N. Bao, C. Cheng and L. Ren, *Chem. Eng. J.*, 2013, **228**, 425–434.
25 J. Yang and K. Qiu, *Chem. Eng. J.*, 2011, **167**, 148–154.
26 J. Fan, J. Zhang, C. Zhang, L. Ren and Q. Shi, *Desalination*, 2011, **267**, 139–146.
27 J. M. Rosas, R. Ruiz-Rosas, J. Rodríguez-Mirasol and T. Cordero, *Carbon N. Y.*, 2012, **50**, 1523–1537.
28 L. Ren, J. Zhang, Y. Li and C. Zhang, *Chem. Eng. J.*, 2011, **168**, 553–561.
29 L. Wang, J. Zhang, R. Zhao, Y. Li, C. Li and C. Zhang, *Bioresour. Technol.*, 2010, **101**, 5808–5814.
30 N. Abdus-Salam, A. V. Ikudayisi-Ugbe and F. A. Ugbe, *Chem. Data Collect.*, 2021, **31**, 100626.
31 R. M. Reema, P. Saravanan, M. D. Kumar and S. Renganathan, *Sep. Sci. Technol.*, 2011, **46**, 1052–1058.
32 M. A. Zulfikar, H. Setiyanto and L. Solakhudin, *Desalin. Water Treat.*, 2015, **56**, 2976–2987.
33 A. Tor and Y. Cengeloglu, *J. Hazard. Mater.*, 2006, **138**, 409–415.
34 M. el A. Zennaki, L. Tennouga and S. Balkaid, *J. Macromol. Sci., Part B:Phys.*, 2024, **63**, 314–332.

Environmental Science Advances

ROYAL SOCIETY OF CHEMISTRY

PAPER

View Article Online
View Journal

Cite this: DOI: 10.1039/d5va00128e

Polymer-enhanced nickel ferrite catalyst for the efficient reduction of 4-nitrophenol as a hazard pollutant

Ghizlene Boudghene Stambouli,[ab] Belkacem Benguella,[b] Makhoukhi Benamar[b] and Ayman H. Kamel *[ac]

The synthesized nickel ferrite ($NiFe_2O_4$)/poly(aniline-*co*-*o*-toluidine) (PAOT) nanocomposite was successfully characterized using XRD, FTIR, SEM, and EDX, confirming the formation of a stable spinel structure with uniform particle distribution (32–68 nm). The material exhibited a low bandgap energy of 1.24 eV and retained magnetic properties, enabling easy recovery and reuse for up to four cycles. The catalytic activity of the $NiFe_2O_4$/PAOT nanocomposite was evaluated for the visible-light-assisted reduction of 4-nitrophenol (4-NP) without external reducing agents. The catalyst achieved reduction efficiencies of 85.83% at 2 ppm, 95% at 10 ppm, and 99% at 15 ppm within 60 min, with improved performance at higher catalyst dosages and temperatures (*e.g.*, 50 °C with 20 mg). Kinetic analysis revealed pseudo-first-order behavior. Compared to other reported catalysts, $NiFe_2O_4$/PAOT offers green synthesis, high efficiency, magnetic recoverability, and operational simplicity, making it a promising material for sustainable wastewater treatment.

Received 9th May 2025
Accepted 26th August 2025

DOI: 10.1039/d5va00128e

rsc.li/esadvances

Environmental significance

The presence of 4-nitrophenol (4-NP) in wastewater poses a significant environmental and health hazard due to its toxicity, persistence, and resistance to conventional degradation methods. This study introduces a highly efficient and sustainable approach for 4-NP reduction using $NiFe_2O_4$/POAT nanocomposite catalysts, which demonstrate exceptional catalytic performance under visible light conditions. The low bandgap energy (1.24 eV) enhances electron transfer, enabling effective degradation of pollutants without reliance on UV irradiation, making the process more energy-efficient. Furthermore, the magnetic properties of the catalyst allow for easy recovery and reuse, reducing secondary waste generation and operational costs. With a 95% reduction efficiency within one hour and reusability over multiple cycles, $NiFe_2O_4$/POAT offers a scalable and environmentally friendly alternative for wastewater treatment. These findings contribute to the development of sustainable catalytic systems that align with green chemistry principles, paving the way for improved strategies in water purification and environmental remediation.

Introduction

Globally, the development of new and creative solutions for the effective treatment of wastewater that contains harmful organic contaminants is very important.[1,2] Water is one of the primary components that sustain life on Earth. Every day, water is used for various purposes and is essential to every bodily function. Numerous things contribute to water contamination, such as agriculture, industry, and urbanization. Agricultural and industrial operations result in water contamination from fertilizers, chemicals, pesticides, heavy metals, diseases, *etc.* The health of both humans and animals is now at risk due to such activities.[3]

Aromatic nitrophenols, including 4-nitrophenol, are significant contributors to water pollution due to their extensive use in industries such as pesticides, fertilizers, dyes, paper, and plasticizers production. Additionally, they serve as precursors in the synthesis of paracetamol in the pharmaceutical industry. These nitrophenols are highly toxic, with exposure linked to carcinogenic effects in humans and other living organisms. The World Health Organization (WHO) and the U.S. Environmental Protection Agency (EPA) classify 4-nitrophenol (4-NP) as a highly toxic substance. To safeguard public health, regulations like the Mexican NOM-127-SSA1-19 945 set its permissible concentration in drinking water at 1 μg L^{-1}.[4] Prolonged or high exposure to 4-NP can impair the nervous system and reduce the blood's oxygen-carrying capacity. Inhalation of 4-NP may result in respiratory issues, including throat and lung irritation, coughing, and shortness of breath, along with systemic effects such as nausea, weakness, rapid heart rate, disorientation, and fever.

[a]*Chemistry Department, College of Science, University of Bahrain, Sakhir 32038, Kingdom of Bahrain. E-mail: ahkamel76@sci.asu.edu.eg; amohamed@uob.edu.bh*
[b]*Inorganic Chemistry and Environment Laboratory, University of Tlemcen, P. O. Box 119, 13000 Tlemcen, Algeria*
[c]*Department of Chemistry, Faculty of Science, Ain Shams University, Cairo 11566, Egypt*

Severe exposure can lead to collapse or even fatal outcomes. These compounds are highly soluble and persist at high concentrations in industrial wastewater, posing significant environmental challenges. As a result, the removal of nitrophenols from wastewater is essential.

To overcome these limitations, magnetic ferrite-based nanomaterials, particularly nickel ferrite ($NiFe_2O_4$), have emerged as promising alternatives. Ferrites exhibit superior redox properties, high surface area, low band gap energy, and excellent magnetic separability, which significantly enhance their catalytic performance while enabling easy post-treatment recovery using an external magnetic field.[5–7] Ferrites have also shown potential in applications such as dye degradation, sensing, drug delivery, and water splitting, demonstrating their multifunctionality and stability.[8,9]

Several remediation methods, including, catalytic reduction,[10] adsorption,[11] photodegradation,[12] and membrane filtration,[13] have been employed. However, these approaches often suffer from high costs and limited removal efficiency.

In catalytic decomposition, traditional catalysts like, carbon nanotubes,[14] activated carbon,[15] oxides,[16] and microporous polymers[17] have been widely utilized. However, these materials present a significant limitation in practical applications due to challenges in separating them from the treated water. This issue becomes particularly problematic in large-scale systems. The incomplete removal of these conventional catalysts from the processed solution can result in their buildup in the environment, potentially causing secondary pollution and introducing new environmental contaminants. The issue has been effectively addressed with the development of magnetic nanocatalysts, which have garnered significant research attention for reducing organic contaminants from wastewater. These materials offer unique advantages, such as a low band gap energy, high reduction capacity, and effortless separation using an external magnetic field. This minimizes the risk of secondary pollution, overcoming the limitations of traditional catalysts that are difficult to separate from contaminated solutions. Recent research has demonstrated that $NiFe_2O_4$ nanostructures can effectively catalyze the reduction of nitroaromatic compounds such as 4-NP under visible light or mild reaction conditions.[18,19] However, bare ferrite nanoparticles often suffer from agglomeration, poor dispersibility in aqueous systems, and reduced active site accessibility, which limit their catalytic efficiency.[20] To address this, researchers have begun incorporating conductive polymers—such as polyaniline (PANI), polypyrrole (PPy), and their derivatives—onto ferrite surfaces to form hybrid nanocomposites with enhanced performance.[7,20] They have been utilized in diverse applications, including dye degradation, electrochemical sensors, cancer treatment, drug delivery, gas sensing, and water splitting, owing to their high surface area and stability. Jiang *et al.* (2025) demonstrated high catalytic performance using core–shell magnetic heterojunctions for 4-NP reduction under visible light.[21] Similarly, Chen *et al.* (2025) reported a bifunctional $NiFe_2O_4$@graphene nanocomposite with enhanced stability and reusability.[22] Their potential for nitro compound removal in wastewater treatment makes them an attractive choice.

Moreover, there is growing interest in enhancing the performance of these magnetic nano-catalyst by incorporating conductive polymers like polyaniline (PANI)[23] and polypyrrole (PPy).[24] These polymers contribute additional benefits, including a low gap energy, flexibility, robust mechanical strength, and distinctive electrical properties, along with functional groups such as –NH. Several studies have highlighted that conductive polymer coatings not only reduce particle agglomeration but also improve charge carrier separation and redox kinetics, especially in ferrite-based nanocomposites.[25,26] These ferrite–polymer nanocomposites benefit from improved electrical conductivity, enhanced charge separation, redox tunability, and better stability in aqueous environments. In particular, polymers like poly(aniline-*co*-*o*-toluidine) (PAOT) possess –NH and $-CH_3$ functional groups that enhance electron delocalization and create strong interfacial interactions with ferrite nanoparticles. Such synergy facilitates electron transfer processes crucial to catalytic reduction reactions.[19,20]

Magnetic ferrite-based systems such as $NiFe_2O_4$ have been extensively utilized in various domains including dye degradation,[27] electrochemical sensors,[28] cancers treatment,[29] drug delivery,[30] gas sensing[31] and water splitting,[32] owing to their stability, high surface area, and electron transfer capabilities.

Despite their potential, $NiFe_2O_4$-based polymer nanocomposites remain underexplored for catalytic detoxification of 4-NP. Previous studies have largely focused on either bare ferrites or composites with conventional polymers. Furthermore, detailed mechanistic studies on the role of polymer-ferrite interfacial bonding, surface charge modulation, and catalyst recyclability in enhancing 4-NP reduction remain scarce. While magnetic $NiFe_2O_4$ nanoparticles have shown promise in pollutant degradation, there remains a significant gap in understanding how copolymer-functionalization, particularly with PAOT, can be leveraged to maximize their performance in wastewater treatment applications. No comprehensive studies have yet reported the synthesis, stability, and catalytic behavior of $NiFe_2O_4$/PAOT nanocomposites toward 4-NP reduction under mild conditions.

In this study, a $NiFe_2O_4$/PAOT nanocomposite was developed by first synthesizing $NiFe_2O_4$ nanoparticles and subsequently modifying them with poly(aniline-*co*-*o*-toluidine) (PAOT). The $-CH_3$ group in the *o*-toluidine aromatic ring enhances electron density, facilitating strong interactions between nickel ferrite molecules and the polymer.[33,34] These non-covalent interactions, particularly between the hydrogen of the metal complex and the electron-rich *o*-toluidine ring, contribute to the nanocomposite's enhanced stability. The use of magnetic metal ferrites, particularly nickel ferrite combined with poly(aniline-*co*-*o*-toluidine), offers notable advantages such as cost-effectiveness, high reduction efficiency, and straightforward preparation, making them highly suitable catalysts for the reduction of 4-nitrophenol. These catalysts have demonstrated significant effectiveness in addressing the challenges associated with 4-nitrophenol reduction. Furthermore, this approach highlights the potential of ferrite-poly(aniline-*co*-*o*-toluidine) composites synthesized through chemical polymerization,

which, to the best of our knowledge, remain relatively underutilized for this application.

Experimental

Chemicals and apparatus

All chemicals were utilized as received without additional purification. Ferric chloride hexahydrate ($FeCl_3 \cdot 6H_2O$, 97%) and nickel chloride hexahydrate ($NiCl_2 \cdot 6H_2O$) were sourced from Sigma-Aldrich, USA. Ammonium persulfate ($(NH_4)_2S_2O_8$), aniline ($C_6H_5NH_2$), and *o*-toluidine (C_7H_9N) were also obtained from the same supplier. Sodium hydroxide (NaOH) and hydrochloric acid (HCl) were procured from Merck, Germany. 4-Nitrophenol ($C_6H_5NO_3$) was acquired from, FLUKA Chemika, Switzerland. All reagents were of analytical grade. Ultrapure water was used for all solution preparations. Both stock and diluted, 4-NP solutions were stored in dark, airtight containers to avoid degradation.

For the instruments, FTIR spectrometer (Sp-3-300, Pye-Unicam, UK) was recorded between wave numbers of 200 and 4000 cm^{-1}. XRD analysis (ULTIMA IV, Rigaku, JAPAN), SEM analysis (JSM-IT800, JEOL Ltd, JAPAN) to examine the surface texture and porosity development, EDX analysis (JSM-IT800, JEOL Ltd, JAPAN), UV-Vis-NIR spectrophotometer (UV-3600, SHIMASZU, JAPAN), UV-visible spectrophotometer (GENESYS 10S, USA).

Synthesis of nano-sized nickel ferrite ($NiFe_2O_4$)

At room temperature (22 ± 2 °C), a solution was prepared using ferric and nickel chloride in a 2 : 1 molar ratio and stirred continuously for 30 min. A 2.0 M sodium hydroxide (NaOH) solution was then gradually introduced at a controlled rate of 1.0 mL min^{-1} until the pH of the mixture reached.[35] The reaction led to the formation of a brown precipitate (Scheme 1), which was subsequently heated to 100 °C while being stirred for one hour. The mixture was then left to mature overnight. The precipitate was thoroughly washed with distilled water until the filtrate reached a neutral pH of 7. The obtained residue was dried at 110 °C for six hours, transforming into a deep dark powder, which was then subjected to calcination at 600 °C for five hours. The final product was ground and stored in a desiccator for further use.

Synthesis of $NiFe_2O_4$/PAOT nanocomposite

Nickel ferrite-based polymer nanocomposites were synthesized through a chemical polymerization process (Scheme 2). Initially, 4.5 g of $NiFe_2O_4$ nanoparticles were dispersed in a solvent mixture containing 20 mL of chloroform and 30 mL of double-distilled water. This dispersion was subjected to ultrasonic treatment for 1 hour at room temperature (22 ± 2 °C). Concurrently, 0.05 moles of both aniline and *o*-toluidine monomers were dissolved in 200 mL of 1.0 M hydrochloric acid and stirred continuously for 30 min. The nanoparticle dispersion was then combined with the monomer solution and further sonicated for 30 minutes. Polymerization was initiated by the dropwise addition of 20 mL of a 0.1 M aqueous ammonium persulfate (APS) solution at a controlled rate of 0.5 mL min^{-1} using a peristaltic pump, while sonication continued for an additional hour. A gradual change to a black coloration was observed during the process.[36] The reaction mixture was left undisturbed overnight. The resulting nickel ferrite-poly(aniline-*co*-*o*-toluidine) composite was separated by vacuum filtration, thoroughly washed with double-distilled water and methanol, and subsequently dried at 60 °C. The final dried product was finely ground into powder for further use.

Catalytic reduction of nitrophenol

The reduction efficiency of the synthesized nanocomposites was evaluated using the batch equilibrium method. A series of 4-

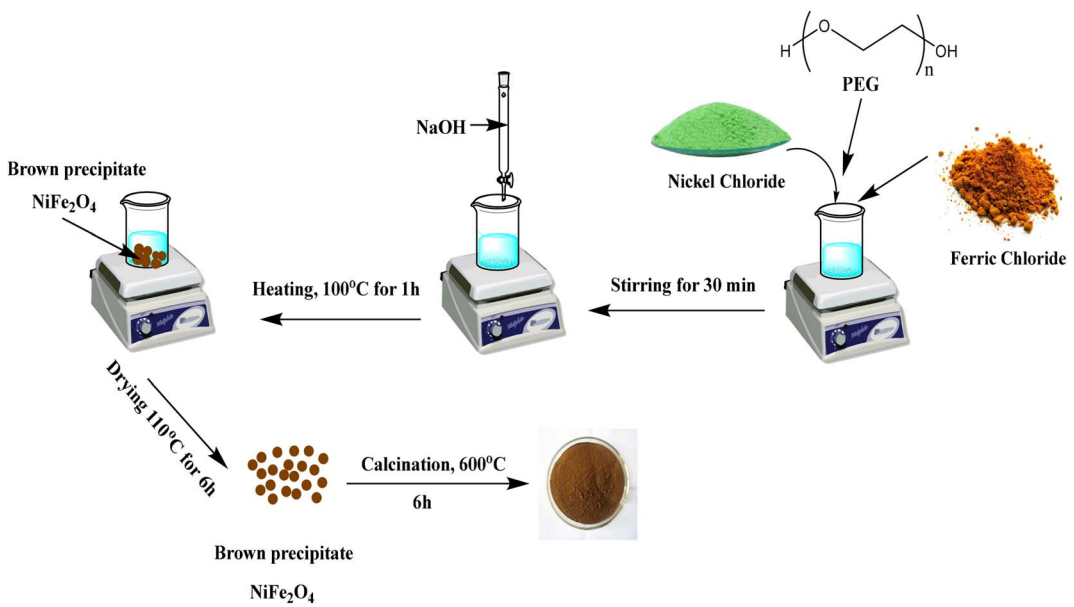

Scheme 1 Schematic representation the preparation of $NiFe_2O_4$ nanoparticles.

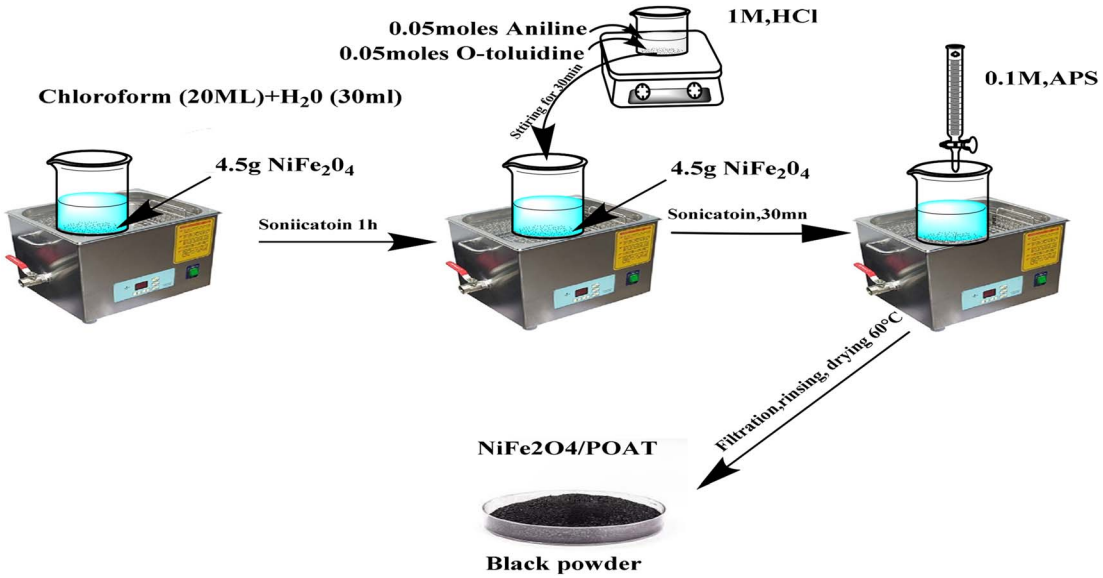

Scheme 2 Schematic representation the preparation of $NiFe_2O_4$/PAOT nanocomposite.

nitrophenol (4-NP) solutions with concentrations of 2, 10, and 15 ppm were prepared. Varying amounts (5, 10, and 20 mg) of the $NiFe_2O_4$/PAOT nanocomposite were dispersed in 10 mL of the prepared 4-NP aqueous solution, maintaining a pH of 7.43. The reaction mixtures were allowed to interact for durations ranging from 2 to 60 minutes at a constant temperature of 25 °C. After the reaction, the $NiFe_2O_4$/PAOT catalyst was separated by centrifugation, with additional recovery facilitated using a magnetic bar. The conversion of 4-nitrophenol (4-NP) to 4-aminophenol (4-AP) was quantitatively analyzed using spectrophotometry. The maximum absorption wavelength (λ_{max}) was recorded at 400 nm for 4-NP and 318 nm for 4-AP.

Results and discussion

Characterization of the nanomaterial composite

Fourier transform infra-red (FT-IR) spectroscopy. Fig. 1 presents the FTIR spectra of $NiFe_2O_4$ nanoparticles post-calcination and the $NiFe_2O_4$/PAOT nanocomposite after copolymerisation. The IR spectrum of calcined $NiFe_2O_4$ (ref. 37) nanoparticles shows a thin, broad band at about 3440 cm^{-3}. This band shows the O–H stretching and vibrational modes of the water that is adsorbed in the KBr pellet manufacturing process. The asymmetric stretching vibrations of the adsorbed carbonate groups account for two additional bands located between 1632 and 1382 cm^{-1}. The characteristic bands seen at 585–453 cm^{-3} are caused by the intrinsic stretching vibrations of the Fe–O and Ni–O bonds in the spinel structure. The spectra of calcinated $NiFe_2O_4$ nanoparticles exhibit no additional peaks.[38] On the other hand, the infrared spectrum of the $NiFe_2O_4$/poly(aniline-*co*-*o*-toluidine) composite shows a broad band in the 3384–3230 cm^{-3} range. This band is due to N–H stretching, which is made wider by hydrogen bonding. A band seen between 2920 and 2852 cm^{-3} shows the stretching vibrations of the $-CH_3$ group in the toluidine moiety. The bands observed in the 1587–1485 cm^{-1} region are attributed to the stretching vibrations of N–H and C=N. Bands present in the 1149–1006 cm^{-1} range are linked to the bending of the C–H plane. Finally, the metal–oxygen vibrations in the spinel crystal lattice are linked to two separate bands that span from 572 to 415 cm^{-3}.

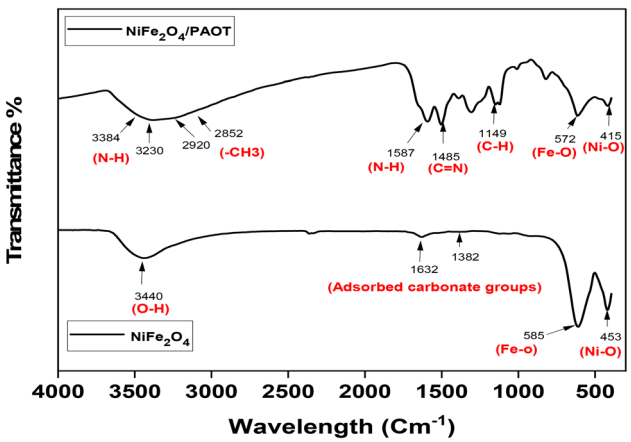

Fig. 1 FTIR spectra of $NiFe_2O_4$ nanoparticles and $NiFe_2O_4$/PAOT nanocomposite.

SEM microscopic analysis. The unique morphological features of $NiFeO_4$ are revealed by the SEM image Fig. 2(a), which emphasises homogeneous particle distribution and nanoscale structure. The distribution of the particle sizes is rather uniform and homogeneous, ranging from roughly 45 nm to 56 nm. This nanoscale size can increase the material's surface area, which is essential to its catalytic and magnetic capabilities. High-quality $NiFeO_4$ synthesis is demonstrated by the tightly packed particle arrangement with little agglomeration. Applications like adsorption, catalytic reduction, and other environmental cleanup procedures benefit from this morphology.[39]

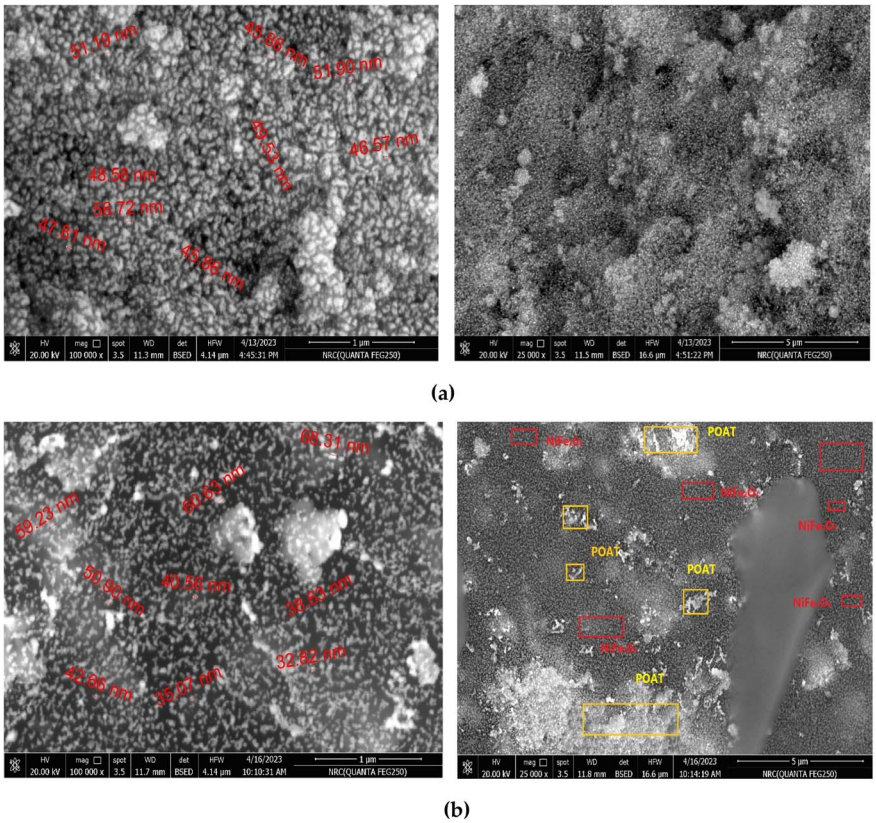

Fig. 2 SEM images of (a) $NiFe_2O_4$, and (b) $NiFe_2O_4$ coated with poly[*co*-*o*-toluidine + aniline].

The SEM image in Fig. 2(b), recorded at a scale of 1 μm, shows the structural and morphological changes in $NiFe_2O_4$ coated with poly(*o*-toluidine-*co*-aniline), resulting from the presence of the polymer.[40] The histograms in Fig. 3 shows the particle sizes vary from about 32 nm to 68 nm, suggesting that the polymer coating causes variations in the distribution. The polymer produces a smoother and more cohesive surface morphology, and the image shows a rather uniform dispersion of particles. The polymer's presence is probably what improves material stability and decreases particle aggregation. While preserving the fundamental nanoscale characteristics of $NiFeO_4$, this coating adds novel surface characteristics that are beneficial for catalytic and environmental applications.

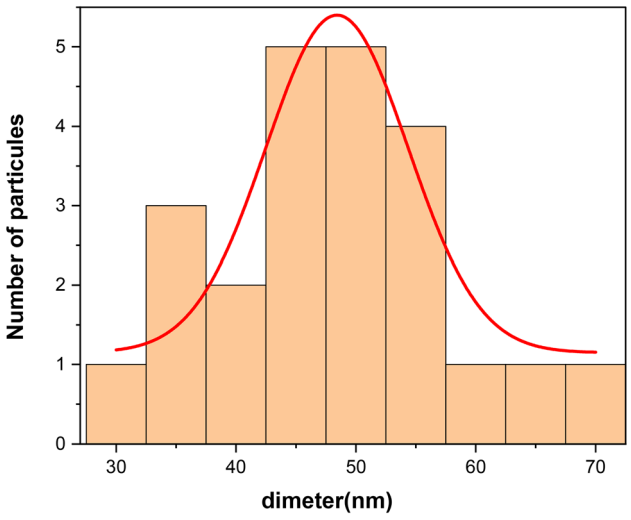

Fig. 3 Particle size distribution histogram of $NiFe_2O_4$ and $NiFe_2O_4$ coated with poly(aniline-*co*-*o*-toluidine) based on SEM analysis.

EDX spectrum. The EDX analysis in Fig. 4 showed that the synthesis and surface modification went well by confirming the elemental makeup of $NiFe_2O_4$ and its polymer-coated form. Following the expected spinel structure, the analysis found that $NiFe_2O_4$ is mostly made up of oxygen, iron, and nickel. Iron had the highest weight percentage (62.71%), indicating its dominant presence in the structure, but oxygen had the lowest weight percentage (26.15%) due to its lower atomic mass. The expected stoichiometric ratio was met by the smaller amounts of nickel (11.13% by weight). Iron and oxygen have modest error margins, indicating accurate measurements. Because lighter elements like carbon and nitrogen were incorporated from the polymer layer, the atomic percentages of metal elements in the polymer-coated $NiFe_2O_4$ sample fell. Furthermore, trace levels of chlorine were found, indicating the presence of small amounts of residual contaminants. The results showed that the polymer coating changed the surface by adding lighter parts while keeping the spinel structure of the core material.

Powder X-ray diffraction (XRD) analysis. The synthesized materials were subjected to analysis of their structural

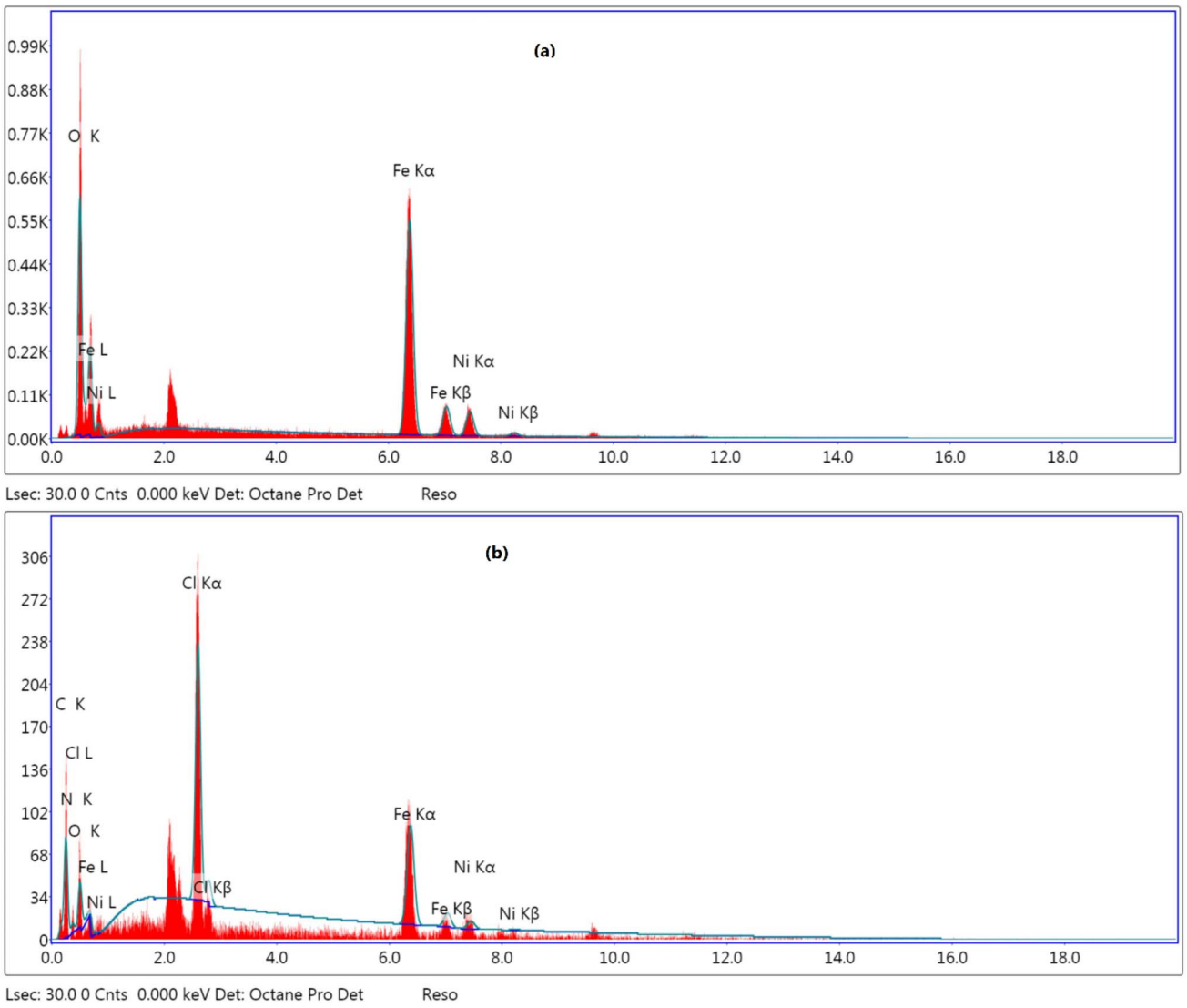

Fig. 4 (a) EDX of $NiFe_2O_4$ (a), (b) EDX spectrum of $NiFe_2O_4$ coated with poly(aniline-*co*-*o*-toluidine).

properties through X-ray diffraction (XRD). XRD patterns for $NiFe_2O_4$ nanoparticles[37] and $NiFe_2O_4$/PAOT nanocomposites were acquired using a powder X-ray diffractometer (PANalytical, Almelo, Netherlands) with CuKα radiation ($\lambda = 0.154$ nm) across a scanning range of 10° to 70°. The diffraction patterns, in accordance with the JCPDS standard (card no. 10-0325), confirmed the formation of a cubic spinel crystal structure, as depicted in Fig. 5.[36,37] No further peaks suggesting the presence of impurities like NiO or FeO_3 were detected. Polymer-enhanced nickel ferrite catalysts for the efficient reduction of 4-nitrophenol pollutants. Seven important diffraction peaks were found at 2, values of 30.24°, 35.48°, 36.94°, 43.06°, 53.80°, 57.20°, and 62.88°, corresponding to the crystal planes (311), (220), (222), (422), (511), (400), and (440). The XRD pattern of $NiFe_2O_4$/PAOT nanocomposites was mostly the same as that of pure $NiFe_2O_4$ nanoparticles, with the addition of a broad diffraction band seen between $2\theta = 15°$ and 25.[36] This was because the PAOT copolymer matrix is amorphous in Fig. 5.[36] The observed decrease in diffraction peak intensities in the nanocomposite relative to the pure $NiFe_2O_4$ nanoparticles suggests that PAOT was successfully integrated onto the $NiFe_2O_4$ surface while maintaining its crystalline structure. The average particle sizes of $NiFe_2O_4$ and $NiFe_2O_4$/PAOT were estimated using Scherrer's equation.

$$D = (K\lambda)/(\beta\cos\theta) \quad (1)$$

The Scherrer equation defines D as the crystallite size, λ as the wavelength of the X-ray radiation (CuKα, 0.154 nm), θ as the Bragg diffraction angle (in radians), and β as the full width at half maximum (FWHM) of the most intense XRD peak, particularly for the (311) plane. The value of the Scherrer constant (k) was set at 0.9. The calculation method yielded estimated average crystallite sizes of 12.3 nm for $NiFe_2O_4$ nanoparticles and 16.7 nm for $NiFe_2O_4$/PAOT nanocomposites.[36]

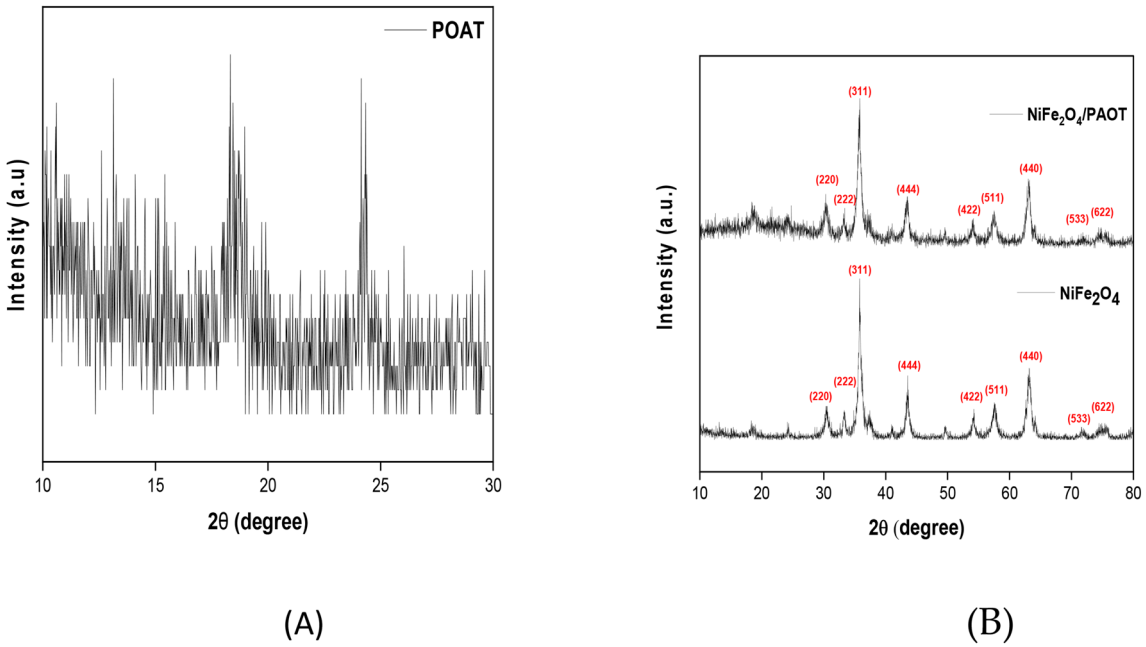

Fig. 5 XRD patterns of (A) PAOT, and (B) $NiFe_2O_4$ nanoparticles and $NiFe_2O_4$/PAOT nanocomposite.

In both the bare $NiFe_2O_4$ and the $NiFe_2O_4$/PAOT nanocomposite, additional diffraction peaks are observed in the high-angle region between 70° and 80° (2θ). These peaks correspond to the (533) and (622) crystallographic planes of the spinel $NiFe_2O_4$ phase, in agreement with the standard JCPDS card no. 10-0325. The presence of these reflections in both samples confirms that the crystalline spinel structure of $NiFe_2O_4$ is retained after polymer coating. The PAOT modification does not introduce new crystalline peaks in this range, indicating that the polymer layer is amorphous in nature and does not alter the fundamental crystal lattice of the ferrite core.

Catalytic degradatoin of 4-nitrophenol (NP). The process of catalytic reduction stands as the most effective method for converting hazardous nitrophenols, exemplified by 4-nitrophenol (4-NP), into benign aminophenols. Solutions that incorporate 4-NP display an absorbance peak within the range of 300 to 400 nm, with distinct absorption maxima identified at 400 nm for 4-NP and at 318 nm for 4-aminophenol (4-AP), as illustrated in Fig. 6. Upon the introduction of $NiFe_2O_4$ coated with poly[*o*-toluidine + aniline], the solution exhibited a discernible colour transition from dark yellow to light yellow within a span of 60 min.

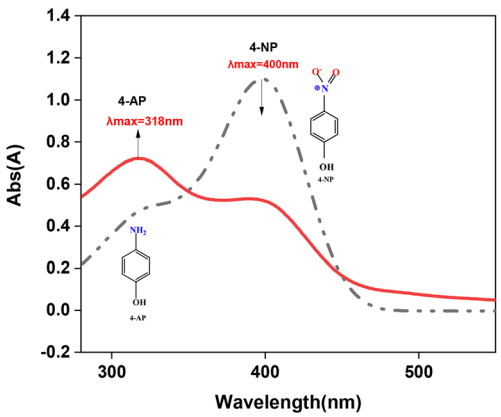

Fig. 6 Absorption peaks of 4-nitrophenol and 4-aminophenol in UV-Vis spectrum.

Solutions with concentrations of 2, 10, and 15 ppm were employed to investigate the catalytic reduction of 4-NP in 10 mL. Due to the magnetic properties of the materials, we implemented a glass stirrer to ensure homogenous suspension agitation. 10 mg of the catalyst was introduced after five minutes of continuous agitation, and the mixture was stirred for an additional 60 min at room temperature thereafter. The darker yellow colouration progressively dissipated during this period. Molecular absorption spectroscopy was employed to monitor the absorbance at 400 nm in order to ascertain the conversion of 4-NP to 4-AP. The relative concentration of 4-NP was then calculated using the following formula:[41]

$$C_t/C_0 = I_t/I_0 \quad (2)$$

The C_0 (mg L^{-1}) value shows how much 4-NP was in the solution before the catalyst was added. The C_t (mg L^{-1}) value shows how much 4-NP was still in the solution at a certain time after the catalyst was added. I_0 and I_t represent the absorbance intensities of 4-NP measured at 400 nm at $t = 0$ (prior to the addition of the catalyst) and at any later reaction time, respectively. The intensities were presumed to have a direct correlation with the concentration of 4-NP in the reaction system.

Effect of 4-NP concentration. The catalytic reduction of 4-nitrophenol (4-NP) to 4-aminophenol (4-AP) was examined using $NiFe_2O_4$ coated with poly[*o*-toluidine + aniline]. The study was conducted at initial concentrations of 2 ppm, 10 ppm, and

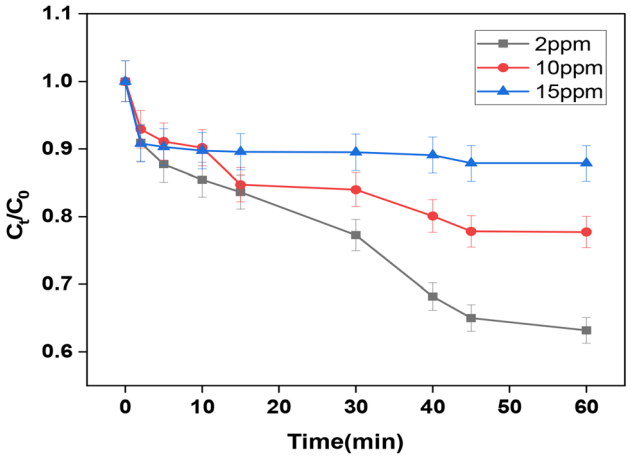

Fig. 7 Effect of $C_{NiFe_2O_4/PAOT}$ on the reduction of (4-NP) [$V_{solution}$ = 10 mL, T = 25 °C, pH = 7.43, [4-NP] = 2, 10, 15 ppm; m = 10 mg].

15 ppm over a reaction period of 60 min using a catalyst dosage of 10 mg, as shown in Fig. 7. At a starting concentration of 2 ppm, the reduction happened faster, as shown by a steeper drop in the C_t/C_0 ratio to 0.631. This means that the catalyst was more effective at lower substrate concentrations. At 10 ppm, the reaction rate exhibited a moderate level, with a more gradual decline in C_t/C_0 relative to 2 ppm, reaching a value of 0.77, indicating a reduction in catalytic activity with increasing concentration. At a concentration of 15 ppm, the reaction progressed most slowly and exhibited the lowest reduction efficiency at equilibrium. After 60 min, the C_t/C_0 ratio was 0.878. Since the catalyst dose was only 10 mg, higher concentrations of 4-NP may stop the reaction. This is probably because the active site is full or there are problems with mass transfer.

The $NiFe_2O_4$/POAT catalyst's conduction band acts as an electron source, allowing interactions between active electrons (e^-) and 4-NP. These interactions help reduce the $-NO_2$ group to $-NH_2$ by moving electrons and protons around. $NiFe_2O_4$/POAT has a low energy band gap, which makes it easier for 4-NP to turn into 4-AP. This is done by efficiently moving electrons between the catalyst and the pollutant, which speeds up the reaction. The polymer layer enhances electron mobility between the catalyst and 4-NP, thereby increasing its catalytic activity. However, this enhancement decreases when the system is saturated or overloaded, resulting in a decline in catalytic efficiency.[42]

Fig. 7 illustrates the spectral evolution of the 4-NP reduction reaction. At 0 minutes, the absorbance peak at 400 nm reaches its maximum, signifying the initial concentration of 4-NP. During the reaction, the peak at 400 nm diminishes progressively, whereas the peak at 318 nm rises, indicating the transformation of 4-NP to 4-AP. At 2 ppm, the absorbance curve drops more quickly at 400 nm than at 10 ppm and 15 ppm. This means that the reaction happens faster at lower concentrations. The observed trends indicate that $NiFe_2O_4$/POAT shows superior catalytic performance at lower concentrations, as diminished competition for active sites enhances electron transfer and reaction advancement.

Fig. 8 illustrates the time-dependent UV-visible spectral changes during the catalytic reduction of 4-nitrophenol (4-NP) to 4-aminophenol (4-AP) using $NiFe_2O_4$/PAOT nanocomposites at initial concentrations of (a) 2 ppm, (b) 10 ppm, and (c) 15 ppm. At the start of the reaction (t = 0 min), a strong absorbance peak is observed at 400 nm in all spectra, corresponding to the 4-nitrophenolate ion. As the reaction proceeds, the intensity of this peak gradually decreases, indicating the progressive consumption of 4-NP. Simultaneously, a new peak appears around 318 nm, which corresponds to the formation of 4-aminophenol (4-AP), the final reduction product. The rate of peak reduction is more rapid at lower concentrations (2 ppm), suggesting enhanced catalytic activity due to reduced competition for active sites. At higher concentrations (10 and 15 ppm), the peak reduction is slower, indicating a concentration-dependent reaction rate. The spectral shift and disappearance of the 400 nm peak, accompanied by the emergence of the 318 nm band, provide clear evidence for the successful transformation of 4-NP into 4-AP, demonstrating the efficiency of $NiFe_2O_4$/PAOT as a visible-light-responsive catalyst under ambient conditions.

Kinetics of the reduction process of nitrophenol. The reduction rate of nitrophenol can be analyzed using a pseudo-first-order kinetic model, as described in prior studies.[43] For the 4-nitrophenol (4-NP) reduction process, the ratio of the concentration of 4-NP at any time t (C_t) to its initial concentration at t = 0 (C_0) is equivalent to the ratio of the corresponding absorbance values A_t/A_0 measured at a wavelength of 400 nm. Based on this relationship, the kinetic equation governing the reduction process can be expressed bu eqn (3):[44]

$$-\ln(C_t/C_0) = -\ln(A_t/A_0) = K_{app}t \quad (3)$$

The apparent rate constant (K_{app}) can be calculated from the slope of the linear graph of $\ln(C_t/C_0)$ *versus* reaction time. Fig. 9 demonstrates a linear relationship between $\ln(A_t/A_0)$ and time, confirming that the reduction of 4-NP using $NiFe_2O_4$/POAT followed pseudo-first-order kinetics. Furthermore, the catalytic reduction of 2-NP with $NiFe_2O_4$/POAT was also examined. Fig. 9 illustrates that the linear trend of $\ln(A_t/A_0)$ against time also suggests that the reduction of 2-NP adhered to pseudo-first-order kinetics. The apparent rate constants (K_{app}) are calculated based on the slopes of the corresponding lines. At 2 ppm ($K_{app} = 1.16 \times 10^{-2}$ min^{-1}, $R^2 = 0.98$), 10 ppm ($K_{app} = 3.5 \times 10^{-3}$ min^{-1}, $R^2 = 0.96$), 15 ppm ($K_{app} = 5.44 \times 10^{-4}$ min^{-1}, $R^2 = 0.94$) dependency on concentration: the reduction rate exhibits significant variation as initial concentrations increase. This change could be caused by differences in how easy it is to get to active sites on the catalyst or by changes in how the 4-NP molecules interact with the surface of the catalyst.

Effect of the catalyst dose. Fig. 10 shows how the amount of $NiFe_2O_4$/PAOT catalyst affects the breakdown of 4-nitrophenol (4-NP). This evaluation was conducted at various initial concentrations (2 ppm, 10 ppm, and 15 ppm) with catalyst amounts of 5 mg, 10 mg, and 20 mg. An increase in catalyst mass led to a decrease in the C_t/C_0 ratio (where C_t denotes the remaining 4-NP concentration and C_0 is the initial

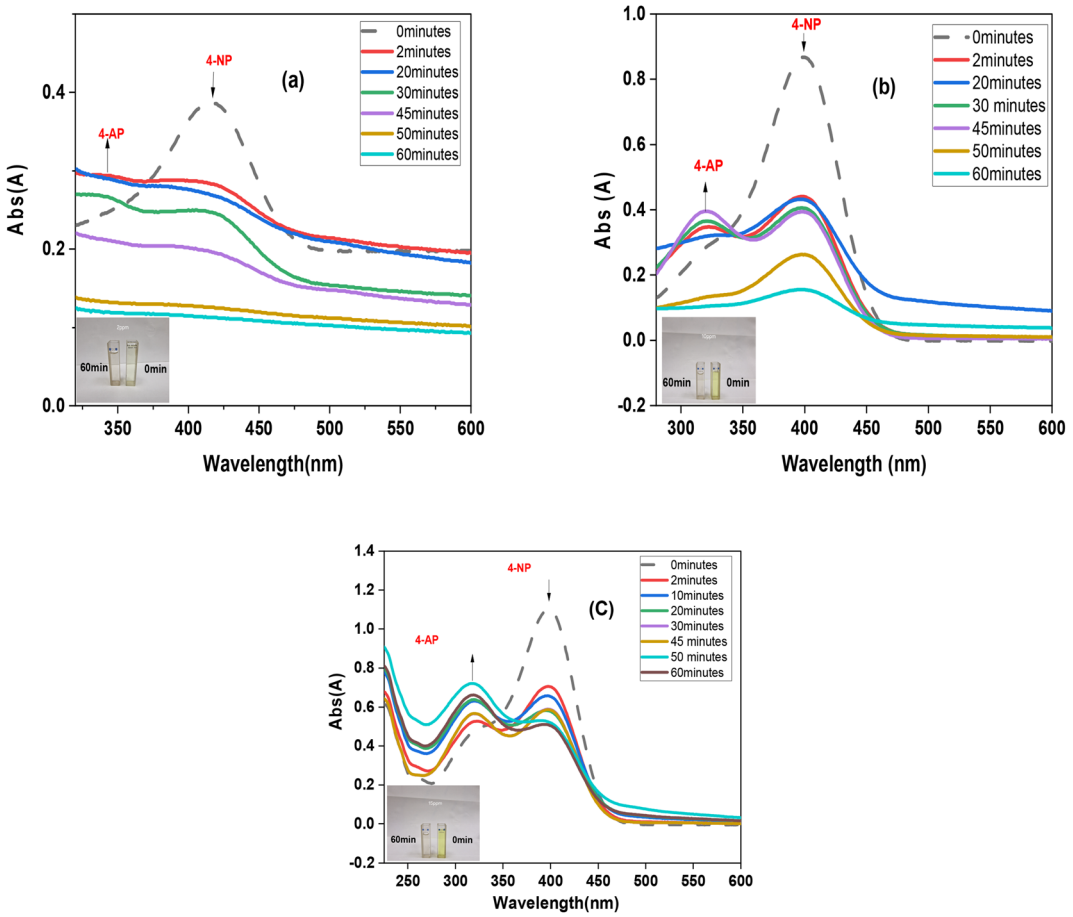

Fig. 8 UV-visible spectra of the reduction reaction of 4-NP to 4-AP at (a) 2 ppm, (b) 10 ppm, and (c) 15 ppm.

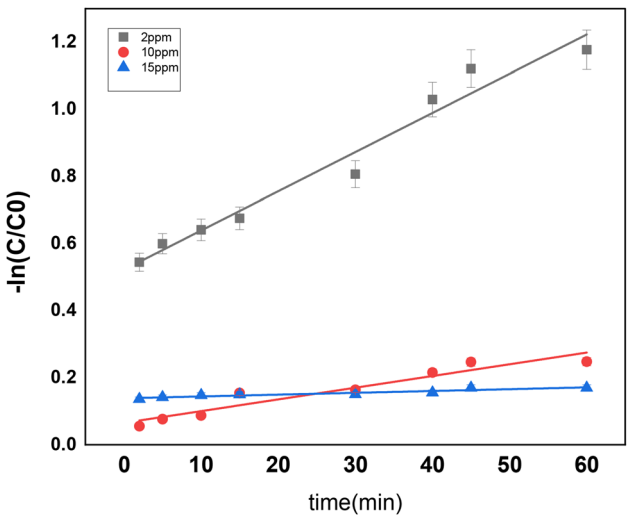

Fig. 9 Rate of reduction of 4-nitrophenol at different concentrations using 10 mg of $NiFe_2O_4$/POAT.

concentration), suggesting enhanced reduction efficiency. The 2 ppm solution exhibited the most notable reduction, with the C_t/C_0 ratio dropping to 0.545 at 20 mg of catalyst, indicating a highly effective degradation process. A comparable trend was noted for the 10 ppm and 15 ppm solutions, with the C_t/C_0 ratio reducing to 0.59 and 0.78, respectively, at 20 mg of catalyst. Nonetheless, the degree of reduction appeared to diminish at elevated concentrations, indicating that a larger catalyst dosage is necessary for efficient reduction as pollutant levels rise. The findings highlight that increasing the catalyst dose improves

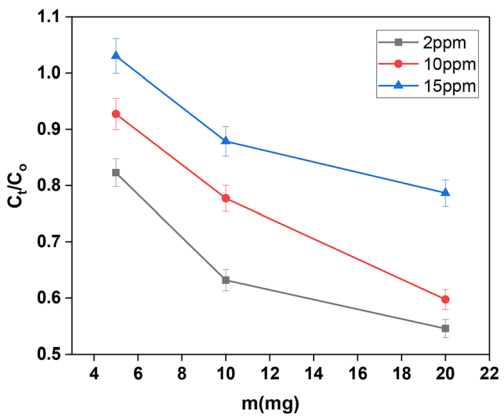

Fig. 10 Effect of dose ($NiFe_2O_4$/PAOT) on the reduction of (4-NP): $V_{solution} = 10$ mL, $T = 25$ °C, pH = 7.43, [4-NP] = 2, 10, 15 ppm, $m = (5, 10, 20)$ mg.

reduction efficiency, with a more pronounced effect observed at lower pollutant concentrations. At higher concentrations, the efficiency gain diminishes, highlighting the importance of optimizing catalyst dosage based on pollutant levels for maximum effectiveness.[45]

Temperature effect. The reduction efficiency of 4-nitrophenol (4-NP) was assessed at two temperatures, 37 °C and 50 °C, employing $NiFe_2O_4$/POAT as a catalyst, as illustrated in Fig. 11. The findings demonstrate that temperature significantly influences the reduction process. At 37 °C, the reduction efficiency is comparatively lower, with 2 ppm reaching a maximum efficiency of over 64%. In contrast, higher concentrations of 10 ppm and 15 ppm yield efficiencies of 38% and 37%, respectively. At 50 °C, the efficiency reduction markedly enhances, achieving 64% for 2 ppm, 63% for 10 ppm, and 61% for 15 ppm, indicating a more effective catalytic process. Elevated temperatures augment the kinetic energy of reactant molecules, facilitating their interaction with the active electrons of $NiFe_2O_4$/POAT. Moreover, increased temperatures may enhance the electron transfer process from 4-NP to 4-AP, which is a vital component of the reduction mechanism. The findings indicate that the reduction of 4-NP is influenced by temperature, with elevated temperatures enhancing catalytic performance. The results suggest that 50 °C may be an optimal temperature for maximizing reduction efficiency under the specified reaction conditions.[46,47]

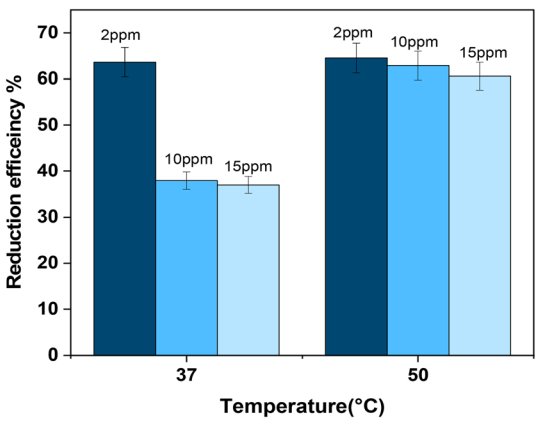

Fig. 11 Effect of temperature on the reduction of 4-NP [$V_{solution}$ = 10 mL, T = (37, 50) °C, pH = 7.43, [4-NP] = 2, 10, 15 ppm].

Catalyst optimization. The UV-visible absorption spectra illustrate the catalytic reduction of 4-NP to 4-AP under optimal conditions, utilising 20 mg of $NiFe_2O_4$/POAT as a catalyst at 50 °C, as shown in Fig. 12. The research was carried out using various initial concentrations of 4-NP (2 ppm, 10 ppm, and 15 ppm) and documented at two time points: t = 0 min and t = 60 min. At the initiation of the reaction (t = 0 min), all samples exhibited a pronounced absorption peak at 400 nm, indicative of the nitrophenolate ion, which represents the characteristic form of 4-NP under alkaline conditions. The absorbance intensity exhibited an increase corresponding to higher concentrations of 4-NP, with the maximum observed for the 15 ppm solution. Following a 60 minute period, a notable decrease in absorbance at 400 nm was recorded across all concentrations, validating the conversion of 4-NP to 4-AP. The calculated percentage reductions were 85.83% for 2 ppm, 95% for 10 ppm, and 99% for 15 ppm, highlighting the effectiveness of $NiFe_2O_4$/POAT in the reduction process. The results show that the catalyst does a good job of helping to change 4-NP. The higher the starting concentration, the faster the reaction goes, and within 60 minutes, almost all the 4-NP has been changed.

The data in Table 1 highlights the efficiency and operating conditions of various catalysts used for the reduction of 4-nitrophenol (4-NP), a hazardous environmental pollutant. Among them, $NiFe_2O_4$ modified with polyaniline (POAT) exhibited exceptional performance, achieving reduction efficiencies of 85%, 95%, and 99% for 2 ppm, 10 ppm, and 15 ppm concentrations, respectively, within 60 minutes. Compared to other reported catalysts, $NiFe_2O_4$/POAT demonstrates significant advantages. While catalysts like $NiFe_2O_4$/RGO and Bi_2S_3@Fe_3O_4 achieved near-complete reduction, $NiFe_2O_4$/POAT maintains consistently high efficiency across varying concentrations, highlighting its robustness and suitability for visible light-driven pollutant reduction in wastewater treatment applications. Unlike many catalysts that require $NaBH_4$ as

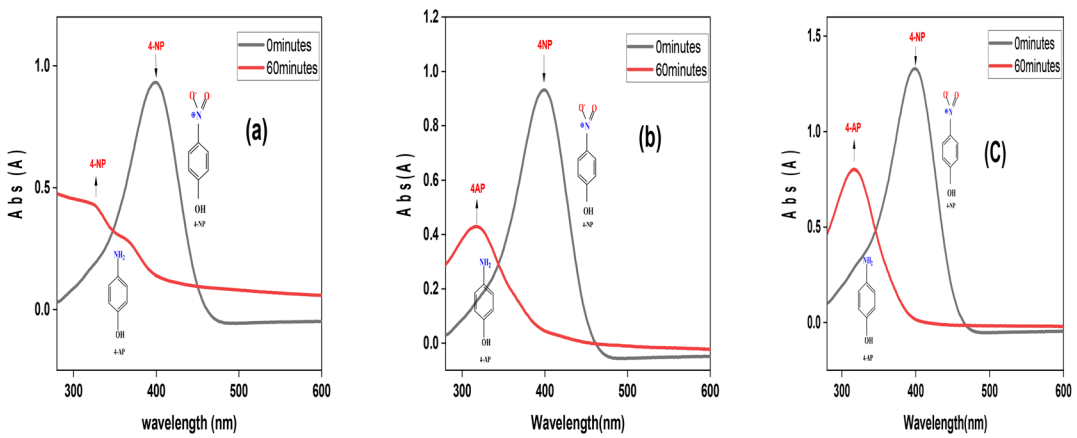

Fig. 12 The UV-Vis absorption spectra change for the reduction process of 4-NP for: (a) 2 ppm, (b) 10 ppm, and (c) 15 ppm.

Table 1 Comparison of previously reported catalysts for 4-nitrophenol reduction

Catalysts	Reduction efficiency (%)	Time (min)	Concentration	Gap energy (eV)	Reducing agent	Ref.
$NiFe_2O_4$	75	120	10 ppm	1.58	—	48
$Ni_{0.7}Cu_{0.3}Fe_2O_4$	82	120	10 ppm	1.48	—	48
$NiZnFe_2O_4$/CQDs	96	20 s	—	1.87	$NaBH_4$	33
$TiO_2/CoFe_2O_4$	95	35	10 ppm	3.2	$NaBH_4$	49
$CuFe_2O_4$	95	40 s	0.005 ppm	—	$NaBH_4$	50
$NiFe_2O_4$/RGO	100	30	0.036 M	—	$NaBH_4$	33
rGO/Cu-BDC MOF	44.67	8	0.04 mM	—	$NaBH_4$	51
$Bi_2S_3@Fe_3O_4$	98	29	0.1 mM	2.72	$NaBH_4$	52
g-C_3N_4/Bi_2S_3	60	60	0.125 mM	—	$NaBH_4$	53
Bi_2S_3 NSs	70	60	0.125 mM	—	$NaBH_4$	53
CuO/kaolinNC-1	99	12	20 ppm	—	$NaBH_4$	47
$BiFeO_3$	96	4.5	20 ppm	2.2	$NaBH_4$	54
$NiFe_2O_4$/POAT	85	60	2 ppm	1.24	—	This work
	95		10 ppm			
	99		15 ppm			

a reducing agent, this study eliminates the use of toxic and expensive chemicals, making $NiFe_2O_4$/POAT an eco-friendly and cost-effective alternative. Its alignment with green chemistry principles minimizes environmental risks and operational costs. Additionally, the lower energy band gap (1.24 eV) enhances electron transfer and catalytic activity, offering advantages over alternatives such as $NiZnFeO_4$/CQDs (1.87 eV), $TiO_2/CoFe_2O_4$ (3.2 eV), and $Bi_2S_3@Fe_3O_4$ (2.72 eV). While catalysts like $CuFe_2O_4$ achieve rapid reduction in 40 seconds, the scalability and stability of $NiFe_2O_4$/POAT over a practical 60 minute timeframe make it more suitable for industrial and real-world wastewater treatment applications. This study presents $NiFe_2O_4$/POAT as a scalable, efficient, and economically viable solution for 4-NP reduction, addressing both environmental and toxicological concerns. Its ability to function without a conventional reducing agent marks a significant step toward sustainable water treatment technologies. Overall, this work contributes to the advancement of green and innovative catalytic systems, paving the way for broader adoption in environmental remediation efforts.

Reusability of $NiFe_2O_4$/PAOT nanocomposite. The usability of $NiFe_2O_4$/PAOT nanocomposite was examined to determine whether the catalyst could be used for repeated reduction of 4-NP in successive cycles. Every cycle was carried out as described above. An external magnet bar was used to separate the catalyst from the test solution at the end of each cycle. After dipping the catalyst in 50 mL of 40 ppm NaOH for one hour, it was repeatedly cleaned with methanol and distilled water until the pH reached about 7, at which point it was dried. Sequential cycles were performed using the regenerated catalyst. eqn (3) (ref. 55) was used to determine the decreasing efficiency for % 4-NP after each cycle:

$$\text{Reduction efficiency (\%)} = ((C_0 - C_{eq})/C_0) \times 100 \quad (4)$$

From Fig. 13, it can be observed that in the first cycle, the catalyst achieves a high reduction efficiency of around 91%, indicating its initial effectiveness in reducing 4-NP. However, as the cycles progress, the reduction in efficiency significantly decreases. In the second cycle, the efficiency drops to approximately 71%, and by the third cycle, it further decreases to around 38%. By the fourth cycle, the catalyst only degrades to a minimal amount of 4-NP (~9%). The drastic decline in the fourth cycle is attributed to severe catalyst deactivation after repeated use. Several factors may contribute to this behavior: (i) partial loss of catalyst mass during recovery despite magnetic separation, (ii) surface fouling by strongly adsorbed intermediates or by-products that block active sites, (iii) structural or morphological changes during repeated reaction-regeneration cycles (including polymer detachment and reduced conductivity), and (iv) agglomeration of magnetic nanoparticles, which decreases the active surface area and dispersion in solution. While the $NiFe_2O_4$/PAOT nanocomposite shows strong catalytic activity in the initial runs, these cumulative effects limit its long-term reusability—a challenge similarly reported for ferrite–polymer composites in previous studies.[56,57]

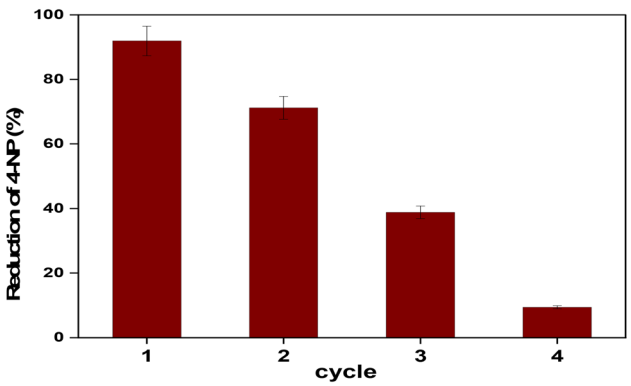

Fig. 13 Reusability of the $NiFe_2O_4$/POAT catalyst for 4-NP reduction.

Mechanism of catalytic reduction of 4-nitrophenol. The catalytic reduction of 4-nitrophenol (4-NP) to 4-aminophenol (4-AP) using $NiFe_2O_4$/POAT composite operates through an electron-driven mechanism facilitated by enhanced charge carrier dynamics.[58] $NiFe_2O_4$ represented by (Fig. 14), a ferrite

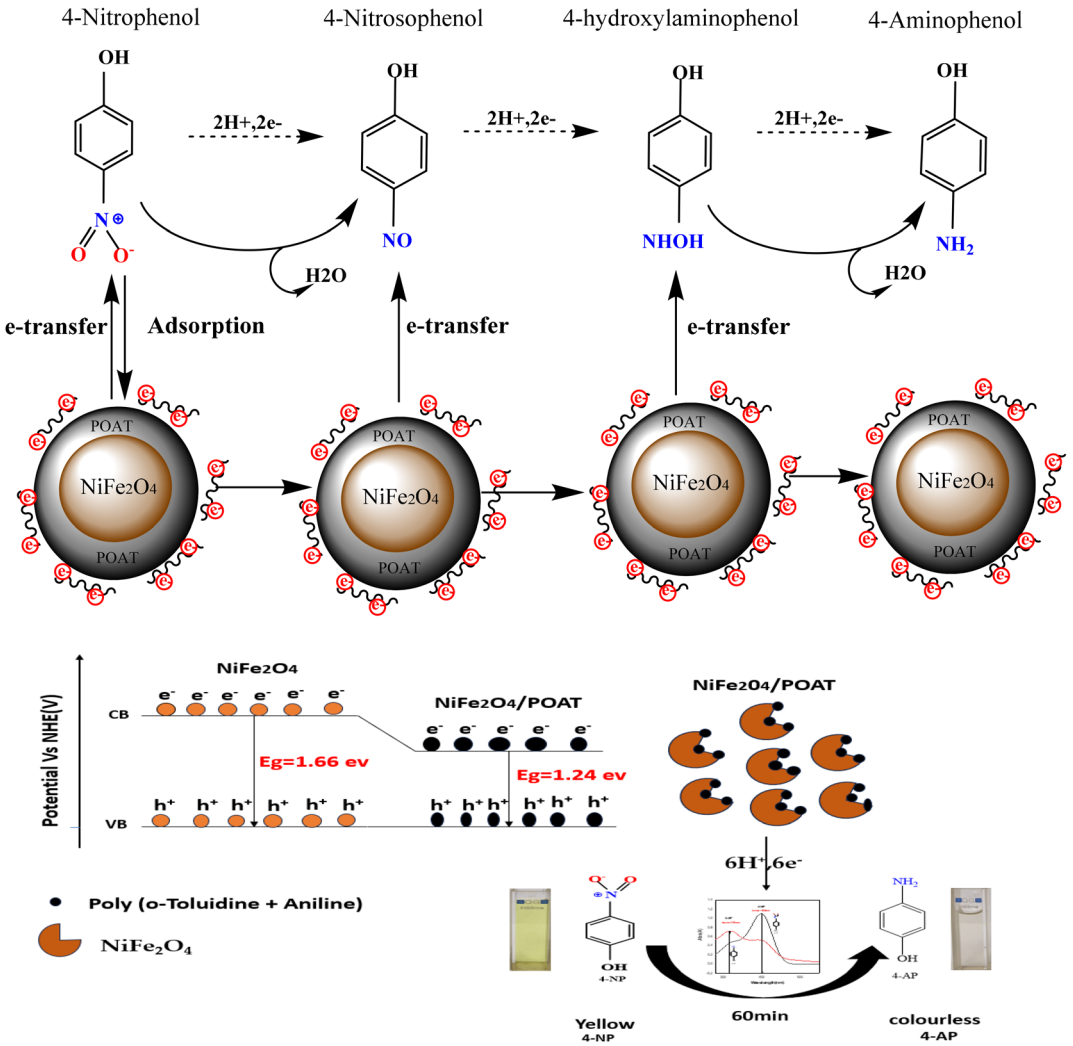

Fig. 14 Proposed mechanism of 4-nitrophenol reduction to 4-aminophenol on the catalyst surface.

material with a bandgap of 1.66 eV, absorbs visible light, generating electron–hole pairs. The incorporation of POAT into $NiFe_2O_4$ reduces the bandgap to 1.24 eV, leading to improved electron mobility and charge separation efficiency. During the reaction, electrons from the conduction band (CB) of $NiFe_2O_4$/POAT are transferred to the nitro group ($-NO_2$) of 4-NP, initiating a stepwise reduction process. The reaction proceeds through intermediate species, including nitroso (–NO) and hydroxylamine (–NHOH), ultimately yielding 4-aminophenol (4-AP) as the final product. Protons from the reaction medium combine with these electrons to complete the reduction. The composite's improved electron transport properties minimize recombination of charge carriers, ensuring a continuous supply of electrons for the reaction. The transformation is evidenced by a color change in the solution from yellow (indicating 4-NP) to colourless (indicating 4-AP). This change is further verified using UV-visible spectroscopy, which shows the disappearance of the characteristic absorption peak of 4-NP at 400 nm, and the appearance of a new peak at 318 nm. The reaction is completed within 60 min, demonstrating the superior catalytic efficiency of the $NiFe_2O_4$/POAT composite.

The 4-nitrophenol (4-NP) molecules are drawn to the surface of $NiFe_2O_4$ due to aromatic interactions: π–π stacking between the aromatic ring of 4-NP and the catalytic surface enhances adsorption. The copolymer poly(aniline-*co*-*o*-toluidine) acts as a source of electrons due to its electroactive nature. The copolymer has good electronic conductivity, which facilitates the transfer of electrons. Thanks to the oxidation/reduction cycles of the aniline and *o*-toluidine units, the polymer provides the necessary electrons for the catalytic reduction process (4-NP to 4-AP). $NiFe_2O_4$ plays the role of a semiconductor here, facilitating the migration of electrons from the copolymer to 4-nitrophenol. The Ni^{2+} and Fe^{3+} ions in the $NiFe_2O_4$ structure provide active sites that promote electron transfer and reduction reactions. The poly(aniline-*co*-*o*-toluidine) transfers electrons to the metal ions (Ni^{2+}/Fe^{3+}) on the surface of $NiFe_2O_4$. Once activated, $NiFe_2O_4$ transfers electrons to 4-nitrophenol, the band gap energy of $NiFe_2O_4$/POAT nanocomposites is low (1.24 eV) enough to excite electrons from the valence band to the conduction band. This is the main reason that facilitates the transfer of electrons from the $NiFe_2O_4$/POAT

nanocomposites to 4-nitrophenol, which is reduced to 4-aminophenol.

The conductive polymer, poly[aniline-*co*-*o*-toluidine], plays a crucial role in providing electrons for the reduction of 4-NP, $NiFe_2O_4$ facilitates electron transfer from first step: reduction of $–NO_2$ to a nitroso (–NO) intermediate[58] eqn (5), second step, reduction of –NO to an amine ($–NH_2$) eqn (6) and conversion of 4-NP to 4-aminophenol (4-AP) is represented as eqn (7).

$$–NO_2 + 2e^- + 2H^+ \rightarrow –NO + H_2O \quad (5)$$

$$–NO + 4e^- + 4H^+ \rightarrow –NH_2 + H_2O \quad (6)$$

$$C_6H_4(NO_2)OH + 6e^- + 6H^+ \rightarrow C_6H_4(NH_2)OH + 2H_2O \quad (7)$$

Conclusion

This study demonstrates the efficiency of $NiFe_2O_4$/PAOT nanocomposites in removing 4-nitrophenol (4-NP) from aqueous solutions. The catalyst demonstrated a reduction efficiency of 85% at a concentration of 2 ppm, indicating its effective performance at low pollutant levels. At concentrations of 10 ppm and 15 ppm, the reduction efficiencies were notable, achieving 95% and 99%, respectively. The consistent performance across varying concentrations highlights the adaptability of $NiFe_2O_4$/PAOT nanocomposites in effectively managing different pollutant loads. The observed bandgap energy of 1.24 eV enhances the catalyst's appeal by indicating a strong capacity for visible light absorption. This characteristic renders the nanocomposite especially appropriate for photocatalytic applications, facilitating activation by natural sunlight or artificial visible light sources, thereby significantly decreasing dependence on costly UV-based systems and enhancing energy efficiency. Leveraging visible light presents a significant advantage for environmental remediation, enhancing both the practicality and cost-effectiveness of the process. The $NiFe_2O_4$/PAOT nanocomposite exhibits high reduction efficiency and significant potential for application in wastewater treatment. The visible light activity and efficient reduction of hazardous aromatic pollutants make it a sustainable and effective solution for cleaning contaminated water sources.

Author contributions

All authors listed have made a substantial, direct, and intellectual contribution to the work and approved it for publication.

Conflicts of interest

The authors declare that the research was conducted in the absence of any commercial or financial relationships that could be constructed as a potential conflict of interest.

Data availability

Data supporting the findings of this study are available within the article.

References

1 A. Gholami, S. B. Mousavi, S. Z. Heris and M. Mohammadpourfard, Nitrate removal performance of a novel magnetic chitosan-based nanocomposite: modeling and optimization using response surface methodology, *Biomass Convers. Biorefin.*, 2024, **14**, 17481–17497.
2 R. Das, V. S. Sypu, H. K. Paumo, M. Bhaumik, V. Maharaj and A. Maity, Silver decorated magnetic nanocomposite (Fe_3O_4@PPy-MAA/Ag) as highly active catalyst towards reduction of 4-nitrophenol and toxic organic dyes, *Appl. Catal. B Environ.*, 2019, **244**, 546–558.
3 S. Z. Heris, M. Etemadi, S. B. Mousavi, M. Mohammadpourfard and B. Ramavandi, Preparation and characterizations of TiO_2/ZnO nanohybrid and its photocatalytic activity for degradation of organic dyes, *J. Photochem. Photobiol., A*, 2023, **443**, 114893.
4 X. Kong, H. Zhu, C. Chen, G. Huang and Q. Chen, Insights into the reduction of 4-nitrophenol to 4-aminophenol on catalysts, *Chem. Phys. Lett.*, 2017, **684**, 148–152.
5 Y. Shen, L. Zhang, Q. Li and X. Wang, *J. Phys. Chem. Solids*, 2022, **167**, 110783.
6 M. R. Kumar, A. S. Sekhar and S. J. Patel, *Results Chem.*, 2023, **5**, 100963.
7 S. Balgude, K. Patil, S. Moharil, M. Puranik, S. Kadam, P. Lokhande, S. Patange and P. More, *Chem. Select*, 2022, **7**, e202200221.
8 R. K. Raval and P. D. Patel, *J. Phys. Chem. Solids*, 2021, **148**, 109700.
9 S. Singh, V. K. Gupta and P. Ghosh, *RSC Adv.*, 2020, **10**, 42766–42776.
10 Z.-F. Jiang, F.-M. Tian, K.-M. Fang, Z.-G. Wang, L. Zhang, J.-J. Feng and A.-J. Wang, Atomically dispersed ternary FeCoNb active sites anchored on N-doped honeycomb-like mesoporous carbon for highly catalytic degradation of 4-nitrophenol, *J. Colloid Interface Sci.*, 2025, **677**, 718–728.
11 X. Zhang, F. Wei and S. Wang, Adsorption and catalytic degradation by $CoFe_2O_4$ coated on metal–organic framework for the removal of 4-nitrophenol and 2,4-dichlorophenol, *Sep. Purif. Technol.*, 2025, **354**, 129458.
12 S. Taghavi Fardood, F. Moradnia and T. M. Aminabhavi, Green synthesis of ZnO nanoparticles using Sargassum muticum aqueous extract and their photocatalytic degradation of methylene blue, *Environ. Pollut.*, 2024, **358**, 124534.
13 X. Liao, X. Wang, L. Zheng, Y. Hu, A. Wu and G. Li, A novel risk assessment model of urban gas pipeline network in expansions by integrating the OPA method and GraphSAGE algorithm, *Process Saf. Environ. Prot.*, 2024, **182**, 1227–1236.
14 Y. Yan, J. Miao, Z. Yang, F. X. Xiao, H. B. Yang, B. Liu and Y. Yang, Carbon nanotube catalysts: recent advances in synthesis, characterization and applications., *Chemical Society Reviews*, 2015, **44**(10), 3295–3346.
15 C. Ge, F. Shu, X. Guo, H. Jiao, D. Shi, C. Du, X. Guo, Q. Zhang, W. Wu, Y. Jin and B. Jiang, Comparison of Pd nanoparticle-decorated softwood and hardwood activated carbon in

catalytic reduction of high-concentrated industrial 4-nitrophenol, *Sep. Purif. Technol.*, 2024, **343**, 127149.
16 H. H. Shanaah, E. F. H. Alzaimoor, S. Rashdan, A. A. Abdalhafith and A. H. Kamel, Development of a novel potentiometric sensor for the determination of ketotifen fumarate in pharmaceutical formulations, *Sustainability*, 2023, **15**, 7336.
17 A. H. Kamel, H. S. M. Abd-Rabboh and A. Hefnawy, Molecularly imprinted polymer-based electrochemical sensors for monitoring the persistent organic pollutants chlorophenols, *RSC Adv.*, 2024, **14**, 20163–20181.
18 H. M. Al-Harbi, R. Kumar, M. A. Gondal and S. Al-Sayari, *Surf. Interfaces*, 2022, **33**, 102189.
19 A. Kumar, S. Sharma and V. Singh, *J. Mater. Sci.: Mater. Electron.*, 2024, **35**, 1636.
20 L. Zhao, F. Chen and M. Liu, *Inorg. Chem. Commun.*, 2024, **170**, 113170.
21 Z.-F. Jiang, F.-M. Tian, K.-M. Fang, Z.-G. Wang, L. Zhang, J.-J. Feng and A.-J. Wang, Atomically dispersed ternary FeCoNb active sites anchored on N-doped honeycomb-like mesoporous carbon for highly catalytic degradation of 4-nitrophenol, *J. Colloid Interface Sci.*, 2025, **677**, 718–728.
22 Y. Chen, H. Zhang, L. Chen, G. Fan and Y. Long, Efficient removal of 4-nitrophenol from aqueous solution using a novel magnetic biochar composite: Adsorption and catalytic degradation performance, *Sep. Purif. Technol.*, 2025, **353**, 128437.
23 A. Ammara, S. Noreen, S. Ali, S. Jamil, S. Bibi, M. J. Latif and S. R. Khan, Synthesis and characterization of chitosan-based nanocomposite for efficient removal of heavy metals from wastewater, *Polym. Bull.*, 2024, **81**, 15153–15182.
24 J. Mahmood, N. Arsalani, S. Naghash-Hamed, Z. Hanif and K. E. Geckeler, Preparation and characterization of hybrid polypyrrole nanoparticles as a conducting polymer with controllable size, *Sci. Rep.*, 2024, **14**, 11653.
25 S. S. M. Hassan, A. H. Kamel, A. A. Hassan, H. A. El-Naby, M. A. Al-Omar and A. Y. A. Sayed, *Molecules*, 2020, **25**(12), 2721.
26 A. H. Kamel, A. A. Hassan, H. H. El-Shalakany and M. A. Al-Omar, Synthesis and characterization of chitosan-based nanocomposite for efficient removal of heavy metals from wastewater, *Nanomaterials*, 2020, **10**(3), 586.
27 D. M. Dotzauer, S. Bhattacharjee, Y. Wen and M. L. Bruening, Nanoparticle-containing membranes for the catalytic reduction of nitroaromatic compounds, *Langmuir*, 2009, **25**(3), 1865–1871.
28 S. S. M. Hassan, A. H. Kamel and M. A. Fathy, A novel screen-printed potentiometric electrode with carbon nanotubes/polyaniline transducer and molecularly imprinted polymer for the determination of nalbuphine in pharmaceuticals and biological fluids, *Anal. Chim. Acta*, 2022, **1227**, 340239.
29 M. N. Ahmed, H. Khan, L. Islam, M. H. Alnasir, S. N. Ahmed, M. T. Qureshi and M. Y. Khan, Investigating nickel ferrite (NiFe2O4) nanoparticles for magnetic hyperthermia applications, *Journal of Materials and Physical Sciences*, 2023, **4**(1), 32–45.
30 Q. Qi, H. Zhang, M. Liu, S. Qi, Z. Huo, Y. Ma, Z. Zhang, Y. Lu, X. Qi, S. Han and G. Wang, Multifunctional nanoplatform for targeted cancer therapy and imaging, *Cancer Nanotechnol.*, 2023, **14**(1), 46.
31 S. Z. Heris, M. Etemadi, S. B. Mousavi, M. Mohammadpourfard and B. Ramavandi, Preparation and characterizations of TiO_2/ZnO nanohybrid and its photocatalytic activity for degradation of organic dyes, *J. Photochem. Photobiol., A*, 2023, **443**, 114893.
32 M. R. Gholipour, C. T. Dinh, F. Béland and T. O. Do, Nanostructured photocatalysts for solar hydrogen production, *Nanoscale*, 2015, **7**(18), 8187–8208.
33 S. Naghash-Hamed, N. Arsalani and E. Sharifi As, Synthesis of novel nano-structured materials for environmental applications, *Nano-Struct. Nano-Objects*, 2023, **35**, 101002.
34 S. Sambhudevan, Green Synthesis of Metal Nanoparticles for Catalytic Applications, *Chem. Pap.*, 2021, **75**, 3697–3710.
35 S. S. M. Hassan, A. H. Kamel, A. A. Hassan, A. E.-G. E. Amr, H. A. El-Naby and E. A. Elsayed, Development of Nanomaterial-Based Sensors for Environmental Monitoring, *Nanomaterials*, 2020, **10**, 254.
36 M. A. Fathy, A. H. Kamel and S. S. M. Hassan, Fabrication of Molecularly Imprinted Electrochemical Sensors for Pharmaceutical Analysis, *RSC Adv.*, 2022, **12**, 7433–7445.
37 O. Baytar, A. Ekinci, Ö. Şahin and A. Akdag, Synthesis of Novel Compounds with Potential Biological Activity, *ChemistrySelect*, 2024, **9**(8), e202304491.
38 A. G. Ramu, S. Salla, S. Chandrasekaran, P. Silambarasan, S. Gopi, S. Seo, K. Yun and D. Choi, Environmental Applications of Nanomaterials: A Review, *Environ. Pollut.*, 2021, **270**, 116063.
39 F. D. Koca and B. Şahin, Green Synthesis of $NiFe_2O_4$ Nanoparticles and Evaluation of Their Photocatalytic Activities, *Inorg. Nano-Met. Chem.*, 2024, **1**, 1–7.
40 M. Shabani, E. Saebnoori, S. A. Hassanzadeh-Tabrizi and H. R. Bakhsheshi-Rad, Synthesis and Characterization of TiO_2/ZnO Nanohybrid and Its Photocatalytic Activity for Degradation of Organic Dyes, *J. Mater. Eng. Perform.*, 2023, **32**, 2165–2182.
41 L. Sabaghzadeh, A. Tadjarodi, N. Steinfeldt and J. Strunk, Facile Synthesis of MFe_2O_4/RGO (M = Ni, Co) Nanocomposites and Their Application in the Reduction of 4-Nitrophenol, *Iran. J. Sci.*, 2024, **48**, 357–372.
42 P. Wang, D. Li, L. Wang, S. Guo, Y. Zhao, H. Shang, D. Wang and B. Zhang, Heteroatom-Doped Noble Carbon-Tailored Pd Nanoparticles for Efficient Catalytic Degradation of 4-Nitrophenol, *Chem. Eng. J.*, 2024, **495**, 153631.
43 D. M. Dotzauer, S. Bhattacharjee, Y. Wen and M. L. Bruening, Nanoparticle-Containing Membranes for the Catalytic Reduction of Nitroaromatic Compounds, *Langmuir*, 2009, **25**, 1865–1871.
44 J. Feng, L. Su, Y. Ma, C. Ren, Q. Guo and X. Chen, $CuFe_2O_4$ Magnetic Nanoparticles: A Simple and Efficient Catalyst for the Reduction of Nitrophenol, *Chem. Eng. J.*, 2013, **221**, 16–24.
45 Y. Chen, H. Zhang, L. Chen, G. Fan and Y. Long, Efficient Removal of 4-Nitrophenol from Aqueous Solution Using

a Novel Magnetic Biochar Composite: Adsorption and Catalytic Degradation Performance, *Sep. Purif. Technol.*, 2025, **353**, 128437.

46 A. O. Cardoso Juarez, E. I. Ocampo Lopez, M. K. Kesarla and N. K. R. Bogireddy, *ACS Omega*, 2024, **9**, 33335–33350.

47 Z. G. Asmare, B. A. Aragaw and M. Atlabachew, Facile Synthesis of Natural Kaolin-Based CuO Catalyst: An Efficient and Eco-Friendly Catalyst for the Reduction of 4-Nitrophenol, *ACS Omega*, 2024, **9**(49), 48014–48031.

48 P. Azhagapillai, K. Gopalsamy, I. Othman, S. Salman Ashraf, F. Banat and M. Abu Haija, Photocatalytic Reduction of 4-Nitrophenol over Eco-Friendly $Ni_xCu_xFe_2O_4$ Without an Additional Reducing Agent in Water, *Mater. Sci. Energy Technol.*, 2024, **7**, 195–204.

49 M. Khatamian, B. Divband and A. Jodaei, Synthesis and Characterization of TiO_2/ZnO Nanohybrid and Its Photocatalytic Activity for Degradation of Organic Dyes, *Mater. Chem. Phys.*, 2012, **134**, 31–37.

50 J. Feng, L. Su, Y. Ma, C. Ren, Q. Guo and X. Chen, $CuFe_2O_4$ Magnetic Nanoparticles: A Simple and Efficient Catalyst for the Reduction of Nitrophenol, *Chem. Eng. J.*, 2013, **221**, 16–24.

51 A. A. Yadav, Y. M. Hunge, S. Majumder, A.-H. I. Mourad, M. M. Islam, T. Sakurai and S.-W. Kang, Catalytic Degradation of 4-Nitrophenol in Polluted Water by Three-Dimensional Co_3O_4 Nanostructures, *J. Colloid Interface Sci.*, 2025, **677**, 161–170.

52 N. Kurnaz Yetim, N. Aslan and M. M. Koç, Synthesis and Characterization of TiO_2/ZnO Nanohybrid and Its Photocatalytic Activity for Degradation of Organic Dyes, *J. Environ. Chem. Eng.*, 2020, **8**, 104258.

53 D. Ayodhya and G. Veerabhadram, Catalytic Degradation of 4-Nitrophenol in Polluted Water by Three-Dimensional Co_3O_4 Nanostructures, *Environ. Technol.*, 2021, **42**, 826–841.

54 S. Parida, B. Sarangi, J. Nanda and B. Pany, Effect of Co^{2+} Doping on Structural, Optical, and Magnetic Properties of $NiFe_2O_4$ Nanoparticles, *Inorg. Chem. Commun.*, 2024, **170**, 113344.

55 G. B. Stambouli, B. Benguella, B. Makhoukhi, M. S. El-ouchdi and A. H. Kamel, Physicochemical properties of mesoporous acid activated materials from Lemna minor for Bezaktiv Red S-MAX dye removal, *J. Anal. Methods*, 2025, **17**, 2134–2143.

56 F. F. Alharbi, S. Gouadria, M. Abdullah, A. G. Abid, F. Mehar-un-Nisa, H. M. T. Farid and S. Aman, Development of High-Performance Alloys for Aerospace Applications, *JOM*, 2024, DOI: **10.1007/s11837-024-06964-x**.

57 T. L. Lambat, P. V. Ledade, J. K. Gunjate, V. R. Bahekar, S. H. Mahmood and S. Banerjee, Recent Developments in the Organic Synthesis Using Nano-$NiFe_2O_4$ as Reusable Catalyst: A Comprehensive Synthesis & Catalytic Reusability Protocol, *Results Chem.*, 2023, **6**, 101176.

58 T. K. Das and N. C. Das, Advances on Catalytic Reduction of 4-Nitrophenol by Nanostructured Materials as Benchmark Reaction, *Int. Nano Lett.*, 2022, **12**, 223–242.

RSC Advances

REVIEW

View Article Online
View Journal | View Issue

Cite this: *RSC Adv.*, 2025, **15**, 6875

Metal oxides and their composites for the remediation of organic pesticides: advanced photocatalytic and adsorptive solutions

Ayman H. Kamel, *[ab] Hisham S. M. Abd-Rabboh, [c] Ahmed Abd El-Fattah, [ad] Ghizlene Boudghene Stambouli[ae] and Lina Adeida[ae]

Metal oxide nanoparticles and their composites have garnered significant attention in water treatment and environmental cleanup due to their unique physicochemical properties. These materials exhibit distinct crystalline structures, tunable morphologies, large surface areas, versatile surface chemistry, and widespread availability. These features make nanostructured metal oxides and their composites highly effective for the selective removal of organic pollutants from the environment, either by adsorption or photodegradation. This article focuses on recent advances, challenges, and opportunities in the use of metal oxides and their composites for the targeted removal of organic contaminants, including insecticides, phenolic compounds, organic dyes, and similar pollutants. The discussion encompasses a broad range of metal oxides and their composites, highlighting their diverse structural, crystallographic, and morphological characteristics that influence their adsorption and photocatalytic performance. Emphasis is placed on the photocatalytic and adsorptive capabilities of these materials, including their photo-stimulation properties and mechanisms. Metal oxides are highlighted as outstanding photocatalysts due to their high photodegradation efficiency, cost-effective synthesis methods, and optimized bandgap engineering. This review serves as a valuable resource for researchers exploring the photocatalytic and adsorptive applications of metal oxide-based materials, particularly in the remediation of hazardous organic pollutants such as pesticides.

Received 16th November 2024
Accepted 22nd December 2024

DOI: 10.1039/d4ra08149h

rsc.li/rsc-advances

[a]*Department of Chemistry, College of Science, University of Bahrain, Zallaq P. O. Box 32038, Bahrain. E-mail: ahmohamed@uob.edu.bh*

[b]*Department of Chemistry, Faculty of Science, Ain Shams University, Cairo 11566, Egypt. E-mail: ahkamel76@sci.asu.edu.eg*

[c]*Chemistry Department, Faculty of Science, King Khalid University, Abha 61413, Saudi Arabia*

[d]*Department of Materials Science, Institute of Graduate Studies and Research, Alexandria University, Alexandria 21526, Egypt*

[e]*Department of Chemistry, Inorganic Chemistry and Environment Laboratory, University of Tlemcen, P. O. Box 119, 13000 Tlemcen, Algeria*

Ayman H. Kamel

Prof. Kamel has completed his PhD degree from Ain Shams University, Cairo, Egypt with a focus on the fabrication and characterization of electrochemical sensors for environmental, biomedical and pharmaceutical analysis. Prof. Kamel has published over 137 research articles in well reputed high impact factor international journals. He is also the author of several book chapters. He serves as guest editor, member, referee, and reviewer for many international renowned scientific journals. He has successfully completed several research projects as Principal Investigator. Professor Ayman H. Kamel is a leading figure in the field of sensors and their applications. His research primarily focuses on developing novel sensor technologies and exploring their potential applications in various fields such as healthcare, environmental monitoring, and industrial automation. Prof. Kamel has made significant contributions to the development of sensors with improved sensitivity, selectivity, and reliability. His work often involves interdisciplinary collaboration, combining principles from fields such as materials science, electrical engineering, and chemistry to advance sensor technology. One of his notable achievements is in the area of biomedical sensors, where he has worked on developing sensors for early disease detection, monitoring of physiological parameters, and drug delivery systems. These sensors have the potential to revolutionize healthcare by providing real-time monitoring and personalized treatment options.

1. Introduction

Wastewater contains a variety of substances, including those that are organic (such as pathogens), inorganic (such as heavy metal ions, metal oxides, metal complexes, salts, and other inorganic substances), and nutrient- and agricultural-runoff-related. Organic pollutants are attracting a lot of interest due to their (a) varied applications and subsequent discharge to terrestrial and aquatic bodies; (b) prolonged persistence; (c) high resistance to degradation; and (d) considerable health and environmental consequences.[1] About 85–90% of all fresh water is used for irrigation of agricultural land in Africa and Asia.[2] Agriculture continues to be the predominant user of global freshwater resources, representing approximately 70% of total withdrawals, with variations observed across regions due to differing irrigation practices.[3] The issue of pesticide contamination remains a critical challenge, as residues from agricultural runoff continue to impact major rivers and aquatic ecosystems worldwide.[4] The two issues underscore the critical necessity for sustainable water management practices within the agricultural sector.[5]

Pesticides are the main cause of organic pollutants in water bodies. Pesticides primarily enter the aquatic system from (a) personal usage, (b) pesticide production industry effluents, and (c) the agriculture sector, where they are heavily used for pest management to protect crops from pest damage. Insecticides, herbicides, fungicides, rodenticides, and plant growth regulators are examples of pesticides. Uncontrolled and excessive pesticide usage contaminates water (agricultural runoff) and is harmful to aquatic life and human health. The current WHO guidelines for drinking water quality specify that acceptable levels of pesticides depend on individual compounds.[6] For instance, guideline values are derived based on toxicity and potential exposure. The maximum acceptable values for individual pesticides often fall within 0.1 μg L^{-1} to 1 μg L^{-1} for specific compounds, with stricter limits for more hazardous pesticides. For total pesticides, the cumulative limit generally aligns with 0.5 μg L^{-1}, but this varies depending on local regulations and risk assessments.[6] Pesticides that are used in excess of the allowed amount can have harmful effects on human health, including endocrine, gastrointestinal, neurological, respiratory, reproductive, and dermatological issues.[7] Contaminated water contributes to scarcity because it becomes unusable for domestic, agricultural, or industrial purposes, reducing the overall accessible water supply. This exacerbates water scarcity, especially in regions where clean water resources are already limited. Water demand has increased because of rising population, economic development, urbanization, dynamic changes in lifestyle, attitudes about water use, and rapid industrialization.[8] Water scarcity is a danger in many parts of the world, and many people are unable to meet their basic needs. As a result, much effort has been made to conserve water and remove toxins from wastewater so that it can be used for domestic and agricultural purposes. The removal of various types of organic pollutants from wastewater using cost-effective and ecologically friendly approaches is a hot topic. The study of the interaction between organic contaminants in water and the materials that may be used to remove or degrade them quickly and cheaply is becoming increasingly important for technological application in this context.

The transition metal oxide nanoparticles are appealing candidates for the adsorption process because of their exceptional surface properties, microstructural features, and large surface area.[9] The increased surface area and active sites make adsorption events simpler. Nanoscale properties, such as high surface-to-volume ratios and increased active sites, enhance adsorption kinetics by providing more interaction points for pollutant molecules. Thermodynamically, the high surface energy at the nanoscale facilitates stronger binding interactions, leading to favorable adsorption equilibria. In order to remove organic contaminants from wastewater, nanoparticles have superior adsorption capability than their bulkier cousins. Metal oxide nanoparticles, either alone or in combination, have demonstrated tremendous promise recently as highly selective adsorbents for the quick and effective removal of organic contaminants from wastewater.[10]

2. Pesticide: risks and benefits

Pesticides are lethal chemical or biological substances that are released into the environment to reduce, eliminate, or control the population of insects, weeds, rodents, fungi, and other pests.[11] The main sources of pesticides in the environment are forestry and agriculture. Even though it is well known that a growing world population needs greater global food production, it is desirable for the pesticide to kill the target organisms to reduce the impact of weed species on both humans and the environment. On the other hand, these organic pollutants could destroy the ecosystem's flora and wildlife if they are applied improperly. In addition, humans and other living things are more negatively impacted by the widespread use of these dangerous chemical pesticides.

Hazardous pesticides are widely used against various organisms. Among them, 80% of pesticide applications are targeted at insect control, followed by 15% for herbicide use and 1% for treating plant fungal diseases, with the remaining 4% used for other purposes. When categorizing the types of pesticides by frequency of use, insecticides constitute 47.5%, herbicides 29.5%, fungicides 17.5%, and other chemicals 5.5%. This discrepancy likely arises from differences in classification—one based on the purpose of application and the other on the types of pesticides sold or applied.[12] The long-term consequences of pesticides and the influence of hazardous chemicals released into water bodies are well known to environmental specialists and farmers.[13] In the past 50–60 years, there has been a rise in the incidence of cancer and chronic diseases because chemical pesticides act as catalysts for carcinogens.[14]

Hazardous chemical pollutants accumulated in the soil have been reduced using treatment techniques like leaching and landfilling. On the other side, the soil remediation process takes a long time and is expensive. To safeguard farmland and limit the use of harmful pesticides, organic waste/earthworm techniques and manure as a soil amendment are required.

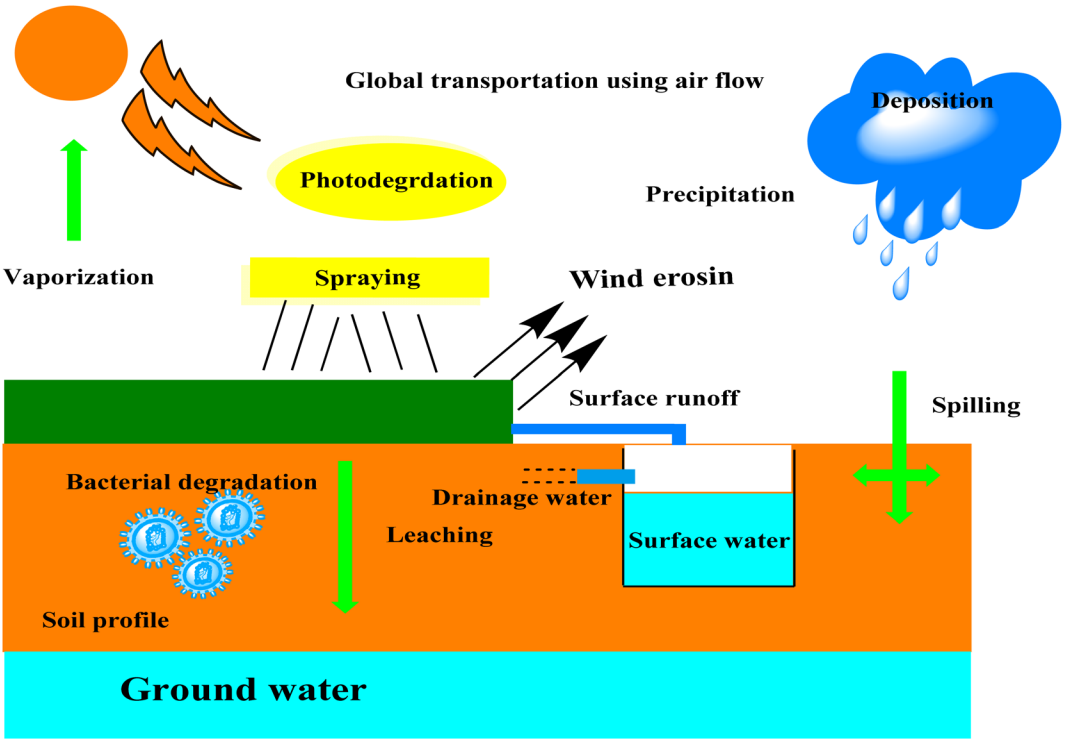

Fig. 1 Different stages of pesticide cycle that reach the ground and surface water.

Numerous beneficial bacteria can create surfactants.[15] On the other hand, more research approaches are needed to address environmental and procedural problems that need in-depth examination to broaden their scope. In recent years, bioremediation techniques, such as the use of microorganisms and metabolic enzymes to break down pesticides and change them into another form through sludge formation, have become less toxic.[16] But many defaulters nevertheless restrict their regular use in a hazardous environment and environmental restoration.[17]

Due to the existence of pesticide toxins and their impact on water quality and agricultural soils through their use, which may be damaging to all forms of life, the problem of pollution is a cause of concern for many developing and developed countries. Although a larger dose of a pesticide can injures humans more than the intended pest, humans can be killed in a variety of ways with very tiny quantities.[18]

Inhibiting sex hormones, impairing ovarian function, and damaging endocrine glands are all fatal impacts of pesticides.[19] Due to their heightened biological function and quick toxicity, pesticides are categorized as being extremely damaging, highly poisonous, and moderately dangerous. The compounds dimethoate, quinalphos, and dichloro-diphenyl-trichloroethane are all a little dangerous. Malathion is a very dangerous substance. Atrazine and other carbamates are unlikely to present a serious concern.[20] If toxic pesticides are misused, agricultural producers are particularly vulnerable to their negative effects.[21] Pesticides tend to settle as sediments, which can turn agricultural soils into a source of organochloride pollutants that can spread and volatilize and pose a risk to the surfaces of soil and water (Fig. 1).[22]

Pesticides can kill and injure soil-dwelling microorganisms, particularly when these substances are employed improperly or excessively, which causes chemical compounds to accumulate in the soil.[23] These chemicals may take several years to break down. Incomplete knowledge exists regarding how pesticides affect soil microorganisms. Numerous studies have shown that pesticides harm soil microorganisms and biochemical processes, whereas other studies have shown that microorganisms break down and absorb pesticide residues.[24]

Pesticides have different impacts on different types of soil microorganisms depending on their stability, concentration, and toxicity, as well as several environmental factors.[24] It is challenging to make definitive judgements about the relationship between pesticides and soil ecology due to the intricate interactions between the variables. The overall metabolic systems governing the nutrition cycle may become compromised by prolonged pesticide use.[24] Additionally, herbicides like triclopyr affect the soil's ability to convert ammonia to nitrite.[25] The ability to measure changes in the various settings of pesticide-treated soil would be greatly enhanced by improved operational allocations of bacterial taxonomic groups.[25] Water serves as a binder, making it simple for pesticides to penetrate moist soil.[26] The amount of pesticide that affects the soil varies according to soil humidity, temperature, sunshine, plants, and physiological features of the soil.[9]

3. Pesticides classifications

Based on their composition, level of toxicity, and intended use, pesticides are classified. The most common technique for classifying pesticides is based on the chemical properties of the

Table 1 Classification of organic pesticides based on their origin[2,9,10]

Origin	Source	Class	Example	Feature
Organic	Natural	Plants phytochemical	Essential oil, plant extracts, and leftover oilseed cakes	Low toxicity, limited persistent in environment, and complicated structures that prevent resistance in pests
	Synthetic	Pyrethroids	Phenthion, diazinon, cypermethrin, deltamethrin, cyfluthrin, and cypermethrin	Effect the sodium channel in insects resulting in paralysis of the organism, highly toxic to insects and fish but less to mammals, unstable upon the exposure of light, and commonly used in food
		Organophosphates	Aldrin, dieldrin, glyphosate, and chlorpyrifos	Cause paralysis resulting in death, and dominant for variety of pests
		Carbamates	Deltamethrin, cypermethrin, fenvalerate, permethrin, cyfluthrin, cyhalothrin, cypermethrin, and carbofuran	Effect the nerve of the pests resulting in poisoning and death, and low pollution caused upon degradation
		Organochlorine	Chlorothalonil and endrin aldehyde	Used for insects, long persistent in environment, and affect the nerve system causing paralysis and death of the pests

pesticide (Table 1) and the characteristics of the target (Table 2). Based on their chemical makeup, pesticides are classified as organochlorines, organophosphorus, carbamates, pyrethrins, and pyrethroids (Table 3). Most insecticides used nowadays are organic and include both synthetic and plant-specific pesticides.[27] Based on the structure, toxicity, and functional categories of pesticides; more groupings are created. Pesticides are used in several ways to prevent the spread of pests or manage their numbers. Some herbicides are used to prevent plant growth, while others have effective photosynthetic control.[28] Nearly all insecticides have the potential to significantly impact the ecosystem. They pose a serious risk to the ecosystem.[28] Fungi and their spores are killed or have their growth slowed by substances referred to as fungicides.[29] Fungicide misuse, storage, and release into moving water all present significant contamination risks.[30]

4. Overview of water cleanup methods

Organic dyes, insecticides, medicines, fertilizers, surfactants, and other chemicals can be found in a wide variety of products. Conversely, excessive use, environmental discharge or disposal, and inadequate treatment contaminate water sources and have detrimental effects on our ecosystem, including humans. As a result, it has proven difficult to eliminate organic pollutants from wastewater. There were numerous efforts made to eliminate or degrade organic pollutants from the water. Utilizing a range of physical, chemical, and biological methods, organic pollutants, and the breakdown products they produce are eliminated or reduced from the aquatic environment (Fig. 2). These techniques are used individually or in combination with others to detoxify contaminated wastewater. Adsorption, membrane filtration, biological degradation, photocatalytic degradation, nanofiltrations, oxidation, reverse osmosis, UV radiation, and other techniques are used to disinfect water.[31,32] The greatest techniques for eliminating pesticides, beta blockers, and medications have been discovered to be chemical oxidation processes such as ozonation (O_3), UV photolysis, and photo-Fenton processes.[33] Among other biological processes, membrane filtration remediation (MFR), activated sludge, and aeration methods were superior at removing endocrine distributing chemicals (EDCs) [*i.e.* endocrine-disrupting chemicals (EDCs) are compounds that interfere with the hormonal systems of organisms, potentially causing adverse developmental, reproductive, neurological, and immune effects].[34] With the activated sludge technique, surfactants, EDCs, and personal care products (PCPs) can be effectively eliminated.[35] Reviewing the importance of employing metal oxide nanocomposites in water remediation is the main goal of this article. The field of wastewater photocatalysis using photocatalyst nanocomposite is driven by ultraviolet (UV) and visible light. Using different kinds of organic waste, full studies showed that photocatalysis led to complete and efficient degradation and the creation of less harmful, eco-friendly products.[36] Toxic byproducts, however, may have been produced because of partial breakdown.[36] Adsorption and photocatalysis are economically scalable due to their reliance on abundant and inexpensive materials (*e.g.*, activated carbon, metal oxides). For instance, the use of sunlight in photocatalysis reduces energy costs, while adsorption processes benefit from renewable or waste-derived adsorbents like biochar.

Recent studies have highlighted the effectiveness of metal oxide nanostructures, particularly TiO_2–ZnO composites, in treating water contaminated with persistent organic pollutants.[37] Exposed to visible light, these nanostructures show significantly higher degradation rates than conventional methods, a critical advancement that could favor their use under ambient light conditions.[37] This research demonstrates how optimizing the structure and porosity of composites can accelerate degradation processes, reducing energy demands and enhancing water purification efficiency under natural conditions.[38]

Table 2 Classification of pesticides based on target[3,5,11]

Class	Example	Target pests	
Acaricides	Bifonazole	Mites	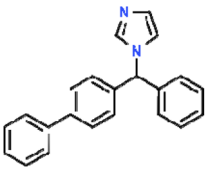
Avicides	Avitrol (4-amino pyridine)	Birds	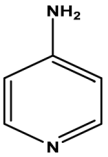
Fungicides	Azoxystrobin	Fungi	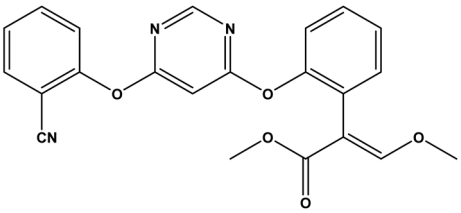
Herbicides	Atrazine	Weeds	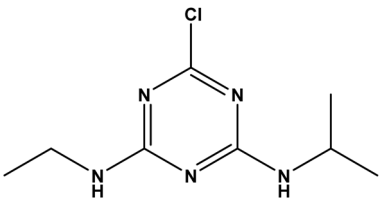
Insecticides	Aldicarb	Insects	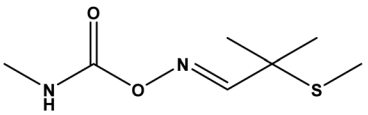
Larvicides	Methoprene	Larvae	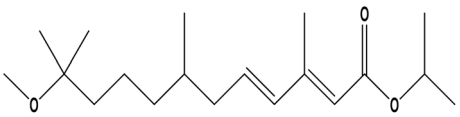
Molluscicides	Metaldehyde	Snail	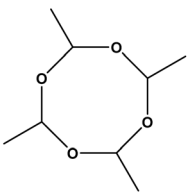
Nematicides	Aldicarb	Nematodes	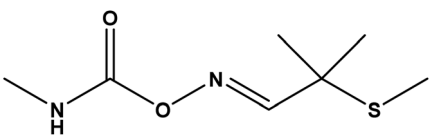
Ovicides	Benzoxazine	Egg – prevents hatching of egg in insects and mites	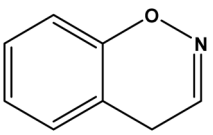

Table 2 (*Contd.*)

Class	Example	Target pests	
Piscicides	Rotenone	Fishes	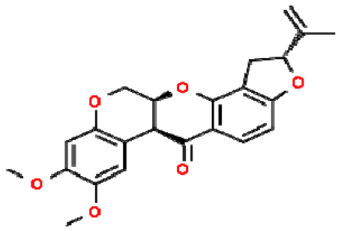
Repellents	Methiocarb	Insects	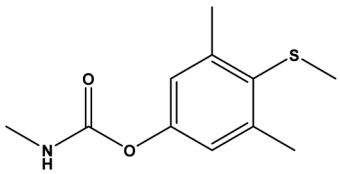
Rodenticides	Warfarin	Rodents	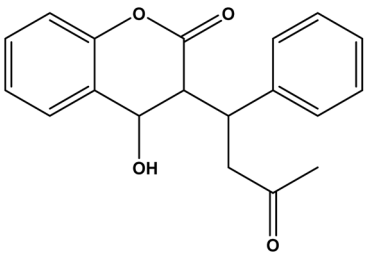
Termiticides	Fipronil	Kills termites	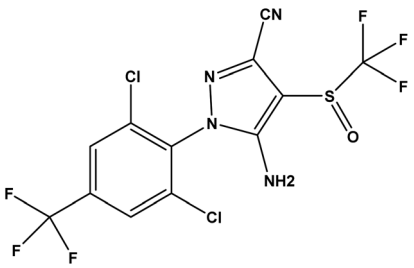

5. Metal oxides-based nanostructured materials

Metal oxide nanoparticles have been studied in a variety of applications, including energy storage, catalysis, electrochemistry, lubrication, sensors, coatings, environmental remediation, and others.[39,40] The surface properties, microstructural features, and high surface area of transition metal oxide nanoparticles make them suitable candidates for the adsorption process.[41] Adsorption is aided by the active sites and large surface area. When the size of materials is lowered from bulk to nano, the surface-to-volume ratio increases rapidly.[42] When it comes to removing organic pollutants from wastewater, nanoparticles have a better adsorption capability than their bulkier counterparts. Activated carbon derived from biomass, as well as novel forms of carbon such as graphene, carbon nanotubes, fibers, and others, displayed good organic pollutant adsorption capabilities in wastewater.[43] Metal oxide nanoparticles have lately shown significant promise as highly selective adsorbents for the quick and effective removal of organic pollutants from wastewater,[44] either as single materials or as composites. Transition metal oxides and their composites have excellent photocatalytic activity for destroying organic pollutants.[45] Wide band gap semiconductors with non-toxicity and water stability for photocatalytic oxidation/degradation of organic pollutants are made from metal oxide-based nanomaterials with well-controlled structural, crystalline, and surface characteristics. Recent advancements in metal oxide nanostructures research have significantly boosted their adsorption and photocatalytic capabilities. For instance, a 2023 study demonstrated that TiO_2 and ZnO nanoparticles, modified with rare-earth dopants, offer increased active sites, allowing for more intensive interactions with pollutants and thereby enhancing degradation efficiency in diverse settings.[46] Adjusting morphology and composition makes these metal oxides particularly promising for use under various environmental conditions.[1]

Table 3 Classification of pesticides based on their chemical makeup[14–16]

Category	Name	Chemical structure
Organophosphorous	Phenthion	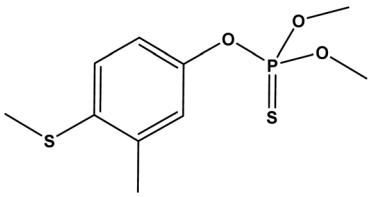
	Diazinon	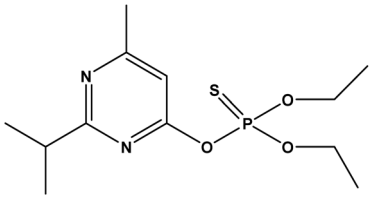
	Glyphosate	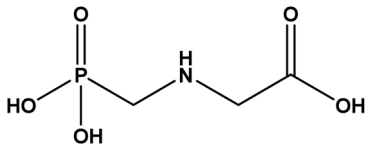
	Dichlorvos	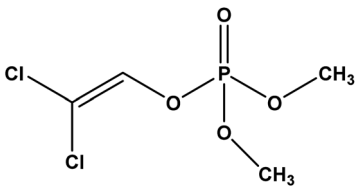
	Acephate	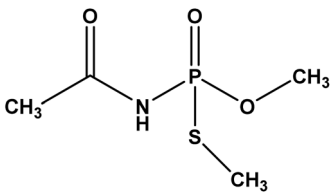
	Parathion	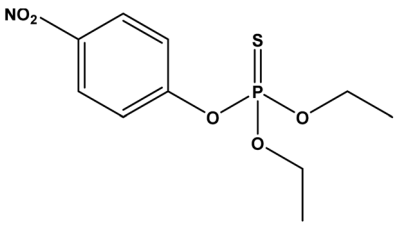
Organochlorine	Aldrin	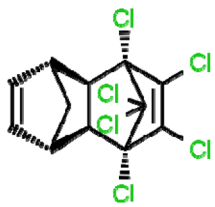
	Dieldrin	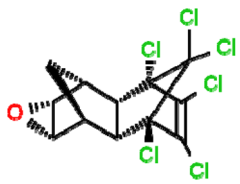
	Cypermethrin	

Table 3 (*Contd.*)

Category	Name	Chemical structure
Carbamates	Chlorpyrifos	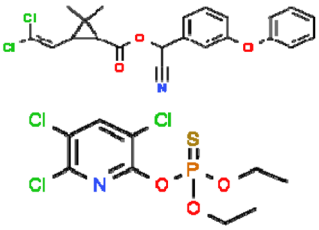
	Cyfluthrin	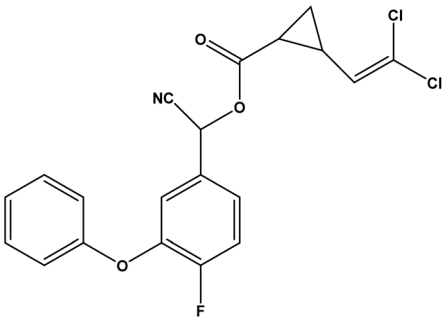
	Chlorothalonil	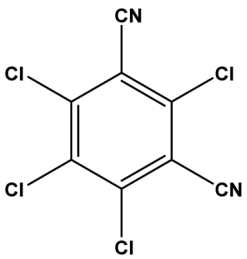
	Endrin	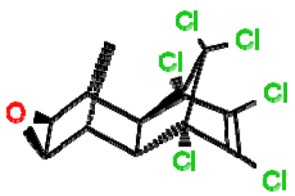
	Carbaryl	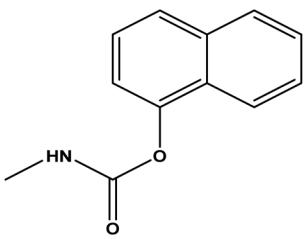
	Carbofuran	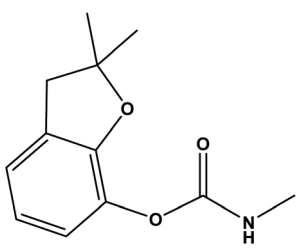
	Methomyl	

Table 3 (*Contd.*)

Category	Name	Chemical structure
		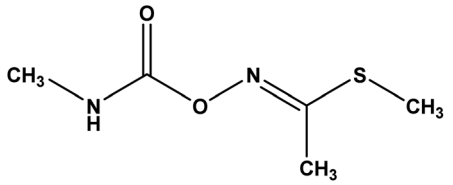
	Aldicarb	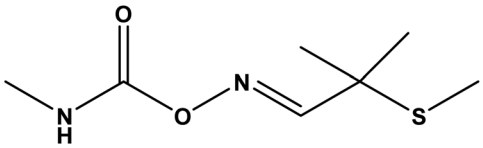
	Oxamyl	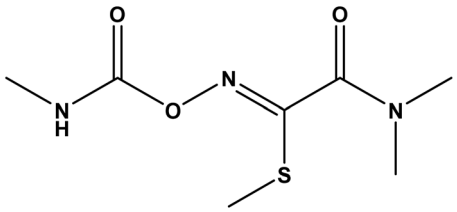
	Terbufos	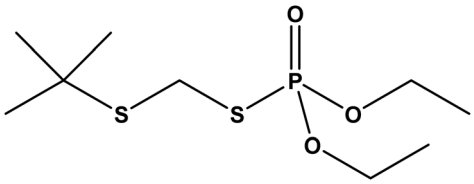
	Carbosulfan	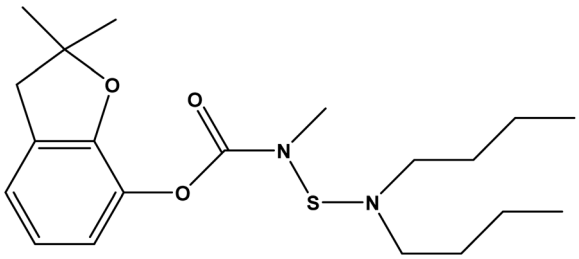
	Carbamic acid	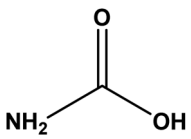

Photo-degradation has long been seen to be one of the most environmentally friendly ways to remove organic pollutants from water.[47] It has several advantages, including the use of renewable energy (solar energy) and the conversion of organic contaminants into non-toxic molecules and gases.[48] Metal oxide semiconductors only use a small fraction of the solar spectrum, specifically UV light (5% of the solar spectrum),[49] which is a major limitation of the photocatalytic process. This disadvantage can be solved through band gap engineering of metal oxide nanoparticles, which comprises chemical and structural changes, heteroatom doping, and nanocomposites.

The best photocatalysts absorb the visible spectrum efficiently, delay hole and electron pair recombination, and perform well as photocatalysts.[50] Metal oxide nanoparticles, such as iron oxides, Al_2O_3, TiO_2, CuO, ZnO, CeO_2, and others, have attracted interest as adsorbents and photocatalysts.[51,52] For enhancing performance efficiency and selectivity, porous materials-supported metal oxides, magnetic metal oxides, metal–metal oxides, graphene–metal oxides, and other metal oxide-based nanocomposites have all been explored.[53,54] The size, texture, and surface characteristics of these nanomaterials influence the adsorption events.[37,39,41,44] Various morphologies

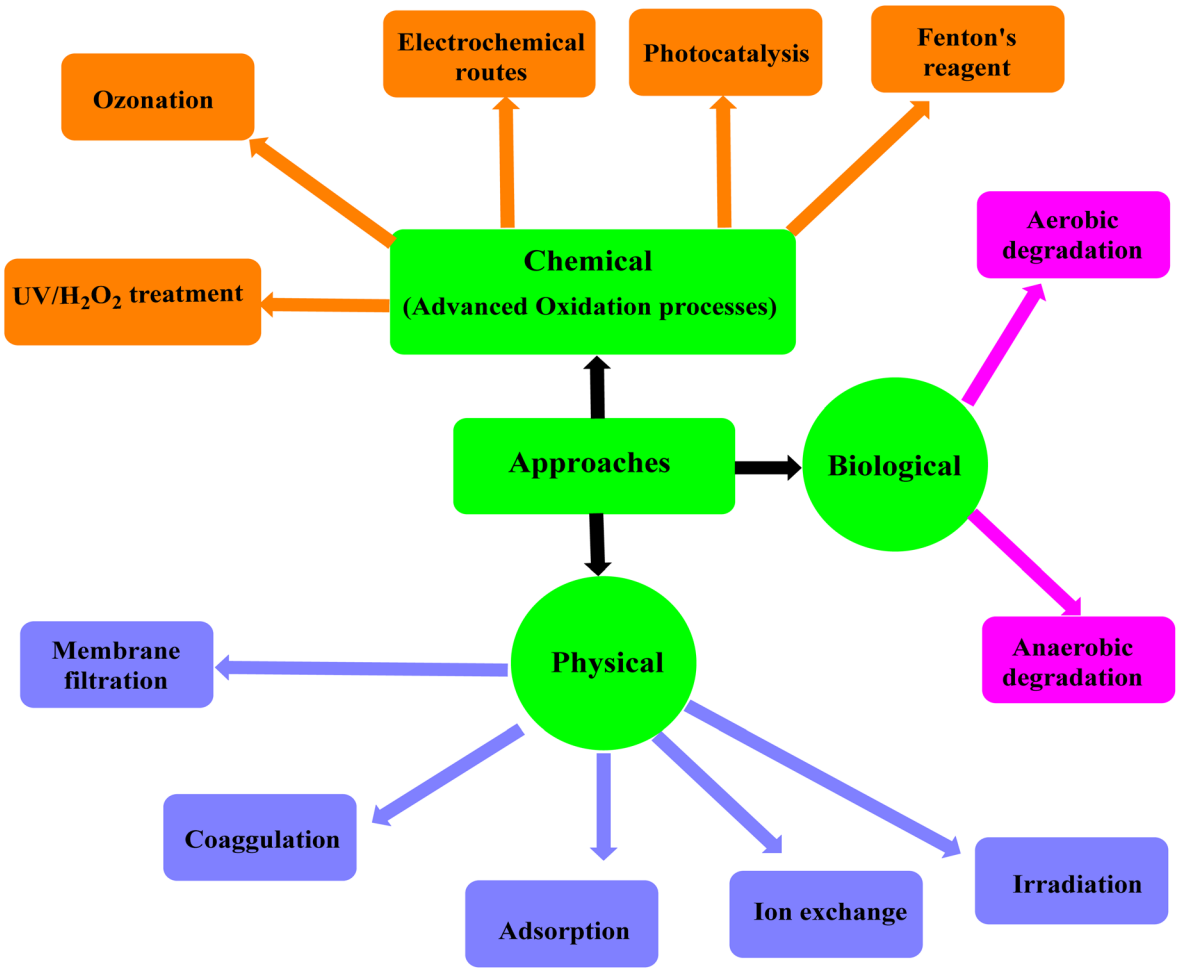

Fig. 2 Chemical, biological, and physical approaches to remove or degrade the organic pollutants in the wastewater.

of nanoparticles provide distinct crystal facets as active sites on the surface of materials for adsorption and photocatalytic applications. Bhatti *et al.*[55] examined the effect of ZnO nanoparticle shape on the photocatalytic degradation of methyl orange dye. This research examines the structural, crystalline, and surface properties of a variety of metal oxide nanoparticles and their nanocomposites for wastewater treatment *via* adsorption and photocatalytic destruction of organic pollutants.

Metal oxide nanostructures have been shown to be effective and flexible in cleaning up the environment, which shows how useful they could be. However, it is also important to think about how safe they are for the environment and how easily they can be recycled for long-term use. Metal oxide nanoparticles, when released into the environment, may present significant risks to aquatic organisms and soil ecosystems because of their elevated reactivity and durability. To address these risks, approaches like surface functionalization and the addition of biocompatible coatings have been investigated, leading to a decrease in toxicity and environmental impact. Additionally, the ability to recycle these materials presents a considerable benefit. For example, magnetic iron oxide nanoparticles can be efficiently retrieved from treated water through the application of external magnetic fields, allowing for their reuse across several cycles with negligible efficiency loss. Research indicates that doped metal oxides or composite structures enhance photocatalytic performance while also improving material stability, thereby supporting their reusability. Highlighting these features promotes a comprehensive understanding of the advantages and obstacles associated with the large-scale implementation of metal oxide nanostructures for water treatment.

6. Photocatalytic degradation of pesticides using metal oxide nanoparticles

The photocatalytic activity of metal oxide nanoparticles is attributed to their semiconducting properties, which enable efficient absorption of light and generation of electron–hole pairs. These properties are critical in driving the redox reactions required for environmental cleanup. These nano particles have an effective and selective photocatalytic activity due to their superconducting nature, which has been exploited in various

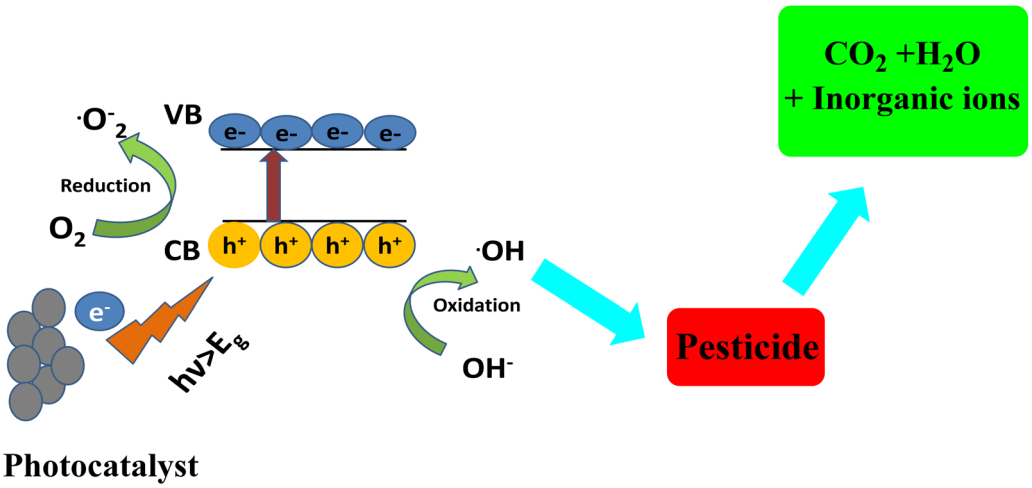

Fig. 3 Photocatalytic degradation of pesticides using photocatalysts.

research projects for pesticide sensing and remediation.[56] Metal oxide nano particles such as silica (SiO_2), zinc oxide (ZnO), titanium oxide (TiO_2), and iron oxide (Fe_2O_3 or Fe_3O_4) have been utilized to detect, degrade, and remove pollutants from various sources.[57,58] The photocatalyst produces pairs of electrons and holes when it absorbs ultraviolet (UV) radiation from sunshine or artificially irradiated light sources (such as fluorescent lamps). When exposed to light radiation, the electron in the semiconductor catalyst's valence band becomes excited. This excited electron's extra energy aids in its transition to the catalyst's conduction band, where it leaves a positive hole behind. The result is the creation of the negative electron (e^-) and positive hole (h^+) pair. The term "photoexcitation" refers to this stage of the semiconductor catalyst. The "bandgap" energy is the difference in energy between the conduction band and the valence band. Fig. 3 illustrates the photocatalytic degradation of pesticides using the photo catalysts.

A recent analysis of the photocatalytic performance of metal oxide composites revealed that incorporating metals like silver and copper into structures such as CuO and Fe_2O_3 extends the lifetime of electron–hole pairs.[59,60] This feature is crucial because it supports more efficient pesticide degradation under visible light exposure. The study showcased significant improvements in breaking down compounds like diazinon and

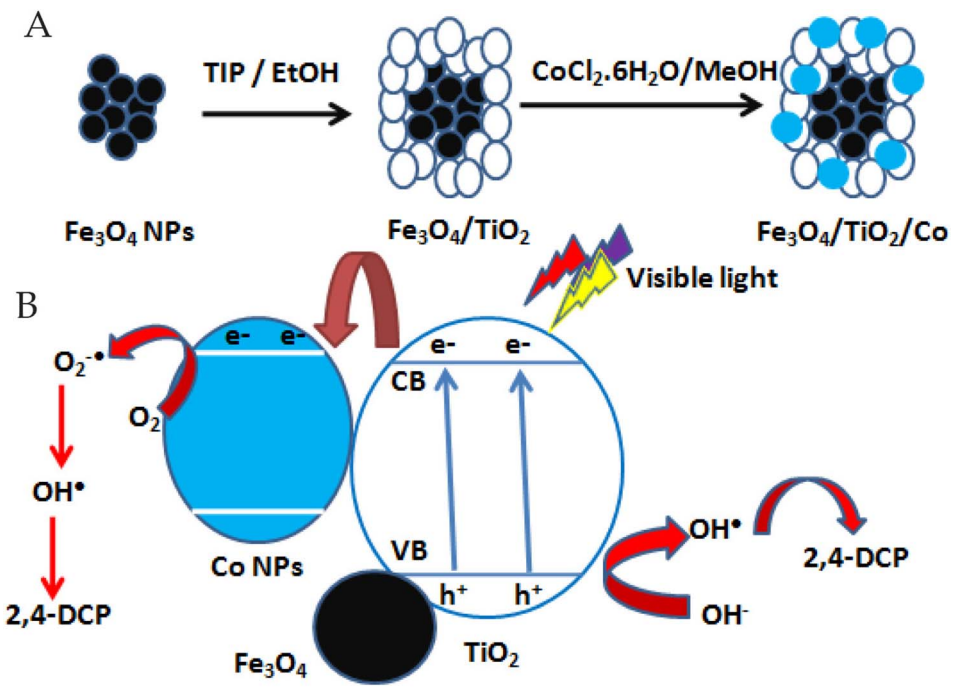

Fig. 4 2,4-Dichlorophenol degradation *via* photo-reactive TiO_2 nanoparticles, (A) preparation of the photocatalyst; (B) the degredation pathway of 2,4-DCP.[69]

chlorpyrifos, underscoring how these structural modifications contribute to practical, sustainable solutions for environmental cleanup.[61]

6.1 Titanium oxide nanoparticles

TiO_2 has attracted the greatest attention from researchers because its unique characteristics, such as excellent photocatalytic activity across a wide range of pH and temperatures, cost-effectiveness, chemical stability, and non-toxicity.[62] TiO_2 nanoparticles' high surface area for photocatalysis has allowed them to be used at the nanoscale to remediate a variety of pollutants from the environment.[63] With a bandgap of 3.2 eV, TiO_2's photocatalytic activity is limited to the UV range.[64] On the other hand, dye sensitization and surface modification of TiO_2 nanoparticles with other metal oxides, non-metals, or carbon-based compounds help to extend the photocatalytic activity of nanoparticles to the visible range.[65] TiO_2 nanoparticles were used as a photocatalyst to degrade chlorpyrifos in water.[66] The photocatalyst was subjected to UV rays to produce pesticide degradation, and it was discovered that as the illumination period was increased, the photo-degradation efficiency rose.[66] To increase their photocatalytic activity against several pesticides, TiO_2 nano particles have been treated with various metal ions. The fungicide carbendazim, for example, was destroyed by TiO_2 nanoparticles doped with Fe and Si ions. The doping improved the photocatalytic activity of nanoparticles, resulting in a 98% breakdown of the fungicide in the presence of sunshine.[67] Also, during the advanced oxidation process (AOP), cobalt (Co)-doped TiO_2 nanoparticles were used as a photocatalyst to decompose 2,4-dichlorophenol (DCP).[68,69] DCP was degraded by TiO_2 nanoparticles in visible light because of the doping. They got 30.42% and 57.84% degradation of 2,4-DCP after 180 min irradiation in the presence of pure TiO_2 and ternary nanocomposite containing 2.92 wt% cobalt (Fe_3O_4/TiO_2 nanocomposite (2.92)), respectively. The higher photocatalytic performance of Fe_3O_4/TiO_2 nanocomposite samples was attributed to the high specific surface areas and the enhancing visible light absorption by cobalt.[69] The pathway of 2,4-dichlorophenol degradation was illustrated in Fig. 4.

Recent studies have confirmed the enhanced photocatalytic properties of TiO_2 doped with metals such as silver and iron, especially for degrading persistent organic pollutants like carbendazim,[70] tebuconazole (TEB) and 2,4-dichlorophenoxyacetic acid (2,4-D) pesticides.[71] Doping with silver, for example, has been shown to increase TiO_2's reactivity under visible light, which reduces the energy needed for activation compared to pure TiO_2.[71] This is particularly significant because it allows for photocatalytic processes to occur under ambient light, making them more feasible for practical applications, including large-scale pollutant degradation.

Molecularly imprinted TiO_2 photocatalysts were added so that the sol–gel method could be used to selectively remove certain pesticides from water.[72] Using TiO_2 imprinted with the appropriate pesticide target, a notable improvement in photocatalytic performance was confirmed.[73] The comparison with the breakdown of pesticides that were not utilized as a template allowed for the verification of the photodegradation process's selectivity, as seen in Fig. 5.

It was looked into how adding foreign materials, like rare earth, transition, and noble metals, to TiO_2 could increase the bathochromic shift, lower the band gap energy, and make photo-generated electron/hole pairs last longer.[73] Many surface parameters, including area, charge, and acidity, are altered by doping TiO_2, making the resulting material more photocatalytically active when exposed to visible light.[73] To make the rare earth lanthanide ions (La^{3+}, Nd^{3+}, Sm^{3+}, Eu^{3+}, Gd^{3+}, and Yb^{3+})-doped TiO_2 nanoparticles, the sol–gel method was used.[74] These were then tested as photocatalysts for dye remediation.[75] The shape, band gap, and particle size of TiO_2 changed when lanthanides were added to it. This made the photocatalytic performance much better than pure TiO_2. The lowest bandgap,

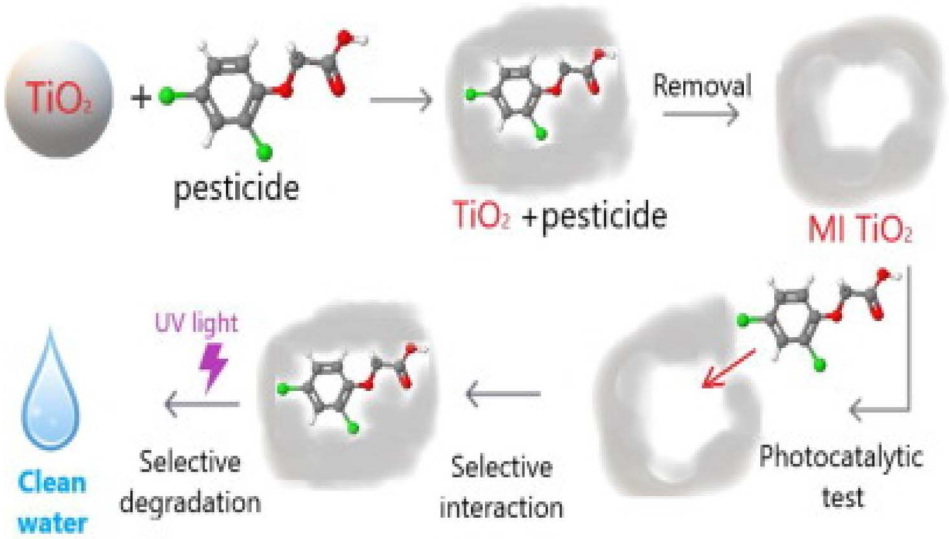

Fig. 5 Preferential removal of pesticides from water by molecular imprinting on TiO_2 photocatalysts.[73]

Table 4 TiO_2 nanomaterials and their composites as photo-catalysts for pesticides degradation

Photo catalyst	Targeted pesticide	Light source	Reaction time	Degradation efficiency (%)	Ref.
TiO_2/Bi_2WO_6 nanostructured hetero-junctions	4-Chlorophenol	Visible	7.5 h	90.5	77
TiO_2/Fe_2O_3 nanocomposite	Diazinon	Visible	45 min	95.1	78
Zn^{2+}-doped TiO_2 nanoparticles	Malathion	UV	81 min	98	79
In and S co-doped TiO_2@rGO	Atrazine	Visible	20 min	99.5	80
SBA-15 loaded with 8–42% TiO_2	Dimethoate	Simulated solar	7 h	100	81

tiniest particle size with the greatest surface area, and pore volume of the lanthanides-doped TiO_2 explained why the Gd^{3+} doping exhibited the highest photocatalytic performance.[76] The nanomaterials based on titanium dioxide and their composites for the photocatalytic destruction of some pesticides are compiled in Table 4.

6.2 Zinc oxide nanoparticles

Because of their distinctive size and high density at the surface's edge points, ZnO nanoparticles have unique chemical and physical properties.[82] These nanoparticles are also known to have high photocatalytic action, which is important for pollutant degradation. The band gap of zinc oxide is 3.25 eV, the same as that of TiO_2 (3–3.25 eV).[83] It is often used in photocatalytic degradation processes to break down organic pollutants in wastewater. Photocatalytic process of zinc oxide and titanium dioxide are very similar. Because of this, ZnO nanoparticles have also been suggested as an alternative to titanium dioxide for cleaning water. ZnO performed better as a photocatalyst when compared to other semiconductors under investigation; this was due to ZnO's ability to absorb a greater portion of the solar spectrum. It was also looked at how to employ ZnO nanoparticles' fluorescence emission properties for the photocatalytic destruction of various organic contaminants.[84] Because ZnO's photocatalytic activity is extremely pH-sensitive and photo-corrosion is facilitated by strongly acidic conditions (pH < 4), its potential is limited in lower pH media.[85] For the purpose of degrading the pesticide diazinon, the photocatalytic activity of nanocrystalline ZnO and commercially available ZnO was evaluated.[86] Nanocrystalline ZnO was found to have better photocatalytic activity than commercial ZnO because of two things: (a) its small crystalline size, which increased the active surface area of the photocatalytic reaction; and (b) the amount of dispersed ZnO particles per volume in the solution, which increased photon absorption for better performance.[86] Using natural sunlight to accelerate the photo-degradation of a variety of pesticides in the leaching water, the $ZnO/Na_2S_2O_8$ nanocomposite was employed as an antioxidant and photosensitizer.[87] Adding $Na_2S_2O_8$ to ZnO made it more effective at oxidation, which cut down on the time needed for photocatalytic pesticide breakdown.[87]

The ZnO–SnO_2 nanorods are a potential material for water purification applications due to its great recyclability and facile remembrance of wasted photocatalysts.[88] Recent studies highlight the potential of ZnO-based photocatalysts for environmental cleanup, particularly when doped with transition metals or combined with nanocomposites.[89] For instance, ZnO doped with $Na_2S_2O_8$ shows enhanced photocatalytic degradation of pesticides like diazinon, especially under natural sunlight in alkaline media, where its stability is higher.[90] In such conditions, the degradation rate can increase by up to 85%, demonstrating a significant improvement over pure ZnO. Similarly,

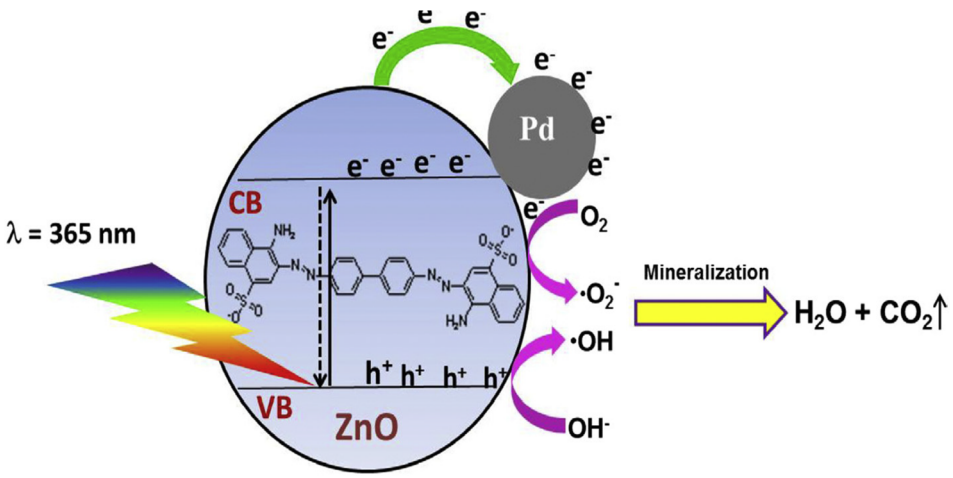

Fig. 6 Schematic diagram illustrating the plausible photocatalytic mechanism for degradation of Congo red dye using the Pd-doped ZnO photocatalyst.[93] Reprinted with permission from Copyright 2016 Elsevier.

Table 5 A summary of the ZnO and their composites that can break down pesticides through photocatalysis

Organic pollutant	ZnO-based nanomaterials	Light source	Degradation efficiency (%)	Ref.
Phenylhydrazine (PHZ)	ZnO supported onto clinoptilolite	UV-vis	69	95
2-Phenylphenol (OPP)	ZnO/TiO_2	UV-vis	100	96
Diazinon	Nanocrystalline ZnO	UV-C	80	97
Azoxystrobin	$ZnO/Na_2S_2O_8$	Sunlight	99	98
Hexaconazole			98	
Kresoximmethyl			100	
Pirimicarb			95	
Propyzamide			97	
Pyrimethanil			96	

doping ZnO with manganese (Mn) improves photocatalytic efficiency by creating surface defects that promote electron–hole separation (ZnO's photocatalytic performance can be significantly improved by increasing its surface area, which reduces defects related to volume and enhances its ability to absorb more light. Studies have shown that doping ZnO with elements like manganese (Mn) or silver (Ag) can further enhance its photocatalytic activity by reducing electron–hole recombination.[91,92] This, in turn, increases the material's efficiency in degrading organic pollutants, making ZnO a more effective photocatalyst under visible light conditions), further boosting its ability to break down organic contaminants. This synergy between ZnO and its dopants or additives promises improved photocatalytic performance, making ZnO an effective solution for large-scale environmental remediation.[86]

Different methods were used to make the Pd-doped ZnO photocatalysts, and their ability to break down Congo red dye varied a lot. These methods included microwave irradiation, borohydride reduction, and photoreduction. Because of the higher doping and good dispersibility of Pd on ZnO, which improved the photodegradation efficiency of organic dye by reducing the recombination of photogenerated electron–hole pairs, the Pd-doped ZnO photocatalyst prepared by the borohydride reduction method exhibited superior photocatalytic activity (Fig. 6).[93] Er-doped ZnO nanoparticles with varying Er concentrations increased photocatalytic activity when exposed to visible light. Adding different amounts of Er to ZnO nanoparticles changed their structure, morphology, band gap, half-life of the photogenerated electron–hole pair, and their ability to absorb visible light. This doped ZnO was used to degrade Red-31 dye.[94] A summary of the ZnO and their composites that can break down pesticides through photocatalysis is shown in Table 5.

6.3 Iron oxide nanoparticles

The n-type semiconductor iron oxide is widely accessible and could break down organic contaminants through photocatalysis.[99] Moreover, the inherent magnetic effect facilitates the material's easy recovery from the aqueous medium, making it a viable photocatalytic material.[99] Fe_2O_3 semiconductors were found to be activated by visible light because of their low band gap energy (2.2 eV).[100] Recent work has shown that gold-doped iron oxide (Fe_2O_3) nanoparticles enhance photocatalytic efficiency for degrading organic dyes. For example, in the degradation of Disperse Blue 79, photocatalytic efficiency improved by 35% when Fe_2O_3 was doped with 1% gold.[101] However, challenges remain, such as the rapid recombination of electron–hole pairs and the need for longer reaction times. These limitations must be addressed to optimize large-scale applications in wastewater treatment and pollutant degradation.

The degrading properties of Fe^{3+} oxides under photocatalysis, including α-Fe_2O_3, γ-Fe_2O_3, α-FeOOH, β-FeOOH, and γ-FeOOH, were examined with the purpose of destroying harmful organic pollutants within the visible spectrum of the sun.[102] Low-band-gap iron oxide nanoparticles can be applied to photocatalytic reactions that occur within the visible portion of the solar spectrum.[103] The quick recombination of the photogenerated electron–hole pair, however, poses a significant obstacle to their viability in photocatalytic uses (Fig. 7).[104]

The recombination events of charge carriers are tuned, and the photocatalytic activity is enhanced through the doping of iron oxide nanostructures with varying metals or metal oxides and the construction of iron oxide-based nanocomposites. When exposed to sunlight, Au–Fe_2O_3 aerogels with different amounts of Au were tested as photocatalysts for breaking down the dye Disperse Blue 79. The metallic gold made Fe_2O_3 more photocatalytic by allowing more photogenerated electrons to build up and delaying the recombination process. So, oxidative species backed by photogenerated charge carriers attacked the azo dye molecules that had stuck to the surface.[105] Iron oxide-based photocatalysts are promising options for the removal of organic pollutants from wastewater due to their high recycling value, inexpensive cost, and practicality. Controlling the size, shape, and surface properties of iron oxide NPs, which play a key role in the detection and destruction of a variety of agrochemicals, can improve the efficacy and specificity of pesticide remediation operations.

6.4 Silica nanoparticles

Silica-based materials have received considerable interest in pesticide degradation owing to their elevated surface area, adjustable porosity, and chemical stability.[106] These characteristics render silica a superior support material for catalytic and photocatalytic applications. Using advanced oxidation processes, different active species, such as titanium dioxide or

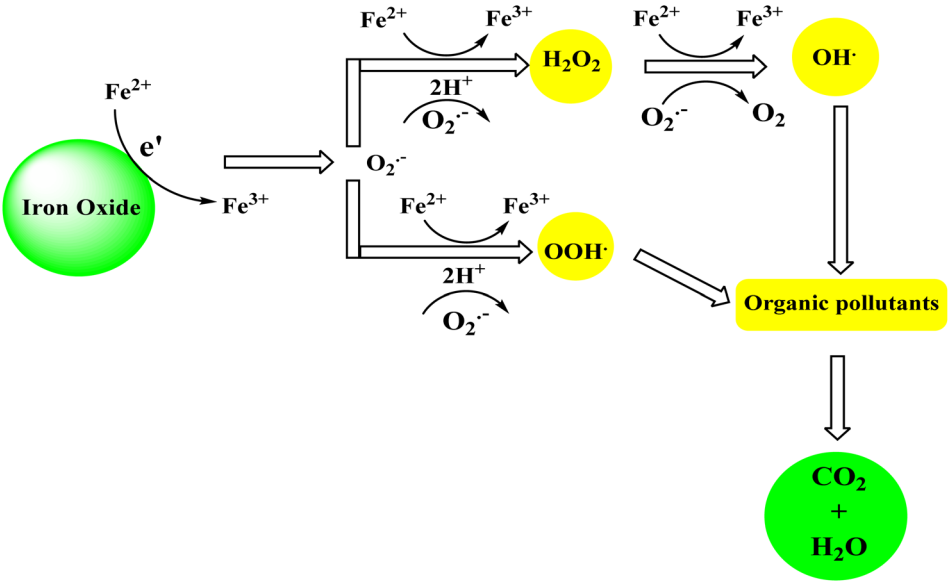

Fig. 7 Photo-degradation pathways for organic pollutants using iron oxide.

transition metal oxides, can be added to silica to make pesticides break down more quickly. Additionally, the biocompatibility and environmental safety of silica make it a favorable choice for sustainable applications. Nonetheless, the application of silica in pesticide degradation presents certain limitations.[107] The synthesis of functionalized silica materials is complex and costly, which may restrict large-scale applications. Silica by itself usually doesn't have much catalytic activity, so it needs to be changed with active agents. If this isn't done properly, it can cause problems for the environment. The regeneration and reuse of silica-based catalysts present challenges, as fouling or activity loss over multiple cycles may diminish their economic viability. Ongoing advancements in material science are enhancing silica's effectiveness in pesticide degradation, despite existing limitations. The integration of nano-engineered features has demonstrated potential in addressing several of these challenges.[108] Recent research highlights the significant role of silica nanoparticles (SiO_2 NPs) in environmental remediation, particularly in the extraction and degradation of pesticides.[109] The unique properties of SiO_2 NPs, such as their high surface area and tunable porosity (microporous, mesoporous, or hollow), make them ideal candidates for sorbent materials in solid-phase extraction (SPE) techniques. For instance, SiO_2 NPs functionalized with *N*-methylimidazole have demonstrated a remarkable ability to adsorb polar pesticides such as sulfonylurea from aqueous samples, with extraction efficiencies reaching up to 85%.[110] Similarly, when co-functionalized with polar cyanopropyltriethoxysilane (CNPrTEOS) and non-polar methyltrimethoxysilane (MTMOS), SiO_2 NPs have been successfully used to extract a variety of organophosphate pesticides, including diazinon, methidathion, and chlorpyrifos, from water samples, achieving extraction efficiencies exceeding 90%.[111] These pesticides were then quantified using high-performance liquid chromatography (HPLC) and gas chromatography-mass spectrometry (GC-MS) for precise analysis. Furthermore, silica molecular imprinted polymers (MIPs) made from SiO_2 NPs have been shown to enhance pesticide extraction, as demonstrated by significant increases in fluorescence or chemiluminescence intensity in response to pesticide concentrations.[112,113]

6.5 Cerium oxide

The potential uses of cerium dioxide (ceria) include fuel cell reformer, hydrocarbon fuel oxidation, and photocatalytic degradation of organic pollutants due to its non-toxicity, high thermal stability, specific chemical reactivity, and rigidity.[114,115] In addition to its exceptional catalytic capabilities, the ceria displays a broad band gap of 3.1 eV.[116] Several organophosphate pesticides have been photodegraded using it.[117,118] The temperature at which ceria is calcined has a significant impact on its photocatalytic capability. Organophosphate pesticides effectively adsorb on the surface of ceria by electrostatic contact with the hydroxyl functions of ceria nanoparticles because of their positive charge on phosphorus. The ceria nanoparticles calcined at a lower temperature effectively adsorb organophosphate insecticides, which photo-catalyzed to break them down.[119] It was shown that CeO_2–Fe_2O_3 composites were magnetically separable and could break down organophosphate insecticides quickly.[120] The CeO_2–Fe_2O_3 composite that was calcined at a temperature of 300–400 °C demonstrated the maximum degrading efficiency and kept its good magnetic characteristics, enabling simple separation. The CeO_2–Fe_2O_3 site was calcined at a temperature greater than 500 °C, which greatly reduced its surface area, active surface sites, and pore volume while concurrently increasing its crystallinity. At high calcination temperatures, these modifications decreased the photocatalytic activity of the CeO_2–Fe_2O_3 composite. When compared to commercially available CeO_2 nanoparticles, one-dimensional CeO_2 nanotubes (CeO_2-NT) with a hollow interior

demonstrated improved photocatalytic degradation of phenols.[121] Researchers found that the CeO_2 nanotubes' higher photocatalytic activity compared to the nanoparticles was since the photocatalytic behavior of ceria changes depending on its shape. It was shown that the CuO–CeO_2 catalyst could degrade methyl orange dye more effectively in the microwave, both with and without H_2O_2.[122] The process of organic pollutants photodegradation is accelerated by the hydroxyl radicals generated by H_2O_2. Rhodamine B dye was degraded by CeO_2–Y_2O_3 binary metal oxide nanostructures with a changeable molar ratio under UV-visible light, and the degradation efficiency was 98%.[123] The photocatalytic degradation of the CeO_2–Y_2O_3 nanocomposites was much better than that of the CeO_2 and Y_2O_3 components alone. Increased oxygen vacancies and a large active surface area were credited with the improved photocatalytic activity. The higher pH and H_2O_2 speeds up the photodegradation reactions by removing electrons from the conduction band and making more hydroxyl radicals.[123]

6.6 Copper oxides

With band gap energy of about 1.4 eV, copper oxides are cheap, widely accessible and environmentally benign p-type semiconductor materials.[124] CuO's tiny band gap makes it possible to absorb visible light, which is necessary for photocatalytic activation. There are two main types of copper oxide: CuO and Cu_2O. CuO has been discovered to have better photocatalytic activity than Cu_2O. The narrow bandgap energy, which promotes recombination of these pairs, hinders the photogenerated electron–hole pairs' potential for photocatalytic applications. Copper oxide nanoparticles have recently been functionalized or doped with different metal oxides (like TiO_2, ZnO, SiO_2, *etc.*), MoS_2, ionic liquids, reduced graphene oxide, and other things to make them better photocatalytic.[125] These modifications have changed the electronic structure, light absorption characteristics, and charge transport characteristics.[126]

The hierarchical 3D metal oxide–CuO nanostructures containing ZnO and Fe_3O_4 improved the photocatalytic properties for the breakdown of Congo red dye under solar light.[127] This might be because the n-type (ZnO/Fe_3O_4) and p-type (CuO) semiconductors have better charge separation at the p–n junction, which is where the two types of semiconductors meet (Fig. 8).[127] The band gap of pure CuO nanowires was changed by making hetero-architectural composites of Fe_3O_4–CuO (1.7 eV) and ZnO–CuO (1.5 eV), which have lower band gap energies than pure Fe_3O_4 (2.19 eV) and ZnO (3.34 eV), respectively.[128]

Doping ZnO with CuO leads to stoichiometric deficiencies and structural flaws in the nanomaterial. These flaws change the band gap energy and make the CuO–ZnO nanocomposite more photocatalytic. Additionally, the presence of exogenous electron acceptors—specifically, H_2O_2, peroxomonosulfate, and

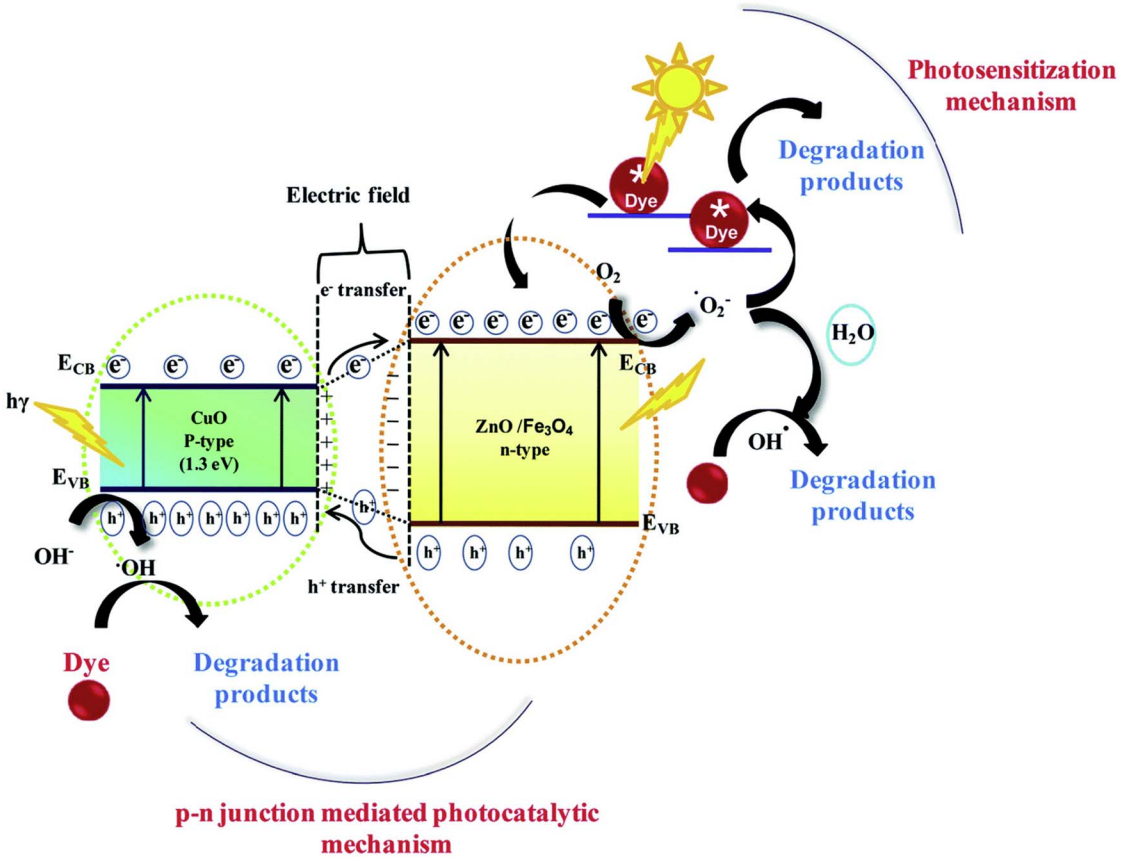

Fig. 8 Photocatalytic degradation pathway under the solar light irradiation using the p–n heterojunctions (ZnO–CuO or Fe_3O_4–CuO).[127] Copyright 2016 Elsevier.

peroxodisulfate—improved the photocatalytic degradation of textile dyes.[129] When exposed to visible light, the p–n junction-type semiconductor CuO–TiO_2 displayed good photocatalytic activity and broke down the azo dyes on the CuO–TiO_2–zeolite. Under visible light, CuOTiO_2–zeolite breaks down 90% of the methylene blue dye in 60 minutes, while zeolite, TiO_2–zeolite, and CuO–zeolite could remove 79.1%, 84.1%, and 85.2% of the dye, respectively, under the same circumstances. The photocatalytic activity under visible light exposure was boosted by bandgap engineering, active surface area-driven suppression of charge carrier recombination, and improved interfacial charge transfer.

6.7 Other metal oxides

Different metal oxides and their composites have also been able to photocatalytically degrade a variety of organic contaminants. The large band gap (3.6 eV) of the n-type semiconductor SnO_2 favors many photocatalytic processes.[130] Functionalizing SnO_2 with MgO prevented the recombination of photogenerated electrons and holes, enhancing the SnO_2–MgO nanocomposite's photocatalytic abilities. SnO_2–MgO nanocomposites have demonstrated the ability to photocatalytically degrade textile colorant compounds.[131]

It was shown that the hetero-structure of Fe_2O_3–WO_3, WO_3–TiO_2, and MoO_3–TiO_2 nanocomposites significantly improved the photocatalytic degradation.[132,133] The photocatalytic properties were improved by the n^+–n heterojunction of the rhombohedral α-Fe_2O_3 nanoparticles that were spread out evenly on the surface of the monoclinic WO_3 structures. The potential energy difference between Fe_2O_3 and WO_3 facilitates the separation of photogenerated charge carriers, which in turn enhances the photocatalytic destruction of organic contaminants (Fig. 9).[132] The p–n heterojunction structure of the Co_3O_4/$BiVO_4$ combination made it last a long time and destroy organic pollutants effectively through photocatalysis.[134] A decrease in the recombination rate of photogenerated charge carriers, according to photoluminescence research,[134] is what led to the increased photocatalytic activity.

Bi_2O_3 is a non-toxic p-type semiconductor with a band gap of 2.8 eV and a greater valence hole oxidation power.[135] It has gotten more attention because it breaks down different dyes. The pharmaceutical component acetaminophen (APAP) has been photodegraded using highly crystalline monodisperse β-Bi_2O_3 nanospheres.[136] A direct-hole oxidation method was suggested to break down APAP. The oxidation process produced comparatively fewer intermediates, which were linked to the high oxidation power of β-Bi_2O_3 nanospheres that had high mineralization efficiency. However, because of the quick recombination of electron–hole pairs produced by visible light, pure Bi_2O_3 exhibits limited photocatalytic efficiency. Adding transition metals or their oxides to Bi_2O_3 made it much better at breaking down organic pollutants through photocatalysis.[136] Matsumura *et al.* studied 2% Ce- and 1.5% Nd-doped Bi_2O_3 nanorods to see how they would break down organic dyes like Acid Yellow 29, Coomassie Brilliant Blue G250, and Acid Green 25.[137] They made it clear that the dopants can easily grab the photogenerated electrons from Bi_2O_3's conduction band. This slows down the recombination process and increases the photocatalytic activity of the nanomaterials.

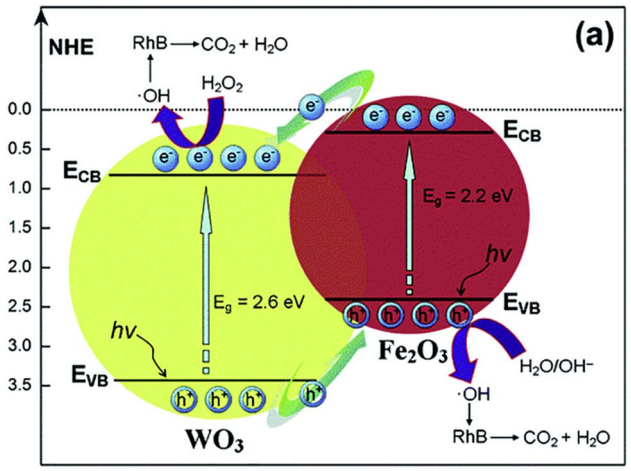

Fig. 9 Mechanism pathway of light-induced charge separation in the Fe_2O_3–WO_3 nanocomposite and photo-degradation of Rhodamine B.[132] Copyright 2014 Royal Society of Chemistry.

7. Pesticides adsorption using metal oxide nanoparticles

Adsorption is the physicochemical surface interaction between the adsorbate and the adsorbent.[138] Temperature, adsorbent–adsorbate interaction forces, medium pH, the presence of foreign components, concentration, and other parameters all affect the adsorption process.[139] Adsorbents should have a large surface area, adequate textural and surface characteristics, and sufficient mechanical stability to remove pesticides from wastewater quickly and efficiently.[140] Organic contaminants in wastewater act as adsorbates, slowly absorbing on adsorbent surfaces until an equilibrium between adsorbent and adsorbate is achieved.[141] Adsorption isotherms of many forms have been created to better understand the adsorption mechanism. Adsorption can be classified as chemisorption or physisorption depending on how they interact with the adsorbates.[141]

In physisorption, a physical interaction through which adsorbable molecule (the adsorptive) is adsorbed onto (surface physisorption) or into (intercalation) the metal oxide and their composites (adsorbent), through van der Waals forces, hydrogen bonding, or dipole–dipole attraction.[141] It falls into three general categories. The most well-known is pure physical adsorption, which is represented as full adsorbate recovery either with an increase in temperature or a drop in the concentration of the surrounding medium. It is a low-temperature phenomenon since the interaction forces get less as the temperature rises.[142] The second category, active adsorption, is characterized by complex formation leading to a partial recovery of the adsorbate. It is a high-temperature process that breaks down complexes above a particular temperature, after which they reach equilibrium.[143] The third

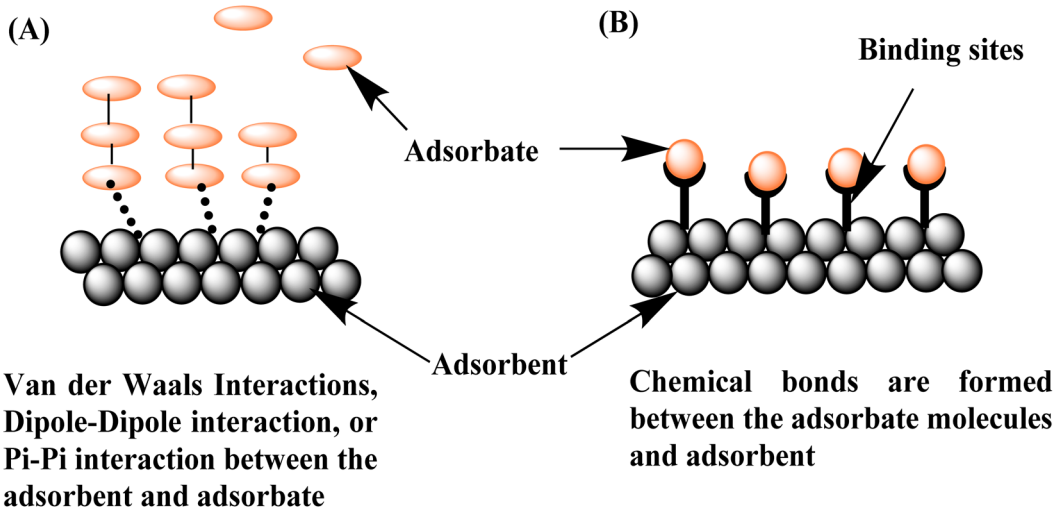

Fig. 10 The adsorption process in: (A) multiple layers (physisorption); and (B) single (chemisorption).

Table 6 Iron oxide-based nanomaterials and their composites as adsorbents for the removal of some pesticides

Adsorbent	Structure	Pesticide	Adsorption removal (%)	Ref.
Fe_3O_4@nSiO_2@mSiO_2	Core–shell microspheres	DDT	97%	159
MWCNTs/iron oxide/β-CD	Magnetic microspheres	*p*-Nitrophenol	69.6%	160
Mg/Al double layered hydroxide	Nanocrystalline particles	Humic acid	98.8	161
		Fulvic acid	97.6	

category is solution, in which the adsorbate is lost through diffusion and is not recovered in the adsorbent core. Chemisorption, in contrast to physisorption, is an adsorption process in which a modifying molecule (the adsorptive) and a surface (the adsorbent) make a chemical connection.[144] Chemisorption occurs either by radical processes or by ionic phenomena.[145] For further explanation, adsorption details are explained in Fig. 10 in both single and multiple-layer models.

The combination of various materials with diameters in the nanoscale range is called a nanocomposite. Combining the qualities of various materials to create a unique nanomaterial with enhanced and better chemical and physical capabilities is the goal of creating nanocomposites. The characteristics of the raw materials and the nanocomposites are very different. In comparison to conventional composite materials, nanocomposites have a huge surface area and a great surface-to-volume ratio.[146] In the realm of environmental studies, these composite materials have garnered interest, particularly for the removal of pesticides from various samples.[147] The main cause of this is the variety and special qualities that the nanomaterials provide, helping with the pesticide removal process. A nanotube is a long, hollow, tubular nanomaterial with a diameter that typically ranges in nanometers and a length that can vary from nm to mm. Because of their high aspect ratio and huge surface area, nanotubes can be used as effective adsorbents for a variety of chemicals. For a variety of uses, different materials, including enzymes, medications, hormones, and nucleic acids, have been entrapped in the lumen of these nanotubes and bonded to their surface. Because of their special qualities and vast surface area, carbon nanotubes (CNTs) and halloysite nanotubes (HNTs) have garnered a lot of interest in the field of environmental remediation.

7.1 Iron oxides

Among the elements that are most prevalent in the crust of the earth is iron. It has a wide range of oxidation states and is quite reactive. The oxidation state and chemical composition of iron determine the crystalline and structural characteristics of iron oxide nanoparticles. The major oxide forms of iron are magnetite (Fe_3O_4), maghemite (γ-Fe_2O_3), and hematite (α-Fe_2O_3).[148] The commonly utilized iron oxide nanoparticles, magnetite, include two separate forms of iron in distinct oxidation states: Fe^{2+} and Fe^{3+}. Iron oxide particles' nano-dimension offers super-paramagnetism and a high surface-area-to-volume ratio. Iron oxide nanoparticles have gotten a lot of attention for a wide range of uses because they are easy to make and change the surface of, they are easy to find, they have unique properties at the nanoscale level, they can separate magnetically, and they are not toxic.[149] For the adsorption of organic contaminants, iron oxide nanoparticles in their pure, doped, and composite forms have been widely employed.[150] After organic pollutants were adsorbed, separating the spent adsorbent from the wastewater has proven to be a significant challenge that calls for energy-intensive procedures like centrifugation. Even so, spent iron oxide-based adsorbents (after removing organic contaminants) are easily separated

Table 7 Titanium dioxide and their composites as adsorbents for the removal of pesticides from the wastewater

Adsorbent	Structure	Pesticides	Adsorbent amount	Contact time	Adsorption removal (%)	Ref
Nano-PP/TiO_2	Nano-polypropylene–titanium dioxide	Malathion	0.5 g L^{-1}	52 min	96	166
Cellulose/PANI/TiO_2	Cellulose/polyaniline/TiO_2 photocomposites	Acetamiprid	—	—	99	167
Nano-PP/TiO_2	Nano-polypropylene–titanium dioxide	Organophosphorous	2.25 g L^{-1}	32.2 min	69.3	168
Fe_3O_4@SiO_2@MOF/TiO_2 nanocomposite	Magnetic metal–organic framework–titanium dioxide nanocomposite	Fungicides (triadimenol, hexaconazole, diniconazole, myclobutanil, and tebuconazole)	—	—	93–95	169

when there is an outside magnetic field.[151] Iron oxide nanoparticles and their composites are therefore becoming more and more popular for use in wastewater treatment applications.[151]

Iron oxide (magnetite) nanoparticles were used to effectively remove chlorinated pesticides such as dieldrin, 2,4-dichlorophenoxyacetic acid (2,4-D), 2,4,5-trichlorophenoxyacetic acid (2,4,5-T), lindane (1,2,3,4,5,6-hexachlorocyclohexane), and hexachlorocyclohexane (α-HCH and γ-HCH) from the polluted water.[152,153] Their chemical structure determines how they adsorb on the iron oxide nanoparticles. Adding surfactants or surface-acting agents to the surface of iron oxide nanoparticles can make them better at absorbing things and being selective.[154] Much work has recently been done on the surface functionalization of iron oxide nanoparticles using a variety of organic species and functionalities, including polyacrylic acid, glutamic acid, organosilane, and so forth. An easy-to-use and practical method for separating used adsorbents must be combined with adsorption properties. The magnetic core of Fe_3O_4, the layer of nonporous silica ($nSiO_2$), and the layer of mesoporous silica ($mSiO_2$) on the outside of the magnetic mesoporous Fe_3O_4@$nSiO_2$@$mSiO_2$ nanoparticles showed a high rate of adsorption and the ability to remove the pesticide DDT.[155]

The immobilized Fe_2O_3 NPs considerably improved palygorskite's ability to retain phenarimol. According to Ouali *et al.*,[156] the material's adsorption capacity demonstrated stability over a two-week period, suggesting a wider application of this material for the long-term elimination of fenarimol. Using a similar strategy, iron oxide nanoparticles (NPs) trapped in mesoporous silica have been used to extract glyphosate from water. Immobilization significantly increased the magnetic adsorbent's surface area and porosity.[157] Fan *et al.*, used Fe_3O_4 nanoparticles and a simple, quick, and sensitive liquid–liquid extraction method to get rid of pyrethroid pesticides from tap, pond, river, and lake water, among others. Four types of pyrethroids were eliminated from water samples.[158]

In conclusion, changing the NPs' size, shape, and surface properties—which are important for finding and getting rid of different agrochemicals—can make these methods that use iron oxide NPs for pesticide cleanup more effective and selective. Because of how they are made, iron oxide nanoparticle surface modifications and mixing them with other nanomaterials will speed up the breakdown and removal of pesticides. Table 6 summarizes the performance of iron oxide-based nanomaterials and their composites as adsorbents for the removal of some pesticides.

7.2 Titanium oxide

Due to its favorable zero point charge (pH_{pzc} = 6–6.8), controlled structural and textural features, high surface reactivity, easy synthesis, and abundant availability of precursors, titanium dioxide (titania) nanomaterials have been investigated as an adsorbent.[152] Additionally, titanium functions as a photocatalytic substance to convert dangerous chemical molecules into harmless ones.[162] One of the most important conditions for

Table 8 Zinc oxide and their composites as adsorbents for the removal of pesticides from the wastewater

Adsorbent	Structure	Pesticide	Adsorption removal (%)	Ref.
CPZiONp-composite	Cucumber peels–zinc oxide nanoparticles composite	Metribuzin	66	172
CS–ZnONPs	Chitosan–zinc oxide nanoparticles	Permethrin	99	173
ZnO-Np	Zinc oxide nanoparticles	Simazine	72	174
ZnO-AC	ZnONP-doped activated carbon	Glyphosate	98	175

Table 9 Silicon dioxide and its composites as adsorbents for the removal of pesticides from the wastewater

Adsorbent	Structure	Pesticide	Adsorption removal (%)	Ref.
SiO_2	Silica nanoparticles	Azoxystrobin	95.21	181
SiO_2	Silica nanoparticles	Cypermethrin	88	182
Ni@SiO_2-G	Nickel@silica-graphene nanocomposites	Organothiophosphate	99	183
PAni:PPy@SiO_2	Polyaniline and polypyrrole with silicon dioxide	2,4-Dichlorophenol	97	184

the photodegradation of organic contaminants is their adsorption on the titania surface. The adsorption of organic pollutants facilitates the interface between the pesticide molecules and surface-active species, or photo-excited holes, and this starts the photo-oxidation events.[163] As a result, the adsorption effectiveness of the titania nanostructure controls the photo-degradation of organic contaminants. Titania's surface properties are influenced by the size, shape, crystallinity, and phase composition of the particles, which in turn affect the adsorption and photocatalytic destruction of organic contaminants. After being manufactured using a hydrothermal technique, the hierarchical nanostructured TiO_2, or TiO_2 1D nanorods, TiO_2 3D0D microspheres, and TiO_2 3D1D microspheres, showed morphological feature-dependent photocatalytic degradation of phenol. Compared to the 1D nanostructured equivalent, the organic pollutants degraded more quickly and efficiently in the hierarchical 3D nanostructured TiO_2 due to its larger degree of surface-active sites and desirable band gap energy.[164]

Six organochlorine pesticides were micro-extracted using mesoporous TiO_2 NPs.[165] These are hexachlororbenzene (HCB), *trans*-chlordane, *cis*-chlordane, *o*,*p*-DDT, *p*,*p*-DDT, and mirex. To remove the pesticides, solid-phase micro-extraction fiber was created using the NPs. Additionally, the produced fiber was utilized to find these chemicals in samples of lake and rainwater.[156] This enhanced adsorption is due to surface charge interactions and hydrogen bonding between the titanol groups of the aerogel and molecules' aromatic rings, nitrogen, and oxygen groups. The ability of the titania aerogel to regenerate adsorption sites at higher pH levels indicates its promise as a durable and efficient adsorbent for environmental cleanup.[152] Table 7 shows TiO_2 and their composites as adsorbents for the removal of pesticides from the wastewater.

7.3 Zinc oxides

ZnO NPs have distinct chemical and physical characteristics because of their high density at the surface's edge points and size. Additionally, these NPs have demonstrated strong photocatalytic activity, which is crucial for the breakdown of contaminants. Zinc oxide nanoparticles' surface functionalization improves both their catalytic and sensing capabilities. In a reported research study, it reveals that the adsorption capacity depends not only on the textural features of the material but also on the functionalization of the nanoparticles. It was found that 1-butyl-3-methylimidazolium tetrafluoroborate (BMTF-IL) functionalized zinc oxide nanoparticles show maximum adsorption capacity (148.3 mg g^{-1}) towards naphthalene removal as compared with CTAB functionalized (89.96 mg g^{-1}) and bare ZnO (66.80 mg g^{-1}) nanoparticles.[170]

Using ZnO NPs, permethrin—a neurotoxic insecticide that is frequently used in agriculture—was eliminated from the water sample. To create beads for the effective removal of the pesticide, NPs and chitosan were mixed. At room temperature and neutral pH, the pesticide's maximum removal efficacy (99%) was achieved using 0.5 g of beads. After three cycles, the beads showed themselves to be a promising material for treating water, with a 56% regeneration effectiveness.[171] Table 8 shows ZnO and their composites as adsorbents for the removal of pesticides from the wastewater.

7.4 Silicon dioxide

The spherical, porous particles known as silica nanoparticles (SiO_2 NPs) can be produced chemically or biologically.[176] Depending on the manufacturing conditions, the particles' porosity can be hollow, mesoporous, or microporous.[177] These particles can conjugate with a variety of chemical and biological substances by undergoing physical and chemical modification. Several environmental contaminants have been remedied using these NPs.[178] They have been applied to various pesticide detection, degradation, and extraction processes.

Pesticides have been extracted from a wide range of materials using solid-phase extraction (SPE). Owing to their substantial surface area, SiO_2 NPs are typically employed in the

Table 10 Silicon dioxide and its composites as adsorbents for the removal of pesticides from the wastewater

Adsorbent	Structure	Pesticide	Adsorption removal (%)	Ref.
MgO NPs	Magnesium oxide nanoparticles	Thiamethoxam	60.13	188
		Chlorpyriphos	80.53	
		Fenpropathrin	92.49	
MTBC	Triadimefon & dinotefuran	Triadimefon	86.42	189
		Dinotefuran	87.86	
MgO/Fe_3O_4-synthesized porous carbons	MgO/Fe_3O_4 modified coconut shell biochar	Atrazine	90.24	190
$MgFe_2O_4$	Mesoporous magnesium ferrite	Chlorpyrifos	91	191

production of sorbents for use in SPE techniques. These NPs' effectiveness and pesticide selectivity are increased when their surfaces are modified. SiO_2 NPs were used to extract sulfonylurea from water samples after they were functionalized with *N*-methylimidazole. Functionalization improved the polar pesticide's ability to bind to NP surfaces.[179] SiO_2 nanoparticles have also been used with cyanopropyltriethoxysilane (CNPrTEOS) and non-polar methyltrimethoxysilane (MTMOS) to get rid of organophosphate pesticides like diazinon, methidathion, malathion, chlorpyrifos, dicrotophos, and mathamidophos.[180] GC-MS or HPLC are then used to test the pesticides that were extracted from different sources using SiO_2 NPs. Table 9 shows SiO_2 and their composites as adsorbents for the removal of pesticides from the wastewater.

7.5 Magnesium oxide

It has been demonstrated that MgO nanoparticles are a promising adsorbent for organic pollutants and hazardous substances.[185,186] Magnesium oxide nanoparticles have a high concentration of low-coordinated sites, controlled textural features, are non-toxic, and have structural flaws, all of which increase their potential for adsorption applications. Furthermore, the adsorption of anionic dyes driven by electrostatic attraction was encouraged by the higher pH (12.4) of the zero-point charge (pH_{pzc}) of MgO. Chlorpyrifos (CPF), a persistent pesticide based on organophosphates, was highly adsorbed (3974 mg g^{-1}) into the hierarchical porous microspheres of MgO nanosheets that were made by precipitation and calcination.[187] Table 10 shows SiO_2 and their composites as adsorbents for the removal of pesticides from the wastewater.

7.6 Other metal oxides

A wide range of distinct metal oxide nanomaterials, such as SnO_2, Cu_2O, MoO_3, MoO_2, ThO_2, CeO_2, *etc.*, have been investigated as adsorbents for wastewater cleanup to remove organic contaminants in addition to iron oxides, titania, zinc oxides, and magnesium oxides. Due to their unique chemical and physical properties, as well as their structural flexibility, manganese oxides have attracted a lot of attention.[192] The MnO_2 nanoparticles' negatively charged surface made it easier for cationic contaminants to stick to them, which was especially true when the pH level was high.[193]

$Ni(OH)_2$ and NiO are significant transition metal hydroxides and oxides used in a variety of applications, such as energy storage devices.[194] The geometrical characteristics and chemical makeup of $Ni(OH)_2$ and NiO regulate their adsorption capacity. When used for effective pesticide removal, the chitosan modified AgO nanoparticles absorbed 99% of the permethrin insecticide from the aqueous solution (0.1 mg L^{-1}), 200% more effectively than pure chitosan (49%).[195]

It was shown that the zirconium-based metal–organic frameworks of UiO-67 could adsorptively remove the pesticides glyphosate and glufosinate from an aqueous solution. The presence of Zr–OH groups in large quantities within UiO-67 particles acted as an anchor for the effective adsorption of herbicides such as glyphosate (537 mg g^{-1}) and glufosinate (360 mg g^{-1}).[196]

8. Adsorptive removal *versus* photocatalytic degradation

In water treatment, two commonly employed techniques for removing organic pollutants are photocatalytic degradation and adsorption. Both methods are efficient and straightforward, but photocatalytic degradation is considered more sustainable than adsorption. While adsorption is a rapid, scalable, and cost-effective technique, it has limitations, as it generates waste after contaminants are absorbed. Additional environmental issues related to adsorption include the disposal of spent adsorbents, potential leaching of pollutants, and challenges in reusing adsorbents for future cycles.[180]

In contrast, photocatalytic degradation converts organic pollutants into less harmful substances or intermediates, eventually yielding mineral end products such as water (H_2O) and carbon dioxide (CO_2), thus minimizing waste.[181] Factors that influence photocatalytic efficiency include the photocatalyst's band-gap structure, the light source, and the ability of pollutants to adhere to the photocatalyst's surface. Enhanced adsorption on the photocatalyst surface aids in effective degradation, as it brings the pollutant molecules into close contact with the catalyst, improving photodegradation.

In summary, while adsorption serves as a useful step to facilitate photodegradation, photocatalytic degradation is ultimately a superior approach due to its ability to fully decompose organic pollutants into harmless byproducts. Nonetheless, effective adsorption is essential for achieving optimal photodegradation rates.

9. Linking adsorption and photocatalysis: synergistic approaches for pollutant remediation

Adsorption and photocatalysis are two distinct but complementary methods for effectively cleaning up organic pollutants. Surface interactions, like van der Waals forces, hydrogen bonding, or chemical bonding, characterize adsorption as a passive process that immobilizes pollutants in the adsorbent material. It exhibits energy efficiency and functions effectively across diverse environmental conditions without requiring external activation. Photocatalysis is an active process that uses light energy to excite electrons in semiconductors. This creates reactive species like hydroxyl radicals ($^{\bullet}OH$) and superoxide ions ($O_2^{\bullet-}$), which help break down pollutants into harmless end products. Photocatalysis necessitates specific conditions, including a suitable light source, optimized material properties, and precise environmental parameters.

The strategic combination of the two methods can enhance remediation efficiency. Adsorption serves as a fundamental capture mechanism, concentrating pollutants on the material's surface. This process removes contaminants from the aqueous phase and facilitates their subsequent degradation. Some materials, like TiO_2 composites with lots of surfaces or metal oxides that have been doped in, make it easier for reactive species made during photocatalysis to reach pollutants that have stuck to them. This process leads to the total mineralization of pollutants, which addresses challenges like incomplete degradation and secondary contamination. The interaction between adsorption and photocatalysis highlights their potential in creating multifunctional materials for advanced water treatment technologies. This section will examine the intricacies of photocatalytic mechanisms, developments in materials, and their roles in pollutant remediation.

10. Summary and future perspectives

Water is essential for the survival of all life forms, yet water pollution has escalated into a critical global issue, with contamination levels rising sharply over time. Numerous remediation techniques have been developed to preserve water quality, each tailored to address specific types of contaminants. Among these, metal oxides and their composites play a significant role as both photocatalytic and adsorptive materials in removing organic pollutants from wastewater. This comprehensive review examines the mechanisms of adsorption and photocatalysis in water treatment, focusing on the various structural, chemical, and surface properties of metal oxide nanomaterials that contribute to their high adsorption efficiency. Different adsorptive pathways—such as chemisorption, physisorption, and charge-driven interactions—demonstrate the versatility of these nanomaterials in capturing organic pollutants.

The application of metal oxide-based nanomaterials and their composites, including those for removing dyes and pesticides from wastewater, is discussed in depth. Materials such as graphene–metal oxide nanocomposites, iron oxides, magnesium oxides, titanium oxides, zinc oxides, tungsten oxides, and copper oxides have shown remarkable potential in this field. This analysis highlights the advancements, opportunities, and challenges associated with using these materials for water purification.

Adsorption is a widely recognized method for removing various contaminants, especially organic pollutants, by transferring them from an aqueous phase to a solid adsorbent phase. Although effective, it has limitations, including the generation of secondary pollutants. Adsorbents are employed across many industries; however, improvements in recyclability, adsorption efficiency, and eco-friendly decomposition of adsorbed pollutants are needed. Recently, metal oxide nanostructured materials and their composites have gained significant interest as photocatalytic agents, capable of degrading organic pollutants or converting them into environmentally benign products. For example, graphene–metal oxide composites, CuO, ZnO, MgO, and TiO_2 have demonstrated the ability to break down organic contaminants upon exposure to light, and these materials offer the advantage of reusability. However, challenges remain, particularly in scaling up the use of these materials for industrial applications with high efficiency.

Developing these materials sustainably and cost-effectively while achieving optimal performance under solar light exposure has been a persistent obstacle. Engineering the crystal structure and surface properties to enhance solar absorption efficiency is another critical challenge. Moving forward, the goal is to design advanced materials for sustainable water remediation that achieve zero pollutant discharge. This requires scientific innovation to create materials with a high specific surface area, optimal crystalline structures, and compatibility with environmentally friendly, economically viable manufacturing processes. The development of such "smart" materials is crucial for advancing water treatment technology toward sustainable and effective pollution control.

Adsorbent/photocatalyst regeneration is another crucial element that supports the process's sustainability and economic feasibility, prevents hazardous disposal, and preserves the equilibrium between water treatment and secondary waste management. Although it hasn't been thoroughly studied, the management of secondary trash is something that needs to be taken very seriously. Catalysis is one of the numerous uses for secondary waste, or used adsorbent.[197] As a result, the possibility of less pollution during the creation of metal oxide nanoparticles and their use in water treatment, as well as their use for other purposes, may help make the platform greener. It took a lot of work to develop economically viable, quicker, greener, and more effective methods for the removal or degradation of organic contaminants in a sustainable way and for the resurgence of safe and clean water for humans and other living things.

Data availability

No primary research results, software or code have been included and no new data were generated or analysed as part of this review.

Author contributions

The listed authors contributed to this work as follows: A. H. K. provided the concepts of the work; A. A., L. A., G. B. S. and H. S. M. A. interpreted the results. A. H. K., A. A. and H. S. M. A. prepared the manuscript; A. H. K. performed the revision before submission. All authors have read and agreed to the published version of the manuscript.

Conflicts of interest

The authors declare that there are no conflicts of interest.

Acknowledgements

The author H. S. M. Abd-Rabboh extends his appreciation to the Deanship of Scientific Research at King Khalid University for funding this work through a large Group Project under grant number (RGP.2/122/46).

References

1 G. Devendrapandi, X. Liu, R. Balu, R. Ayyamperumal, M. V. Arasu, M. Lavanya, V. R. M. Reddy, W. K. Kim and P. C. Karthika, *Environ. Res.*, 2024, 118404.
2 M. Wang, B. L. Bodirsky, R. Rijneveld, F. Beier, M. P. Bak, M. Batool, B. Droppers, A. Popp, M. T. van Vliet and M. Strokal, *Nat. Commun.*, 2024, **15**, 880.
3 M. M. Mekonnen, M. M. Kebede, B. W. Demeke, J. A. Carr, A. Chapagain, C. Dalin, P. Debaere, P. D'Odorico, L. Marston, C. Ray and L. Rosa, *Nat. Rev. Earth Environ.*, 2024, **5**, 890–905.
4 P. K. Singh, U. Kumar, I. Kumar, A. Dwivedi, P. Singh, S. Mishra, C. S. Seth and R. K. Sharma, *Environ. Sci. Pollut. Res.*, 2024, **31**, 56428–56462.
5 M. Rastogi, S. M. Kolur, A. Burud, T. Sadineni, M. Sekhar, R. Kumar and A. Rajput, *J. Geogr. Environ. Earth Sci. Int.*, 2024, **28**, 41–53.
6 F. Edition, *WHO Chron.*, 2011, **38**, 104–108.
7 R. Kaur, D. Choudhary, S. Bali, S. S. Bandral, V. Singh, M. A. Ahmad, N. Rani, T. G. Singh and B. Chandrasekaran, *Sci. Total Environ.*, 2024, 170113.
8 N. Talat, *Water Conserv. Glob. Clim. Change*, 2021, pp. 47–71.
9 L. Wang, C. Shi, L. Pan, X. Zhang and J. J. Zou, *Nanoscale*, 2020, **12**, 4790–4815.
10 R. Gusain, K. Gupta, P. Joshi and O. P. Khatri, *Adv. Colloid Interface Sci.*, 2019, **272**, 102009.
11 Y. Abubakar, H. Tijjani, C. Egbuna, C. O. Adetunji, S. Kala, T. L. Kryeziu, J. C. Ifemeje and K. C. Patrick-Iwuanyanwu, *Nat. Remedies Pest Dis. Weed Control*, 2020, pp. 29–42.
12 A. Shattuck, M. Werner, F. Mempel, Z. Dunivin and R. Galt, *Glob. Environ. Change*, 2023, **81**, 102693.
13 M. Tudi, H. Daniel Ruan, L. Wang, J. Lyu, R. Sadler, D. Connell, C. Chu and D. T. Phung, *Int. J. Environ. Res. Public Health*, 2021, **18**, 1112.
14 V. M. Pathak, V. K. Verma, B. S. Rawat, B. Kaur, N. Babu, A. Sharma, S. Dewali, M. Yadav, R. Kumari, S. Singh and A. Mohapatra, *Front. Microbiol.*, 2022, **13**, 962619.
15 K. K. Gautam and V. K. Tyagi, *J. Oleo Sci.*, 2006, **55**, 155–166.
16 S. G. Parte, A. D. Mohekar and A. S. Kharat, *Afr. J. Microbiol. Res.*, 2017, **11**, 992–1012.
17 M. L. Ortiz-Hernández, E. Sánchez-Salinas, E. Dantán-González and M. L. Castrejón-Godínez, *Biodegrad.: Life Sci.*, 2013, **10**, 251–287.
18 A. D. Kumar and N. Reddy, *Adverse Effects of Pesticides*, 2024.
19 R. Kaur, D. Choudhary, S. Bali, S. S. Bandral, V. Singh, M. A. Ahmad, N. Rani, T. G. Singh and B. Chandrasekaran, *Sci. Total Environ.*, 2024, 170113.
20 N. L. Mdeni, A. O. Adeniji, A. I. Okoh and O. O. Okoh, *Molecules*, 2022, **27**, 618.
21 P. G. Bertrand, *Pesticides*, 2019, 1–14.
22 P. M. Njogu, *Assessment Pollution Prediction Environ. Risks*, 2014.
23 O. G. Okon and U. E. Antia, *One Health Implications Agrochemicals*, 2023, pp. 441–460.
24 M. Shahid and M. S. Khan, *Pestic. Biochem. Physiol.*, 2022, **188**, 105272.
25 S. Antunes-Kenyon and G. Kennedy, *Massachusetts Dep. Agric. Resour.*, 2004.
26 D. K. Hazra and A. Purkait, *J. Pharmacogn. Phytochem.*, 2019, **8**, 686–693.
27 N. Chaudhary, K. K. Choudhary, S. Agrawal and M. Agrawal, *Pestic. Crop Prod.*, 2020, 159–180.
28 W. Draber, K. Tietjen, J. F. Kluth and A. Trebst, *Angew. Chem., Int. Ed.*, 1991, **30**, 1621–1633.
29 J. A. Martinez, Natural fungicides obtained from plants, *Fungicides for Plant and Animal Diseases*, ed. D. Dhanasekaran, InTech, 2012, vol. 10, p. 26336, ISBN: 978-953-307-804-5.
30 K. S. Rajmohan, R. Chandrasekaran and S. Varjani, *Indian J. Microbiol.*, 2020, **60**, 125–138.
31 M. L. Chen, X. W. Yao, Z. H. Diao, J. C. Jin, W. Qian, Y. Q. Yi, X. Chen and L. J. Kong, *Sep. Purif. Technol.*, 2023, **327**, 125013.
32 R. Gao, S. H. Gao, J. Li, Y. Su, F. Huang, B. Liang, L. Fan, J. Guo and A. Wang, *Engineering*, 2024, DOI: **10.1016/j.eng.2024.08.022**.
33 N. N. Roslan, H. L. H. Lau, N. A. A. Suhaimi, N. N. M. Shahri, S. B. Verinda, M. Nur, J. W. Lim and A. Usman, *Catalysts*, 2024, **14**, 189.
34 M. H. Shahverdian, F. Delfani, M. Z. Pedram, M. Hosseini, A. Sohani, H. Fazeli and H. Sayyaadi, *Sustainable Technol. Remediation Pollut.*, 2024, pp. 13–28.
35 O. A. Abiodun and O. O. Ayeleru, *Smart Nanomater. Environ. Appl.*, 2025, pp. 487–525.
36 R. Meena, M. M. Abdullah, V. Vasanthakumar, D. Ravichandran and S. Murugesan, *Ionics*, 2024, **30**, 5639–5650.
37 T. H. H. Al-Aqbi, T. Rafique, I. Mazahirul, S. M. H. Gardazi, W. Ahmad, A. Gupta, R. F. Alshehri and M. M. Ali, *Nanomater. Environ. Remediat.*, 2024.

38 Z. H. Diao and W. Chu, *Sci. Total Environ.*, 2021, **754**, 142155.
39 Y. Khan, H. Sadia, S. Z. Ali Shah, M. N. Khan, A. A. Shah, N. Ullah, M. F. Ullah, H. Bibi, O. T. Bafakeeh, N. B. Khedher and S. M. Eldin, *Catalysts*, 2022, **12**, 1386.
40 J. C. Védrine, *ChemSusChem*, 2019, **12**, 577–588.
41 L. Wang, C. Shi, L. Pan, X. Zhang and J. J. Zou, *Nanoscale*, 2020, **12**, 4790–4815.
42 K. V. Kumar, S. Gadipelli, B. Wood, K. A. Ramisetty, A. A. Stewart, C. A. Howard, D. J. Brett and F. Rodriguez-Reinoso, *J. Mater. Chem. A*, 2019, **7**, 10104–10137.
43 M. M. Sabzehmeidani, S. Mahnaee, M. Ghaedi, H. Heidari and V. A. Roy, *Mater. Adv.*, 2021, **2**, 598–627.
44 R. Gusain, K. Gupta, P. Joshi and O. P. Khatri, *Adv. Colloid Interface Sci.*, 2019, **272**, 102009.
45 S. Gautam, H. Agrawal, M. Thakur, A. Akbari, H. Sharda, R. Kaur and M. Amini, *J. Environ. Chem. Eng.*, 2020, **8**, 103726.
46 M. A. Gatou, A. Syrrakou, N. Lagopati and E. A. Pavlatou, *Reactions*, 2024, **5**, 135–194.
47 K. Kaur, R. Badru, P. P. Singh and S. Kaushal, *J. Environ. Chem. Eng.*, 2020, **8**, 103666.
48 A. Saravanan, P. S. Kumar, S. Jeevanantham, S. Karishma, B. Tajsabreen, P. R. Yaashikaa and B. Reshma, *Chemosphere*, 2021, **280**, 130595.
49 N. K. Elumalai, C. Vijila, R. Jose, A. Uddin and S. Ramakrishna, *Mater. Renewable Sustainable Energy*, 2015, **4**, 1–25.
50 R. B. Marcelino and C. C. Amorim, *Environ. Sci. Pollut. Res.*, 2019, **26**, 4155–4170.
51 A. Venkateshaiah, M. Černík and V. V. Padil, *Nanotechnol. Environ. Remediat.*, 2022, pp. 183–213.
52 P. Joshi, K. Gupta, R. Gusain and O. P. Khatri, *Metal Oxide Nanocomposites: Synthesis and Applications*, 2020, pp. 361–397.
53 R. Gusain, K. Gupta, P. Joshi and O. P. Khatri, *Adv. Colloid Interface Sci.*, 2019, **272**, 102009.
54 I. Ali, M. Suhail, E. C. López, R. A. Khattab and H. M. Albishri, *Arabian J. Geosci.*, 2022, **15**, 521.
55 M. A. Bhatti, A. A. Shah, K. F. Almani, A. Tahira, S. E. Chalangar, A. Chandio, O. Nur, M. Willander and Z. H. Ibupoto, *Ceram. Int.*, 2019, **45**, 23289–23297.
56 H. Chawla, S. Garg, J. Rohilla, Á. Szamosvölgyi, A. Efremova, I. Szenti, P. P. Ingole, A. Sápi, Z. Kónya and A. Chandra, *J. Cleaner Prod.*, 2022, **367**, 132923.
57 B. Karthikeyan, G. Gnanakumar and A. T. Alphonsa, *Nano Metal Oxides*, 2023.
58 *Handbook of Green and Sustainable Nanotechnology: Fundamentals, Developments and Applications*, ed. U. Shanker, C. M. Hussain and M. Rani, Springer Nature, 2023.
59 I. Abdelfattah and A. M. El-Shamy, *Sci. Rep.*, 2024, **14**, 27175.
60 A. A. M. Raub, R. Bahru, M. A. Mohamed, R. Latif, M. A. S. M. Haniff, K. Simarani and J. Yunas, *Nanotechnology*, 2024, **35**, 242004.
61 M. Ortiz-Martínez, J. A. Molina González, G. Ramírez García, A. Luna Bugallo, M. A. Justo Guerrero and E. C. Strupiechonski, *Environ. Toxicol. Chem.*, 2024, **43**, 1468–1484.
62 I. Arora, H. Chawla, A. Chandra, S. Sagadevan and S. Garg, *Inorg. Chem. Commun.*, 2022, **143**, 109700.
63 M. M. Mahlambi, C. J. Ngila and B. B. Mamba, *J. Nanomater.*, 2015, **2015**, 790173.
64 K. Nagaveni, M. S. Hegde, N. Ravishankar, G. N. Subbanna and G. Madras, *Langmuir*, 2004, **20**, 2900–2907.
65 A. T. Kuvarega and B. B. Mamba, *Crit. Rev. Solid State Mater. Sci.*, 2017, **42**, 295–346.
66 J. F. Budarz, E. M. Cooper, C. Gardner, E. Hodzic, P. L. Ferguson, C. K. Gunsch and M. R. Wiesner, *J. Hazard. Mater.*, 2019, **372**, 61–68.
67 R. Goswami, B. Kamal and A. Mishra, *Pestic. Bioremediation*, 2022, pp. 281–309.
68 S. N. Hoseini, A. K. Pirzaman, M. A. Aroon and A. E. Pirbazari, *J. Water Process Eng.*, 2017, **17**, 124–134.
69 M. Mehdipour, A. E. Pirbazari and G. Khayati, *Desalin. Water Treat.*, 2019, **155**, 329–340.
70 T. Kaur, A. Sraw, R. K. Wanchoo and A. P. Toor, *Sol. Energy*, 2018, **162**, 45–56.
71 R. de Oliveira and A. C. Sant'Ana, *Chemosphere*, 2023, **338**, 139490.
72 R. Fiorenza, A. Di Mauro, M. Cantarella, C. Iaria, E. M. Scalisi, M. V. Brundo, A. Gulino, L. Spitaleri, G. Nicotra, S. Dattilo and S. C. Carroccio, *Chem. Eng. J.*, 2020, **379**, 122309.
73 M. A. Rauf, M. A. Meetani and S. Hisaindee, *Desalination*, 2011, **276**, 13–27.
74 M. Janus, *Titanium Dioxide*, BoD – Books on Demand, 2017, ch. 2, 9789535134138.
75 D. Madan, K. P. Misra, S. Chattopadhyay and N. Halder, *Ceram. Sci. Eng.*, 2022, pp. 215–234.
76 K. Singh, S. Harish, J. Archana, M. Navaneethan, M. Shimomura and Y. Hayakawa, *Appl. Surf. Sci.*, 2019, **489**, 883–892.
77 M. Sattari, M. Farhadian, A. R. S. Nazar and M. Moghadam, *J. Photochem. Photobiol., A*, 2022, **431**, 114065.
78 S. R. Mirmasoomi, M. M. Ghazi and M. Galedari, *Sep. Purif. Technol.*, 2017, **175**, 418–427.
79 S. Nasseri, M. O. Borna, A. Esrafili, R. R. Kalantary, B. Kakavandi, M. Sillanpää and A. Asadi, *Appl. Phys. A*, 2018, **124**, 329–340.
80 A. H. C. Khavar, G. Moussavi, A. R. Mahjoub, M. Satari and P. Abdolmaleki, *Chem. Eng. J.*, 2018, **345**, 300–311.
81 G. Li, B. Wang, W. Q. Xu, Y. Han and Q. Sun, *Dyes Pigm.*, 2018, **155**, 265–275.
82 S. Raha and M. Ahmaruzzaman, *Nanoscale Adv.*, 2022, **4**, 1868–1925.
83 S. Maiti, S. Pal and K. K. Chattopadhyay, *CrystEngComm*, 2015, **17**, 9264–9295.
84 C. Hariharan, *Appl. Catal., A*, 2006, **304**, 55–61.
85 N. Daneshvar, D. Salari and A. R. Khataee, *J. Photochem. Photobiol., A*, 2004, **162**, 317–322.

86 N. Daneshvar, S. Aber, M. S. Dorraji, A. R. Khataee and M. H. Rasoulifard, *Sep. Purif. Technol.*, 2007, **58**, 91–98.
87 S. Navarro, J. Fenoll, N. Vela, E. Ruiz and G. Navarro, *J. Hazard. Mater.*, 2009, **172**, 1303–1310.
88 E. K. Kirupa Vasam Jino, *Adv. Environ. Technol.*, 2023, **9**, 124–137.
89 F. H. Abdullah, N. A. Bakar and M. A. Bakar, *J. Hazard. Mater.*, 2022, **424**, 127416.
90 N. Daneshvar, S. Aber, M. S. Dorraji, A. R. Khataee and M. H. Rasoulifard, *Sep. Purif. Technol.*, 2007, **58**, 91–98.
91 T. Iqbal, M. Afzal, B. A. Al-Asbahi, S. Afsheen, I. Maryam, A. Mushtaq, S. Kausar and A. Ashraf, *Mater. Sci. Semicond. Process.*, 2024, **173**, 108152.
92 S. M. Hosseini, I. A. Sarsari, P. Kameli and H. Salamati, *J. Alloys Compd.*, 2015, **640**, 408–415.
93 N. Güy, S. Çakar and M. Özacar, *J. Colloid Interface Sci.*, 2016, **466**, 128–137.
94 S. Bhatia, N. Verma and R. K. Bedi, *Opt. Mater.*, 2016, **62**, 392–398.
95 A. Nezamzadeh-Ejhieh and F. Khodabakhshi-Chermahini, *J. Ind. Eng. Chem.*, 2014, **20**, 695–704.
96 A. A. Khodja, T. Sehili, J. F. Pilichowski and P. Boule, *J. Photochem. Photobiol., A*, 2001, **141**, 231–239.
97 N. Daneshvar, S. Aber, M. S. Dorraji, A. R. Khataee and M. H. Rasoulifard, *Sep. Purif. Technol.*, 2007, **58**, 91–98.
98 S. Navarro, J. Fenoll, N. Vela, E. Ruiz and G. Navarro, *J. Hazard. Mater.*, 2009, **172**, 1303–1310.
99 W. Wu, C. Jiang and V. A. Roy, *Nanoscale*, 2015, **7**, 38–58.
100 M. Mishra and D. M. Chun, *Appl. Catal., A*, 2015, **498**, 126–141.
101 C. T. Wang, *J. Non-Cryst. Solids*, 2007, **353**, 1126–1133.
102 P. Hao, G. Wang, J. Wen, X. Li, Y. Suo, H. Zhan, S. Bi and W. Liu, *J. Environ. Chem. Eng.*, 2022, **10**, 107728.
103 N. S. M. Shahrodin, J. Jaafar, A. R. Rahmat, N. Yusof, M. H. Dzarfan Othman and M. A. Rahman, *Micro Nano Syst.*, 2020, **12**, 4–22.
104 N. Arif, M. N. Zafar, M. Batool, M. Humayun, M. A. Iqbal, M. Younis, L. Li, K. Li and Y. J. Zeng, *J. Mater. Chem. C*, 2024, **12**, 12653–12691.
105 V. Selvaraj, T. S. Karthika, C. Mansiya and M. Alagar, *J. Mol. Struct.*, 2021, **1224**, 129195.
106 E. Akhayere, D. Kavaz and A. Vaseashta, *Appl. Sci.*, 2022, **12**, 9279.
107 G. Bapat, C. Labade, A. Chaudhari and S. Zinjarde, *Adv. Colloid Interface Sci.*, 2016, **237**, 1–14.
108 X. P. Kong, B. H. Zhang and J. Wang, *J. Agric. Food Chem.*, 2021, **69**, 6735–6754.
109 D. Rawtani, N. Khatri, S. Tyagi and G. Pandey, *J. Environ. Manage.*, 2018, **206**, 749–762.
110 M. J. Lerma-García, E. F. Simó-Alfonso, M. Zougagh and Á. Ríos, *Talanta*, 2013, **105**, 372–378.
111 W. A. W. Ibrahim, W. N. W. Ismail and M. M. Sanagi, *J. Teknol.*, 2013, **62**, 3.
112 N. Sadegh, A. Asfaram, H. Javadian, H. Haddadi and E. Sharifpour, *J. Chromatogr. B*, 2021, **1171**, 122640.
113 S. B. Al Massati, Synthesis and characterization of molecularly imprinted polymers for the selective extraction of organophosphorus pesticides from vegetable oils, *Doctoral dissertation*, Université Pierre et Marie Curie-Paris VI, 2017.
114 N. Farooq, Z. ur Rehman, M. I. Khan, W. Iman, I. Kanwal, S. Khan, A. Shanableh, S. Manzoor and R. Luque, *Inorg. Chem. Commun.*, 2024, 113086.
115 R. Gusain, K. Gupta, P. Joshi and O. P. Khatri, *Adv. Colloid Interface Sci.*, 2019, **272**, 102009.
116 S. Tsunekawa, J. T. Wang and Y. Kawazoe, *J. Alloys Compd.*, 2006, **408**, 1145–1148.
117 A. Salerno, I. Pitault, T. Devers, J. Pelletier and S. Briançon, *Environ. Toxicol. Pharmacol.*, 2017, **53**, 18–28.
118 R. Fiorenza, S. A. Balsamo, L. D'Urso, S. Sciré, M. V. Brundo, R. Pecoraro, E. M. Scalisi, V. Privitera and G. Impellizzeri, *Catalysts*, 2020, **10**, 446.
119 P. Janos, P. Kuran, M. Kormunda, V. Stengl, T. M. Grygar, M. Dosek, M. Stastny, J. Ederer, V. Pilarova and L. Vrtoch, *J. Rare Earths*, 2014, **32**, 360–370.
120 P. Janoš, P. Kuráň, V. Pilařová, J. Trögl, M. Šťastný, O. Pelant, J. Henych, S. Bakardjieva, O. Životský, M. Kormunda and K. Mazanec, *Chem. Eng. J.*, 2015, **262**, 747–755.
121 M. K. Diallo, *SSRN Electron. J.*, 2022, 4441684.
122 D. Xiong, C. Fei, L. Qizeng and D. Ping, *Catal. Today*, 2014, **226**, 171–178.
123 C. M. Magdalane, K. Kaviyarasu, J. J. Vijaya, B. Siddhardha, B. Jeyaraj, J. Kennedy and M. Maaza, *J. Alloys Compd.*, 2017, **727**, 1324–1337.
124 T. K. Wong, S. Zhuk, S. Masudy-Panah and G. K. Dalapati, *Materials*, 2016, **9**, 271.
125 V. Molahalli, A. Sharma, K. Bijapur, G. Soman, A. Shetty, B. Sirichandana, B. M. Patel, N. Chattham and G. Hegde, *ACS Nano*, 2024, **18**, 33.
126 P. Raizada, A. Sudhaik, S. Patial, V. Hasija, A. A. P. Khan, P. Singh, S. Gautam, M. Kaur and V. H. Nguyen, *Arabian J. Chem.*, 2020, **13**, 8424–8457.
127 D. Malwal and P. Gopinath, *Catal. Sci. Technol.*, 2016, **6**, 4458–4472.
128 A. A. Umar and M. Oyama, *Cryst. Growth Des.*, 2007, **7**, 2404–2409.
129 S. Jung and K. Yong, *Chem. Commun.*, 2011, **47**, 2643–2645.
130 A. Chawla, A. Sudhaik, P. Raizada, A. A. P. Khan, A. Singh, Q. Van Le, T. Ahamad, S. M. Alshehri, A. M. Asiri and P. Singh, *J. Ind. Eng. Chem.*, 2022, **116**, 515–542.
131 N. Bayal and P. Jeevanandam, *Mater. Res. Bull.*, 2013, **48**, 3790–3799.
132 S. Bai, K. Zhang, J. Sun, R. Luo, D. Li and A. Chen, *CrystEngComm*, 2014, **16**, 3289–3295.
133 S. Bai, H. Liu, J. Sun, Y. Tian, S. Chen, J. Song, R. Luo, D. Li, A. Chen and C. C. Liu, *Appl. Surf. Sci.*, 2015, **338**, 61–68.
134 M. Long, W. Cai, J. Cai, B. Zhou, X. Chai and Y. Wu, *J. Phys. Chem. B*, 2006, **110**, 20211–20216.
135 H. Chawla, S. Garg, S. Upadhyay, J. Rohilla, Á. Szamosvölgyi, A. Sapi, P. P. Ingole, S. Sagadevan, Z. Konya and A. Chandra, *Chemosphere*, 2022, **297**, 134122.
136 H. Chawla, A. Chandra, P. P. Ingole and S. Garg, *J. Ind. Eng. Chem.*, 2021, **95**, 1–15.

137 W. Raza, M. M. Haque, M. Muneer, T. Harada and M. Matsumura, *J. Alloys Compd.*, 2015, **648**, 641–650.
138 X. W. Yao, X. Chen, M. L. Chen, N. J. Feng, L. Y. Tong, Y. Q. Yi, W. Qian and Z. H. Diao, *Process Saf. Environ. Prot.*, 2024, **186**, 808–818.
139 R. Natarajan, K. Saikia, S. K. Ponnusamy, A. K. Rathankumar, D. S. Rajendran, S. Venkataraman, D. B. Tannani, V. Arvind, T. Somanna, K. Banerjee and N. Mohideen, *Chemosphere*, 2022, **287**, 131958.
140 M. H. Dehghani, S. Ahmadi, S. Ghosh, M. S. Khan, A. Othmani, W. A. Khanday, Ö. Gökkuş, C. Osagie, M. Ahmaruzzaman, S. R. Mishra and E. C. Lima, *Appl. Surf. Sci. Adv.*, 2024, **19**, 100558.
141 H. H. Shanaah, E. F. Alzaimoor, S. Rashdan, A. A. Abdalhafith and A. H. Kamel, *Sustainability*, 2023, **15**, 7336.
142 L. W. Bruch, M. W. Cole and E. Zaremba, *Phys. Adsorpt. Forces Phenom.*, 2007.
143 D. C. Wang, Y. H. Li, D. Li, Y. Z. Xia and J. P. Zhang, *Renewable Sustainable Energy Rev.*, 2010, **14**, 344–353.
144 M. Králik, *Chem. Pap.*, 2014, **68**, 1625–1638.
145 A. Clark, *Chemisorptive Bond Basic Concepts*, 2012, vol. 32.
146 C. C. Okpala, *Int. J. Eng. Res. Dev.*, 2013, **8**, 17–23.
147 M. H. Dehghani, S. Ahmadi, S. Ghosh, M. S. Khan, A. Othmani, W. A. Khanday, Ö. Gökkuş, C. Osagie, M. Ahmaruzzaman, S. R. Mishra and E. C. Lima, *Appl. Surf. Sci. Adv.*, 2024, **19**, 100558.
148 R. M. Cornell and U. Schwertmann, *Iron Oxides Struct. Prop. React. Uses*, 2003, vol. 664.
149 M. E. McHenry and D. E. Laughlin, *Acta Mater.*, 2000, **48**, 223–238.
150 A. M. Gutierrez, T. D. Dziubla and J. Z. Hilt, *Rev. Environ. Health*, 2017, **32**, 111–117.
151 F. X. Dong, L. Yan, X. H. Zhou, S. T. Huang, J. Y. Liang, W. X. Zhang, Z. W. Guo, P. R. Guo, W. Qian, L. J. Kong and W. Chu, *J. Hazard. Mater.*, 2021, **416**, 125930.
152 R. Gusain, K. Gupta, P. Joshi and O. P. Khatri, *Adv. Colloid Interface Sci.*, 2019, **272**, 102009.
153 P. Kajitvichyanukul, V. H. Nguyen, T. Boonupara, L. A. P. Thi, A. Watcharenwong, S. Sumitsawan and P. Udomkun, *Environ. Res.*, 2022, **212**, 113336.
154 Y. Wang, R. Cheng, Z. Wen and L. Zhao, *Chem. Eng. J.*, 2012, **181**, 823–827.
155 F. Liu, H. Tian and J. He, *J. Colloid Interface Sci.*, 2014, **419**, 68–72.
156 A. Ouali, L. S. Belaroui, A. Bengueddach, A. L. Galindo and A. Peña, *Appl. Clay Sci.*, 2015, **115**, 67–75.
157 S. Fiorilli, L. Rivoira, G. Calì, M. Appendini, M. C. Bruzzoniti, M. Coïsson and B. Onida, *Appl. Surf. Sci.*, 2017, **411**, 457–465.
158 C. Fan, Y. Liang, H. Dong, G. Ding, W. Zhang, G. Tang, J. Yang, D. Kong, D. Wang and Y. Cao, *Anal. Chim. Acta*, 2017, **975**, 20–29.
159 F. Liu, H. Tian and J. He, *J. Colloid Interface Sci.*, 2014, **419**, 68–72.
160 W. Liu, X. Jiang and X. Chen, *Appl. Surf. Sci.*, 2014, **320**, 764–771.
161 L. Fang, J. Hou, C. Xu, Y. Wang, J. Li, F. Xiao and D. Wang, *Appl. Surf. Sci.*, 2018, **442**, 45–53.
162 A. Markowska-Szczupak, M. Endo-Kimura, O. Paszkiewicz and E. Kowalska, *Nanomaterials*, 2020, **10**, 2065.
163 U. Qumar, J. Z. Hassan, R. A. Bhatti, A. Raza, G. Nazir, W. Nabgan and M. Ikram, *J. Mater. Sci. Technol.*, 2022, **131**, 122–166.
164 J. Zhang, G. Xiao, F. X. Xiao and B. Liu, *Mater. Chem. Front.*, 2017, **1**, 231–250.
165 M. Hadei, A. Mesdaghinia, R. Nabizadeh, A. H. Mahvi, S. Rabbani and K. Naddafi, *Environ. Sci. Pollut. Res.*, 2021, **28**, 13055–13071.
166 M. Gholami, Z. Mosakhani, A. Barazandeh and H. Karyab, *J. Environ. Health Sci. Eng.*, 2023, **21**, 35–45.
167 T. Benhalima, M. Mokhtari and H. Ferfera-Harrar, *J. Water Process Eng.*, 2024, **57**, 104670.
168 A. Barazandeh, H. A. Jamali and H. Karyab, *Korean J. Chem. Eng.*, 2021, **38**, 2436–2445.
169 H. Su, Y. Lin, Z. Wang, Y. L. E. Wong, X. Chen and T. W. D. Chan, *J. Chromatogr. A*, 2016, **1466**, 21–28.
170 Y. Kaur, Y. Bhatia, S. Chaudhary and G. R. Chaudhary, *J. Mol. Liq.*, 2017, **234**, 94–103.
171 S. M. Dehaghi, B. Rahmanifar, A. M. Moradi and P. A. Azar, *J. Saudi Chem. Soc.*, 2014, **18**(4), 348–355.
172 A. U. Haq, M. Saeed, M. Muneer, M. A. Jamal, T. Maqbool and T. Tahir, *Sci. Rep.*, 2022, **12**, 5840.
173 S. M. Dehaghi, B. Rahmanifar, A. M. Moradi and P. A. Azar, *J. Saudi Chem. Soc.*, 2014, **18**(4), 348–355.
174 Z. Samuel, M. O. Ojemaye, O. O. Okoh and A. I. Okoh, *Mater. Today Commun.*, 2023, **34**, 105435.
175 K. Sen and N. K. Mondal, *J. Ind. Eng. Chem.*, 2024, **136**, 150–166.
176 L. K. Harada, M. Guilger-Casagrande, T. Germano-Costa, N. Bilesky-José, L. F. Fraceto and R. Lima, *Silicon Adv. Sustainable Agric. Hum. Health*, 2024, pp. 191–208.
177 S. H. Wu, C. Y. Mou and H. P. Lin, *Chem. Soc. Rev.*, 2013, **42**(9), 3862–3875.
178 J. Tejedor, V. H. Guerrero, K. Vizuete and A. Debut, *J. Phys.: Conf. Ser.*, 2022, **2238**, 012005.
179 V. Bueno, *Synthesis, Characterization and Application of Pesticide-Encapsulated Silica Nanoparticles in Agriculture*, McGill University, Canada, 2021.
180 N. Muhamad, W. A. W. Ibrahim and M. M. Sanagi, *J. Teknol.*, 2014, **71**(5), 57–62.
181 F. Malhat, O. I. Abdallah, M. Hussien, A. M. Youssef, F. M. Alminderej and S. M. Saleh, *Coatings*, 2023, **13**(7), 1286.
182 S. N. Ul Ain, M. S. Khan, N. Riaz, A. Khan, A. Sarwar, A. Khalid, A. Jan, Q. Mahmood and A. Al-Harrasi, *ACS Omega*, 2024, **9**(12), 13803–13817.
183 G. Wu, C. Zhang, C. Liu, X. Li, Y. Cai, M. Wang, D. Chu, L. Liu, T. Meng and Z. Chen, *J. Hazard. Mater.*, 2023, **457**, 131788.
184 A. Bekhoukh, M. Kiari, I. Moulefera, L. Sabantina and A. Benyoucef, *Polymers*, 2023, **15**(9), 2032.
185 M. Nagpal and R. Kakkar, *Sep. Purif. Technol.*, 2019, **211**, 522–539.

186 A. Fouda, S. E. D. Hassan, E. Saied and M. F. Hamza, *J. Environ. Chem. Eng.*, 2021, **9**(4), 105346.
187 L. Sharma and R. Kakkar, *ACS Appl. Mater. Interfaces*, 2017, **9**(44), 38629–38642.
188 A. Kar, S. Deole, B. G. Gadratagi, N. Patil, G. Guru-Pirasanna-Pandi, B. Mahapatra and T. Adak, *Environ. Sci. Pollut. Res.*, 2023, **30**(45), 101467–101482.
189 X. Chen, X. W. Yao, Y. Diao, H. Liu, M. L. Chen, N. J. Feng, W. Qian, X. H. Zhou, P. R. Guo, L. J. Kong and Z. H. Diao, *Sep. Purif. Technol.*, 2024, **336**, 126213.
190 L. Y. George, L. Ma, W. Zhang and G. Yao, *Environ. Sci. Eur.*, 2023, **35**(1), 21.
191 L. Sharma and R. Kakkar, *J. Environ. Chem. Eng.*, 2018, **6**(6), 6891–6903.
192 S. Chaudhary, Y. Kaur, A. Umar and G. R. Chaudhary, *J. Mol. Liq.*, 2016, **224**, 1294–1304.
193 A. K. Sharma, R. K. Tiwari and M. S. Gaur, *Arabian J. Chem.*, 2016, **9**, 1755–1764.
194 D. U. Lee, J. Fu, M. G. Park, H. Liu, A. Ghorbani Kashkooli and Z. Chen, *Nano Lett.*, 2016, **16**(3), 1794–1802.
195 M. V. Bagal and S. Raut-Jadhav, in *Handbook of Nanomaterials for Wastewater Treatment*, Elsevier, 2021, pp. 957–1007.
196 F. Fang, Q. Lv, P. Li, Y. Tao, Y. Zhang, Y. Zhou, X. Li and J. Li, *J. Environ. Chem. Eng.*, 2022, **10**(3), 107824.
197 T. Velempini, M. E. H. Ahamed and K. Pillay, *Results Chem.*, 2023, **5**, 100901.

Résumé

Des matières premières peu coûteuses comme Lemna minor ont été transformées en charbons actifs par activation acide à l'aide de H_3PO_4 (ALM-P) et d'acide citrique (ALM-C). Les analyses BET indiquent des surfaces spécifiques de 208,5 et 216,1 $m^2 \cdot g^{-1}$ respectivement, tandis que le spectre FTIR révèle la présence de fonctions hydoxyle, carboxyle, amide et phosphate. Ces fonctionnalités favorisent la fixation du colorant Bezaktiv Red S-MAX via une adsorption chimique ou échange ionique, avec une capacité maximale en monocouche de 16,86 et 7,69 $mg \cdot g^{-1}$. Le processus suit un modèle cinétique pseudo-second ordre et une isotherme de Langmuir, partiellement régulé par une diffusion intra-particules. L'adsorption est spontanée et endothermique, avec un rendement de 77,7 % à pH 3, 25 °C en 90 min.

Par ailleurs, un catalyseur nanocomposite $NiFe_2O_4$ modifié avec poly(aniline-co-o-toluidine) (POAT) a permis une réduction rapide (95 % en 1 h, solution 20 $mg \cdot L^{-1}$) de 4-nitrophénol, démontrant une efficacité élevée et une adaptation aux traitements rapides des eaux usées. L'analyse optique a mis en évidence une énergie de gap de 1,24 eV, indiquant une bonne absorption dans le visible et une pertinence pour des applications photo-catalytiques. Les caractérisations (EDX, XRD, FTIR, SEM) confirment la bonne synthèse et structure du nanocomposite. Celui-ci conserve une stabilité notable avec une réutilisation possible au moins quatre cycles, et sa séparation par un champ magnétique externe renforce sa facilité d'utilisation dans des processus de dépollution.

Mots Clés : Adsorption, Lemna minor, Bezaktiv-Red, Réduction, Nanocomposite, 4-Nitrophénol.

Abstract

Low-cost raw materials such as *Lemna minor* were converted into activated carbons through acid activation using H_3PO_4 (ALM-P) and citric acid (ALM-C). BET analyses indicated specific surface areas of 208.5 and 216.1 $m^2 \cdot g^{-1}$, respectively, while FTIR spectra revealed the presence of hydroxyl, carboxyl, amide, and phosphate functional groups. These functionalities promote the binding of the Bezaktiv Red S-MAX dye through chemical adsorption or ion exchange, with maximum monolayer adsorption capacities of 16.86 and 7.69 $mg \cdot g^{-1}$. The process follows a pseudo-second-order kinetic model and fits the Langmuir isotherm, with partial control by intra-particle diffusion. Adsorption was found to be spontaneous and endothermic, achieving a removal efficiency of 77.7% at pH 3 and 25 °C within 90 minutes.

In addition, a $NiFe_2O_4$ nanocomposite catalyst modified with poly(aniline-co-o-toluidine) (PAOT) enabled rapid reduction of 4-nitrophenol (95% within 1 h, 20 $mg \cdot L^{-1}$ solution), demonstrating high efficiency and suitability for fast industrial wastewater treatment. Optical analysis revealed a band gap energy of 1.24 eV, indicating strong visible light absorption and potential for photocatalytic applications. Characterization techniques (EDX, XRD, FTIR, SEM) confirmed the successful synthesis and structure of the nanocomposite. The material also exhibited notable stability, maintaining reusability for at least four cycles, and its separation by an external magnetic field further enhances its practicality in water depollution processes.

Keywords: Adsorption, Lemna minor, Bezaktiv-Red, Reduction, Nanocomposite,4-Nitrophenol.

ملخص:

تم تحويل المواد الخام منخفضة التكلفة مثل نبات" لمنة صغرى - عدس الماء" إلى كربونات نشطة من خلال التنشيط الحمضي باستخدام حمض الفسفوريك (ALM-P) وحمض الستريك (ALM-C) أشارت تحليلات BET إلى مساحات سطحية محددة تبلغ 208.5 و216.1 $م^2 \cdot غ^{-1}$ على التوالي، بينما كشفت أطياف "FTIR" عن وجود مجموعات وظيفية هيدروكسيل وكربوكسيل وأميد وفوسفات. تُعزز هذه الوظائف ارتباط صبغة " Bezaktiv Red S-MAX"من خلال الامتزاز الكيميائي أو تبادل الأيونات، بأقصى سعات امتصاص أحادية الطبقة والتي تبلغ (16.86 - 7.69 $ملغ \cdot غ^{-1}$). العملية تتبع نموذج حركي من الدرجة الثانية الزائفة وتتناسب مع نموذج لانجمويرالامتزازي" معادلة خط لانجمويرالمتساوي الحرارة، مع تحكم جزئي من خلال الانتشار داخل الجسيمات. كما تبين أن الامتزاز كان تلقائيًا وماصًا للحرارة، حيث تم تحقيق كفاءة إزالة بنسبة 77.7% عند درجة حموضة 3 ودرجة حرارة 25 درجة مئوية خلال مدة 90 دقيقة.

بالإضافة إلى ذلك، تمكن محفز نانو مركب من $NiFe_2O_4$ معدل بـ poly(aniline-co-o-toluidine) (PAOT) من تقليل سريع لـ بارا-نيتروفينول "4-نيتروفينول" (95% خلال ساعة واحدة، محلول بتركيز 20 $ملغ \cdot لتر^{-1}$)، مما يظهر كفاءة عالية وملاءمة لعمليات معالجة سريعة لمياه الصرف الصناعي. كما كشفت التحليلات البصرية عن طاقة فجوة قدرها 1.24 إلكترون فولت، مما يشير إلى امتصاص قوي للضوء المرئي وإمكانية التطبيقات الضوئية التحفيزية. وايضا أكدت تقنيات التوصيف (EDX ، XRD، FTIR، SEM)النجاح في تخليق المركب النانوي. وأظهرت المادة أيضًا استقرارًا ملحوظًا، حيث حافظت على قابليتها لإعادة الاستخدام لمدة لا تقل عن أربع دورات، كما أن فصلها بواسطة مجال مغناطيسي خارجي يعزز من فاعلياتها في عمليات تنقية المياه.

الكلمات المفتاحية: الامتزاز، لمنة صغرى - عدس الماء ، Bezaktiv-Red ، الاختزال، مركب نانو، بارا-نيتروفينول "4-نيتروفينول".